

First Principles Design of Nanomaterials: Tuning Electronic, Magnetic, Chemical and Topological Properties

A Thesis

Submitted For the Degree of
DOCTOR OF PHILOSOPHY
in the Faculty of Science

by

Rajdeep Banerjee



THEORETICAL SCIENCES UNIT
JAWAHARLAL NEHRU CENTRE FOR ADVANCED SCIENTIFIC
RESEARCH
Bangalore – 560 064, India

MAY 2019

To My Family

DECLARATION

I hereby declare that the matter embodied in the thesis entitled “**First Principles Design of Nanomaterials: Tuning Electronic, Magnetic, Chemical and Topological Properties**” is the result of investigations carried out by me at the Theoretical Sciences Unit, Jawaharlal Nehru Centre for Advanced Scientific Research, Bangalore, India under the supervision of Prof. Shobhana Narasimhan and that it has not been submitted elsewhere for the award of any degree or diploma.

In keeping with the general practice in reporting scientific observations, due acknowledgement has been made whenever the work described is based on the findings of other investigators. Any omission that might have occurred by oversight or error of judgement is regretted.

Rajdeep Banerjee

CERTIFICATE

I hereby certify that the matter embodied in this thesis entitled “**First Principles Design of Nanomaterials: Tuning Electronic, Magnetic, Chemical and Topological Properties**” has been carried out by Mr. Rajdeep Banerjee at the Theoretical Sciences Unit, Jawaharlal Nehru Centre for Advanced Scientific Research, Bangalore, India under my supervision and that it has not been submitted elsewhere for the award of any degree or diploma.

Prof. Shobhana Narasimhan
(Research Supervisor)

Acknowledgements

First of all, I would like to thank my Ph.D. supervisor Prof. Shobhana Narasimhan for her support and guidance throughout the course of my Ph.D. She has helped me develop an understanding of the basics, and showed me how to define a problem, attack it from different perspectives, and finally present the results in a way that is easily comprehensible. Moreover, she provided the atmosphere for independent research, and instilled in me the qualities of a good researcher. Her collaborations both in India, and abroad, made it possible for me to visit different research groups across the globe, and learn different techniques that I have employed in my research work. These visits have enriched me both academically, and culturally. She was there, whenever I needed valuable guidance from her, even if it was outside the field of research. She always encouraged me to enhance my poetry writing skills, and I enjoyed those long discussions about different poets and their poems. I will miss the cakes she baked for us for our birthdays. Most importantly, she created a wonderful research atmosphere in the lab which propelled the research work during my Ph.D.

I would like to thank my experimental and theoretical collaborators: Somesh Kumar Bhattacharya, Sananda Biswas, Manish Jain, Awadhesh Narayan, Tanmoy Das, Sreebrata Goswami, Krishna Kumar Menon, Sreetosh Goswami, Debabrata Sen-gupta, Ashish Kundu, Vincent Repain, Syvie Rousset, Yannick J. Dappe, Alexander Smogunov, Cyrille Barreteau, Ralph Gebauer, Nicola Seriani, and Sourav Mondal.

I thank my course instructors Prof. U. V. Waghmare, Prof. Subir K. Das, Prof.

N. S. Vidhyadhiraja, Prof. Swapan K. Pati, and Prof. Balasubramanian. I want to thank all the faculties from TSU. I want to acknowledge the present and past chair persons of TSU. I am thankful to Prof. Sridhar Rajaram, Prof. M. Weinert, Prof. David Vanderbilt, Prof. Simone Piccinin, and Dr. Prasenjit Ghosh for the useful scientific discussions I had with them, at different times during the course of my Ph.D.

I acknowledge the financial help from the TUE-CMS, Indo-French CEFIPRA grant, CEA-Saclay, and JNCASR for supporting my research.

I thank everyone in the Academic Section, especially Dr. Princy and Sukanya Maam. I would like to thank Mr. Jayachandra, Ms. Jayamangala, Mr. Joydeep Deb, and all others in the Administrative Section for their help with all the administrative procedures. I thank Dr. Archana and all the Dhanvantari staff for the medical assistance they provided. I am thankful to the CCMS staff Vijay, Anand, Anoop, and Suresh for their help and support with computing facilities. I want to thank all the library staff and the hostel staff.

I thank all my past and present labmates: Mighfar, Madhura, Nisha, Kanchan, Sananda, Vasudevan, Bulumoni, Debarati, Debdipto, Sukanya, Rajiv, Devina, Somesh, Saikat, Sourav, Nandana, Arpan, and Abhishek for providing a lively and pleasant environment in the lab.

I thank my past and present colleagues, especially Shubhajit, Soumalya, Sandhya, Anirban, Dibyajyoti, Koushik, Pawan, and Manoj, for the wonderful time we had together which made the time I spent in JNCASR, more enjoyable.

I thank my friends from school and college, Santanab, Torsa, Debdut, Durbar, Saikat, and Sayanti for being there when the times were hard.

My respectful gratitude to Prof. C. N. R. Rao for providing excellent research facilities and scientific environment in the institute.

Finally, I thank my parents, and my sister for their love, constant support, and motivation, which made it possible to finish my Ph.D.

Preface

In this thesis, I have designed materials at the nanoscale to tune their energetics, electronic, magnetic and topological properties using density functional theory (DFT) computations.

In **Chapter 1**, I provide a brief introduction to the problems studied in this thesis. I have followed a program of ‘rational design’ of materials to tune various properties so as to make them suitable for desired applications. The primary result that one gets from a DFT calculation is the total energy of a system. Using DFT total energy calculations, I have studied the size-dependent ionization and etching of Pt nanoparticles. The parameters varied are the nanoparticle size and the chemical environment, which is either the gas phase or in the presence of an appropriately chosen ligand. I present these results in Chapter 3. In Chapter 4, I compute a set of descriptors to find the optimal candidate dye for use in dye sensitized solar cells (DSSCs). These descriptors depend on the electronic properties of the dye+substrate complex, which have been tuned by changing the chemical substituents in the dye molecules. In Chapters 5 and 6, I study the layer-dependent structural and magnetic phase transitions in Fe/Ir(001) systems and the structure and magnetic properties of V deposited on Ag(100), respectively. Here, the magnetic properties have been tuned as a function of film thickness. In Chapters 7 and 8, topological phases occurring in germanene-like materials have been studied. The topological properties have been tuned as a function of chemical pressure induced by introducing chemical

functionalization. All the projects included in the thesis, except those presented in Chapters 7 and 8, have been done in collaboration with experimentalists. While the systems studied in this thesis are diverse, the projects have in common a research philosophy motivated by the rational design of materials, as implemented using ab initio density functional theory.

In **Chapter 2**, I discuss the computational techniques and theoretical formalisms used in this thesis: DFT, spin polarized DFT, the DFT-D2 technique to include dispersion interactions, fully relativistic calculations to include spin orbit interactions, and density functional perturbation theory (DFPT) to calculate the phonon spectra.

In **Chapter 3**, I study the size-selective ionization and etching of Pt nanoparticles. Pt is well known to be a noble metal. Pt nanoparticles, although widely used as catalysts, do not get ionized or etched away during chemical reactions. In contrast to their generally acknowledged behavior of sintering, experiments done by our collaborators show that Pt nanoparticles, in the presence of specific ligands, show size-dependent etching. In other words, instead of smaller particles coming together to form larger ones, they get etched away to form even smaller nanoparticles. Using DFT, I compute the energetics of the Pt nanoparticles in the gas phase and in the presence of ligands. A simple equation, based on thermodynamic considerations, that dictates the maximum size of nanoparticles up to which etching is favored, is derived analytically. The maximum size for etching is found to depend on the binding energy of the Pt atom to the ligands; thus this size can be tuned by a suitable choice of ligand. The theoretical predictions of maximum nanoparticle size up to which etching occurs in the presence of specific ligands match well with the corresponding experimental findings.

In **Chapter 4**, I calculate a set of descriptors that can be used for predicting the performance of a dye molecule in a DSSC. Using these descriptors, one can hope to avoid computationally expensive excited state calculations, or lengthy experiments. Using DFT, I investigate different electronic properties of the dye+TiO₂ complex

to formulate a set of descriptors that take into account the strength of coupling between the dye lowest unoccupied molecular orbital (LUMO) and the conduction band of TiO_2 , the amount of available states in the TiO_2 conduction band and the electron-hole separation to prevent recombination. I combine these descriptors together to formulate a single descriptor that can predict the performance of a dye molecule in DSSC. The prediction using this descriptor matches with the prediction using the transition dipole moment that gives the probability of electron transition between the highest occupied molecular orbital (HOMO) and the LUMO.

In **Chapter 5**, I find thickness-dependent magnetic and structural phase transitions in Fe/Ir(001) systems. Experiments on the layer by layer growth of Fe on Ir(001), done by our collaborators, find an onset of ferromagnetic ordering beyond 4 monolayers (ML) of Fe. My results show the presence of an antiferromagnetic (AFM) to ferromagnetic (FM) transition beyond 4 ML of Fe/Ir(001), which matches with the experimental findings. I find that above 4 ML, the FM ordering is favored over AFM ordering due to a higher exchange splitting in the FM configuration compared to the AFM configuration. DFT calculations of structural and elastic properties indicate the presence of a face centered tetragonal (FCT) structure up to 4 ML and a body centered tetragonal (BCT) structure beyond 8 ML. These results agree well with the results of cantilever stress measurements done in previous experimental studies.

In **Chapter 6**, I find the magnetic and structural properties of a V monolayer deposited on Ag(001). Angle-resolved photoemission spectroscopy (ARPES) experiments on a monolayer of V deposited on Ag(001) show the presence of additional surface states, when compared to the ARPES spectra of the bare Ag(001) system. This suggests that there might be Ag segregation on top of V. I perform DFT calculations on different V/Ag(100) systems which differ in how far the V layer is buried under the Ag layer. My calculations show that V wants to go subsurface, i.e., V gets buried under a single layer of Ag, and prefers AFM ordering. The DFT calculated band structure projected on the surface layers, shows the presence of surface states,

whose dispersion agrees with that seen in the ARPES data. I find that these surface states arise from the sub-surface V atoms.

In **Chapter 7**, I show that chemical pressure can induce a topological phase transition in germanene-like systems and can produce topological insulators (TI) at ambient conditions. Topological insulators are materials that have an insulating gap in the bulk but conducting edge states. Though $-\text{CH}_3$ functionalized germanene has been predicted to undergo a topological transition when subjected to an external biaxial strain, achieving the required large values of strain by mechanical means is essentially impossible. I show that, instead, chemical functionalization by $-\text{CX}_3$ ($\text{X} = \text{H}, \text{F}, \text{Cl}, \text{Br}$ and I) and $-\text{CXY}_2$ ($\text{X}, \text{Y} = \text{F}$ or Cl) induces giant chemical strains on the germanene lattice that can drive the system into a TI phase. I find that GeCCl_3 is a topological insulator at ambient conditions and it stabilizes itself by a symmetry-lowering distortion, leading to distorted (D)- GeCCl_3 . I also succeed in achieving a TI phase at ambient conditions in GeCFCl_2 which has a lower chemical pressure than GeCCl_3 . Moreover, GeCFCl_2 is found to be a large gap TI with a band gap of 0.23 eV, more than double the band gap of GeCCl_3 . I hope that this work will motivate experiments for the synthesis of the above mentioned materials.

In **Chapter 8**, I show that it is possible to observe a number of non-trivial topological phases in the three-dimensional (3D) bulk of a single material, GeCCl_3 , under suitable conditions. Calculation of the 3D band structure [excluding spin orbit coupling (SOC)] and the nodal line structure in the 3D k -space of the inversion symmetric system, shows that it is a Dirac nodal straight line semimetal. Breaking the inversion symmetry by stacking turns it into a Weyl nodal straight line semimetal. When SOC is turned on, the inversion symmetric system becomes a weak TI (WTI), whereas the non-inversion symmetric system becomes a trivial insulator. I show that by applying hydrostatic pressure it is possible to turn both the WTI and the trivial insulator into strong topological insulator. My work shows the possibility to study different topological phases and Fermions in a single material.

In **Chapter 9**, the main conclusions in each chapter are summarized and possible directions for future work are discussed.

List of Publications

Included in thesis

1. “Structure-property relationship of π -extended Boron-dipyrromethene derivatives towards optoelectronic applications”, Jittikarn Songkhao, Rajdeep Banerjee, Saikat Debnath, Shobhana Narasimhan, Napaporn Wannaprom, Parichatr Vanalabhpata, Nicola Seriani, Ralph Gebauer and Patchanita Thamyongkit, *Dyes and Pigments* **142**, 558 (2017).
2. “Topological phase transitions induced by giant strains produced by chemical pressure”, Rajdeep Banerjee, Manish Jain and Shobhana Narasimhan (under review).
3. “Size-selective ionization and etching of Pt-nanoparticles”, Debabrata Sengupta, Sreetosh Goswami, Rajdeep Banerjee, Anirban Dutta, Rajib Pramanick, T. Venkatesan, Shobhana Narasimhan, Narayan Pradhan, and Sreebrata Goswami (preprint available).
4. “GeCCl₃: a Model Topological Material”, Rajdeep Banerjee, Awadhesh Narayan, Tanmoy Das, Manish Jain and Shobhana Narasimhan (manuscript under preparation).
5. “Thickness dependent magnetic and structural phase transition in Fe on Ir(100): Spin polarized electron scattering and DFT study”, Pradeep A V,

Rajdeep Banerjee, Somesh Kumar Bhattacharya, Sananda Biswas, Shobhana Narasimhan, and PS Anil Kumar (manuscript under preparation).

6. “Growth and electronic structure of monolayer and multilayered V films on Ag(001)”, Ashish Kundu, Rajdeep Banerjee, Shobhana Narasimhan, and K. K. Menon (manuscript under preparation).

Not included in thesis

1. “Symmetry aspects of spin filtering in molecular junctions: Hybridization and quantum interference effects”, Dongzhe Li, Rajdeep Banerjee, Sourav Mondal, Ivan Maliyov, Mariya Romanova, Yannick J. Dappe, and Alexander Smogunov, Phys. Rev. B **99**, 115403 (2019).
2. “Electronic structure of a buried two-dimensional antiferromagnetic layer: Experimental and theoretical investigation of Ag/Cr/Ag(001)”, Jayanta Das, Sananda Biswas, Kanchan Ulman, Rajdeep Banerjee, Gaurav Gautam, Asish K. Kundu, Shobhana Narasimhan, and Krishnakumar S. R. Menon, Phys. Rev. B **98**, 075137 (2018).
3. “On the importance of epitaxial strain at a spin-crossover molecule-metal interface”, Cynthia Fourmental, Sourav Mondal, Rajdeep Banerjee, Amandine Bellec, Yves Garreau, Alessandro Coati, Cyril CHacon, Yann Girard, Jérôme Lagoute, Sylvie Rousset, Marie-Laure Boillot, Talal Mallah, Cristian Enachescu, Cyrille Barreteau, Yannick Dappe, Alexander Smogunov, Shobhana Narasimhan, and Vincent Repain (under review).
4. “Descriptors for the reactivity of Au nanoclusters: Evaluating the performance of the *d*-band center, the effective coordination number and the dual-center descriptor”, Nisha Mammen, Sukanya Ghosh, Rajdeep Banerjee, Debdipto Acharya,

Sourav Mondal, Devina Sharma, Aruna Nair, and Shobhana Narasimhan (under review).

List of Abbreviations

$\Delta\mu$	Change in Dipole Moment
ΔE_{ex}	Exchange Splitting
ρ	Charge density
C_{inj}	Coefficient of Injection
E_F	Fermi energy
E_{HOMO}	Energy of Highest Occupied Molecular Orbital
E_F	Fermi Energy
E_g	Band Gap
EHS	Electron Hole Separation
1D	One-dimensional
2D	Two-dimensional
3D	Three-dimensional
AFM	Antiferromagnetic
ARPES	Angle Resolved Photoemission Spectroscopy

BCT Body Centered Tetragonal

BODIPY Boron Dipyrromethene

BZ Brillouin Zone

COHP Crystal Orbital Hamilton Population

DFPT Density Functional Perturbation Theory

DFT Density Functional Theory

DSSC Dye Sensitized Solar Cell

FCT Face Centered Tetragonal

FM Ferromagnetic

GGA Generalized Gradient Approximation

HOMO Highest Occupied Molecular Orbital

KS Kohn Sham

LEED Low Energy Electron Diffraction

LUMO Lowest Unoccupied Molecular Orbital

ML Monolayer

MOKE Magneto Optic Kerr Effect

NLS Nodal Line Semimetal

NM Nonmagnetic

NP Nanoparticle

PBE Perdew, Burke and Ernzerhof

PDOS Projected Density of States

QE Quantum ESPRESSO

SIESTA Spanish Initiative for Electronic Simulations with Thousands of Atoms

SOC Spin Orbit Coupling

STI Strong Topological Insulator

TI Topological Insulator

TRIM Time Reversal Invariant Momenta

VASP Vienna Ab initio Simulation Package

WTI Weak Topological Insulator

Contents

Acknowledgements	v
Preface	vii
List of Publications	xiii
List of Figures	xxvii
List of Tables	xli
1 Introduction	1
1.1 Rational Design of Materials at the Nanoscale	1
Bibliography	9
2 Methods	17
2.1 Density Functional Theory	17
2.1.1 The Many Body Problem	17
2.1.2 Born-Oppenheimer Approximation or Adiabatic Approximation	18
2.1.3 The Hohenberg-Kohn Theorems	19
2.1.4 The Kohn-Sham Ansatz	20
2.1.5 Approximations for the Exchange-Correlation Functional	23
2.1.6 Hybrid Functionals	24

2.1.7	Basis Sets	25
2.1.8	Pseudopotential Approximation	27
2.1.9	k-point Sampling and Smearing	28
2.1.10	Calculation of Forces and Stresses	29
2.1.11	Spin Polarized DFT	30
2.1.12	Dispersion Interactions: The DFT-D2 Method	31
2.2	Relativistic DFT	32
2.2.1	Spin-Orbit Interactions	33
2.3	Phonon Calculations: Density Functional Perturbation Theory	34
2.3.1	Lattice Dynamics from Electronic-Structure Theory	34
2.3.2	Linear Response	35
2.4	Crystal Orbital Hamilton Population	36
2.5	Calculation of Z_2 Topological Indices	38
2.6	Calculation of Surface States	40
2.7	Codes Used	41
	Bibliography	41
3	Size-selective Ionization and Etching of Pt Nanoparticles	49
3.1	Introduction	49
3.2	Experimental background	51
3.3	Systems under study	54
3.4	Computational details	56
3.5	Results and Discussion	57
3.5.1	Ligands in the gas phase	57
3.5.2	Formation of the Pt(L) ₂ complex	58
3.5.3	Thermodynamics of sintering vs. etching	60
3.6	Conclusions	66
	Bibliography	67

4	Identifying Optimal Dye Sensitizers for Use in Solar Cells	73
4.1	Introduction	73
4.2	Experimental background	75
4.3	Systems under study	77
4.4	Computational details	78
4.5	Results and discussion	79
4.5.1	Adsorption geometry and energetics	79
4.5.2	Alignment of frontier orbitals	82
4.5.3	Theoretical prediction of performance of dyes in DSSCs	86
4.6	Conclusions	93
	Bibliography	93
5	Magnetic and structural phase transitions in Fe thin films on Ir(001)	103
5.1	Introduction	103
5.2	Recent experimental results	105
5.3	Systems studied	107
5.4	Methods	108
5.5	Results and Discussion	109
5.5.1	Magnetic phase transition in Fe thin films on Ir(001)	109
5.6	Structural phases in Fe/Ir(001) system	112
5.6.1	Structure changes in Fe/Ir(001) as a function of Fe film thickness	114
5.6.2	Structural changes manifested in elastic properties	115
5.7	Conclusions	118
	Bibliography	118
6	Electronic and magnetic structure of thin films: V deposited on Ag(001)	123
6.1	Introduction	123
6.2	Experimental motivation	125

6.3	Computational details and systems	126
6.3.1	Unfolding and projection of band structure	129
6.4	Results and Discussion	131
6.4.1	Stability and magnetic ordering	131
6.4.2	Comparison with experimental results	135
6.5	Conclusions	140
	Bibliography	140
7	Topological Phase Transitions Induced by Giant Strains Produced by Chemical Pressure	145
7.1	Introduction	145
7.2	Systems under study	148
7.3	Computational details	150
7.4	Results and Discussion	151
7.4.1	Geometry and energetics	151
7.4.2	Electronic properties: effect of mechanical strain in GeCH ₃ and GeCF ₃	154
7.4.3	Topological phase transitions	156
7.4.4	Dynamical stability	161
7.5	Conclusions	163
	Bibliography	164
8	GeCCl₃: A Model Topological Material	171
8.1	Introduction	171
8.2	Systems under study	173
8.3	Computational details	174
8.4	Results and Discussion	176
8.4.1	Nodal lines in <i>D</i> -GeCCl ₃	176
8.4.2	Surface states in <i>D</i> -GeCCl ₃	178

8.4.3	Effect of SOC and hydrostatic pressure	178
8.5	Conclusions	182
	Bibliography	183
9	Summary and Outlook	189

List of Figures

2.1	Flowchart showing the self-consistency loop for solving the KS equation, Eq. (2.14).	23
3.1	Panels (a), (b) show schematic presentation of chemical reactivity of Pt NPs with L^1 : smaller size NPs ($d \leq 6$ nm) react but larger NPs do not. (c), (d) show TEM images before and after reaction between NPs with $d \leq 6$ nm and L^1 and, (e) the corresponding NP size distribution in pre- and post-reaction samples. (f)-(h) Same as (c)-(e) for NPs with $d > 6$ nm. (i) TEM images before the reaction of a NP sample with a wide range (2-20 nm) of NP sizes. (j) Post reaction TEM image of the sample shown in (i), where only the smaller NPs (≤ 6 nm) react. (k) Histogram corresponding to (i), (j). Note, from Fig. 1(e), it can be argued that even a NP of 7 nm reacted and that could be the threshold. However, the number of such particles is too small. In several batches experiments do not show particles of 7 nm at all. Hence, the fact that post reaction image does not contain 7 nm NPs as unreacted, could be due to sampling uncertainty. Even NPs of size ~ 6.5 nm have been found to remain unreacted. Hence, the threshold size has been indicated as 6 nm. Experimental data courtesy of Prof. Sreebrata Goswami and Debabrata Sengupta.	53

3.2	The optimized geometries of the Pt nanoparticles (Pt_n , $n = 1 - 2057$) are shown. The largest nanoparticle considered for DFT calculations has 2057 atoms, which corresponds to a diameter $d = 4.4$ nm.	55
3.3	The chemical structure of the di imine ligands: (a) 9,10-phenanthroline (Λ^1), (b) 2-(phenylimino) pyridine (Λ^2), and (c) 2,2-bipyridine (Λ^3), and a family of 2-(arylazo) pyridines (L); viz. (d) 2-(phenylazo) pyridine (L^1), (e) 4-chloro-2-(phenylazo) pyridine (L^2), (f) 2,6-dimethyl-2-(phenylazo) pyridine (L^3), and (g) 4-methyl-2-(phenylazo) pyridine (L^4).	56
3.4	Comparison of the DFT (Gau-PBE hybrid functional) calculated (red dashed) HOMO-LUMO gaps of the ligands in the gas phase, with the experimental HOMO-LUMO gaps (black solid) measured using UV-Vis and cyclic voltammetry. Experimental data courtesy of Prof. Sreebrata Goswami, and Debabrata Sengupta.	57
3.5	The optimized geometry of the $\text{Pt}(L^1)_2$ complex, with labels used to denote bond parameters, is shown in (a). (b) shows the spin density with red and green lobes indicating up and down spins, respectively. (isosurface value: 0.003 e/Bohr ³)	59
3.6	Comparison of experimental (upper panel) and DFT computed (lower panel) Raman spectra. The blue curve shows the difference of Raman spectra before (red) and after (green) reaction. The red and green arrows indicate the frequencies corresponding to the azo-stretching modes, before and after the reaction, respectively. In both the experiment and the DFT results, we see a blue shift in the frequencies correspondin to the azo-stretching modes. Experimental data courtesy of Prof. Sreebrata Goswami and Debabrata Sengupta.	60

3.7 Theoretical explanation for reversal of behavior in the presence of ligands L: We consider the thermodynamics of sintering vs. etching in the gas phase (a)-(c) and in the presence of the ligands L^1 (d)-(f) and Λ^1 (g)-(h). The horizontal lines represent the total energies ΔE_{tot} , as computed from DFT, of the system of either (a)-(c) Pt_n nanoparticle + $(N - n)$ free Pt atoms, or (d)-(i) Pt_n nanoparticle + $(N - n - 1)$ $Pt(L)_2$ moieties + $2(n - 1)$ free ligands L, as a function of n . Here L is the ligand L^1 or Λ^1 . A negative/positive slope for ΔE_{tot} vs. n implies that sintering/etching is favoured. The inset in (c) shows that the slope of the fitted curve remains negative for all n , indicating sintering is always favourable for Pt nanoparticles in the gas phase. In contrast, the inset to (f) and the graph (i) show that the slope changes sign beyond a certain value n_{max} in the presence of the ligands L^1 and Λ^1 . The corresponding maximum cluster sizes beyond which etching no longer occurs are found to be $n_{\text{max}} = 9,930$ (6.6 nm) and $n_{\text{max}} = 43$ (1.07 nm), respectively. 61

3.8 Thermodynamics of etching in presence of ligands (a) L^2 , (b) L^3 , (c) L^4 , (d) Λ^2 , and (e) Λ^3 . The horizontal lines represent the total energies ΔE_{tot} , as computed from DFT, of the system of Pt_n nanoparticle + $(N - n - 1)$ $Pt(L)_2$ moieties + $2(n - 1)$ free ligands L ($L = L^2, L^3, L^4, \Lambda^2$, and Λ^3), as a function of nanoparticle size n . The positive/negative slope of the ΔE_{tot} vs. n plots suggests etching/sintering is favored. The maximum allowed nanoparticle size (n_{max}) for etching, is indicated by labels and arrows in magenta. 63

4.1 Structures of BODIPYs and dipyrins of interest are shown. Compounds **2**, **3** and **4** have carboxyl anchor groups ($R = -\text{COOH}$) in the theoretical calculations, whereas in the experiments ethyl ester groups ($R = -\text{COOEt}$) are present for the corresponding compounds **2'**, **3'** and **4'**. 77

4.2 Lowest energy adsorption geometries for dye molecules **3a**, **3b**, **3c** and **4b**, adsorbed on TiO_2 substrate. Labels in **3c** indicate the notation used to distinguish various Ti, O and C atoms. The dihedral angles θ_1 and θ_2 are defined as $\angle\text{C1-Ti2-Ti2}'$ and $\angle\text{C2-C1-Ti2}$, respectively, where $\text{Ti2}'$ is the periodic image of Ti2 along the $+a$ direction. Note that all the molecules have a sesquidentate geometry consisting of one monodentate and one bidentate tethering. 80

4.3 The projected density of states of the molecule + TiO_2 system. The energy is shifted by the highest occupied molecular orbital (HOMO) of the corresponding molecule, so that the zero of x-axis represents the HOMO of the molecule. The band gap region of TiO_2 is represented by the black shaded region. The color codes in the legends depict contributions from different atomic species. We see that for all the molecules the HOMO lies within the band gap of TiO_2 , whereas the lowest unoccupied molecular orbital (LUMO) is in the conduction band of TiO_2 83

4.4 Experimental and theoretical energy level diagrams of the target BODIPYs (**1a** and **1b**) and the benzo-BODIPYs in comparison to the conduction band edge of TiO₂ and the I⁻/I₃⁻ oxidation potential. Panel (a) shows the experimentally obtained values for **1a**, **1b**, **4b'**, **3a'**, **3b'** and **3c'**, while panel (b) shows the results from DFT for **4b**, **3a**, **3b** and **3c** when adsorbed on TiO₂. The theoretical values are referenced with respect to the vacuum energy. The shaded regions correspond to the valence and conduction bands of TiO₂; VBM and CBM indicate the theoretically computed valence band maximum and conduction band minimum, respectively. Note that while DFT underestimates the energy gaps, as expected, the trends across the molecules are same in the experiment and the theory. 85

4.5 Correlation between the experimental results for **3a'**, **3b'**, **3c'** and **4b'**, and the theoretical results for the HOMO-LUMO gaps for **3a**, **3b**, **3c** and **4b**. The black squares show the experimental values, while the red circles and blue triangles show the values as calculated from DFT for the molecules in the gas phase and when adsorbed on TiO₂, respectively. Note that the same trends are observed in the experiment and the theory, though DFT underestimates the energy gaps, as expected. 87

4.6 The isosurfaces of the charge densities for states corresponding to the HOMO (left image of each panel and the LUMO (right image for each panel) for **4b**, **3a**, **3b** and **3c** on TiO₂ are shown. The isosurfaces corresponding to a value of 0.004 e/Å³ are plotted as green lobes.) . . 88

4.7 DFT results for various factors affecting the performance of the four compounds studied here when used in the DSSCs in combination with TiO_2 . Bar diagrams corresponding to the computed values of (a) full width at half maximum (FWHM) of the LUMO of the dye molecules when adsorbed on TiO_2 , (b) coefficient of injection (C_{inj}), (c) electron-hole separation (EHS), (d) $C_{\text{inj}} \times EHS$ and (e) difference of dipole moments correspondin to LUMO and HOMO ($\Delta\mu$). 91

5.1 Experimental results showing (a) MEED oscillations and (b) Kerr rotation as a function of film thickness for Fe/Ir(001). The sudden decrease in the amplitude of the MEED oscillation signifies a bct to bcc transition beyond 11 MLs of Fe on Ir(001). The non-zero Kerr rotation beyond 4.5 MLs, denotes a FM magnetic ordering. Beyond 12 MLs, the Kerr rotation more or less saturates indicating a bulk bcc-Fe phase. Experimental data courtesy of Pradeep A V and PS Anil Kumar. 106

- 5.2 Examples of different AFM configurations of the Fe layers considered for DFT calculations are shown in panel (a). Three different *AFM* configurations are considered, and are shown for 1 – 4 ML. Dashed circles denote Fe atoms in the $\sqrt{2} \times \sqrt{2}$ surface cell. Up and down spins are represented by red up and blue down arrows, respectively. The difference between *AFM*₁ and *AFM*₂ configurations can be understood by comparing the spin configurations in layer 1 and 3, in each case. In *AFM*₁, layer 1 and 3 have identical spin configuration, whereas in case of *AFM*₂, in layer 3, up spins of layer 1 is replaced by down spins, and vice versa. *AFM*₃ shows intra-layer *FM* ordering and inter-layer *AFM* ordering. In panel (b), the AFM configuration in the 1Fe/Ir(001) structure is shown. Fe and Ir atoms are shown in red and grey, respectively. The spin orientations are nominally shown to be in-plane, using blue arrows. 108
- 5.3 Results from DFT calculations for the energy difference between the (lowest energy) *AFM* and the *FM* configurations per Fe atom, plotted against the Fe layer thickness. The *FM* configuration is higher in energy than the *AFM* configuration for ≤ 4 ML, beyond 4 ML, the *FM* configuration becomes energetically favorable over the *AFM* configuration. 110
- 5.4 DFT results for the evolution of magnetic moments with thickness of the Fe film. Average magnetic moment (μ_B/layer) as a function of Fe layer thickness, is shown in (a). The black line (solid) shows the value of the magnetic moment calculated for Fe BCC bulk. The blue and orange background show, respectively, the regions where *AFM* and *FM* ordering is preferred. Similarly, panel (b) shows average magnetic moment per atom (μ_B/atom), as a function of number of Fe ML. . . . 111

5.5	Projected density of states (PDOS) per atom, for (a) 4 MLs Fe (b) 5 MLs Fe and (c) 6 MLs Fe films deposited on Ir(001). The blue up and down triangles denote the band centers for the up spin and down spin density of states, respectively, for the FM configuration.	113
5.6	Exchange splitting ΔE_{ex} for 2-6 layer Fe/Ir(001). The plots show that the stabilization of <i>FM</i> structure over <i>AFM</i> structure beyond 4Fe/Ir(001) is due to the increase in ΔE_{ex} , when one goes from 4Fe/Ir(001) to 5Fe/Ir(001).	114
5.7	Panel (a) shows the schematic of an fct unit cell (dashed lines) of lattice constant $\sqrt{2}a$, inside a bcc lattice of lattice constant a . (b), and (c) show the DFT results for the changes in geometry as a result of Fe film thickness. The first two interlayer spacings (d_{ij}) as a function of the thickness of the Fe film in different Fe/Ir(001) systems are shown in (b). The average c/a ratio of the Fe layers as a function of Fe ML is plotted in (c).	116
5.8	Panel (a) shows the results of cantilever stress measurements by Martin <i>et al</i> ,[1] where the cantilever stress change [$\Delta(\tau_{FF}t_F)$] versus Fe layer thickness (ML) is plotted. In (b) the DFT results of in-plane stress as a function of number of Fe ML is shown. In both experimental and DFT calculated results, positive/negative slope indicates fct/bct phase of Fe.	117
6.1	ARPES data showing surface states at \bar{M} for (a) bare Ag(001), and (b) 1 ML V/Ag(001) grown at 108 K. Upon deposition of V, additional surface states can be seen to occur near the \bar{M} point in (b), suggesting Ag segregation over V.	126

- 6.2 The top view of atomic arrangements of (a) Ag(001) and (b) V/Ag(001) systems are shown. The dark blue, dark gray, and light gray spheres represent V, first substrate layer, and second substrate layers of Ag atoms, respectively. The primitive surface unit cells are indicated by solid orange lines. 127
- 6.3 The (a) side view, and (b) the top view of the atomic structure of V/Ag(001) in the antiferromagnetic configuration. Blue and gray spheres represent V and Ag atoms, respectively. The red arrows indicate the direction of the spins, which, here, are shown to be in-plane. However, the out-of-plane directions are also equivalent. 128
- 6.4 The variation of interlayer distance d_{ij} for (a) V/Ag(001), (b) 1Ag/V/Ag(001), (c) 2Ag/V/Ag(001), and (d) 3Ag/V/Ag(001) in NM (shown in orange diamonds), FM (shown in blue circles) and AFM (shown in red squares) configurations. 133
- 6.5 The projected density of states (PDOS) of the $3d$ states of V atoms of both AFM (shown in red dashed lines) and FM (shown in solid blue lines) configuration in (a) V/Ag(001), (b) 1Ag/V/Ag(001), (c) 2Ag/V/Ag(001) and (d) 3Ag/V/Ag(001). 134
- 6.6 The projected density of states (PDOS) of the Ag $4d$ states (shown by gray filled curve for the layer above V monolayer and by red dashed lines for the layer below the V monolayer) and V $3d$ states (shown by solid blue lines) in the antiferromagnetic (AFM) configuration of (a) V/Ag(001), (b) 1Ag/V/Ag(001), (c) 2Ag/V/Ag(001) and (d) 3Ag/V/Ag(001). 135

6.7 (a) shows the calculated projected band structure of the bare Ag(001) along the high symmetry direction $\bar{\Gamma} - \bar{X} - \bar{\Gamma}$, as shown in the surface Brillouin zone in (b). The ARPES data along the same path is shown in (c). Experimental data provided courtesy of K. S. R. Menon. E_F denotes the Fermi energy. In the colour scale of the calculated band structure, ‘yellow’ and ‘dark blue’ indicates highest (one) and lowest (zero) projection. 136

6.8 Calculated band structure of 1Ag/V/Ag(001) system for the AFM configuration is plotted in (a), along the high-symmetry direction $\bar{\Gamma} - \bar{X} - \bar{\Gamma}$. (b) shows the surface Brillouin zone corresponding to the 1×1 cell (solid square and high symmetry points $\bar{\Gamma}, \bar{X}$, and $\bar{\Gamma}$), and $\sqrt{2} \times \sqrt{2}$ cell (dashed square and high symmetry points $\bar{\Gamma}', \bar{X}'$ and $\bar{\Gamma}'$). The second derivative of the ARPES data along the same direction is shown in (c). Experimental data provided courtesy of K. S. R. Menon. E_F denotes the Fermi energy. In the colour scale of the calculated band structure, ‘red’ and ‘dark blue’ indicates highest (one) and lowest (zero) projection. 137

6.9 The top [(a)-(e)] and side views [(f)-(g)] of the electronic charge densities (magenta) corresponding to states $S_1 - S_5$ of the AFM 1Ag/V/Ag(001) system. The top view correspond to the $x - y$ plane whereas side views correspond to $x - z$ plane. The blue and gray spheres represent V and Ag atoms respectively. The isosurface value used for the charge density is 0.002 electron/a.u.³. 139

7.1	Panels (a) and (b) show schematic top and side views, respectively for the P - GeCX_3 structure. Panel (c) shows the top view of the D -structure of GeCCl_3 . (d) and (e) show the top and side views, respectively for the GeCXY_2 structure. The shaded rhombuses in (a) and (d) denote the unit cells of the respective structures. Red, Green and Blue spheres indicate Ge, C and X atoms, respectively. X can be H, F, Cl, Br or I in GeCX_3 , whereas X and Y can be F or Cl in GeCXY_2 . The black and magenta colored zigzag lines in (c) show bonds of different lengths due to distortion. In contrast, all the Ge-Ge bonds in (a) are equal in length.	149
7.2	We compare equilibrium lattice constants as obtained from DFT and a hard-sphere model in (a). Panel (b) shows how the buckling Δ changes with the lattice constant of GeCX_3 . The star in (b) denotes the value for germanene monolayer.	152
7.3	Straining the germanene lattice by chemical pressure: the P structure of GeCX_3 . Panels (a) and (b) show the band gap E_g (without SOC) for GeCH_3 and GeCF_3 , respectively. Negative (positive) strains correspond to compressive (tensile) strains, and filled (empty) symbols represent PBE (HSE) results. In (c) we show how E_g varies with lattice constant a for all halogens X	155
7.4	-COHP plots of GeCH_3 for (a) VBM and (b) CBM, at different values of strain. Turquoise squares and violet circles indicate contributions to COHP from Ge-C and Ge-Ge pairwise interactions.	156
7.5	Orbital projected band structure of P - GeCF_3 at strain $\epsilon^X =$ (a) 0% and (b) 5%. The color indicates the fractional contribution of Ge- sp orbitals (yellow) relative to Ge- p orbitals (blue).	157

7.6	Band structure of a nanoribbon of GeCF_3 under 5% tensile strain. A pair of topologically protected edge states can be seen to cross the Fermi level at the zone center. The inset shows the zoomed in view of the pair of edge states crossing the Fermi level near the zone center. .	158
7.7	(Projected band structures (PBE+SOC) of (a) $P\text{-GeCCl}_3$ and (b) $D\text{-GeCCl}_3$, for the topmost valence band and lowest-lying conduction band. The color indicates the fractional contribution of p , $j = 3/2$ relative to p , $j = 1/2$, with red color corresponding to totally $j = 3/2$ character; note that the color scales are different in (a) and (b). The inset in (b) shows the 2D Brillouin zone.	159
7.8	Band structure of $D\text{-GeCCl}_3$ (PBE+SOC): Panel (a) shows the topography of the topmost valence band and the bottommost conduction band, and (b) shows the band structure of a nanoribbon, characterized by the presence of topologically protected edge states crossing the Fermi level.	160
7.9	Orbital projected band structure (PBE+SOC) of GeCFCl_2 . The color indicates the fractional contribution of Ge- sp orbitals (yellow) relative to Ge- p orbitals (blue).	161
7.10	Phonon band structures of GeCF_3 at (a) 0%, and (b) 5% strains. In panels (c) and (d) we plot the phonon bands for the $P\text{-GeCCl}_3$, and $D\text{-GeCCl}_3$ systems. (e) shows the phonon band structure of GeCFCl_2 .	162

8.1	Structures of D -GeCCl ₃ : panels (a) and (b) [(c) and (d)] show the schematic top (side) views of D -GeCCl ₃ . (a) and (c) correspond to AA -stacking (with IS), whereas (b) and (d) correspond to AB -stacking (without IS). The shaded rhombus in Blue in (a) and (b) depicts a unit cell. Red, Green and Blue spheres indicate Ge, C and Cl atoms, respectively. Magenta and black colored lines in (a) show bonds of different lengths due to in-plane distortion. Panel (e) shows the bulk BZ and its (010) surface (in pink).	174
8.2	3D band structures (without SOC) and structure of nodal lines: panels (a) and (b) show the 3D band structures of Dirac and Weyl NLSs, respectively at $k_z = 0$. Two Dirac nodes can be seen in (a), each of which splits into a pair of Weyl nodes as the inversion symmetry is broken by stacking, as shown in (b). The straight lines in Red in (c) [(d)] shows the structure of the nodal lines of Dirac (Weyl) NLS. The computed Berry phases in closed loops around nodal lines are also shown in (c) and (d).	177
8.3	Surface states: panels (a) and (b) show the <i>drumhead</i> surface states corresponding to the Dirac and Weyl NLSs, respectively. In (c) [(d)] the zoomed in view of the surface states near the Fermi energy is shown for the Dirac (Weyl) NLS. In case of the Dirac NLS, a single surface state connects the Dirac nodes, whereas in Weyl NLS, a pair of surface states connects the pair of Weyl nodes.	179
8.4	3D band structure of D -GeCCl ₃ (with SOC): panels (a), and (b) show the 3D band structures (with SOC) of the IS (AA -stacked), and NIS (AB -stacked) systems, respectively. In both cases we see opening of band gap due to spin-orbit interactions.	180

8.5 Projected band structures (PBE+SOC) for IS (*AA*-stacked) [panels (a), (b) and (c)] and NIS (*AB*-stacked) [panels (c), (d) and (e)] *D*-GeCCl₃ at different hydrostatic pressures. The corresponding magnitudes of hydrostatic pressure are also shown. The color indicates the fractional contribution of $p, j = 3/2$ relative to $p, j = 1/2$, with red color corresponding to totally $j = 3/2$ character. 181

List of Tables

3.1	Bond parameters: experimental and DFT optimized bond distances (\AA) and bond angles ($^\circ$) of complex $\text{Pt}(\text{L}^1)_2$ complex. For the labeling of the atoms, see Fig. 3.5.	58
3.2	Comparison of the maximum nanoparticle size n_{max} in Pt_n , where etching stops, nanoparticle diameter d (nm) corresponding to n_{max} and the binding energies of the Pt atom to the corresponding ligands, in the $\text{Pt}(\text{L})_2$ complex.	65
4.1	The photophysical properties of the target BODIPYs and dipyrins. λ_{abs} , ϵ , λ_{em} and ϕ_f denote the absorption wavelength, the molar extinction coefficients, emission wavelength and the fluorescence quantum yields, respectively.	78
4.2	Adsorption geometries as determined from DFT calculations. The bond lengths between O of the dye molecules and Ti of TiO_2 , the dihedral angle corresponding to different dye molecules on the TiO_2 substrate, and the adsorption energies of the molecules. See Fig. 4.2 for the naming convention for atoms.	81
5.1	Magnetic configurations and the energy differences with respect to the lowest energy configuration (ΔE), for 1 – 6 ML Fe on Ir(001).	109

6.1	Energetics of FM, AFM and NM configurations of V on Ag(001) systems are presented. ΔE represents the difference in energy of a given configuration with that of the lowest energy configuration. . . .	132
7.1	The following table shows the lattice constants (a_0^X), Ge-Ge bond lengths, buckling (Δ), strains with respect to P -GeCH ₃ lattice constant (ϵ) and cohesive energies (E_{coh}), of germanene, P -GeCH ₃ and P -GeCX ₃ (X = F, Cl, Br and I) systems.	152
7.2	The following table shows the in-plane lattice constants along x and y, a_1 and a_2 , respectively, Ge-Ge bond lengths, buckling (Δ), strains with respect to P -GeCH ₃ lattice constants along a_1 and a_2 , ϵ_1 and ϵ_2 , respectively, and cohesive energies (E_{coh}), of GeCF ₂ Cl and GeCFCl ₂ systems.	153

Chapter 1

Introduction

1.1 Rational Design of Materials at the Nanoscale

Nanomaterials, or materials at nanometric dimensions, show properties that are completely different from their bulk counterparts, due to a high surface to volume ratio, and the possible appearance of quantum effects.[1] Examples of nanomaterials include zero-dimensional materials like molecules and nanoparticles,[2, 3] one-dimensional materials like nanowires, nanotubes, nanoribbons,[3–6] and two-dimensional materials such as monolayers and surfaces.[7, 8]

The conceptual origin of the broad area of nanoscience and technology, can possibly be traced back to Nobel laureate physicist Prof. Richard P. Feynman’s 1959 lecture, ‘There’s plenty of room at the bottom’,[9] where he indicated that it might be possible to manipulate atoms and molecules to change the properties of materials. The field of nanoscience got a major boost with the discovery of the scanning tunneling microscope in 1981,[10] and the atomic force microscope in 1982,[11] which enabled experimentalists to ‘directly’ observe phenomena such as surface reconstruction, defect formation, adsorption, nanocatalysis, etc.[12–14] Advances in computational power due to rapid development in semiconductor technology in line with Moore’s law,[15] also aided the discovery of new materials with novel properties. Some of the most active areas in the field of nanoscale materials research in recent times, that have a

broad range of applications in industry, and that we have worked on in this thesis, include materials discovery for solar cell applications, reactions using nanoparticles, magnetism in thin films for use in magnetic storage and spintronic devices, materials with novel topological properties for use in electronic and spintronic devices, and quantum computers.

Technological applications drive the search for nanomaterials with novel properties. In this regard, designing materials that fulfill the requirements of industry for their desired applications, is of critical importance. The rational design of materials is based on the concept of ‘design on purpose’,^[16] which makes it necessary to define the problem clearly to start the design of nanomaterials. After the problem is well defined, conceptual design of the nanomaterials, and theoretical prediction of their properties using different theoretical tools are performed. Once the design phase is over, experimentalists synthesize the material, and the experimental characterization tells us whether the predicted properties match the measured properties of the synthesized material. If a deviation from the predicted properties is observed, a thorough analysis to find the reason for deviation is done, and with the insights gained, we go back to redesigning the nanomaterial.

Often, limitations of the experiments hold us back from a detailed understanding of the material properties. Experiments, in general, are also costly, and time consuming. Therefore, computational techniques are required, for the rational design of the nanomaterials, and for an in-depth understanding of the material properties.

Ab initio density functional theory (DFT),^[17, 18] molecular dynamics techniques,^[19] Monte Carlo simulations,^[20] etc., are a few popular choices of computational methods. *Ab initio* or first principles calculations do not need any experimental input or empirical parameterization, and can complement the experimental results. This is why first principles methods are widely used by both chemists and physicists as a predictive tool to search for and design new materials with novel properties. The increase in computational power with the advent of supercomputers has made it possible

to simulate real life materials, starting from their constituent atoms. Sometimes, limitations imposed by the availability of computing facilities, make it difficult to study realistic systems with first principles methods. In such scenarios, one can still work with prototypical models that can capture the essential physics in the experiment.

In this thesis, we have followed a program of ‘rational design’ of nanomaterials to tune their energetics, electronic, magnetic, and topological properties, so as to make them suitable for desired applications. Although the problems dealt with in this thesis are diverse, they have a common underlying philosophy of rational design of materials, implemented through *ab initio* density functional theory.

In Chapter 1, we provide a brief introduction to the problems studied in this thesis. Any DFT calculation produces the total energy of the system as the primary result. In Chapter 3, using DFT total energy calculations, we have studied the size-selective ionization and etching of Pt nanoparticles. The size of the nanoparticles, and the chemical environment, are the parameters tuned to study the energetics. The chemical environment can be either the gas-phase, or in the presence of appropriately chosen ligands. In Chapter 4, we compute descriptors that depend on the electronic properties of the dye + substrate complex, to find the most suitable candidate dye, from a set of dye molecules, for use in dye sensitized solar cells (DSSCs). We also tune the magnetic properties of thin films as a function of film thickness. In Chapter 5, we study the structural, and magnetic phase transition of a Fe thin film, during its layer by layer growth on Ir(001). In Chapter 6, the growth of a V monolayer on a Ag(001) substrate is studied. We also show that that topological properties can be tuned as a function of chemical pressure induced by the use of different functionalizations in germanene-like systems. These results are presented in Chapters 7 and 8. All the projects included in the thesis, except those presented in Chapters 7 and 8, have been done in collaboration with experimentalists.

In Chapter 2, we discuss the computational techniques and theoretical formalisms

used in this thesis: DFT, spin polarized DFT, the DFT-D2 technique to include dispersion interactions, fully relativistic calculations to include spin orbit interactions, and density functional perturbation theory (DFPT) to calculate the phonon spectra.

A great deal of the research in the field of catalysis is driven by the need for the production of cleaner and inexpensive fuels,[21] and reduction of harmful by-products during manufacturing processes.[22, 23] Nanoparticles, which often show very different properties than their bulk counterparts, have drawn huge attention in the last couple of decades due to their applications in catalysis,[24–26] electrocatalysis,[27] fuel cells,[28] water purification,[29] etc. Moreover, the size-dependent reactivity of nanoparticles, provides controllability of reactions. A major challenge in the performance of nanoparticle catalysts is the tendency of the nanoparticles to agglomerate, or sinter, to form bigger nanoparticles. The general strategy to overcome this problem is to use supports or media for dispersion.[30] Tunability of the size of the nanoparticles down to a single atom, is essential in heterogeneous catalysis, and it requires etching of atoms from bigger nanoparticles to form smaller nanoparticles. Hence, etching is a crucial requirement for the chemical reactivity of the nanoparticles, and for the controllability of the reactions they are used in. In Chapter 3, we study the size-selective ionization and etching of Pt nanoparticles. Pt is well known to be a noble metal. Pt nanoparticles have been widely used as catalysts for various chemical reactions.[24–26] Interestingly, Pt nanoparticles do not get ionized or etched away during chemical reactions. The general tendency of the nanoparticles is to coalesce together to form bigger nanoparticles, a tendency known as sintering. Since the reactivity of the nanoparticles decreases with their increase in size,[31] this sintering tendency poses a major problem for the application of these nanoparticles as catalysts in chemical reactions. Experiments done by our collaborators show that Pt nanoparticles, in the presence of specific ligands, show size-dependent etching. In other words, instead of smaller particles coming together to form larger ones, they get etched away to form even smaller nanoparticles, which is a very surprising and interesting result.

Using DFT, we compute the energetics of the Pt nanoparticles in the gas phase and in the presence of ligands. Based on thermodynamic considerations, we analytically derive a simple equation, that dictates the maximum size of nanoparticles up to which etching is favored. The maximum size for etching is found to depend on the binding energy of the Pt atom to the ligands; thus this size can be tuned by a suitable choice of ligand. The theoretical predictions of maximum nanoparticle size up to which etching occurs in the presence of specific ligands match well with the corresponding experimental findings. The results obtained in this work can provide new routes to Pt chemistry, and can find uses in various technological applications.

Continuous depletion of fossil fuels, and the need for cleaner sources of energy to counter global warming, have provided an enormous impetus to the search for new solar cell materials, in recent years. The search for new materials and devices that can replace the present silicon based photovoltaic devices, and increase the conversion efficiency, is still ongoing. Candidate materials include perovskites,[32] chalcogenides,[33] and organic dyes,[34, 35] which constitute the ‘third generation’ solar cells.[36] Among these, dye sensitized solar cells (DSSCs) provide a low cost alternative, that are also mechanically robust. Moreover, the large number of available organic dye molecules, as well as their structural, and electronic tunability make DSSCs an attractive candidate in solar cell technology. On the other hand, the availability of such a big sample space of potential dye molecules, makes it absolutely necessary to devise methods for theoretical prediction of the efficacy of the dyes in DSSCs, to avoid performing a vast number of time consuming and expensive experiments. In Chapter 4, we calculate a set of descriptors that can be used for predicting the performance of a dye molecule in a DSSC. The availability of a large pool of organic dye molecules, makes it difficult for experimentalists to choose the right candidate dyes that have the potential to show high conversion efficiency in a DSSC. Using the formulated descriptors, one could possibly avoid computationally expensive excited state calculations, or lengthy experiments. Using DFT, we investigate different

electronic properties of the dye+TiO₂ complex to formulate a set of descriptors that take into account the strength of coupling between the dye LUMO and the conduction band of TiO₂, the amount of available states in the TiO₂ conduction band and the electron-hole separation to prevent recombination. We combine these descriptors together to formulate a single descriptor that can predict the performance of a dye molecule in DSSC. The prediction using this descriptor matches with the prediction using the transition dipole moment that gives the probability of electron transition between the HOMO and the LUMO. These descriptors can be used individually, or may be implemented in a machine learning model as key performance indicators (KPIs) to filter a large pool of organic dye molecules, and choose a smaller set, which can then be used in experiments to test their performance in DSSCs.

The discovery of giant magnetoresistance (GMR) in 1988,[37, 38] and tunnel magnetoresistance (TMR) in 1991,[39] and subsequent application of these phenomena in magnetic read/write devices,[40] have encouraged research in the area of magnetic thin films. Due to broken symmetry and reduced dimensionality, magnetic thin films show different properties from their bulk counterparts. Some materials, which are nonmagnetic in their bulk, can show magnetic properties at the thickness of a few monolayers.[41, 42] Also, magnetic materials such as Fe, and Ni, show thickness dependent magnetic phase transitions.[43, 44] In this regard, a thorough understanding of the formation of magnetic monolayers on nonmagnetic substrates, as well as their layer-by-layer growth, is crucial for their application in devices to be effective. In Chapter 5, we find thickness-dependent magnetic and structural phase transitions in Fe/Ir(001) systems. Understanding the structure and magnetic properties of thin films is essential for their application in magnetic storage or spintronic devices. Experiments on the layer-by-layer growth of Fe on Ir(001), performed by our collaborators, find an onset of ferromagnetic ordering beyond 4 monolayers (ML) of Fe. Our results show the presence of an antiferromagnetic (AFM) to ferromagnetic (FM) transition beyond 4 ML of Fe/Ir(001), which matches with the experimental findings. We find

that above 4 ML, the FM ordering is favored over AFM ordering due to a higher exchange splitting in the FM configuration compared to the AFM configuration. DFT calculations of the structural and elastic properties indicate the presence of a face centered tetragonal (FCT) structure up to 4 ML and a body centered tetragonal (BCT) structure beyond 8 ML. These results agree well with the results of cantilever stress measurements done in previous experimental studies.[45] The results suggest a minimum thickness in a Fe thin film on Ir(001), beyond which it can be used as a ferromagnetic thin film, for different applications.

In Chapter 6, we find the magnetic and structural properties of a V monolayer deposited on Ag(001). Previous experimental and theoretical studies performed on V thin films on Ag, show conflicting results,[42, 46, 47] which may arise due to the fact that the surface energy of V is more than that of Ag, making the formation of a monolayer of V on Ag, unfavourable,[42] but leaves room for the possibility of cluster formation, or Ag segregation. Angle-resolved photoemission spectroscopy (ARPES) experiments on a monolayer of V deposited on Ag(001) show the presence of additional surface states, when compared to the ARPES spectra of the bare Ag(001) system. This suggests that there might be Ag segregation on top of V. We perform DFT calculations on different V/Ag(001) systems which differ in how far the V layer is buried under the Ag layer. Our calculations show that V wants to go sub-surface, i.e., V gets buried under a single layer of Ag, and prefers antiferromagnetic (AFM) ordering. The DFT calculated band structure projected on the surface layers, shows the presence of surface states, whose dispersion agrees with that seen in the ARPES data. We find that these surface states arise from the sub-surface V atoms. Our results shed new light on the long standing debate on the structure, and magnetic properties of a V monolayer deposited on Ag(001). Similar methodology can be applied to study the magnetic behaviour in monolayers, of other nonmagnetic systems.

Since the theoretical proposal of topological insulators by Kane and Mele,[48, 49] and subsequent experimental realization by König *et al.*,[50] the class of topological

materials has drawn a lot of attention due to their unique properties, and potential application in spintronic devices, and as dissipationless transistors for quantum computers. The topological materials discovered till now can be broadly classified into the categories of topological insulators (strong and weak),[\[51, 52\]](#) Dirac semimetals,[\[53\]](#) Weyl (type-I and II) semimetals,[\[54\]](#) and nodal line semimetals.[\[55\]](#) A lot of materials in each of these classes have been theoretically predicted, and experimentally realized, but the scope of research for realizing new topological materials that can be incorporated at low cost in the present day silicon or germanium based device technology, is still open. In Chapter 7, we show that chemical pressure can induce a topological phase transition in germanene-like systems and can produce topological insulators (TI) at ambient conditions. Topological insulators are materials that have an insulating gap in the bulk but conducting edge states. The discovery of materials that are topological insulators at ambient conditions, and can be incorporated in the present Si or Ge-based semiconductor technology, is of prime importance for their possible applications in spintronics and quantum computers. The inability to form stable monolayers of germanene while keeping its topological properties unharmed, has led to the idea of functionalizing germanene to improve its stability.[\[56, 57\]](#) Though $-\text{CH}_3$ functionalized germanene has been predicted to undergo a topological transition when subjected to an external biaxial strain, achieving the required large values of strain by mechanical means is essentially impossible. We show that, instead, chemical functionalization by $-\text{CX}_3$ ($X = \text{H}, \text{F}, \text{Cl}, \text{Br}$ or I) and $-\text{CXY}_2$ ($X, Y = \text{F}$ or Cl) induces giant chemical strains on the germanene lattice that can, in some cases, drive the system into a TI phase. We find that GeCCl_3 is a topological insulator at ambient conditions and it stabilizes itself by a symmetry-lowering distortion, leading to distorted (D)- GeCCl_3 . We also succeed in achieving a TI phase at ambient conditions in GeCFCl_2 which has a lower chemical pressure than GeCCl_3 . Moreover, GeCFCl_2 is found to be a large gap TI with a band gap of 0.23 eV, more than double the band gap of GeCCl_3 . We hope that this work will motivate experiments for the synthesis of the above

mentioned materials.

In Chapter 8, we show that it is possible to observe a number of non-trivial topological phases in the three-dimensional (3D) bulk of a single material, GeCCl_3 , under suitable conditions. Semimetals (Dirac and Weyl), and nodal line semimetals, are examples of types of materials other than topological insulators, that show topologically non-trivial properties. The observation of these different topological phases in a single material is rare, and achieving such a feat can open up possibilities in a broad range of applications. Here, we use the presence or absence of inversion symmetry, along with hydrostatic pressure, in the 3D bulk of GeCCl_3 to obtain all the topological phases mentioned above. Computation of the 3D band structure [excluding spin orbit coupling (SOC)] and the nodal line structure in the 3D k -space of the inversion symmetric system, show that it is a Dirac nodal straight line semimetal. Breaking the inversion symmetry by appropriate stacking, turns it into a Weyl nodal straight line semimetal. When SOC is turned on, the inversion symmetric system becomes a weak TI (WTI), whereas the non-inversion symmetric system becomes a trivial insulator. We show that by applying hydrostatic pressure it is possible to turn both the WTI and the trivial insulator into a strong topological insulator. Our work shows the possibility of studying different topological phases and fermions in a single material.

In Chapter 9, the main conclusions in each chapter are summarized and possible directions for future work are discussed.

Bibliography

- [1] A. G. S. Filho and S. B. Fagan, *Nanomaterials Properties*, pp. 5–22. Berlin, Heidelberg: Springer Berlin Heidelberg, 2011.
- [2] H. W. Kroto, J. R. Heath, S. C. O'Brien, R. F. Curl, and R. E. Smalley, "C₆₀: Buckminsterfullerene," *Nature*, vol. 318, p. 162, 1985.

-
- [3] W. A. de Heer, “The physics of simple metal clusters: experimental aspects and simple models,” *Rev. Mod. Phys.*, vol. 65, pp. 611–676, Jul 1993.
- [4] H. Ohnishi, Y. Kondo, and K. Takayanagi, “Quantized conductance through individual rows of suspended gold atoms,” *Nature*, vol. 395, p. 780, 1995.
- [5] X. Li, X. Wang, L. Zhang, S. Lee, and H. Dai, “Chemically derived, ultrasmooth graphene nanoribbon semiconductors,” *Science*, vol. 319, no. 5867, pp. 1229–1232, 2008.
- [6] J. Cai, P. Ruffieux, R. Jaafar, M. Bieri, T. Braun, S. Blankenburg, M. Muoth, A. P. Seitsonen, M. Saleh, X. Feng, *et al.*, “Atomically precise bottom-up fabrication of graphene nanoribbons,” *Nature*, vol. 466, p. 470, 2010.
- [7] K. S. Novoselov, A. K. Geim, S. V. Morozov, D. Jiang, M. I. Katsnelson, I. V. Grigorieva, S. V. Dubonos, and A. A. Firsov, “Two-dimensional gas of massless dirac fermions in graphene,” *Nature*, vol. 438, p. 197, 2005.
- [8] J. Tersoff, “Surface-confined alloy formation in immiscible systems,” *Phys. Rev. Lett.*, vol. 74, pp. 434–437, Jan 1995.
- [9] R. P. Feynman, “There’s plenty of room at the bottom.” <http://resolver.caltech.edu/CaltechES:23.5.1960Bottom>.
- [10] G. Binnig, H. Rohrer, C. Gerber, and E. Weibel, “ 7×7 reconstruction on si(111) resolved in real space,” *Phys. Rev. Lett.*, vol. 50, pp. 120–123, Jan 1983.
- [11] G. Binnig, C. F. Quate, and C. Gerber, “Atomic force microscope,” *Phys. Rev. Lett.*, vol. 56, pp. 930–933, Mar 1986.
- [12] P. S. Weiss, *Scanning Probe Microscopy and Spectroscopy. Theory, Techniques, and Applications*. University of Pennsylvania: Wiley-VCH: New York, 2 ed., 2001.

-
- [13] Borionetti, G., Bazzali, A., and Orizio, R., “Atomic force microscopy: a powerful tool for surface defect and morphology inspection in semiconductor industry,” *Eur. Phys. J. Appl. Phys.*, vol. 27, pp. 101–106, 2004.
- [14] E. I. Altman, M. Z. Baykara, and U. D. Schwarz, “Noncontact atomic force microscopy: An emerging tool for fundamental catalysis research,” *Accounts of Chemical Research*, vol. 48, no. 9, pp. 2640–2648, 2015.
- [15] G. E. Moore, “Readings in computer architecture,” ch. Cramming More Components Onto Integrated Circuits, pp. 56–59, San Francisco, CA, USA: Morgan Kaufmann Publishers Inc., 2000.
- [16] R. Li, L. Zhang, and P. Wang, “Rational design of nanomaterials for water treatment,” *Nanoscale*, vol. 7, pp. 17167–17194, 2015.
- [17] P. Hohenberg and W. Kohn, “Inhomogeneous electron gas,” *Phys. Rev.*, vol. 136, pp. B864–B871, Nov 1964.
- [18] W. Kohn and L. J. Sham, “Self-consistent equations including exchange and correlation effects,” *Phys. Rev.*, vol. 140, pp. A1133–A1138, Nov 1965.
- [19] A. Rahman, “Correlations in the motion of atoms in liquid argon,” *Phys. Rev.*, vol. 136, pp. A405–A411, Oct 1964.
- [20] N. Metropolis and S. Ulam., “The monte carlo method,” *JSTOR*, vol. 44, pp. 335–341, 1949.
- [21] Y. Gong, T. Dou, S. Kang, Q. Li, and Y. Hu, “Deep desulfurization of gasoline using ion-exchange zeolites: Cu(I)- and Ag(I)-beta,” *Fuel Processing Technology*, vol. 90, no. 1, pp. 122 – 129, 2009.
- [22] J. McCaskie and S. Redding, “Successful automotive applications for electroless nickel: Hex-chrome alternative dramatically improves personnel safety while

- reducing environmentally harmful wastes,” *Metal Finishing*, vol. 106, no. 4, pp. 25 – 27, 2008.
- [23] N. Josiane, D. Paul-Andr, and H. Michle, “Elimination of volatile organic compounds by biofiltration: A review,” *Reviews on Environmental Health*, vol. 22, p. 273, 2007.
- [24] D. Astruc, *Nanoparticles and Catalysis*. John Wiley & Sons, Ltd, 1 ed., 2008.
- [25] E. Roduner, *Nanoscopic Materials*. The Royal Society of Chemistry, 2006.
- [26] D. Astruc, F. Lu, and J. R. Aranzaes, “Nanoparticles as recyclable catalysts: The frontier between homogeneous and heterogeneous catalysis,” *Angewandte Chemie International Edition*, vol. 44, no. 48, pp. 7852–7872, 2005.
- [27] A. Wieckowski, E. R. Savinova, and C. G. Vayenas, *Catalysis and Electrocatalysis at Nanoparticle Surfaces*. CRC Press, 1 ed., Wieckowski.
- [28] F. Zhu, J. Kim, K.-C. Tsao, J. Zhang, and H. Yang, “Recent development in the preparation of nanoparticles as fuel cell catalysts,” *Current Opinion in Chemical Engineering*, vol. 8, pp. 89 – 97, 2015. Nanotechnology Separation engineering.
- [29] I. Gehrke, A. Geiser, and A. Somborn-Schulz, “Innovations in nanotechnology for water treatment,” *Nanotechnology, science and applications*, vol. 8, pp. 1177–8903, 2015.
- [30] A. Z. Moshfegh, “Nanoparticle catalysts,” *Journal of Physics D: Applied Physics*, vol. 42, p. 233001, nov 2009.
- [31] L. Li, A. H. Larsen, N. A. Romero, V. A. Morozov, C. Glinsvad, F. Abild-Pedersen, J. Greeley, K. W. Jacobsen, and J. K. Nørskov, “Investigation of catalytic finite-size-effects of platinum metal clusters,” *The Journal of Physical Chemistry Letters*, vol. 4, no. 1, pp. 222–226, 2013.

- [32] G. Niu, X. Guo, and L. Wang, “Review of recent progress in chemical stability of perovskite solar cells,” *J. Mater. Chem. A*, vol. 3, pp. 8970–8980, 2015.
- [33] J. N. Freitas, A. S. Goncalves, and A. F. Nogueira, “A comprehensive review of the application of chalcogenide nanoparticles in polymer solar cells,” *Nanoscale*, vol. 6, pp. 6371–6397, 2014.
- [34] K. Kalyanasundaram and M. Grätzel, “Applications of functionalized transition metal complexes in photonic and optoelectronic devices,” *Coordination Chemistry Reviews*, vol. 177, no. 1, pp. 347 – 414, 1998.
- [35] J. Gong, J. Liang, and K. Sumathy, “Review on dye-sensitized solar cells (dsscs): Fundamental concepts and novel materials,” *Renewable and Sustainable Energy Reviews*, vol. 16, no. 8, pp. 5848 – 5860, 2012.
- [36] S. Almosni, A. Delamarre, Z. Jehl, D. Suchet, L. Cojocar, M. Giteau, B. Behaghel, A. Julian, C. Ibrahim, L. Tatry, H. Wang, T. Kubo, S. Uchida, H. Segawa, N. Miyashita, R. Tamaki, Y. Shoji, K. Yoshida, N. Ahsan, K. Watanabe, T. Inoue, M. Sugiyama, Y. Nakano, T. Hamamura, T. Toupance, C. Olivier, S. Chambon, L. Vignau, C. Geffroy, E. Cloutet, G. Hadziioannou, N. Cavassilas, P. Rale, A. Cattoni, S. Collin, F. Gibelli, M. Paire, L. Lombez, D. Aureau, M. Bouttemy, A. Etcheberry, Y. Okada, and J.-F. Guillemoles, “Material challenges for solar cells in the twenty-first century: directions in emerging technologies,” *Science and Technology of Advanced Materials*, vol. 19, no. 1, pp. 336–369, 2018.
- [37] M. N. Baibich, J. M. Broto, A. Fert, F. N. Van Dau, F. Petroff, P. Etienne, G. Creuzet, A. Friederich, and J. Chazelas, “Giant magnetoresistance of (001)fe/(001)cr magnetic superlattices,” *Phys. Rev. Lett.*, vol. 61, pp. 2472–2475, Nov 1988.

-
- [38] G. Binasch, P. Grünberg, F. Saurenbach, and W. Zinn, “Enhanced magnetoresistance in layered magnetic structures with antiferromagnetic interlayer exchange,” *Phys. Rev. B*, vol. 39, pp. 4828–4830, Mar 1989.
- [39] M. Julliere, “Tunneling between ferromagnetic films,” *Physics Letters A*, vol. 54, no. 3, pp. 225 – 226, 1975.
- [40] E. Adler, J. K. DeBrosse, S. F. Geissler, S. J. Holmes, M. D. Jaffe, J. B. Johnson, C. W. Koburger, III, J. B. Lasky, B. Lloyd, G. L. Miles, J. S. Nakos, W. P. Noble, Jr., S. H. Voldman, M. Armacost, and R. Ferguson, “The evolution of IBM CMOS DRAM technology,” *IBM J. Res. Dev.*, vol. 39, pp. 167–188, Feb. 1995.
- [41] S. Blügel, M. Weinert, and P. H. Dederichs, “Ferromagnetism and antiferromagnetism of 3d-metal overlayers on metals,” *Phys. Rev. Lett.*, vol. 60, pp. 1077–1080, Mar 1988.
- [42] R. L. Fink, C. A. Ballentine, J. L. Erskine, and J. A. Araya-Pochet, “Experimental probe for thin-film magnetism in $p(1 \times 1)$ Pd and V on Ag(100),” *Phys. Rev. B*, vol. 41, pp. 10175–10178, May 1990.
- [43] M. Stampanoni, A. Vaterlaus, M. Aeschlimann, and F. Meier, “Magnetism of epitaxial bcc iron on Ag(001) observed by spin-polarized photoemission,” *Phys. Rev. Lett.*, vol. 59, pp. 2483–2485, Nov 1987.
- [44] C. A. Ballentine, R. L. Fink, J. Araya-Pochet, and J. L. Erskine, “Magnetic phase transition in a two-dimensional system: $p(1 \times 1)$ -Ni on Cu(111),” *Phys. Rev. B*, vol. 41, pp. 2631–2634, Feb 1990.
- [45] V. Martin, W. Meyer, C. Giovanardi, L. Hammer, K. Heinz, Z. Tian, D. Sander, and J. Kirschner, “Pseudomorphic growth of Fe monolayers on Ir(001)– (1×1) : From a fct precursor to a bct film,” *Phys. Rev. B*, vol. 76, p. 205418, Nov 2007.

-
- [46] C. Rau, G. Xing, and M. Robert, “Ferromagnetic order and critical behavior at surfaces of ultrathin V(100)p(1 × 1) films on Ag(100),” *Journal of Vacuum Science & Technology A*, vol. 6, no. 3, pp. 579–581, 1988.
- [47] M. Stampanoni, A. Vaterlaus, D. Pescia, M. Aeschlimann, F. Meier, W. Dürr, and S. Blügel, “Lack of evidence for ferromagnetism in the vanadium monolayer on Ag(001),” *Phys. Rev. B*, vol. 37, pp. 10380–10382, Jun 1988.
- [48] C. L. Kane and E. J. Mele, “Quantum spin Hall effect in graphene,” *Phys. Rev. Lett.*, vol. 95, p. 226801, Nov 2005.
- [49] C. L. Kane and E. J. Mele, “ Z_2 topological order and the quantum spin Hall effect,” *Phys. Rev. Lett.*, vol. 95, p. 146802, Sep 2005.
- [50] M. König, S. Wiedmann, C. Brüne, A. Roth, H. Buhmann, L. W. Molenkamp, X.-L. Qi, and S.-C. Zhang, “Quantum spin Hall insulator state in HgTe quantum wells,” *Science*, vol. 318, no. 5851, pp. 766–770, 2007.
- [51] M. Z. Hasan and C. L. Kane, “Colloquium: Topological insulators,” *Rev. Mod. Phys.*, vol. 82, pp. 3045–3067, Nov 2010.
- [52] A. Bansil, H. Lin, and T. Das, “Colloquium: Topological band theory,” *Rev. Mod. Phys.*, vol. 88, p. 021004, Jun 2016.
- [53] S. M. Young, S. Zaheer, J. C. Y. Teo, C. L. Kane, E. J. Mele, and A. M. Rappe, “Dirac semimetal in three dimensions,” *Phys. Rev. Lett.*, vol. 108, p. 140405, Apr 2012.
- [54] N. P. Armitage, E. J. Mele, and A. Vishwanath, “Weyl and dirac semimetals in three-dimensional solids,” *Rev. Mod. Phys.*, vol. 90, p. 015001, Jan 2018.
- [55] C. Fang, H. Weng, X. Dai, and Z. Fang, “Topological nodal line semimetals,” *Chinese Physics B*, vol. 25, p. 117106, nov 2016.

-
- [56] E. Bianco, S. Butler, S. Jiang, O. D. Restrepo, W. Windl, and J. E. Goldberger, “Stability and exfoliation of germanane: A germanium graphane analogue,” *ACS Nano*, vol. 7, no. 5, pp. 4414–4421, 2013.
- [57] S. Jiang, S. Butler, E. Bianco, O. D. Restrepo, W. Windl, and J. E. Goldberger, “Improving the stability and optical properties of germanane via one-step covalent methyl-termination,” *Nature Communications*, vol. 5, p. 3389, 2014.

Chapter 2

Methods

2.1 Density Functional Theory

All materials consist of many interacting nuclei and electrons. Density functional theory (DFT) provides us with a formalism to treat this many body problem exactly. Over the years it has become an indispensable tool for the calculation of electronic structure in condensed matter systems. In this chapter we present an overview of DFT, which has been used in all the computations throughout this thesis.

2.1.1 The Many Body Problem

The Hamiltonian for a many-body interacting system is given by:[1]

$$\hat{H} = - \sum_I \frac{\hbar^2}{2M_I} \nabla_I^2 - \frac{\hbar^2}{2m_e} \sum_i \nabla_i^2 + \frac{1}{2} \sum_{I \neq J} \frac{Z_I Z_J e^2}{|\mathbf{R}_I - \mathbf{R}_J|} - \sum_{i,I} \frac{Z_I e^2}{|\mathbf{r}_i - \mathbf{R}_I|} + \frac{1}{2} \sum_{i \neq j} \frac{e^2}{|\mathbf{r}_i - \mathbf{r}_j|}, \quad (2.1)$$

where h is Planck's constant and $\hbar = h/2\pi$. \mathbf{r}_i is the position coordinate of the i^{th} electron of mass m_i and charge e , and \mathbf{R}_I is the position coordinate of the I^{th} nucleus of mass M_I and charge $Z_I e$. The indices i, j run over all the electrons and I, J run over all the nuclei in the many-body system. The first two terms on the right-hand-side of Eq. (2.1) represent the nuclear and electronic kinetic energies respectively. The subsequent terms are the nuclei-nuclei Coulomb repulsion, electron-nuclei Coulomb

attraction and the electron-electron Coulomb repulsion, respectively.

2.1.2 Born-Oppenheimer Approximation or Adiabatic Approximation

The nuclear masses M_I are much larger than the electronic mass m_e . This results in different time scales associated with the motion of nuclei and electrons; the electrons move much faster than the nuclei. Motivated by this fact, Born and Oppenheimer proposed a scheme for separating the electronic and nuclear degrees of freedom in the equations of motion.^[2] They showed that a perturbation series can be defined based on the inverse masses of the nuclei $\{1/M_I\}$, valid for the full interacting system. Setting the masses of the nuclei to infinity, one can then ignore the kinetic energy of the nuclei. This would essentially mean electrons instantaneously following the motion of the nuclei, and is the very essence of the Born-Oppenheimer approximation. Ignoring the kinetic energy of the nuclei, then, the many-body Hamiltonian can be written as

$$\hat{H} = \hat{T} + \hat{V}_{\text{ext}} + \hat{V}_{\text{int}} + E_{II}, \quad (2.2)$$

where \hat{T} is the electronic kinetic energy operator given by:

$$\hat{T} = \sum_i -\frac{\hbar^2}{2m_e} \nabla_i^2, \quad (2.3)$$

\hat{V}_{ext} is the potential acting on the electrons due to the nuclei,

$$\hat{V}_{\text{ext}} = \sum_i V_{\text{ext}}(\mathbf{r}_i), \quad (2.4)$$

\hat{V}_{int} is the potential representing electron-electron interaction,

$$\hat{V}_{\text{int}} = \frac{1}{2} \sum_{i \neq j} \frac{e^2}{|\mathbf{r}_i - \mathbf{r}_j|}, \quad (2.5)$$

and E_{II} includes the classical interaction between nuclei and any other terms that contribute to the total energy of the system.[1]

2.1.3 The Hohenberg-Kohn Theorems

In an attempt to formulate an exact theory of interacting particles, Hohenberg and Kohn (HK) proved two theorems.[3] The formulation applies to any system of interacting particles in an external potential $V_{ext}(\mathbf{r})$. Since the nuclei-nuclei interactions E_{II} can be added later, the Hamiltonian in Eqs. (2.2) – (2.5) can be rewritten as

$$\hat{H} = -\frac{\hbar^2}{2m_e} \sum_i \nabla_i^2 + \sum_i V_{ext}(\mathbf{r}_i) + \frac{1}{2} \sum_{i \neq j} \frac{e^2}{|\mathbf{r}_i - \mathbf{r}_j|}. \quad (2.6)$$

The Hohenberg-Kohn theorems are stated below.

Theorem I: For any system of interacting particles in an external potential $V_{ext}(\mathbf{r})$, the potential $V_{ext}(\mathbf{r})$ is determined uniquely, except for a constant, by the ground state particle density $n_0(\mathbf{r})$.

As a consequence of this theorem, one can uniquely determine the external potential from the knowledge of the ground state particle density which in turn can be computed from the solution of the many-body wave function that is the solution of the Schrödinger equation involving the potential. This results in a self-consistent solution procedure for determining the ground state particle density, as will be described in the next section.

Theorem II: A universal functional of energy $E[n]$ in terms of the density $n(\mathbf{r})$ can be defined, valid for any external potential $V_{ext}(\mathbf{r})$. For any particular $V_{ext}(\mathbf{r})$, the exact ground state energy of the system is the global minimum value of this functional, and the density $n(\mathbf{r})$ that minimizes the functional is the exact ground state density $n_0(\mathbf{r})$.

The HK theorems show that all the properties such as the kinetic energy, etc., are uniquely determined once $n(\mathbf{r})$ is specified. Each such property then can be

considered as a functional of $n(\mathbf{r})$, and hence the total energy functional $E_{HK}[n]$ can be written as

$$E_{HK}[n] = F[n] + \int d^3r V_{ext}(\mathbf{r})n(\mathbf{r}). \quad (2.7)$$

Comparing Eq. (2.7) with Eq. (2.6), one finds that the functional $F[n]$ consists of the kinetic energy of the electrons ($T[n]$) and the electron-electron interaction ($E_{e-e}[n]$),

$$F[n] = T[n] + E_{e-e}[n], \quad (2.8)$$

where the first term $F[n]$ is a universal functional of the density that is the same for all electronic systems. Knowing $F[n]$ will therefore enable us to obtain the exact ground state density and energy by minimizing the total energy of the system, given by Eq. (2.7), with respect to variations in the density $n(\mathbf{r})$.

However, the exact form of the universal functional $F[n]$ is not known. The HK theorem is only an existential proof and does not provide the form of $F[n]$. The reason behind the success of DFT lies in the proposal of a very effective approximation for the universal energy functional $F[n]$, by Kohn and Sham in 1965,[4] which we discuss further below.

2.1.4 The Kohn-Sham Ansatz

The Kohn-Sham (KS) ansatz, which is by far the most widely used way in which density functional theory has been applied, provides a method of mapping the problem of an interacting N -electron system onto an equivalent problem of N non-interacting fictitious electrons. It rests upon two assumptions:[1]

1. The exact ground state density can be represented by the ground state density of an auxiliary system of non-interacting particles.
2. The auxiliary Hamiltonian is chosen to have the usual kinetic energy operator and an effective local potential $V_{\text{eff}}(\mathbf{r})$ acting on an electron at point \mathbf{r} .

Using the above two assumptions, the Kohn-Sham approach replaces the Hohenberg-Kohn universal energy functional $F[n]$ with:

$$F[n] = T_s[n] + E_H[n] + E_{xc}[n], \quad (2.9)$$

where, $T_s[n]$ is the kinetic energy of the non-interacting electrons, given by (using Hartree atomic units $\hbar = m_e = e = 4\pi/\epsilon_0 = 1$):

$$T_s = -2\frac{1}{2} \sum_{\alpha}^{N/2} \int \psi_{\alpha}^*(\mathbf{r}) \nabla^2 \psi_{\alpha}(\mathbf{r}) d\mathbf{r} = - \sum_{\alpha}^{N/2} \int \psi_{\alpha}^*(\mathbf{r}) \nabla^2 \psi_{\alpha}(\mathbf{r}) d\mathbf{r}, \quad (2.10)$$

where the multipliers 2 and 1/2 in first term on the right hand side of the equation come due to the two spins and $\hbar^2/2m_e$, respectively.

In Eq. (2.10), the electron-electron interaction term $E_{e-e}[n]$ of Eq. (2.8) has been replaced by the sum of the Hartree energy ($E_H[n]$), defined as the classical Coulomb interaction energy of the electron density $n(\mathbf{r})$ interacting with itself, and a residual energy contribution due to the exchange asymmetry and correlations. The Hartree energy is given as:

$$E_H[n] = \frac{1}{2} \int d^3r d^3r' \frac{n(\mathbf{r})n(\mathbf{r}')}{|\mathbf{r} - \mathbf{r}'|}. \quad (2.11)$$

The residual energy contribution due to the exchange asymmetry and correlations can be put together along with the kinetic energy difference into the so-called exchange-correlation energy E_{xc} , which is defined as:

$$E_{xc}[n] = \langle \hat{T} \rangle - T_s[n] + \langle \hat{V}_{e-e} \rangle - E_H[n], \quad (2.12)$$

where $\langle \hat{T} \rangle = \sum_i -\frac{1}{2} \nabla_i^2$, and $V_{e-e} = \frac{1}{2} \sum_{i \neq j} \frac{1}{|\mathbf{r}_i - \mathbf{r}_j|}$ is the potential energy representing electron-electron interactions.

The KS total energy functional ($E_{KS}[n]$) is given by:

$$E_{KS} = F[n] + \int d\mathbf{r} V_{\text{ext}}(\mathbf{r})n(\mathbf{r}). \quad (2.13)$$

The variation of $E_{KS}[n]$ with respect to the density $n(\mathbf{r})$, with the constraint that the total number of electrons in the system is fixed, leads us to the Kohn-Sham Schrödinger-like equations, which essentially describe the problem of an interacting many-electron system as a system of N fictitious non-interacting Kohn-Sham electrons moving in an effective potential $V_{KS}[n(\mathbf{r})]$, given by:

$$\left\{ -\frac{1}{2}\nabla^2 + V_{KS}(\mathbf{r}) \right\} \psi_\alpha(\mathbf{r}) = \epsilon_\alpha \psi_\alpha(\mathbf{r}), \quad (2.14)$$

where the first term is the kinetic energy of the fictitious non-interacting electrons and V_{KS} is the effective potential experienced by the non-interacting particles, given by:

$$V_{KS}(\mathbf{r}) = V_{\text{ext}}(\mathbf{r}) + V_H(\mathbf{r}) + V_{xc}(\mathbf{r}), \quad (2.15)$$

where $V_H(\mathbf{r}) = \frac{\delta E_H}{\delta n(\mathbf{r})}$ is the Hartree potential and $V_{xc}(\mathbf{r}) = \frac{\delta E_{xc}}{\delta n(\mathbf{r})}$ is the exchange-correlation potential. The potential $V_{KS}(\mathbf{r})$ needs to be found self-consistently with the resulting density given as:

$$n(\mathbf{r}) = 2 \sum_{\alpha=1}^{N/2} \psi_\alpha^*(\mathbf{r}) \psi_\alpha(\mathbf{r}). \quad (2.16)$$

A flowchart demonstrating the self-consistent procedure to solve Eqs. (2.14) - (2.16) is shown in Fig. 2.1. The KS-approach explicitly separates out the independent particle kinetic energy and the long-range Hartree terms. The remaining exchange-correlation term can be reasonably approximated as a local or nearly-local functional of density, as we will see in the next section.

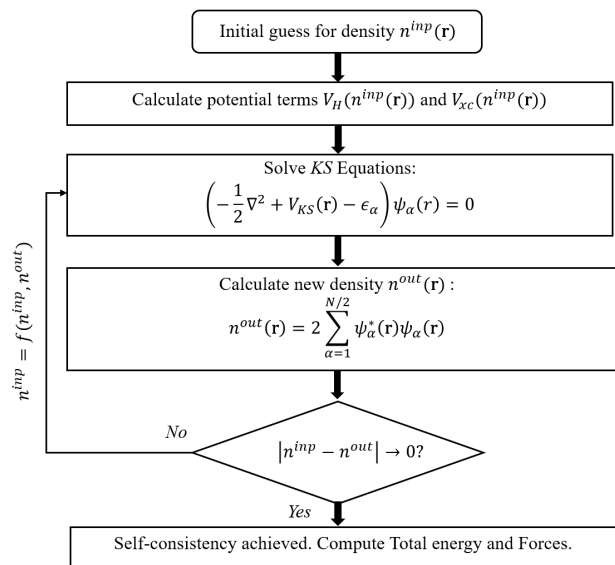


Figure 2.1: Flowchart showing the self-consistency loop for solving the KS equation, Eq. (2.14).

2.1.5 Approximations for the Exchange-Correlation Functional

The exchange energy arises from the fact that electrons obey Pauli's exclusion principle, as a result of which electrons of the same spin experience a repulsive interaction between them, called the exchange interaction. The corresponding exchange energy is defined as the difference between the Hartree and Hartree-Fock energies. The correlation energy is a result of complicated many-body interactions between the electrons, whereby the electrons try to reduce the Coulomb repulsion between themselves by screening themselves. It is given by the difference between the exact energy and the Hartree-Fock energy.

Since the exact form of the exchange-correlation potential is not known, it is generally approximated as a local [Local Density Approximation (LDA)] or semilocal [Generalized Gradient Approximation (GGA)] functional of the density and is expressed in the general form

$$E_{xc}[n] = \int d\mathbf{r} n(\mathbf{r}) \epsilon_{xc}[n(\mathbf{r})], \quad (2.17)$$

where $\epsilon_{xc}[n(\mathbf{r})]$ is an exchange-correlation energy per electron at point \mathbf{r} that depends only upon the density $n(\mathbf{r})$ in some neighbourhood of point \mathbf{r} .

In the LDA, the exchange-correlation being local in nature, depends on each point in space independent of other points and the exchange-correlation energy is locally assumed to be same as that of a homogeneous electron gas,[4] i.e.,

$$\epsilon_{xc}[n(\mathbf{r})] = \epsilon_{xc}^{\text{hom}}[n(\mathbf{r})]. \quad (2.18)$$

Approximate forms of $\epsilon_{xc}^{\text{hom}}(n(\mathbf{r}))$ have been obtained from Quantum Monte Carlo simulations by Ceperley and Alder,[5] which were later parametrized by Perdew and Zunger,[6] using a simple analytical form.

The LDA does not take into account the variation of electron density from one place to another. To overcome this deficiency, the exchange-correlation energy can be evaluated with an approximation that, at each point in space, is not only a functional of $n(\mathbf{r})$ but also of its gradient:

$$\epsilon_{xc}(n(\mathbf{r})) = \epsilon_{xc}(n(\mathbf{r}), |\nabla n(\mathbf{r})|). \quad (2.19)$$

A variety of ways were proposed,[7–9] to apply this idea and these are collectively known as the Generalized Gradient Approximations (GGA). Two of the most widely used GGA functionals are the Perdew-Burke-Ernzerhof (PBE) functional,[9] and the Perdew-Wang functional.[8]

2.1.6 Hybrid Functionals

In a system of interacting particles usually the exchange contributions are significantly larger in absolute value than the corresponding correlation effects.[10] An accurate representation of the exchange functional is therefore necessary to obtain meaningful results from DFT. The observation that the LDA and the GGA trends are opposite to those of the Hartree-Fock and the fact that within the Hartree-Fock

picture the exchange effects can be exactly computed, motivated the development of approximations which combine these two approaches.[11] This resulted in the hybrid exchange-correlation functionals with DFT correlation and a combination of DFT and Hartree-Fock exchange, having the following general form:

$$E_{xc}^{\text{hyb}} = \alpha E_x^{\text{HF}} + (1 - \alpha) E_x^{\text{DFT}} + E_c^{\text{DFT}}, \quad (2.20)$$

where the weight α is found by fitting the results of the corresponding functional to the experimental or calculated data, or set *a priori* in the case of adiabatic connection functionals.[12] It turns out that the hybrid functionals are more reliable in calculating band gaps in solids or HOMO-LUMO gaps in molecules, atomic enthalpies, transition or excited state geometries and vibrational frequencies. Some popular examples of hybrid functionals include B3LYP,[13, 14] PBE0,[12] HSE,[15] and Meta hybrid GGA.[16] In this thesis we have used HSE (Heyd-Scuseria-Ernzerhof) and B3LYP (Becke, three-parameter, Lee-Yang-Parr) hybrid functionals.

2.1.7 Basis Sets

Solving the KS equations usually requires expansion of the electronic wavefunctions in a basis set $\{\phi_\beta(\mathbf{r})\}$. Many types of basis sets exist e.g., plane waves,[17, 18], Gaussians,[19] Muffin Tin Orbitals,[20] localized atomic orbitals,[21] etc. We have used a plane wave basis for the majority of the work done in this thesis. For optimizing the structure of large nanoparticles and calculating the ground state properties of a few ligand complexes, a basis set of localized atomic-like orbitals has been used, as implemented in SIESTA.[21] A brief description of these basis functions is presented below.

Plane Waves

Since the electrons experience a periodic potential in an extended system, Bloch's theorem suggests that the electronic wavefunctions can be expanded in terms of plane

waves. The KS orbitals can then be represented as:

$$\psi_{\alpha,\mathbf{k}}(\mathbf{r}) = \sum_{\mathbf{G}} c_{\alpha,\mathbf{k}+\mathbf{G}} e^{i(\mathbf{k}+\mathbf{G})\cdot\mathbf{r}}, \quad (2.21)$$

where \mathbf{G} is a reciprocal lattice vector, α is the band index, and \mathbf{k} is a wavevector in the first Brillouin zone. This summation is truncated by a kinetic energy cutoff (E_{cut}) which determines the number of plane waves in the basis, and is given as $(\hbar^2/2m)|\mathbf{k} + \mathbf{G}|^2 \leq E_{\text{cut}}$.

The computational cost while using plane waves depends on the number of plane waves in the expansion, which increases greatly if one tries to expand the wavefunctions in the core region. This problem is resolved by the use of pseudopotentials, as described later.

The set of plane waves is discrete only if the system is periodic. This requires the use of artificially periodic supercells if the system is not periodic. For example, if the system is not periodic in one or more dimensions, it is made artificially periodic along that direction by the introduction of a vacuum spacing.

Localized Basis Set

When using a plane wave basis set to perform calculations on systems of low dimensionality, such as molecules, nanoparticles etc., a significant part of the computational effort is spent to represent the vacuum that fills the supercells. A common approach to overcome this problem is to use basis functions that decay exponentially to zero at sufficiently large distances. Atomic orbitals (AO),^[22] Slater-type orbitals (STO),^[23] Gaussian-type orbitals (GTO),^[24] etc., are examples of commonly used localized basis sets.

STOs are expressed as:^[23]

$$\phi_{STO}^{nlm\zeta}(r, \theta, \phi) = \alpha Y_{lm}(\theta, \phi) r^{n-1} e^{-\zeta r} \quad (2.22)$$

where α is a normalization constant and $Y_{lm}(\theta, \phi)$ is a spherical harmonic and n, l

and m are principal, orbital angular momentum and magnetic quantum numbers, respectively. ζ determines the radius of the orbit. Since STOs are nodeless functions, so except for lowest lying states ($1s$, $2p$, etc.) one needs a linear combination of several STOs with variable exponents to represent each atomic orbital.

In GTOs, the exponentials in STOs are replaced by Gaussian-type orbitals. This is advantageous since all the Coulomb integrals now can be performed analytically, which saves computational cost. The GTOs are represented as:[24]

$$\phi_{GTO}^{nlm\zeta}(r, \theta, \phi) = \alpha Y_{lm}(\theta, \phi) r^{2n-2-l} e^{-\zeta r^2} \quad (2.23)$$

The accuracy of a calculation depends on the size of the basis set. Increasing the number of basis functions improves the quality of the calculation, e.g., in SIESTA, if a single basis function per atomic orbital is used, this is called a minimal or single- ζ basis set. To improve accuracy one can add more basis functions of the same type, which leads to double- ζ (DZ), triple- ζ (TZ) and in general n -tuple ζ basis sets.

2.1.8 Pseudopotential Approximation

The core states of an atom are highly localized, and do not take part in the chemical bonding. Moreover, representation of these states requires a large number of basis functions in an all-electron plane wave DFT calculation. This leads to a huge computational cost. One can however replace the core region of the atom by an effective potential that treats the interaction between the ‘ionic core’ and valence electrons with sufficient accuracy. This is known as the pseudopotential approximation.[25, 26] The oscillations of valence electrons in the core region are removed with a constraint that the pseudo-wavefunctions match the actual valence wavefunctions beyond a certain cut-off radius. A good pseudopotential should have the following properties:[27]

1. *smoothness*: the pseudo-wavefunction and its first and second derivatives should match smoothly at the core radius cutoff.

2. *transferability*: the same pseudopotential can be used in different chemical and structural environments.
3. *softness*: it should require a low plane wave cutoff.

It was believed that to ensure good transferability, the norm of the pseudo-wavefunction should be equal to the norm of the all-electron wavefunction in the core region. This is known as the norm-conservation criterion and such pseudopotentials are known as Norm-conserving pseudopotentials.[1] The norm-conservation criterion is relaxed in Ultrasoft pseudopotentials.[28] However, due to relaxation of this criterion, some charge in the core region is lost and has to be added as ‘augmentation charge’.

2.1.9 **k**-point Sampling and Smearing

Many physical quantities such as the total energy, density of states, etc., are obtained by integrating over the wavevectors in the first Brillouin zone (BZ). In practice this integration over the first BZ is replaced by a summation over a finite mesh of **k**-points. Generally, the most widely used **k**-point mesh is the Monkhorst-Pack grid. [29] In this scheme, the **k**-point grid is generated using the formula:

$$\mathbf{k}_{n_1, n_2, n_3} = \sum_{\beta=1}^3 \frac{2n_\beta - N_\beta - 1}{2N_\beta} \mathbf{b}_\beta, \quad (n_\beta = 1, 2, 3, \dots, N_\beta) \quad (2.24)$$

where N_β is the number of divisions in the reciprocal space along the β direction ($\beta = 1, 2, 3$) and \mathbf{b}_1 , \mathbf{b}_2 and \mathbf{b}_3 are the primitive reciprocal lattice vectors.

Increasing the number of **k**-points in numerical integrations increases the accuracy of the calculations, but at the same time the computational cost also goes up. One can use the symmetries of the system (point group symmetries) to reduce the BZ to the irreducible BZ (IBZ), and consider only the **k**-points in the IBZ.

In order to obtain faster convergence one can consider fewer **k**-points by using the smearing technique, especially for metallic systems. For insulators and semiconductors, the density of states goes to zero before the Fermi level or the occupied states. For

metals the density of states does not go to zero and remains finite at k-points separating the occupied and unoccupied states in reciprocal space. One therefore introduces a step function to ensure zero contribution from the unoccupied states. However, the resolution of a step function at the Fermi energy is very difficult in plane waves. Using the smearing technique, one can replace the step function with a smoothly varying function for the occupation of states near the Fermi energy. Some of the existing smearing techniques are Gaussian smearing, [30] Methfessel-Paxton smearing, [31] and Marzari-Vanderbilt smearing. [32]

2.1.10 Calculation of Forces and Stresses

To obtain the optimized geometry of any system one needs to minimize the forces and stresses in the system. Zero force implies the atomic coordinates are relaxed and zero stress means the cell parameters are optimized.

The force on an ion I is equal to the derivative of the total energy with respect to the ionic position R_I , which according to the Hellmann-Feynman (HF) theorem is related to the expectation value of the derivative of Hamiltonian, [33] given as:

$$F_I = -\frac{\partial E(\mathbf{R}_I)}{\partial \mathbf{R}_I} = -\langle \psi | \frac{\partial \hat{H}}{\partial \mathbf{R}_I} | \psi \rangle \quad (2.25)$$

where ψ is the eigenfunction of the Hamiltonian \hat{H} . This theorem relieves one from calculating the total energy of a system at many configurations to compute the derivative and shows that computation of the total energy at a single configuration is sufficient to calculate the forces. The HF theorem assumes that the basis set used in the computation of forces is complete. But in actual cases the basis sets are truncated and/or position-dependent, giving rise to Pulay forces. [34, 35] The use of a position-independent basis set such as a plane wave basis set avoids this problem and is one of the major advantages of using a plane wave basis set.

Similarly, stresses can be calculated using the Nielsen and Martin theorem, [36] which relates the derivative of the total energy E_{tot} with respect to the strain $\epsilon_{\alpha\beta}$, to

the expectation value of the derivative of the Hamiltonian with respect to the strain, given as:

$$\sigma_{\alpha\beta} = -\frac{1}{\Omega} \frac{\partial E_{tot}}{\partial \epsilon_{\alpha\beta}} = -\frac{1}{\Omega} \langle \psi | \frac{\partial \hat{H}}{\partial \epsilon_{\alpha\beta}} | \psi \rangle, \quad (2.26)$$

where Ω is the volume of the system. Similar to HF forces, the truncated basis set can lead to errors in the computed stress values. To reduce these errors the stress calculations usually require a higher energy cut-off E_{cut} for plane waves than that would be required for total energy convergence.

2.1.11 Spin Polarized DFT

To extend the KS theory to the spin-polarized system it is sufficient to consider the total electronic density to be composed of two independent spin densities as $n(\mathbf{r}) = n^\uparrow(\mathbf{r}) + n^\downarrow(\mathbf{r})$. Each spin density is evaluated separately as is done in normal DFT:

$$n^\sigma(\mathbf{r}) = 2 \sum_{\alpha=1}^{N^\sigma} \psi_\alpha^{\sigma*}(\mathbf{r}) \psi_\alpha^\sigma(\mathbf{r}), \quad (2.27)$$

where $\sigma = \{\uparrow, \downarrow\}$ is the spin of the electron, and N^σ is the number of orbitals of spin σ . The spin-polarization or magnetization density is defined as $m(\mathbf{r}) = n^\uparrow(\mathbf{r}) - n^\downarrow(\mathbf{r})$.

The KS equations can now be written in terms of the spin polarized charge density and the magnetization density as (in Hartree units):

$$\left\{ -\frac{1}{2} \nabla^2 + V_{KS}^\sigma(\mathbf{r}) \right\} \psi_\alpha^\sigma(\mathbf{r}) = \epsilon_\alpha^\sigma \psi_\alpha^\sigma(\mathbf{r}), \quad (2.28)$$

where V_{KS}^σ is the KS effective potential, given as:

$$V_{KS}^\sigma(\mathbf{r}) = V_{ext}(\mathbf{r}) + V_H(\mathbf{r}) + V_{xc}^\sigma(\mathbf{r}), \quad (2.29)$$

where the exchange-correlation potential is defined as:

$$V_{xc}^\sigma(\mathbf{r}) = \frac{\delta E_{xc}[n(\mathbf{r}), m(\mathbf{r})]}{\delta n^\sigma(\mathbf{r})}. \quad (2.30)$$

These equations can be solved in a similar fashion to the non-spin-polarized KS equations, with approximations for the XC functional.

2.1.12 Dispersion Interactions: The DFT-D2 Method

Dispersion interactions are a form of attractive, long range, non-local interactions which arise as a response of the electrons in one region to instantaneous charge density fluctuations in another region.[37, 38] They are also known as van der Waals interactions or London interactions. The leading term of such an interaction is an instantaneous dipole-induced dipole interaction and the corresponding energy decays as $-\frac{1}{R^6}$, where R is the interatomic separation. Dispersion interactions play an important role in many systems, such as layered materials, molecules on surfaces, DNA, proteins, etc.

The dispersion interactions can be included in the DFT calculations either as semi-empirical corrections on top of the existing local functionals,[39, 40] or as non-local exchange-correlation functionals that incorporate the London interactions.[41, 42] In this thesis, wherever needed we have included the London dispersion interactions using the ‘‘DFT-D2’’ treatment of Grimme.[39] In this method the dispersion corrected total energy is given as:

$$E_{\text{DFT-D2}} = E_{\text{DFT}} + E_{\text{disp}}, \quad (2.31)$$

where E_{DFT} is the total energy from DFT calculations and E_{disp} is the dispersion correction given by:

$$E_{\text{disp}} = -s_6 \sum_{I=1}^{N_{\text{at}}-1} \sum_{J=I+1}^{N_{\text{at}}} \frac{C_6^{IJ}}{R_{IJ}^6} f_{\text{damp}}(R_{IJ}), \quad (2.32)$$

where N_{at} is the number of atoms in the system, C_6^{IJ} denotes the dispersion coefficient for a pair of atoms I and J ,

$$C_6^{IJ} = \sqrt{C_6^I C_6^J}, \quad (2.33)$$

s_6 is a global scaling factor that depends only on the approximate functional used,

and R_{IJ} is the interatomic distance between the atoms I and J . $f_{damp}(R_{IJ})$ is a damping function used to avoid singularity at small R_{IJ} , given as:

$$f_{damp}(R_{IJ}) = \frac{1}{1 + e^{-d(R_{IJ}/R_r - 1)}}, \quad (2.34)$$

where R_r is the sum of atomic van der Waals radii,[43] and d is a damping parameter with a typical value of 20.[39]

2.2 Relativistic DFT

To take into account the relativistic effects of the electrons it is necessary to solve the Dirac equation instead of the Schrödinger equation. In the presence of an electromagnetic field, the Dirac equation gives rise to the spin-orbit coupling term in addition to the relativistic corrections to the kinetic and potential energies of the electron.[44] Starting from the Dirac equation, the relativistic Kohn-Sham equation can be written as:[45]

$$(c\alpha \cdot \mathbf{p} + \beta m_e c^2 + V_{eff}(\mathbf{r}) + \mathbf{B}_{xc} \cdot \boldsymbol{\sigma})\psi_\nu(\mathbf{r}) = E_\nu \psi_\nu(\mathbf{r}), \quad (2.35)$$

where c is the velocity of light, \mathbf{p} is the momentum operator, E_ν is the eigenvalue of the equation including the rest mass energy, and α and β are 4×4 matrices given by:

$$\alpha = \begin{pmatrix} 0 & \boldsymbol{\sigma} \\ \boldsymbol{\sigma} & 0 \end{pmatrix}, \quad (2.36)$$

and

$$\beta = \begin{pmatrix} \mathbf{I}_2 & 0 \\ 0 & -\mathbf{I}_2 \end{pmatrix}, \quad (2.37)$$

ψ_ν is the 4-component vector:

$$\psi_\nu(\mathbf{r}) = \begin{pmatrix} \phi_\nu^\uparrow(\mathbf{r}) \\ \phi_\nu^\downarrow(\mathbf{r}) \\ \chi_\nu^\uparrow(\mathbf{r}) \\ \chi_\nu^\downarrow(\mathbf{r}) \end{pmatrix}, \quad (2.38)$$

where \uparrow and \downarrow indicate the spin-up and spin-down electrons, respectively, ϕ_ν and χ_ν are large and small components of the wavefunction, respectively, and $\boldsymbol{\sigma}$ denote the Pauli spin matrices.

The Hamiltonian in Eq. (2.35) can be rewritten as the sum of three terms: the Hamiltonian of the spin-polarized KS equations H_{SP} , the contributions coming from spin-orbit interaction H_{SO} and the contribution coming from the relativistic terms other than that of spin-orbit (mass-velocity, Darwin, and non-hermitian) H_1 . In the scalar relativistic approximation, H_{SO} is neglected.

2.2.1 Spin-Orbit Interactions

The spin-orbit interaction is a relativistic effect. An electron in its rest frame sees the nucleus moving in an orbit around it, generating a magnetic field proportional to the orbital angular momentum, which in turn interacts with the spin dipole moment of the electron. This is the origin of spin-orbit coupling, which results in a splitting of electron energy levels. In general, spin-orbit coupling becomes more and more prominent as the nuclear charge increases. Thus for heavier atoms relativistic effects need to be included for a reliable description of the electronic properties of the system.

As discussed in Section 2 above, spin-orbit effects are included in the *ab initio* calculations by solving the relativistic generalization of the KS equations presented in Eq. (2.35), which is the sum of three terms, H_{SP} , H_{SO} and H_1 . The spin-orbit

operator H_{SO} can be written as:

$$H_{SO} = \frac{1}{2m_e^2c^2} \boldsymbol{\sigma} \cdot (\nabla V_{eff}) \times \hat{\mathbf{p}}, \quad (2.39)$$

where $\hat{\mathbf{p}}$ is the momentum operator.

In this thesis spin-orbit coupling is included in the calculations by the use of fully relativistic pseudopotentials,[46] to study the topological properties of germanene-like systems.

2.3 Phonon Calculations: Density Functional Perturbation Theory

A wide range of physical properties of solids such as resistivity of metals, superconductivity, etc., depend on the lattice-dynamical behavior. With the development of DFT it is possible to obtain accurate phonon dispersions on a fine grid of wave vectors covering the entire Brillouin zone (BZ) using linear response theory of lattice vibrations, also known as the density functional perturbation theory (DFPT).[47–49]

2.3.1 Lattice Dynamics from Electronic-Structure Theory

The adiabatic approximation described in Section 1.2 lets us decouple the vibrational degrees of freedom from the electronic degrees of freedom. Using this approximation the lattice-dynamical properties of a system can be determined by the eigenvalues ε and the eigenfunctions Φ of the Schrödinger equation:

$$\left\{ - \sum_I \frac{\hbar^2}{2M_I} \frac{\partial^2}{\partial R_I^2} + E(\mathbf{R}) \right\} \Phi(\mathbf{R}) = \varepsilon \Phi(\mathbf{R}). \quad (2.40)$$

where \mathbf{R}_I is the coordinate of I th nucleus, M_I its mass and $E(\mathbf{R})$ is the Born-Oppenheimer energy surface.

The equilibrium geometry is found by equating the Hellman-Feynman forces (see Section 1.9) to zero, $\mathbf{F}_I = -\frac{\partial E(\mathbf{R})}{\partial \mathbf{R}_I} = 0$. The vibrational frequencies ω corresponding

to this geometry are found by determining the eigenvalues of the Hessian of the Born-Oppenheimer energy, scaled by nuclear masses:

$$\det \left| \frac{1}{\sqrt{M_I M_J}} \frac{\partial^2 E(\mathbf{R})}{\partial \mathbf{R}_I \partial \mathbf{R}_J} - \omega^2 \right| = 0. \quad (2.41)$$

The Hessian of the Born-Oppenheimer energy surface appearing in Eq. (2.41) is obtained by differentiating the Hellman-Feynman forces with respect to nuclear coordinates:

$$\frac{\partial^2 E(\mathbf{R})}{\partial \mathbf{R}_I \partial \mathbf{R}_J} = - \frac{\partial \mathbf{F}_I}{\partial \mathbf{R}_J}, \quad (2.42)$$

where the Hellman-Feynman forces are given as:

$$\mathbf{F}_I = - \int n_{\mathbf{R}}(\mathbf{r}) \frac{\partial V_{\mathbf{R}}(\mathbf{r})}{\partial \mathbf{R}_I} d\mathbf{r} - \frac{\partial E_N(\mathbf{R})}{\partial \mathbf{R}_I}, \quad (2.43)$$

where $E_N(\mathbf{R})$ is the electrostatic interaction between different nuclei. Calculation of Eq. (2.42) involves finding the ground-state electron charge density $n_{\mathbf{R}}(\mathbf{r})$ as well as its linear response to a distortion of the nuclear geometry, $\partial n_{\mathbf{R}}(\mathbf{r})/\partial \mathbf{R}_I$. This is shown in the next section.

2.3.2 Linear Response

The electron-density response $\partial n_{\mathbf{R}}(\mathbf{r})/\partial \mathbf{R}_I$ needed to determine the matrix of interatomic force constants, can be evaluated by linearizing the one-electron KS equation, charge density and the effective potential, with respect to the wave function, density and potential variations, respectively.

Linearizing the charge density leads us to:

$$\Delta n(\mathbf{r}) = 4 \operatorname{Re} \sum_{n=1}^{N/2} \psi_n^*(\mathbf{r}) \psi_n(\mathbf{r}), \quad (2.44)$$

where Δ is the finite-difference operator. The variation of Kohn-Sham orbitals,

$\Delta\psi_n(\mathbf{r})$, is obtained by first-order perturbation theory as follows:

$$(H_{SCF} - \epsilon_n)|\Delta\psi_n\rangle = -(\Delta V_{SCF} - \Delta\epsilon_n)|\psi_n\rangle, \quad (2.45)$$

where H_{SCF} is the unperturbed KS Hamiltonian and $\Delta\epsilon_n = \langle\psi_n|\Delta V_{SCF}|\psi_n\rangle$ is the first-order variation of KS eigenvalues ϵ_n . The first-order correction to the self-consistent potential is given by

$$\Delta V_{SCF}(\mathbf{r}) = \Delta V(\mathbf{r}) + e^2 \int \frac{\Delta n(\mathbf{r}')}{|\mathbf{r} - \mathbf{r}'|} d\mathbf{r}' + \left. \frac{dv_{xc}(n)}{dn} \right|_{n=n(\mathbf{r})} \Delta n(\mathbf{r}). \quad (2.46)$$

Equations (2.44) – (2.46) form a set of self-consistent equations for the perturbed system completely analogous to the KS equations in the unperturbed case, with the KS eigenvalue equation being replaced by the solution of a linear system, given by Eq. (2.45). Note that $\Delta V_{SCF}(\mathbf{r})$ is a linear functional of $\Delta n(\mathbf{r})$, which in turn depends linearly on the $\Delta\psi$'s, casting the whole self-consistent calculation in terms of a generalized linear problem.

The advantage of DFPT over other nonperturbative methods for calculating the vibrational properties (such as the frozen-phonon method, where the total energies are calculated for a series of displaced atomic positions, and numerical differences are then computed), is that the responses to perturbations of different wavelengths are decoupled. This feature allows one to calculate phonon frequencies at arbitrary wave vector \mathbf{q} , avoiding the use of supercells and with a computational load independent of phonon wavelength.

2.4 Crystal Orbital Hamilton Population

Crystal orbital Hamilton population (COHP), first proposed by Prof. Roald Hoffmann,[50] is a technique to analyze chemical bonds in molecules or solids using orbital-pair interactions. It is a bonding indicator constructed by weighting the density of states (DOS), by the corresponding elements of the Hamiltonian. A related concept

to COHP is the crystal orbital overlap population (COOP), where, as the name suggests, the DOS is weighted by the overlap population. Since in the Hamiltonian, a negative hopping term indicates bonding, a negative COHP indicates a bonding contribution, whereas a positive COHP indicates an antibonding contribution. To understand the formulation of COHP, we start with the definition of local density of states (LDOS), given by:[51]

$$\text{LDOS}_{\mu\mathbf{T},\mu\mathbf{T}'}(E) = \sum_{j,\mathbf{k}} C_{\mu\mathbf{T}',j}^*(\mathbf{k}) C_{\mu\mathbf{T},j}(\mathbf{k}) \delta(\epsilon_j(\mathbf{k}) - E), \quad (2.47)$$

where $C(\mathbf{k})$ contains the coefficients of linear combinations of atomic orbitals (AOs) μ , to represent crystal orbitals (LCAO-CO), building the wavefunction of the j^{th} band. The indices of the AOs are a short-hand notation ($\mu \equiv A, L$) to represent the orbital at atom A , positioned at a point \mathbf{R}_A in the unit cell given by the lattice vector \mathbf{T} , with the quantum numbers L ($\equiv n, l$ and m). Note, in the LCAO definition, one speaks of LDOS, whereas in the projected framework, one works with projected DOS (pDOS); the only difference is the route to obtain the coefficient matrices $C(\mathbf{k})$. The COHP is then defined as the LDOS weighted by the Hamiltonian matrix elements, given as:[51, 52]

$$\text{COHP}_{\mu\mathbf{T},\nu\mathbf{T}'} = H_{\mu\mathbf{T},\nu\mathbf{T}'} \sum_{j,\mathbf{k}} C_{\mu\mathbf{T},j}^*(\mathbf{k}) C_{\nu\mathbf{T}',j}(\mathbf{k}) \delta(\epsilon_j(\mathbf{k}) - E). \quad (2.48)$$

where $H_{\mu\mathbf{T},\nu\mathbf{T}'}$ are the elements of the Hamiltonian matrix H . In our work we have used the COHP method, as implemented in the LOBSTER package,[53] to understand the bonding and antibonding contributions corresponding to the valence band maximum, and conduction band minimum in germanene-like materials, as discussed in Chapter 7.

2.5 Calculation of Z_2 Topological Indices

Topological insulators (TIs) are materials with non-trivial band topology characterized by what are called the Z_2 invariants.[54] TIs display an insulating band gap in the bulk while having conducting edge states corresponding to the surface. For two-dimensional (2D) systems a single Z_2 index identifies a TI, whereas for three-dimensional systems (3D) there are four indices; one strong and three weak. These indices broadly divides the TIs into two classes, viz. the strong TI (STI) where the strong index is always 1, and the weak TI, where the strong index is 0, but at least one of the weak indices is 1. Note, for 2D systems, the absence of weak indices mean that all the 2D TIs are STIs.

The calculation of the Z_2 indices for inversion symmetric systems (in 2D and 3D) is quite straightforward, and it involves the computation of the parity of the bands at the time reversal invariant momenta (TRIM) points, as described below. For 2D systems, the topological invariant Z_2 is computed by evaluating the parity of the bands at the *four* time reversal invariant momenta (TRIM) points in the BZ, using the following equations:[55]

$$\delta_i = \prod_m \xi_m(\Lambda_i), \quad (2.49)$$

where the product is over the pairs of parity eigenvalues of the occupied Kramers doublets resulting from the time reversal symmetry, at the TRIM points Λ_i , given by $\xi_m(\Lambda_i)$, without multiplying the corresponding time reversed partners. The Z_2 invariant ν is then given by

$$(-1)^\nu = \prod_{i=1}^4 \delta_i. \quad (2.50)$$

The Z_2 topological index, for the inversion symmetric structures in 3D, has been calculated using the parity of the bands at the *eight* time reversal invariant momenta

(TRIM) points in the Brillouin zone (BZ), using the following equation:[55]

$$\delta_i = \prod_m \xi_m(\Lambda_i), \quad (2.51)$$

where the product is over the pairs of parity eigenvalues of the occupied Kramers doublets resulting from the time reversal symmetry, at the TRIM points Λ_i , given by $\xi_m(\Lambda_i)$, without multiplying the corresponding time reversed partners. The strong topological invariant ν_0 is then expressed as

$$(-1)^{\nu_0} = \prod_{i=1}^8 \delta_i. \quad (2.52)$$

The other three weak invariants are given by the product of the δ_i 's for which the TRIM points $\Lambda_{i=(n_1 n_2 n_3)} = \frac{1}{2}(n_1 \mathbf{b}_1 + n_2 \mathbf{b}_2 + n_3 \mathbf{b}_3)$, ($\mathbf{b}_1, \mathbf{b}_2$, and \mathbf{b}_3 being the reciprocal lattice vectors), reside in the same plane, given as

$$(-1)^{\nu_k} = \prod_{n_k=1; n_j \neq k=0,1} \delta_{i=(n_1 n_2 n_3)}. \quad (2.53)$$

There are several methods to calculate the Z_2 invariant for a system without inversion symmetry.[56–58] Among them, the Wilson loop,[57] and the Wannier charge center (WCC) method[58] are equivalent. In this thesis we have followed the WCC method prescribed by Soluyanov *et al.*, and implemented in the WannierTools package.[59] The WCC corresponding to the home unit cell is defined as:

$$\bar{x}_n = \frac{i}{2\pi} \int_{-\pi}^{\pi} dk \langle u_{nk} | \partial_k | u_{nk} \rangle. \quad (2.54)$$

where $|u_{nk}\rangle$ are the Bloch states corresponding to the band n ($n = 1 \dots N/2$) and k is a \mathbf{k} -point in the BZ. To calculate the Z_2 index, one needs to calculate the number of jumps in the gap centers (Δ_m ; $m \in [0, M]$), defined as the center of the largest gap between two adjacent WCC, along a k -path (along k_x , k_y or k_z) divided into $(M + 1)$

points. The Z_2 index is then defined as:[60]

$$\Delta = \sum_{m=0}^M \Delta_m \pmod{2}. \quad (2.55)$$

This suggests that even/odd number of jumps result in Z_2 index of 0/1, indicating trivial/topological insulator.

2.6 Calculation of Surface States

The surface states carry signature of the bulk topology, and are an important indicator for the non-trivial nature of the bands in topological insulators and semimetals. We use the surface Green's function (SGF) technique for calculating surface states for a semi-infinite system, as implemented in the WannierTools package.[59] It employs the iterative Green's function method developed by Guinea *et al.* and Sancho *et al.*,[61, 62] involving the concept of principal layers large enough so that the hopping between next nearest layers are negligible. One keeps on replacing the principal layer by two principal layers iteratively, until the interaction between the effective layers (each iteration doubles the number of layers included in the new effective layer) become as small as desired. The detailed algorithm is presented in Ref.[62]. The quantity of interest is the surface spectrum function $A(\mathbf{k}_{||}, \omega)$, obtained from the imaginary part of the SGF, and is given as:[59]

$$A(\mathbf{k}_{||}, \omega) = -\frac{1}{\pi} \lim_{\eta \rightarrow 0^+} \text{Im Tr } G_s(\mathbf{k}_{||}, \omega + i\eta). \quad (2.56)$$

where $\mathbf{k}_{||}$ are the k -points in the surface BZ, ω is the energy, and G_s is the SGF. Surface states are plotted so that the intensity of the bands is proportional to the surface spectral function.

2.7 Codes Used

The density functional theory computations used in this thesis are performed using the Quantum ESPRESSO,[17] VASP,[63] SIESTA,[21] and Gaussian09[64] packages. Calculation of surface states, and Z_2 indices for systems without inversion symmetry, have been done with the help of WannierTools package.[59] Computation of COHP for bonding analysis has been performed using the LOBSTER package.[53]

The atomistic structures of systems and charge density plots reported in this thesis are obtained using the XCrysden[65] and VESTA[66] software packages. Various two- and three-dimensional graphs are obtained using the Xmgrace and gnuplot software packages, respectively.

Bibliography

- [1] R. M. Martin, *Electronic Structure: Basic Theory and Practical Methods*. Cambridge University Press, 2004.
- [2] M. Born and R. Oppenheimer, “Zur quantentheorie der molekeln,” *Annalen der Physik*, vol. 389, no. 20, pp. 457–484, 1927.
- [3] P. Hohenberg and W. Kohn, “Inhomogeneous electron gas,” *Phys. Rev.*, vol. 136, pp. B864–B871, Nov 1964.
- [4] W. Kohn and L. J. Sham, “Self-consistent equations including exchange and correlation effects,” *Phys. Rev.*, vol. 140, pp. A1133–A1138, Nov 1965.
- [5] D. M. Ceperley and B. J. Alder, “Ground state of the electron gas by a stochastic method,” *Phys. Rev. Lett.*, vol. 45, pp. 566–569, Aug 1980.
- [6] J. P. Perdew and A. Zunger, “Self-interaction correction to density-functional approximations for many-electron systems,” *Phys. Rev. B*, vol. 23, pp. 5048–5079, May 1981.

-
- [7] A. D. Becke, “Density-functional exchange-energy approximation with correct asymptotic behavior,” *Phys. Rev. A*, vol. 38, pp. 3098–3100, Sep 1988.
- [8] J. P. Perdew and Y. Wang, “Accurate and simple analytic representation of the electron-gas correlation energy,” *Phys. Rev. B*, vol. 45, pp. 13244–13249, Jun 1992.
- [9] J. P. Perdew, K. Burke, and M. Ernzerhof, “Generalized gradient approximation made simple,” *Phys. Rev. Lett.*, vol. 77, pp. 3865–3868, Oct 1996.
- [10] W. Koch and M. C. Holthausen, *A Chemist’s Guide to Density Functional Theory*. Wiley-VCH, 2001.
- [11] J. Kohanoff, *Electronic Structure Calculations for Solids and Molecules: Theory and Computational Methods*. Cambridge University Press, 2006.
- [12] J. P. Perdew, M. Ernzerhof, and K. Burke, “Rationale for mixing exact exchange with density functional approximations,” *The Journal of Chemical Physics*, vol. 105, no. 22, pp. 9982–9985, 1996.
- [13] K. Kim and K. D. Jordan, “Comparison of density functional and MP2 calculations on the water monomer and dimer,” *The Journal of Physical Chemistry*, vol. 98, no. 40, pp. 10089–10094, 1994.
- [14] P. J. Stephens, F. J. Devlin, C. F. Chabalowski, and M. J. Frisch, “Ab initio calculation of vibrational absorption and circular dichroism spectra using density functional force fields,” *The Journal of Physical Chemistry*, vol. 98, no. 45, pp. 11623–11627, 1994.
- [15] J. Heyd, G. E. Scuseria, and M. Ernzerhof, “Hybrid functionals based on a screened Coulomb potential,” *The Journal of Chemical Physics*, vol. 118, no. 18, pp. 8207–8215, 2003.

- [16] Y. Zhao and D. G. Truhlar, “The m06 suite of density functionals for main group thermochemistry, thermochemical kinetics, noncovalent interactions, excited states, and transition elements: two new functionals and systematic testing of four M06-class functionals and 12 other functionals,” *Theoretical Chemistry Accounts*, vol. 120, pp. 215–241, May 2008.
- [17] P. Giannozzi, S. Baroni, N. Bonini, M. Calandra, R. Car, C. Cavazzoni, D. Ceresoli, G. L. Chiarotti, M. Cococcioni, I. Dabo, A. D. Corso, S. de Gironcoli, S. Fabris, G. Fratesi, R. Gebauer, U. Gerstmann, C. Gougoussis, A. Kokalj, M. Lazzeri, L. Martin-Samos, N. Marzari, F. Mauri, R. Mazzarello, S. Paolini, A. Pasquarello, L. Paulatto, C. Sbraccia, S. Scandolo, G. Sclauzero, A. P. Seitsonen, A. Smogunov, P. Umari, and R. M. Wentzcovitch, “QUANTUM ESPRESSO: a modular and open-source software project for quantum simulations of materials,” *Journal of Physics: Condensed Matter*, vol. 21, p. 395502, sep 2009.
- [18] X. Gonze, J.-M. Beuken, R. Caracas, F. Detraux, M. Fuchs, G.-M. Rignanesi, L. Sindic, M. Verstraete, G. Zerah, F. Jollet, M. Torrent, A. Roy, M. Mikami, P. Ghosez, J.-Y. Raty, and D. Allan, “First-principles computation of material properties: the ABINIT software project,” *Computational Materials Science*, vol. 25, no. 3, pp. 478 – 492, 2002.
- [19] M. J. Frisch *et al.*, “Gaussian16 Revision B.01,” 2016. Gaussian Inc. Wallingford CT.
- [20] O. K. Andersen *et al.*, *Electronic Structure and Physical Properties of Solids. The Uses of LMTO Method*. Springer, New York, 2000.
- [21] J. M. Soler, E. Artacho, J. D. Gale, A. García, J. Junquera, P. Ordejón, and D. Sánchez-Portal, “The SIESTA method for *ab initio* order-N materials simulation,” *Journal of Physics: Condensed Matter*, vol. 14, pp. 2745–2779, mar 2002.

- [22] E. R. Davidson and D. Feller, “Basis set selection for molecular calculations,” *Chemical Reviews*, vol. 86, no. 4, pp. 681–696, 1986.
- [23] F. Jensen, *Introduction to Computational Chemistry*. USA: John Wiley & Sons, Inc., 2006.
- [24] P. Manninen and J. Vaara, “Systematic Gaussian basis-set limit using completeness-optimized primitive sets. a case for magnetic properties,” *Journal of Computational Chemistry*, vol. 27, no. 4, pp. 434–445, 2006.
- [25] J. C. Phillips and L. Kleinman, “New method for calculating wave functions in crystals and molecules,” *Phys. Rev.*, vol. 116, pp. 287–294, Oct 1959.
- [26] W. E. Pickett, “Pseudopotential methods in condensed matter applications,” *Computer Physics Reports*, vol. 9, no. 3, pp. 115 – 197, 1989.
- [27] D. R. Hamann, M. Schlüter, and C. Chiang, “Norm-conserving pseudopotentials,” *Phys. Rev. Lett.*, vol. 43, pp. 1494–1497, Nov 1979.
- [28] D. Vanderbilt, “Soft self-consistent pseudopotentials in a generalized eigenvalue formalism,” *Phys. Rev. B*, vol. 41, pp. 7892–7895, Apr 1990.
- [29] H. J. Monkhorst and J. D. Pack, “Special points for Brillouin-zone integrations,” *Phys. Rev. B*, vol. 13, pp. 5188–5192, Jun 1976.
- [30] C. L. Fu and K. M. Ho, “First-principles calculation of the equilibrium ground-state properties of transition metals: Applications to Nb and Mo,” *Phys. Rev. B*, vol. 28, pp. 5480–5486, Nov 1983.
- [31] M. Methfessel and A. T. Paxton, “High-precision sampling for Brillouin-zone integration in metals,” *Phys. Rev. B*, vol. 40, pp. 3616–3621, Aug 1989.
- [32] N. Marzari, D. Vanderbilt, A. De Vita, and M. C. Payne, “Thermal contraction and disordering of the Al(110) surface,” *Phys. Rev. Lett.*, vol. 82, pp. 3296–3299, Apr 1999.

-
- [33] R. P. Feynman, “Forces in molecules,” *Phys. Rev.*, vol. 56, pp. 340–343, Aug 1939.
- [34] P. Pulay, “Ab initio calculation of force constants and equilibrium geometries in polyatomic molecules,” *Molecular Physics*, vol. 17, no. 2, pp. 197–204, 1969.
- [35] M. Scheffler, J. P. Vigneron, and G. B. Bachelet, “Total-energy gradients and lattice distortions at point defects in semiconductors,” *Phys. Rev. B*, vol. 31, pp. 6541–6551, May 1985.
- [36] O. H. Nielsen and R. M. Martin, “First-principles calculation of stress,” *Phys. Rev. Lett.*, vol. 50, pp. 697–700, Feb 1983.
- [37] D. C. Langreth, B. I. Lundqvist, S. D. Chakarova-Käck, V. R. Cooper, M. Dion, P. Hyldgaard, A. Kelkkanen, J. Kleis, L. Kong, S. Li, P. G. Moses, E. Murray, A. Puzder, H. Rydberg, E. Schröder, and T. Thonhauser, “A density functional for sparse matter,” *Journal of Physics: Condensed Matter*, vol. 21, p. 084203, jan 2009.
- [38] I. E. Dzyaloshinskii, E. M. Lifshitz, and L. P. Pitaevskii, “General theory of van der waals’ forces,” *Phys. Usp.*, vol. 4, no. 2, pp. 153–176, 1961.
- [39] S. Grimme, “Semiempirical GGA-type density functional constructed with a long-range dispersion correction,” *Journal of Computational Chemistry*, vol. 27, no. 15, pp. 1787–1799, 2006.
- [40] A. Tkatchenko and M. Scheffler, “Accurate molecular van der Waals interactions from ground-state electron density and free-atom reference data,” *Phys. Rev. Lett.*, vol. 102, p. 073005, Feb 2009.
- [41] M. Dion, H. Rydberg, E. Schröder, D. C. Langreth, and B. I. Lundqvist, “Van der Waals density functional for general geometries,” *Phys. Rev. Lett.*, vol. 92, p. 246401, Jun 2004.

-
- [42] O. A. Vydrov and T. Van Voorhis, “Nonlocal van der Waals density functional made simple,” *Phys. Rev. Lett.*, vol. 103, p. 063004, Aug 2009.
- [43] S. Grimme, “Accurate description of van der waals complexes by density functional theory including empirical corrections,” *Journal of Computational Chemistry*, vol. 25, no. 12, pp. 1463–1473, 2004.
- [44] M. Weissbluth, *Atoms and Molecules*. Elsevier Science, 2012.
- [45] A. K. Rajagopal and J. Callaway, “Inhomogeneous electron gas,” *Phys. Rev. B*, vol. 7, pp. 1912–1919, Mar 1973.
- [46] A. Dal Corso and A. Mosca Conte, “Spin-orbit coupling with ultrasoft pseudopotentials: Application to Au and Pt,” *Phys. Rev. B*, vol. 71, p. 115106, Mar 2005.
- [47] N. Zein, “Sov. phys. solid state 26, 1825 (1984),” *Sov. Phys. Solid State*, vol. 26, p. 1825, 1984.
- [48] S. Baroni, P. Giannozzi, and A. Testa, “Green’s-function approach to linear response in solids,” *Phys. Rev. Lett.*, vol. 58, pp. 1861–1864, May 1987.
- [49] S. Baroni, S. de Gironcoli, A. Dal Corso, and P. Giannozzi, “Phonons and related crystal properties from density-functional perturbation theory,” *Rev. Mod. Phys.*, vol. 73, pp. 515–562, Jul 2001.
- [50] R. Hoffmann, “How chemistry and physics meet in the solid state,” *Angewandte Chemie International Edition in English*, vol. 26, no. 9, pp. 846–878, 1987.
- [51] S. Maintz, V. L. Deringer, A. L. Tchougreff, and R. Dronskowski, “Analytic projection from plane-wave and PAW wavefunctions and application to chemical-bonding analysis in solids,” *Journal of Computational Chemistry*, vol. 34, no. 29, pp. 2557–2567, 2013.

- [52] R. Dronskowski and P. E. Bloechl, “Crystal orbital Hamilton populations (COHP): energy-resolved visualization of chemical bonding in solids based on density-functional calculations,” *The Journal of Physical Chemistry*, vol. 97, no. 33, pp. 8617–8624, 1993.
- [53] S. Maintz, V. L. Deringer, A. L. Tchougreff, and R. Dronskowski, “LOBSTER: A tool to extract chemical bonding from plane-wave based DFT,” *Journal of Computational Chemistry*, vol. 37, no. 11, pp. 1030–1035, 2016.
- [54] C. L. Kane and E. J. Mele, “ Z_2 topological order and the quantum spin Hall effect,” *Phys. Rev. Lett.*, vol. 95, p. 146802, Sep 2005.
- [55] L. Fu and C. L. Kane, “Topological insulators with inversion symmetry,” *Phys. Rev. B*, vol. 76, p. 045302, 2007.
- [56] T. Fukui and Y. Hatsugai, “Quantum spin Hall effect in three dimensional materials: Lattice computation of Z_2 topological invariants and its application to Bi and Sb,” *Journal of the Physical Society of Japan*, vol. 76, no. 5, p. 053702, 2007.
- [57] R. Yu, X. L. Qi, A. Bernevig, Z. Fang, and X. Dai, “Equivalent expression of Z_2 topological invariant for band insulators using the non-Abelian Berry connection,” *Phys. Rev. B*, vol. 84, p. 075119, Aug 2011.
- [58] A. A. Soluyanov and D. Vanderbilt, “Computing topological invariants without inversion symmetry,” *Phys. Rev. B*, vol. 83, p. 235401, Jun 2011.
- [59] Q. Wu, S. Zhang, H.-F. Song, M. Troyer, and A. A. Soluyanov, “Wanniertools : An open-source software package for novel topological materials,” *Computer Physics Communications*, vol. 224, pp. 405 – 416, 2018.
- [60] A. A. Soluyanov and D. Vanderbilt, “Computing topological invariants without inversion symmetry,” *Phys. Rev. B*, vol. 83, p. 235401, Jun 2011.

-
- [61] F. Guinea, C. Tejedor, F. Flores, and E. Louis, “Effective two-dimensional Hamiltonian at surfaces,” *Phys. Rev. B*, vol. 28, pp. 4397–4402, Oct 1983.
- [62] M. P. L. Sancho, J. M. L. Sancho, J. M. L. Sancho, and J. Rubio, “Highly convergent schemes for the calculation of bulk and surface Green functions,” *Journal of Physics F: Metal Physics*, vol. 15, pp. 851–858, apr 1985.
- [63] J. Hafner, “Ab-initio simulations of materials using VASP: Density-functional theory and beyond,” *Journal of Computational Chemistry*, vol. 29, no. 13, pp. 2044–2078, 2008.
- [64] M. J. Frisch *et al.*, “Gaussian09,” 2009. Gaussian Inc. Wallingford CT.
- [65] A. Kokalj, “XCrySDen: a new program for displaying crystalline structures and electron densities,” *Journal of Molecular Graphics and Modelling*, vol. 17, no. 3, pp. 176 – 179, 1999.
- [66] K. Momma and F. Izumi, “*VESTA3* for three-dimensional visualization of crystal, volumetric and morphology data,” *Journal of Applied Crystallography*, vol. 44, pp. 1272–1276, Dec 2011.

Chapter 3

Size-selective Ionization and Etching of Pt Nanoparticles

In this chapter, we study the size-selective ionization and etching of Pt nanoparticles. In contrast to their generally acknowledged behavior of sintering, experiments carried out by our collaborators in the group of Prof. Sreebrata Goswami, show that Pt nanoparticles, in the presence of specific ligands, show size-dependent etching. Using density functional theory calculations, we study the energetics of Pt nanoparticles in the gas phase, and in the ligand environment, to confirm this finding, and also to understand why the usual behavior of sintering is reversed to etching in the presence of the ligands. We also find the condition dictating the maximum size of the Pt nanoparticles, up to which etching is favored in the presence of the ligands.

3.1 Introduction

Nanoparticles, due to their high surface to volume ratio, and effects of quantum confinement, show properties that are significantly different from their bulk counterparts.[1] Early experiments by Haruta *et al.* showed gold nanoparticles of size < 10 nm deposited on transition metal oxides, can be used for low temperature oxidation of hydrogen and carbon monoxide.[2] Subsequently, Gardner *et al.* compared the catalytic activity of Pt and Au nanoparticles in terms of low temperature CO

oxidation.[3] Around the same time, Yang *et al.* used Cu, Co, and Mn as catalysts for CO oxidation.[4] These experiments opened up the area of metal nanoparticle assisted catalytic reactions. Since then, in the last couple of decades, metal nanoparticles have found their applications not only in catalysis,[5–7] but also in electrocatalysis,[8] fuel cells,[9, 10] water purification,[11] etc. The catalytic activity of a nanoparticle can be tuned by varying its size and shape, to control important reactions in heterogeneous catalysis, such as hydrogen evolution reaction (HER),[12, 13] oxygen reduction reactions (OER),[14, 15] etc.

Although Pt is a noble metal, its nanoparticle form has long been used in heterogeneous catalysis.[12–15] The interest of the research community in Pt nanoparticles (Pt NPs) is growing fast due to their wide range of applications involving ‘green technology’, including in catalytic converters,[16] for decomposition of polluting aromatic compounds,[17] photochemical solar energy harvesting,[18] and water treatment.[19] Several other applications of Pt NPs include gas sensors,[20, 21] bio imaging,[22, 23] detection of important biological molecules,[24, 25] and even nanomedicine.[26] Such widespread applications have resulted in an ever-increasing demand for Pt, whereas its abundance in Earth’s crust is quite limited (0.01 ppm). This demands in optimization and controllability in the structure and size of Pt at the nanoscale to increase its effectiveness in various applications.

One can tune the size and shape of Pt NPs to gain controllability over their reactivity.[27, 28] A major obstacle in controlling the size of the nanoparticles is the tendency of the nanoparticles to agglomerate, or sinter, to form bigger nanoparticles. To prevent sintering, surfactants, and polymers are used in suspension with the nanoparticles,[29, 30] which sometimes reduce the number of surface binding sites, affecting the catalytic activity of the nanoparticle. One could also possibly tune the size of the nanoparticles by etching, where atoms get detached from bigger NPs, to form smaller NPs, and which also happens to be a crucial requirement for chemical reactions. Very recently, it has been shown that gold nanoparticles can be etched to

control their shape, with proper choice of ligands.[31] However, it is found that Pt nanoparticles (Pt NPs), in general, do not want to ionize or dissociate in most of the chemical reactions, with the exception of in the presence of aqua regia, and fluorine gas.

In this work we show that the tendency of the Pt NPs to sinter, can be reversed to a tendency of etching. We find that the Pt NPs participate in stoichiometric chemical reactions, in the presence of specific ligands (L) through the formation of a monometallic di-radical complex, $\text{Pt}(\text{L})_2$. The reaction is found to be size-selective, in that it results in complete dissolution of Pt NPs up to a maximum nanoparticle size. This maximum size of the nanoparticle is found to be dependent on the type of the ligand used, and can be tuned by changing the ligand by modifying its different derivatives. We believe that these results present a drastic deviation from our present understanding of the chemical reactivity of platinum, and increase the possibility of the use of zero valent noble metal NPs in stoichiometric chemical reactions.

3.2 Experimental background

In this section we have described the experiments done on the size-selective etching of Pt NPs in the presence of a π -acidic azo-aromatic ligand L, by our collaborators in the group of Prof. Sreebrata Goswami at IACS, Kolkata. The experimental design is schematically depicted in Figs. 3.1 (a), (b), the details of which can be found in the PhD thesis of Dr. Debabrata Sengupta.[32] Different batches of Pt NPs with sizes ranging from 2 to 30 nm are synthesized and mixed with a solution of 2-(phenylazo)pyridine, L^1 , in chloroform solvent. After reaction, the solution is drop cast on a carbon-coated copper grid. Transmission electron microscopy (TEM) images of the drop-cast film are taken to determine the size of the NPs contained in the film (and hence in the solution), which show the size-dependent reactivity of the NPs. The size d of a NP is defined here as the diameter of the minimal bounding circle enclosing its TEM image. It is observed that in the presence of L^1 , the color of the solution

changes from red to green [see the insets to Figs. 3.1(a) and 1(b)], and only Pt NPs of size $d \leq 6$ nm get ionized and are etched away. In contrast, NPs with size > 6 nm remain unreacted.

The experimental results are presented in three groups, divided according to the sizes of the NPs before the reaction: (1) **Group 1**, for approximately monodisperse NPs with size < 6 nm [shown in Figs. 3.1(c)-(e)], (2) **Group 2**, for approximately monodisperse NPs with size > 6 nm [see Figs. 3.1(f)-(h)], and (3) **Group 3**, for NPs with a distribution of sizes ranging from 2 nm to 20 nm [Figs. 3.1(i)-(k)].

Fig. 3.1(c) shows a TEM image taken before the reaction for **Group 1**. NPs with size ≤ 6 nm are visible in the image before the reaction, all of which disappear after the reaction [Figs. 3.1(c)-(d)]. The pre-reaction histogram in Fig. 3.1(e), for the sample of **Group 1**, shows the NP size distribution before the reaction ($d = 3.92 \pm 1.89$ nm). No corresponding post-reaction histogram is available in this case, since all the NPs get dissolved during the course of the reaction. In contrast, for **Group 2**, which is comprised of NPs with $d > 6$ nm, no reaction occurs after mixing with L^1 , indicated by the color of the solution that remains unchanged. Clear traces of unreacted NPs are also observed in the post-reaction TEM image [see Figs. 3.1(f)-(g)]. Importantly, the size distribution of NPs before and after the reaction remains virtually unchanged, as indicated in the histograms in Fig. 3.1(h), with $d = 11.65 \pm 3.60$ nm before reaction, and 12.19 ± 3.94 nm after reaction. It is also worth noting that in the post-reaction TEM images, it is found that unreacted NPs tend to agglomerate. This is supported by our theoretical understanding (presented further below).

The size-selectivity of this reaction is further investigated using a mixture of NP sizes (**Group 3**). Instead of using a monodisperse collection of NPs, a collection of NPs with a broad distribution in size, ranging from 2 nm to 20 nm, is taken for reaction with L^1 . It is found that only those NPs with size $d \leq 6$ nm, get dissolved selectively, while the rest remain unreacted. Figs. 3.1(i) and 3.1(j) show representative TEM images before and after the reaction occurs. As shown in Fig. 3.1(k), the distribution

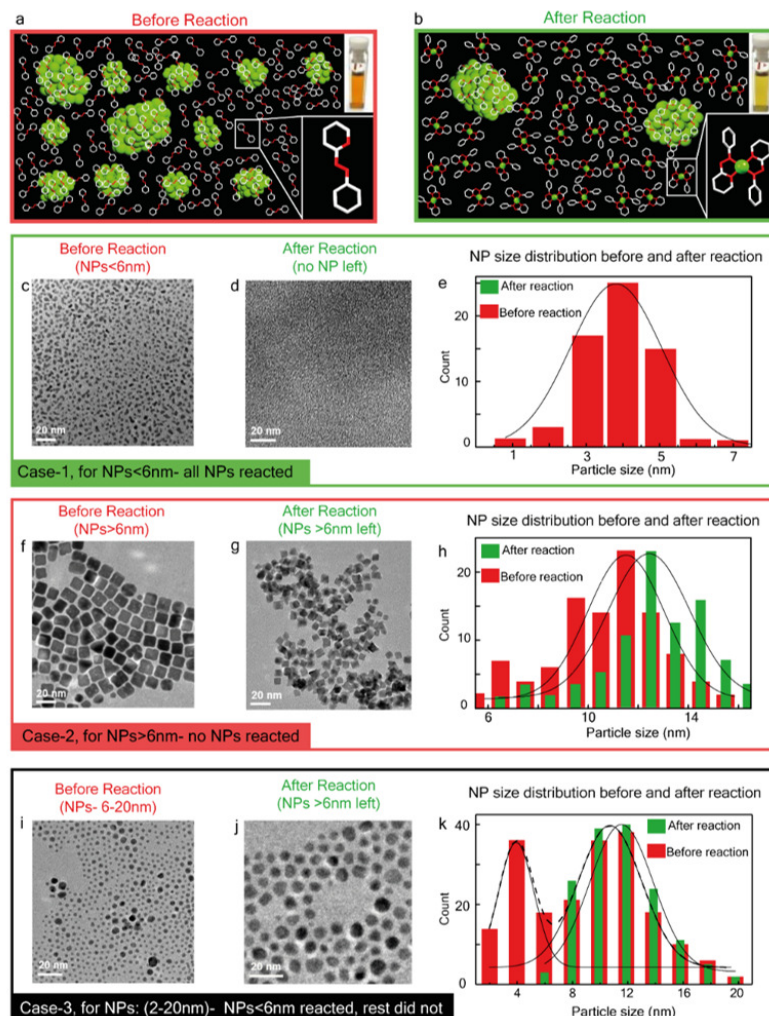


Figure 3.1: Panels (a), (b) show schematic presentation of chemical reactivity of Pt NPs with L^1 : smaller size NPs ($d \leq 6$ nm) react but larger NPs do not. (c), (d) show TEM images before and after reaction between NPs with $d \leq 6$ nm and L^1 and, (e) the corresponding NP size distribution in pre- and post-reaction samples. (f)-(h) Same as (c)-(e) for NPs with $d > 6$ nm. (i) TEM images before the reaction of a NP sample with a wide range (2-20 nm) of NP sizes. (j) Post reaction TEM image of the sample shown in (i), where only the smaller NPs (≤ 6 nm) react. (k) Histogram corresponding to (i), (j). Note, from Fig. 1(e), it can be argued that even a NP of 7 nm reacted and that could be the threshold. However, the number of such particles is too small. In several batches experiments do not show particles of 7 nm at all. Hence, the fact that post reaction image does not contain 7 nm NPs as unreacted, could be due to sampling uncertainty. Even NPs of size ~ 6.5 nm have been found to remain unreacted. Hence, the threshold size has been indicated as 6 nm. Experimental data courtesy of Prof. Srebrata Goswami and Debabrata Sengupta.

of NP sizes before the reaction can be approximated as a superposition of two Gaussians centered at ~ 4.00 nm and 10.98 nm (see the red bars in the figure). After

the reaction, only a Gaussian centered at ~ 11 nm remains, while the other disappears (see the green bars in the figure), indicating that even in a mixture, only the NPs smaller than the threshold size of 6 nm undergo selective dissolution.

It is found that the reaction proceeds by sequential detachment of Pt atoms through the formation of $\text{Pt}(\text{L}^1)_2$ complex. The presence of the $\text{Pt}(\text{L}^1)_2$ complex has been verified by various spectroscopic techniques, viz., *in situ* nuclear magnetic resonance (NMR), ultraviolet-visible (UV-Vis) and ^1H NMR. The structure of the $\text{Pt}(\text{L}^1)_2$ complex is determined using X-ray diffraction (XRD), and the oxidation state of the Pt atom in the complex, using X-ray photoelectron spectroscopy (XPS). The electronic state of the L^1 ligand was further verified using Raman spectroscopy, which matches well with the DFT simulated Raman spectra as discussed further below.

Motivated by the experiments described above, which show the counter-intuitive behaviour of size-selective etching of Pt NPs in presence of L^1 ligands, we perform DFT computations on Pt NPs, to study their energetics in the gas phase and in the presence of L^1 and six other related ligands. The results are discussed further below.

3.3 Systems under study

To understand the size-selectivity of etching of Pt NPs by azo-aromatic ligands, we consider NPs Pt_n of selected sizes up to $n = 2057$ atoms (~ 4.4 nm) as shown in Fig. 3.2. The initial guesses for the structures of the nanoparticles of sizes up to $n = 70$, are taken from the Cambridge cluster database; [33] the structures are then optimized using DFT and Hellmann-Feynman forces. NPs with $n = 309, 923$ and 2057, are assumed to have cuboctahedral structure which is a common practice in the literature,[34] and optimized with DFT calculations. We note that for computational reasons, it was not feasible to perform DFT on larger sized clusters, our size-dependent trends were therefore extrapolated to larger sizes.

A total of seven azo-aromatic ligands are studied which can be divided into two groups: (i) a family of 2-(arylazo) pyridines (L); viz. 2-(phenylazo) pyridine

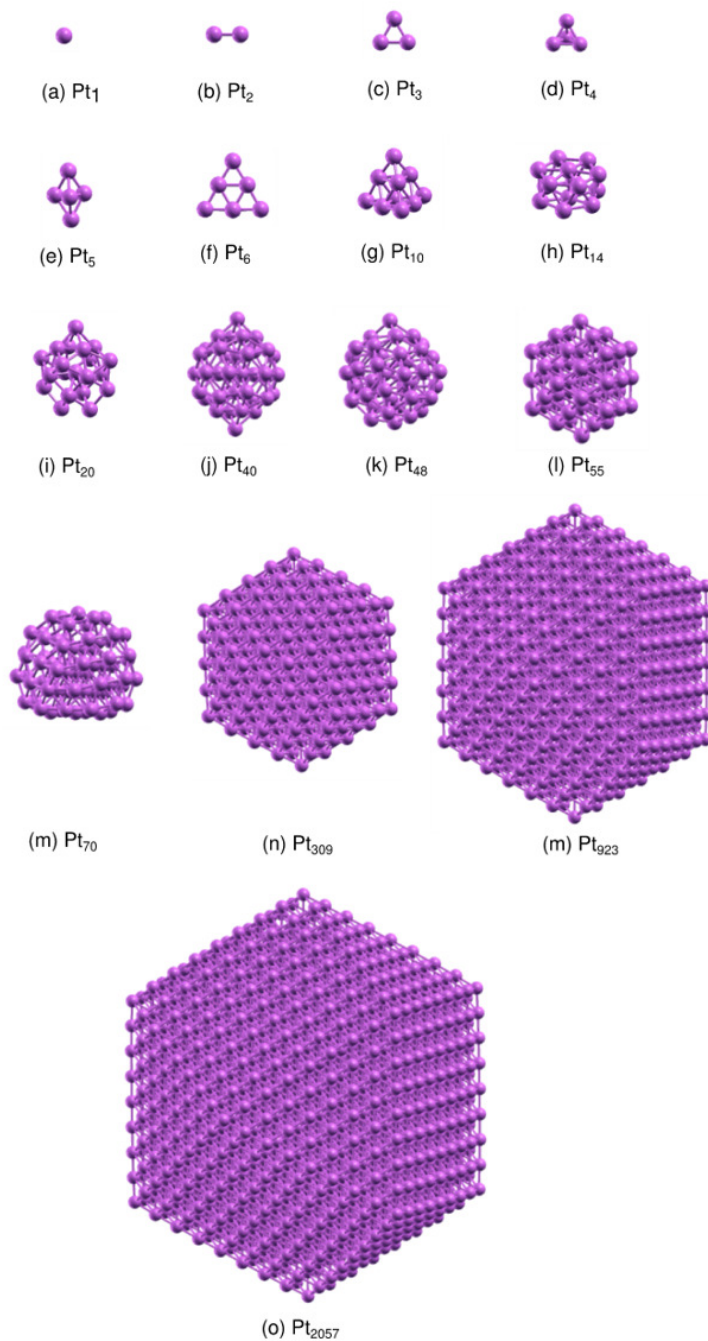


Figure 3.2: The optimized geometries of the Pt nanoparticles (Pt_n , $n = 1 - 2057$) are shown. The largest nanoparticle considered for DFT calculations has 2057 atoms, which corresponds to a diameter $d = 4.4$ nm.

(L¹), 4-chloro-2-(phenylazo) pyridine (L²), 2,6-dimethyl-2-(phenylazo) pyridine (L³), 4-methyl-2-(phenylazo) pyridine (L⁴) and (ii) common di imine ligands; viz. 9,10-phenanthroline (Λ^1), 2-(phenylimino) pyridine (Λ^2) and 2,2-bipyridine (Λ^3). The chemical structures of these ligands are presented in Fig. 3.3.

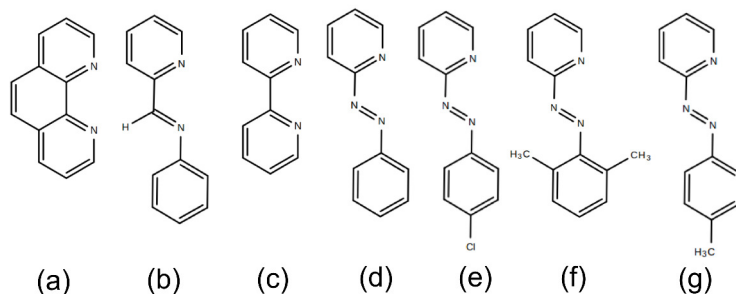


Figure 3.3: The chemical structure of the diimine ligands: (a) 9,10-phenanthroline (Λ^1), (b) 2-(phenylimino) pyridine (Λ^2), and (c) 2,2'-bipyridine (Λ^3), and a family of 2-(arylaazo) pyridines (L); viz. (d) 2-(phenylazo) pyridine (L^1), (e) 4-chloro-2-(phenylazo) pyridine (L^2), (f) 2,6-dimethyl-2-(phenylazo) pyridine (L^3), and (g) 4-methyl-2-(phenylazo) pyridine (L^4).

The energetics of the Pt_n NPs are studied in the gas phase and in presence of the seven ligands mentioned above.

3.4 Computational details

Our calculations have been performed within the framework of *ab initio* spin polarized density functional theory, using the Quantum ESPRESSO (QE),^[35] SIESTA,^[36] and Gaussian^[37] packages. A combination of packages is used because different codes have different capabilities regarding which properties can be easily calculated. In all cases exchange-correlation interactions are treated using the PBE form for the generalized gradient approximation.^[38] Van der Waals interactions are incorporated using the DFT-D2 method.^[39, 40] In QE, the Kohn-Sham equations are expanded using a plane wave basis set, with cut-offs of 40 Ry for wavefunctions and 400 Ry for charge densities. Interactions between the ionic cores and valence electrons are described using ultrasoft pseudopotentials.^[41] The Gau-PBE hybrid functional has been used for accurate estimation of the gap in energy between the highest occupied molecular orbital (HOMO) and the lowest unoccupied molecular orbital (LUMO) of the ligands.^[42] In SIESTA, we use a double- ζ polarized localized basis with a mesh cutoff size of real-space grid taken to be 200 Ry. The Raman spectra of the ligand L^1 and the $Pt(L^1)_2$ complex have been computed using the Gaussian package, using

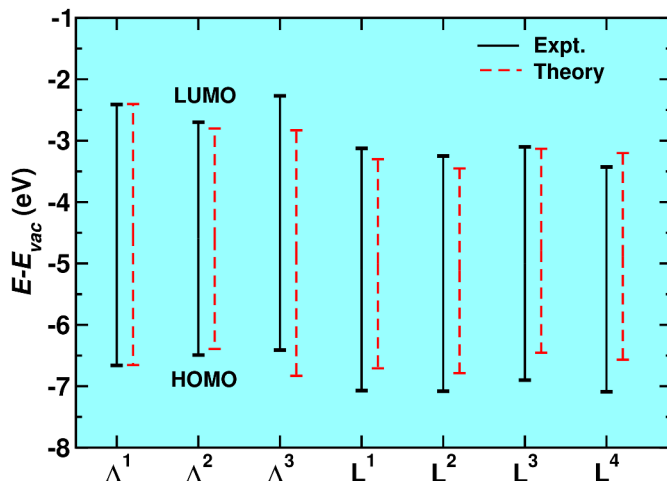


Figure 3.4: Comparison of the DFT (Gau-PBE hybrid functional) calculated (red dashed) HOMO-LUMO gaps of the ligands in the gas phase, with the experimental HOMO-LUMO gaps (black solid) measured using UV-Vis and cyclic voltammetry. Experimental data courtesy of Prof. Sreebrata Goswami, and Debabrata Sengupta.

6-311G(*d,p*) basis for lighter atoms (C, H and N) and SDD basis for Pt atoms. In all cases, a vacuum spacing of at least 10 Å is introduced along all non-repeating directions and the reciprocal space sampling is done at the zone center only.

3.5 Results and Discussion

3.5.1 Ligands in the gas phase

Before looking at the properties of the di-radical complex, it is instructive to compare the electronic properties of the ligands in the gas phase, with the experiments. We thus verify the position of the HOMO and the LUMO of the ligands in the gas phase, as computed from DFT using the Gau-PBE hybrid functional, with the experimental values obtained from cyclic voltammetry and UV-Vis spectral analysis (see Fig. 3.4). Note that all the energies are calculated with respect to the vacuum energy. We find that the HOMO-LUMO gap of the ligands in the gas phase is reproduced well in the DFT calculations, which provides verification of the method used.

Table 3.1: Bond parameters: experimental and DFT optimized bond distances (\AA) and bond angles ($^\circ$) of complex $\text{Pt}(\text{L}^1)_2$ complex. For the labeling of the atoms, see Fig. 3.5.

Bond Parameters	$\text{Pt}(\text{L}^1)_2$ complex	
	Experimental	Theoretical (DFT)
Pt-N ₁	2.006(3)	2.0676
Pt-N ₃	1.965(3)	2.0650
Pt-N _{1a}	2.006(3)	2.0677
Pt-N _{3a}	1.965(3)	2.0650
N ₂ -N ₃	1.335(5)	1.3284
\angle N ₁ -Pt-N ₃	76.59(12) $^\circ$	76.4642 $^\circ$
\angle N _{1a} -Pt-N ₃	103.41(12) $^\circ$	104.6774 $^\circ$

3.5.2 Formation of the $\text{Pt}(\text{L})_2$ complex

The etching of Pt nanoparticles proceeds through sequential detachment of the Pt atoms in the form of a $\text{Pt}(\text{L})_2$ complex. It is experimentally verified that in the presence of the chosen ligand, L^1 , $\text{Pt}(\text{L}^1)_2$ is formed. The XRD data suggests that the geometry of the $\text{Pt}(\text{L}^1)_2$ complex is square planar. In Fig. 3.5(a), we show the DFT optimized geometry of the complex, with appropriate symbols used to define the bond parameters. A comparison of the bond lengths and angles obtained from experiment and theory is presented in Table 3.1. We see that the DFT computed bond lengths and angles match very well with the experimental values. In Fig. 3.5(b), we plot the spin density of the $\text{Pt}(\text{L}^1)_2$ complex, where up (red) and down (green) spin densities can be seen to be located on the two ligands, leading to an antiferromagnetic coupling. This observation also agrees well with the fact that the Pt atom loses one electron to each of the ligands resulting in a +2 oxidation state, as confirmed by the XPS data.

Raman spectroscopy is used for further verification of the electronic state of the L^1 ligands. By performing natural bond orbital (NBO) analysis, we find that in the electron acceptor orbitals of the LUMO and the LUMO+1, 73% and 58%, respectively, of the charge density is localized around the azo-group. Hence, we monitor the azo-stretching modes in the ligand L^1 present before the reaction and in the $\text{Pt}(\text{L}^1)_2$ complex formed after the reaction, to assess the ligand redox state.

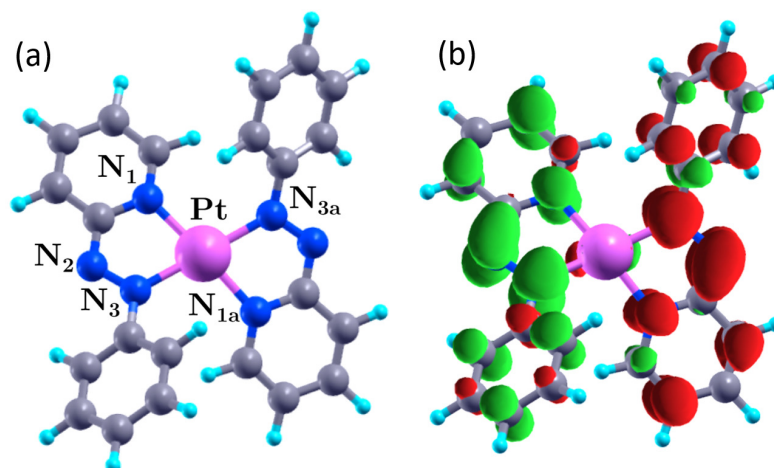


Figure 3.5: The optimized geometry of the $\text{Pt}(\text{L}^1)_2$ complex, with labels used to denote bond parameters, is shown in (a). (b) shows the spin density with red and green lobes indicating up and down spins, respectively. (isosurface value: $0.003 \text{ e}/\text{Bohr}^3$)

In Fig. 3.6, we show the differential Raman spectra (in solid blue), obtained from the difference of the spectra before and after the reaction. The upper and lower panels represent the experimental and DFT computed Raman spectra, respectively. The differential vibrational frequencies corresponding to the azo-stretching modes obtained by simulating the Raman spectra of L^1 (indicated by the red arrows in the figure) using DFT calculations are assigned at 1555 , 1478 and 1459 cm^{-1} ; and of $\text{Pt}(\text{L}^1)_2$ (indicated by green arrows in the figure) at 1410 , 1323 and 1274 cm^{-1} . These results show a good match to the vibrational peaks of the azo-modes from experimentally obtained differential Raman spectra (before reaction: 1493 , 1450 and 1423 cm^{-1} ; after reaction: 1367 , 1295 and 1255 cm^{-1}), providing convincing evidence of the formation of the diradical complex.

To summarize, in this section we compared our DFT computed results with the experimental data, which confirms that in the process of etching of Pt NPs, Pt atoms are 2-electron ionized and etched from the NP by the L^1 ligand, resulting in the formation of the diradical $\text{Pt}(\text{L}^1)_2$ complex. Next, we investigate the size-selectivity of the etching process and show that the threshold size of etching can be tuned by

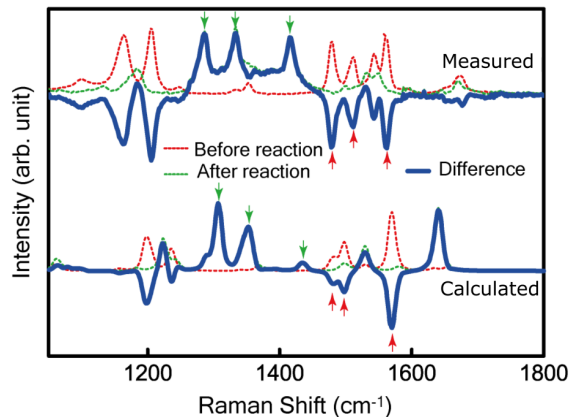


Figure 3.6: Comparison of experimental (upper panel) and DFT computed (lower panel) Raman spectra. The blue curve shows the difference of Raman spectra before (red) and after (green) reaction. The red and green arrows indicate the frequencies corresponding to the azo-stretching modes, before and after the reaction, respectively. In both the experiment and the DFT results, we see a blue shift in the frequencies corresponding to the azo-stretching modes. Experimental data courtesy of Prof. Sreebrata Goswami and Debabrata Sengupta.

suitable choice of ligands.

3.5.3 Thermodynamics of sintering vs. etching

Both ionization and etching of Pt nanoparticles are counter-intuitive, and completely opposite to the usually observed phenomena of inertness and sintering. In order to understand and confirm this experimental finding, we perform DFT calculations. We consider the thermodynamics, as a function of nanoparticle size n , of a sequential process where one Pt atom is either added to a Pt_n cluster to form a Pt_{n+1} cluster (sintering) or detached from it to form a Pt_{n-1} cluster (etching). The energetics of these two processes are compared in the gas phase and in the ligand-environment, where L^1 ligands are available to bind to Pt atoms. We note that because of the high computational cost, we perform DFT calculations only for selected sizes up to $n = 2057$, where n is the number of Pt atoms in the nanoparticle, beyond this, results are obtained by extrapolation.

In Figs. 3.7 [(a)-(c)], we study the energetics, as computed from DFT, when out of N Pt atoms in the gas phase, n atoms form a Pt_n nanoparticle, while the

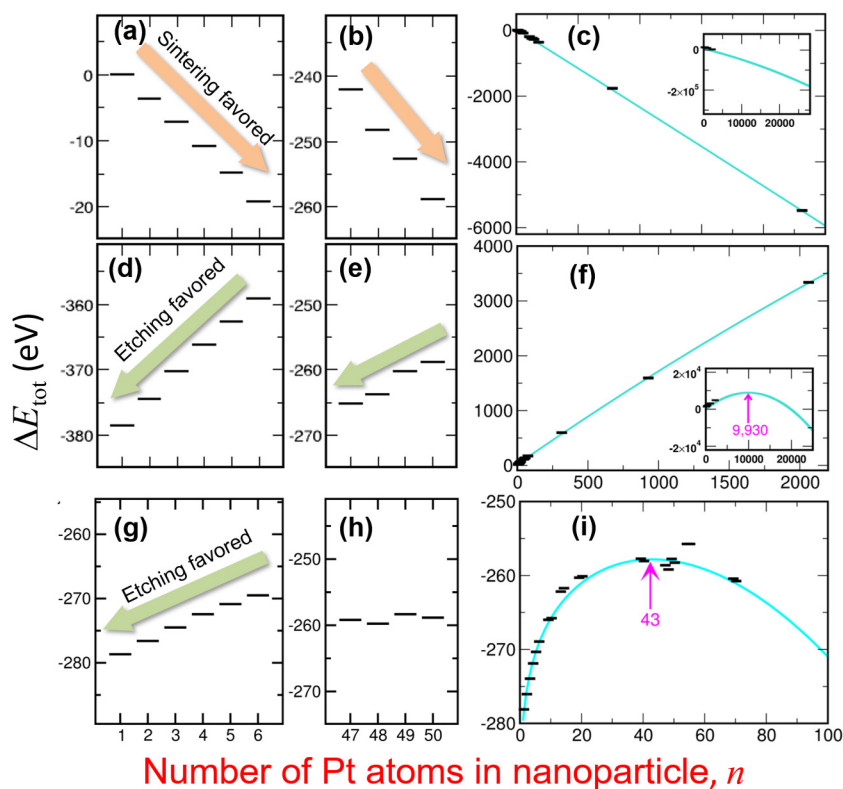


Figure 3.7: Theoretical explanation for reversal of behavior in the presence of ligands L: We consider the thermodynamics of sintering vs. etching in the gas phase (a)-(c) and in the presence of the ligands L^1 (d)-(f) and Λ^1 (g)-(h). The horizontal lines represent the total energies ΔE_{tot} , as computed from DFT, of the system of either (a)-(c) Pt_n nanoparticle + $(N - n)$ free Pt atoms, or (d)-(i) Pt_n nanoparticle + $(N - n - 1)$ $\text{Pt}(L)_2$ moieties + $2(n - 1)$ free ligands L, as a function of n . Here L is the ligand L^1 or Λ^1 . A negative/positive slope for ΔE_{tot} vs. n implies that sintering/etching is favoured. The inset in (c) shows that the slope of the fitted curve remains negative for all n , indicating sintering is always favourable for Pt nanoparticles in the gas phase. In contrast, the inset to (f) and the graph (i) show that the slope changes sign beyond a certain value n_{max} in the presence of the ligands L^1 and Λ^1 . The corresponding maximum cluster sizes beyond which etching no longer occurs are found to be $n_{\text{max}} = 9,930$ (6.6 nm) and $n_{\text{max}} = 43$ (1.07 nm), respectively.

remaining $N - n$ atoms remain as free atoms. The small horizontal line at each n indicates the total energy of the system as a function of n , we see that the slope of the graph is always negative, indicating that sintering is always favored in the gas phase, irrespective of nanoparticle size n . Similarly, in Figs. 3.7 [(d)-(f)] we plot the total energy in the ligand environment for $\text{Pt}_n + (N - n)$ number of $\text{Pt}(\text{L}^1)_2$ moieties + $2(n - 1)$ free ligands L^1 . This represents a sequential process where a Pt nanoparticle containing n Pt atoms can change in size to one containing one less Pt atom by detachment of one Pt atom to two L^1 ligands forming the $\text{Pt}(\text{L}^1)_2$ moiety. We see that in the presence of the ligand L^1 , the shape of the graph is quite different from that in the gas phase: it is clear that the slope of the graph starts out at $n = 1$ as strongly positive and reduces as n increases; the calculated slope remains positive till $n = 9,930$ ($d \sim 6.6$ nm) beyond which the slope becomes negative. From the extrapolated results, beyond $n = 2057$, one can clearly see that there is a critical nanoparticle size of ~ 6.6 nm ($n = 9,930$) below which etching is favored, whereas for nanoparticles bigger than this, sintering is energetically favored. This is in remarkably good agreement with the experiments, where it was found that the reactions occurred only for nanoparticles when d is ≤ 6 nm. This also supports the experimental observation that larger nanoparticles tend to agglomerate (sinter) when mixed with L^1 , as can be seen from the TEM image in Fig. 3.1(g), (j).

To extrapolate our results for larger nanoparticle sizes, we use the following quadratic equation to fit the DFT results:

$$\Delta E_{tot} = a_0 n^2 + a_1 n + a_2, \quad (3.1)$$

where ΔE_{tot} is the total energy, and n is the nanoparticle size. Eq. (3.1) is used to fit the plot of the energies of both $\text{Pt}_n + (N - n)\text{Pt}$ system, vs. n , in the gas phase, and the energies of $\text{Pt}_n + (N - n) \text{Pt}(\text{L})_2$ moieties + $2(n - 1)$ free ligands L , vs. n , in the ligand environment.

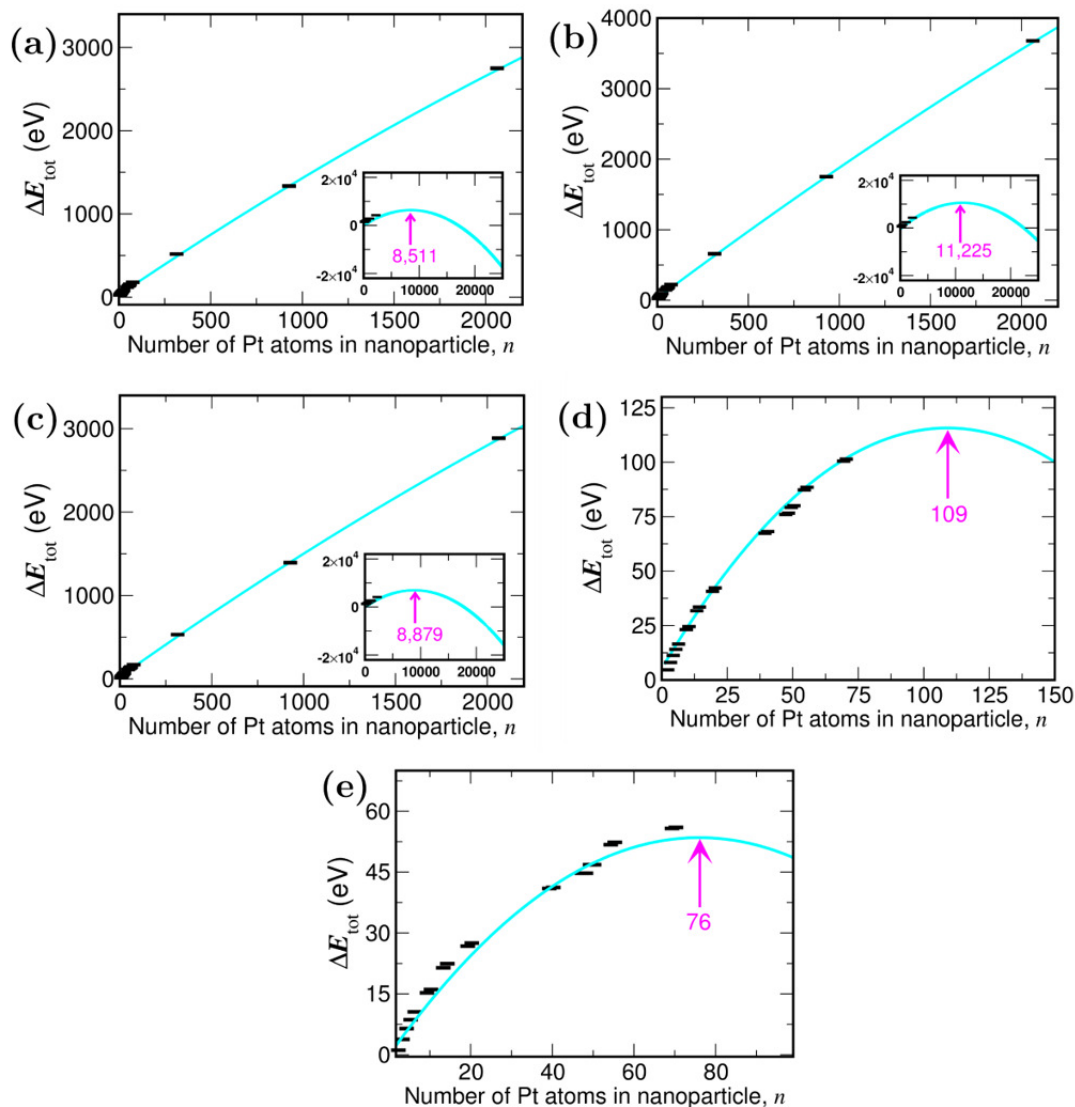


Figure 3.8: Thermodynamics of etching in presence of ligands (a) L^2 , (b) L^3 , (c) L^4 , (d) Λ^2 , and (e) Λ^3 . The horizontal lines represent the total energies ΔE_{tot} , as computed from DFT, of the system of Pt_n nanoparticle + $(N - n - 1)$ $\text{Pt}(\text{L})_2$ moieties + $2(n - 1)$ free ligands L ($\text{L} = L^2, L^3, L^4, \Lambda^2$, and Λ^3), as a function of nanoparticle size n . The positive/negative slope of the ΔE_{tot} vs. n plots suggests etching/sintering is favored. The maximum allowed nanoparticle size (n_{max}) for etching, is indicated by labels and arrows in magenta.

In the following, we derive the condition determining the maximum size n_{max} where the etching stops in presence of the ligand L. We show that the condition is quite general and is applicable not only to L^1 , but also to other related ligands (L^1 , L^2 , L^3 , L^4). As discussed above, the positive/negative slope of the graph of ΔE_{tot} vs. n (see Fig. 3.7) indicates that etching/sintering is favored. In the absence of the ligands, the slope of the graph is given by:

$$E(Pt_n) - E(Pt_{n-1}) - E(Pt) = -E_{sub}(n), \quad (3.2)$$

where $E(X)$ is the total energy of the system X , Pt_n is a gas phase cluster containing n Pt atoms, and $E_{sub}(n)$ is the sublimation energy defined as:

$$E_{sub}(n) = -[E(Pt_n) - E(Pt_{n-1}) - E(Pt)]; \quad E_{sub}(n) > 0, \forall n. \quad (3.3)$$

We note that the right hand side of Eq. (3.2) is always negative. This implies that in the gas phase sintering is always favored. In the presence of the ligand L, the slope of ΔE_{tot} vs. n can be written as:

$$\begin{aligned} & E(Pt_n) - E(Pt_{n-1}) - E(Pt(L)_2) + 2L \\ & = E_{sub}(n) + E_b(Pt(L)_2) < 0, \forall n < n_{max} \end{aligned} \quad (3.4)$$

where, $E_b(Pt(L)_2)$ is the binding energy of the Pt atom to the two ligands in the $Pt(L)_2$ complex, given by:

$$E_b(Pt(L)_2) = -[E(Pt(L)_2) - E(Pt) - 2E(L)]. \quad (3.5)$$

In Eq. (3.4), n_{max} is the size of cluster at which the slope of ΔE_{tot} vs. n becomes 0. In other words, the etching stops when $E_{sub}(n_{max}) = E_b(Pt(L)_2)$. This is the condition for the maximum cluster size n_{max} , up to which etching takes place in the presence of

Table 3.2: Comparison of the maximum nanoparticle size n_{max} in Pt_n , where etching stops, nanoparticle diameter d (nm) corresponding to n_{max} and the binding energies of the Pt atom to the corresponding ligands, in the $Pt(L)_2$ complex.

Ligands	n_{max}	d (nm)	E_b (eV)
L^1	9,930	6.58	7.72
L^2	8,511	6.25	7.66
L^3	11,285	6.87	8.29
L^4	8,879	6.34	7.68
Λ^1	43	1.07	5.68
Λ^2	109	1.46	6.88
Λ^3	76	1.29	6.27

the ligand L. We note that $E_{sub}(n)$ is, in general, an increasing function of n . Thus, if we are to change the ligand L^1 to other ligands L with a smaller/larger the binding energy to the Pt atom, the critical size at which the etching stops would also become smaller/larger.

To verify this hypothesis further, we consider two classes of closely related ligands: (i) a family of 2-(arylazo) pyridines (L); viz., 4-chloro-2-(phenylazo) pyridine (L^2), 2,6-dimethyl-2-(phenylazo) pyridine (L^3), 4-methyl-2-(phenylazo) pyridine (L^4) and (ii) common di imine ligands; viz., 9,10-phenanthroline (Λ^1), 2-(phenylimino) pyridine (Λ^2) and 2,2-bipyridine (Λ^3).

In Fig. 3.8, we show the energetics of the $Pt_n + (N - n) Pt(L)_2$ moieties + $2(n - 1)$ free ligands L, vs. n , where $L = L^2, L^3, L^4, \Lambda^1, \Lambda^2$, and Λ^3 . The fit and extrapolation have been done using Eq. 3.1, and the extrapolated results are shown in the insets of Fig. 3.8 (a)-(c). In all the cases we see that the slope is positive at first and then decreases to a point where the slope becomes zero, indicating the maximum nanoparticle size n_{max} , up to which etching is favoured, and then the slope decreases showing the presence of sintering. The n_{max} values are shown using arrows in magenta, and are tabulated in Table 3.2.

We find, from DFT, that $E_b(Pt(L)_2)$, calculated using Eq. 3.5, for the ligands $L^1 - L^4$ has values of 7.72, 7.66, 8.29 and 7.68 eV, respectively. The E_b values for the Λ family of ligands $E_b(Pt(\Lambda)_2)$ with $L = \Lambda^1 - \Lambda^3$, are 5.68, 6.88 and 6.27 eV, respectively,

and are smaller than the E_b values of the L-family of ligands, which result in n_{max} values as small as 43, 109 and 76, respectively [see, Figs. 3.7(i), 3.8(d) and (e) for Λ^1 , Λ^2 and Λ^3 , respectively]. The n_{max} values for $L^2 - L^4$ as shown in Figs. 3.8[(a)-(c)] are found to be 8,511 (~ 6.2 nm), 11,225 (~ 6.9 nm) and 8,869 (~ 6.3 nm), respectively, implying a threshold size of ~ 6 nm for this reaction while the threshold for Λ -series comes out as ~ 1 nm. The ligands with their corresponding n_{max} and E_b values are tabulated in Table 3.2. Experimentally, all the ligands of the L-series dissolve Pt NPs with $d \leq 6$ nm, while those of the Λ -series do not. This matches well with our theoretical findings. Since $> 95\%$ of the isolated NP-size have $d > 1$ nm, the threshold for Λ -series could not be experimentally detected. Nonetheless, the insights developed above, can provide guidance in further design of ligands with different E_b values that can control the occurrence of the reaction as well as the NP size-threshold for the reaction.

3.6 Conclusions

The work presented in this chapter shows size-elective ionization and etching of Pt NPs. In a radical departure from their tendency of sintering, experiments done by our collaborators show that Pt nanoparticles, in the presence of π -acidic azo-aromatic ligands, show size-dependent etching. In other words, instead of smaller particles coming together to form larger ones, they get etched away to form even smaller nanoparticles. Based on thermodynamic considerations of the nanoparticles in the gas phase and in the presence of ligands, we derive a simple equation that dictates the maximum size of nanoparticles up to which etching is favored. The maximum size for etching is found to depend on the binding energy of the Pt atom to the ligands; thus this size can be tuned by a suitable choice of ligand. The theoretical predictions of maximum nanoparticle size up to which etching occurs in the presence of specific ligands match well with the corresponding experimental findings. We anticipate that this strategy might be relevant for other metals as well, and that it potentially offers

a new chemical route in metal-radical chemistry. The ligands and their derivatives can also be used to dissolve Pt nanoparticles in catalytic converters in the form of di-radical complex, and later reduced to extract the platinum from the complex, providing a simpler and cleaner way of reusing the platinum, that can help solve a major challenge in the automobile industry.

Bibliography

- [1] F. Vies, J. R. B. Gomes, and F. Illas, “Understanding the reactivity of metallic nanoparticles: beyond the extended surface model for catalysis,” *Chem. Soc. Rev.*, vol. 43, pp. 4922–4939, 2014.
- [2] M. Haruta, N. Yamada, T. Kobayashi, and S. Iijima, “Gold catalysts prepared by coprecipitation for low-temperature oxidation of hydrogen and of carbon monoxide,” *Journal of Catalysis*, vol. 115, no. 2, pp. 301 – 309, 1989.
- [3] S. D. Gardner, G. B. Hoflund, B. T. Upchurch, D. R. Schryer, E. J. Kielin, and J. Schryer, “Comparison of the performance characteristics of Pt/SnOx and Au/MnOx catalysts for low-temperature CO oxidation,” *Journal of Catalysis*, vol. 129, no. 1, pp. 114 – 120, 1991.
- [4] B. Yang, S. Chan, W. Chang, and Y. Chen, “Surface enrichment in mixed oxides of Cu, Co, and Mn, and its effect on CO oxidation,” *Journal of Catalysis*, vol. 130, no. 1, pp. 52 – 61, 1991.
- [5] D. Astruc, *Nanoparticles and Catalysis*. John Wiley & Sons, Ltd, 1 ed., 2008.
- [6] E. Roduner, *Nanoscopic Materials*. The Royal Society of Chemistry, 2006.
- [7] D. Astruc, F. Lu, and J. R. Aranzaes, “Nanoparticles as recyclable catalysts: The frontier between homogeneous and heterogeneous catalysis,” *Angewandte Chemie International Edition*, vol. 44, no. 48, pp. 7852–7872, 2005.

-
- [8] A. Wieckowski, E. R. Savinova, and C. G. Vayenas, *Catalysis and Electrocatalysis at Nanoparticle Surfaces*. CRC Press, 1 ed., Wieckowski.
- [9] M. K. Debe, “Electrocatalyst approaches and challenges for automotive fuel cells,” *Nature*, vol. 486, no. 43, 2012.
- [10] N. Tian, Z.-Y. Zhou, S.-G. Sun, Y. Ding, and Z. L. Wang, “Synthesis of tetrahedral platinum nanocrystals with high-index facets and high electro-oxidation activity,” *Science*, vol. 316, no. 5825, pp. 732–735, 2007.
- [11] I. Gehrke, A. Geiser, and A. Somborn-Schulz, “Innovations in nanotechnology for water treatment,” *Nanotechnology, science and applications*, vol. 8, pp. 1177–8903, 2015.
- [12] N. Cheng, S. Stambula, D. Wang, M. N. Banis, J. Liu, A. Riese, B. Xiao, R. Li, T.-K. Sham, L.-M. Liu, *et al.*, “Platinum single-atom and cluster catalysis of the hydrogen evolution reaction,” *Nature Communications*, vol. 7, p. 13638, 2016.
- [13] O. Khaselev and J. A. Turner, “A monolithic photovoltaic-photoelectrochemical device for hydrogen production via water splitting,” *Science*, vol. 280, no. 5362, pp. 425–427, 1998.
- [14] I. E. L. Stephens, A. S. Bondarenko, U. Grnbjerg, J. Rossmeisl, and I. Chorkendorff, “Understanding the electrocatalysis of oxygen reduction on platinum and its alloys,” *Energy Environ. Sci.*, vol. 5, pp. 6744–6762, 2012.
- [15] K. Yamamoto, T. Imaoka, W.-J. Chun, O. Enoki, H. Katoh, M. Takenaga, and A. Sonoi, “Size-specific catalytic activity of platinum clusters enhances oxygen reduction reactions,” *Nature Chemistry*, vol. 1, p. 397, 2009.
- [16] K. Taylor, “Automobile catalytic converters,” in *Catalysis and Automotive Pollution Control* (A. Crucq and A. Frennet, eds.), vol. 30 of *Studies in Surface Science and Catalysis*, pp. 97 – 116, Elsevier, 1987.

- [17] C. J. Kliewer and G. A. Somorjai, "Structure effects on pyridine hydrogenation over Pt(111) and Pt(100) studied with sum frequency generation vibrational spectroscopy," *Catalysis Letters*, vol. 137, pp. 118–122, Jul 2010.
- [18] K. K. Kasem, "Role of platinum in photoelectrochemical studies related to solar energy harvesting," *Platinum Metals Review*, vol. 56, no. 4, pp. 221–228, 2012.
- [19] I. Kumakiri, S. Diplas, C. Simon, and P. Nowak, "Photocatalytic membrane contactors for water treatment," *Industrial & Engineering Chemistry Research*, vol. 50, no. 10, pp. 6000–6008, 2011.
- [20] W. P. Kang and C. K. Kim, "Novel platinumtin oxidesilicon nitridesilicon dioxidesilicon gas sensing component for oxygen and carbon monoxide gases at low temperature," *Applied Physics Letters*, vol. 63, no. 3, pp. 421–423, 1993.
- [21] A. Harley-Trochimczyk, T. Pham, J. Chang, E. Chen, M. A. Worsley, A. Zettl, W. Mickelson, and R. Maboudian, "Gas sensors: Platinum nanoparticle loading of boron nitride aerogel and its use as a novel material for low-power catalytic gas sensing (adv. funct. mater. 3/2016)," *Advanced Functional Materials*, vol. 26, no. 3, pp. 314–314, 2016.
- [22] S.-I. Tanaka, J. Miyazaki, D. K. Tiwari, T. Jin, and Y. Inouye, "Fluorescent platinum nanoclusters: Synthesis, purification, characterization, and application to bioimaging," *Angewandte Chemie International Edition*, vol. 50, no. 2, pp. 431–435, 2011.
- [23] D. Chen, S. Gao, W. Ge, Q. Li, H. Jiang, and X. Wang, "One-step rapid synthesis of fluorescent platinum nanoclusters for cellular imaging and photothermal treatment," *RSC Adv.*, vol. 4, pp. 40141–40145, 2014.
- [24] M. I. Kim, M. S. Kim, M.-A. Woo, Y. Ye, K. S. Kang, J. Lee, and H. G. Park, "Highly efficient colorimetric detection of target cancer cells utilizing superior

- catalytic activity of graphene oxidemagnetic-platinum nanohybrids,” *Nanoscale*, vol. 6, pp. 1529–1536, 2014.
- [25] Y. Song, X. Xia, X. Wu, P. Wang, and L. Qin, “Integration of platinum nanoparticles with a volumetric bar-chart chip for biomarker assays,” *Angewandte Chemie*, vol. 126, no. 46, pp. 12659–12663, 2014.
- [26] M. Moglianetti, E. De Luca, D. Pedone, R. Marotta, T. Catelani, B. Sartori, H. Amenitsch, S. F. Retta, and P. P. Pompa, “Platinum nanozymes recover cellular ros homeostasis in an oxidative stress-mediated disease model,” *Nanoscale*, vol. 8, pp. 3739–3752, 2016.
- [27] M. Shao, A. Peles, and K. Shoemaker, “Electrocatalysis on platinum nanoparticles: Particle size effect on oxygen reduction reaction activity,” *Nano Letters*, vol. 11, no. 9, pp. 3714–3719, 2011. PMID: 21806027.
- [28] S. Mostafa, F. Behafarid, J. R. Croy, L. K. Ono, L. Li, J. C. Yang, A. I. Frenkel, and B. R. Cuenya, “Shape-dependent catalytic properties of Pt nanoparticles,” *Journal of the American Chemical Society*, vol. 132, no. 44, pp. 15714–15719, 2010. PMID: 20949968.
- [29] J. Seo, S. Lee, B. Koo, and W. Jung, “Controlling the size of Pt nanoparticles with a cationic surfactant, CnTABr,” *CrystEngComm*, vol. 20, pp. 2010–2015, 2018.
- [30] K. Niesz, M. Grass, and G. A. Somorjai, “Precise control of the Pt nanoparticle size by seeded growth using EO13PO30EO13 triblock copolymers as protective agents,” *Nano Letters*, vol. 5, no. 11, pp. 2238–2240, 2005.
- [31] M. Domingo, M. Shahrokhi, I. N. Remediakis, and N. Lopez, “Shape control in gold nanoparticles by n-containing ligands: Insights from density functional theory and wulff constructions,” *Topics in Catalysis*, vol. 61, pp. 412–418, May 2018.

- [32] D. Sengupta, *Ligand controlled catalytic reactions using d^8 -metal complexes of azo-aromatics*. PhD thesis, Department of chemistry, Jadavpur University (Indian Association for the Cultivation of Science), 2016.
- [33] D. J. Wales *et al.*, “The cambridge cluster database.” <http://www-wales.ch.cam.ac.uk/CCD.html>.
- [34] L. Li, A. H. Larsen, N. A. Romero, V. A. Morozov, C. Glinsvad, F. Abild-Pedersen, J. Greeley, K. W. Jacobsen, and J. K. Nørskov, “Investigation of catalytic finite-size-effects of platinum metal clusters,” *The Journal of Physical Chemistry Letters*, vol. 4, no. 1, pp. 222–226, 2013.
- [35] P. Giannozzi, S. Baroni, N. Bonini, M. Calandra, R. Car, C. Cavazzoni, D. Ceresoli, G. L. Chiarotti, M. Cococcioni, I. Dabo, A. D. Corso, S. de Gironcoli, S. Fabris, G. Fratesi, R. Gebauer, U. Gerstmann, C. Gougoussis, A. Kokalj, M. Lazzeri, L. Martin-Samos, N. Marzari, F. Mauri, R. Mazzarello, S. Paolini, A. Pasquarello, L. Paulatto, C. Sbraccia, S. Scandolo, G. Sclauzero, A. P. Seitsonen, A. Smogunov, P. Umari, and R. M. Wentzcovitch, “QUANTUM ESPRESSO: a modular and open-source software project for quantum simulations of materials,” *Journal of Physics: Condensed Matter*, vol. 21, p. 395502, sep 2009.
- [36] J. M. Soler, E. Artacho, J. D. Gale, A. García, J. Junquera, P. Ordejón, and D. Sánchez-Portal, “The SIESTA method for ab initio order-n materials simulation,” *Journal of Physics: Condensed Matter*, vol. 14, pp. 2745–2779, mar 2002.
- [37] M. J. Frisch *et al.*, “Gaussian 09,” *Gaussian, Inc., Wallingford CT*, 2016.
- [38] J. P. Perdew, K. Burke, and M. Ernzerhof, “Generalized gradient approximation made simple,” *Phys. Rev. Lett.*, vol. 77, pp. 3865–3868, Oct 1996.
- [39] S. Grimme, “Accurate description of van der waals complexes by density functional theory including empirical corrections,” *Journal of Computational Chemistry*, vol. 25, no. 12, pp. 1463–1473, 2004.

-
- [40] S. Grimme, “Semiempirical gga-type density functional constructed with a long-range dispersion correction,” *Journal of Computational Chemistry*, vol. 27, no. 15, pp. 1787–1799, 2006.
- [41] D. Vanderbilt, “Soft self-consistent pseudopotentials in a generalized eigenvalue formalism,” *Phys. Rev. B*, vol. 41, pp. 7892–7895, Apr 1990.
- [42] J. W. Song, K. Yamashita, and K. Hirao, “Communication: a new hybrid exchange correlation functional for band-gap calculations using a short-range gaussian attenuation (gaussian-perdue-burke-ernzerhof),” *J. Chem. Phys.*, vol. 135 (7), p. 071103, 2011.

Chapter 4

Identifying Optimal Dye

Sensitizers for Use in Solar Cells

In this chapter, we have identified and computed a set of descriptors to find the optimal candidate dye for use in dye sensitized solar cells (DSSCs). Experiments carried out by our collaborators in the group of Prof. Patchanita Thamyongkit, show high absorptivity in the long wavelength region, for a set of novel (not previously considered) dye molecules. We choose these molecules as our candidate dyes and perform density functional theory (DFT) calculations on them in the gas phase and on a TiO_2 substrate, in an attempt to determine which of these dyes might provide the best performance as a sensitizer in DSSCs. Many of the results presented in this Chapter have been published in Ref. [1].

4.1 Introduction

Dye-sensitized solar cells (DSSCs) have attracted considerable attention in recent years as a low-cost alternative to conventional solid-state photovoltaic devices.[2, 3] Large absorption coefficients, ease of structural modification, the possibility of large-scale synthesis and economically friendly production have made organic DSSCs ideal candidates for solar cell applications. In a DSSC set-up, dye molecules in the electrolyte get adsorbed on the substrate, preferably TiO_2 , acting as the cathode material.

The dye molecules absorb solar energy and the electrons in the highest occupied molecular orbital (HOMO) of the molecule get excited to the lowest unoccupied molecular orbital (LUMO) of the dye, and then to the conduction band of the TiO₂. The holes left behind in the HOMO of the dye, get replenished by the electrons supplied by the redox reaction occurring in the electrolyte.

Previous theoretical and experimental studies have shown that several parameters, corresponding to these different stages of the DSSC operation, can be tuned to control the energy conversion efficiency of the dyes in a DSSC.[4–8] First of all, the dye molecule must have large electronic absorptivity in the visible region for efficient absorption of solar energy and excitation of electrons to the LUMO. The absorptivity can be tuned by modification of the π -conjugated donor-acceptor structure.[4, 9] The position of the frontier orbitals of the dye with respect to TiO₂ valence and conduction bands is also crucial: Bahers *et al.*[7] suggested that the HOMO of the dye must lie within the band gap of the TiO₂ substrate, and the LUMO of the dye must lie right above the conduction band bottom edge of TiO₂. In this regard the interaction of the dye with the electrolyte may be important as it has been shown to affect the energy of the conduction band edge.[10] de Angelis *et al.*[6] have shown theoretically, that the effective electronic coupling between the dye and the substrate is also important as it affects the injection of the excited electrons from the dye to the substrate. This coupling between the dye and the TiO₂ has been shown to depend on the anchoring group and the adsorption geometry of the dye molecule on the substrate. Kim *et al.*[11] have shown that the structure of the molecule, especially the donor-acceptor geometry affects the charge separation and hence the recombination of electrons and holes. It has been shown that the extended π -conjugation in the donor structure results in larger electron-hole separation,[12] ultimately affecting the conversion efficiency of the dye in a DSSC.

Thus, the factors determining the performance of the dye molecules in a DSSC include alignment of frontier orbitals of the dye molecule with respect to the band

gap and conduction band edge of TiO_2 , coupling between the molecule and the substrate, and the electron-hole separation. Tuning these parameters needs an in-depth understanding of the electronic properties of the dye+substrate complex. As will be discussed further below, in our work we have formulated a set of descriptors that can capture these different factors affecting the performance of a dye molecule in a DSSC.

Difluoro-4-bora-3a, 4a-diaza-s-indacenes or so-called BODIPYs are very well known organic dyes widely used for several optoelectronic and optical applications. Due to their high absorption coefficients and fluorescence quantum yields, high (photo)chemical stability and improved synthetic availability,[13] they have been used in organic solar cells,[14–17] as fluorescent dyes for imaging,[13, 18–20] optical sensors,[21–24] and laser dyes,[25–27] etc. Their photophysical and electrochemical properties can be tuned by changing the substituents in a BODIPY core structure. In this study we have investigated theoretically (while our collaborators have, simultaneously, investigated experimentally), the effect of aromatic-derived or aryl *meso*-groups and extended π -conjugated systems at β -positions, on the photophysical and electrochemical behaviour of the BODIPY, with a view to determining its suitability as a dye-sensitizer. Based on the electronic properties of the dye + substrate complex, we have calculated using density functional theory (DFT), a set of descriptors to find the optimal candidate dye from a set dyes, for use in DSSCs.

4.2 Experimental background

Our experimental collaborators in the group of Patchanita Thamyongkit have recently synthesized a series of novel BODIPYs with phenyl, thienyl and bithiophenyl *meso*-substituents, with the goal of examining their photophysical and electrochemical properties.[1] Thienyl and bithiophenyl groups are chosen due to the fact that thiophene and polythiophene derivatives are known to have good electronic properties, environmental stability and structural versatility,[28] and are widely used for

optoelectronic applications.[29–31] The structures of the target BODIPY, benzo-dipyrrin, benzo-BODIPY and cyclohexyl-fused BODIPY derivatives bearing thienyl and bithiophenyl meso-substituents are shown in Chart 4.1. By such systematic structural variation, the effects on the photophysical and electrochemical properties of the presence of boron-chelation, the number of thiophene units in the meso-group, and the fused rings at the β -positions of the BODIPY core, compared with phenyl group, can be intensively studied. To avoid an interfering effect from a reactive carboxyl group on the photophysical and electrochemical measurements, the derivatives with ethyl ester groups, as a protected form of the carboxyl groups, at α -carbons of the BODIPY core (compounds **2'**, **3'** and **4'** in Chart 4.1) are used in the measurement. In theoretical calculations, the molecules having carboxyl meso-groups at the α -carbons (compounds **2**, **3** and **4** in Chart 1) were taken into consideration to explore the possibility of using these compounds as a photosensitizer in dye-sensitized solar cells (DSSCs), because the dye molecule requires such a group to attach onto a TiO₂ substrate.

A comparison of the absorption maxima ($\lambda_{abs,max}$) of **1a**, **1b** and **1c**, with that of **3a'**, **3b'** and **3c'**, respectively, from UV-visible spectroscopy measurements [see Table 4.1] shows that the presence of the benzo-fused rings and the α -ester groups on the pyrrolic rings of **3a'**, **3b'** and **3c'**, causes a red shift of $\lambda_{abs,max}$ by 139 – 142 nm. Moreover, a similar comparison of $\lambda_{abs,max}$ of **2a'** vs. **3a'**, **2b'** vs. **3b'** and **2c'** vs. **3c'** reveals that the boron-complexation of the benzo-dipyrrins leads to a red shift of $\lambda_{abs,max}$ by 68 – 77 nm. Therefore, the boron-complexation and the introduction of the benzo-fused ring at the β -positions of the BODIPY cores play a major role in the compounds achieving high absorptivity in the long wavelength region, which is preferable for photovoltaic devices.

Motivated by the above experimental results, we have carried out density functional theory (DFT) calculations on the benzo-BODIPY's, which exhibit high absorptivity in the long wavelength region. We therefore focus here on molecules **3a**, **3b** and

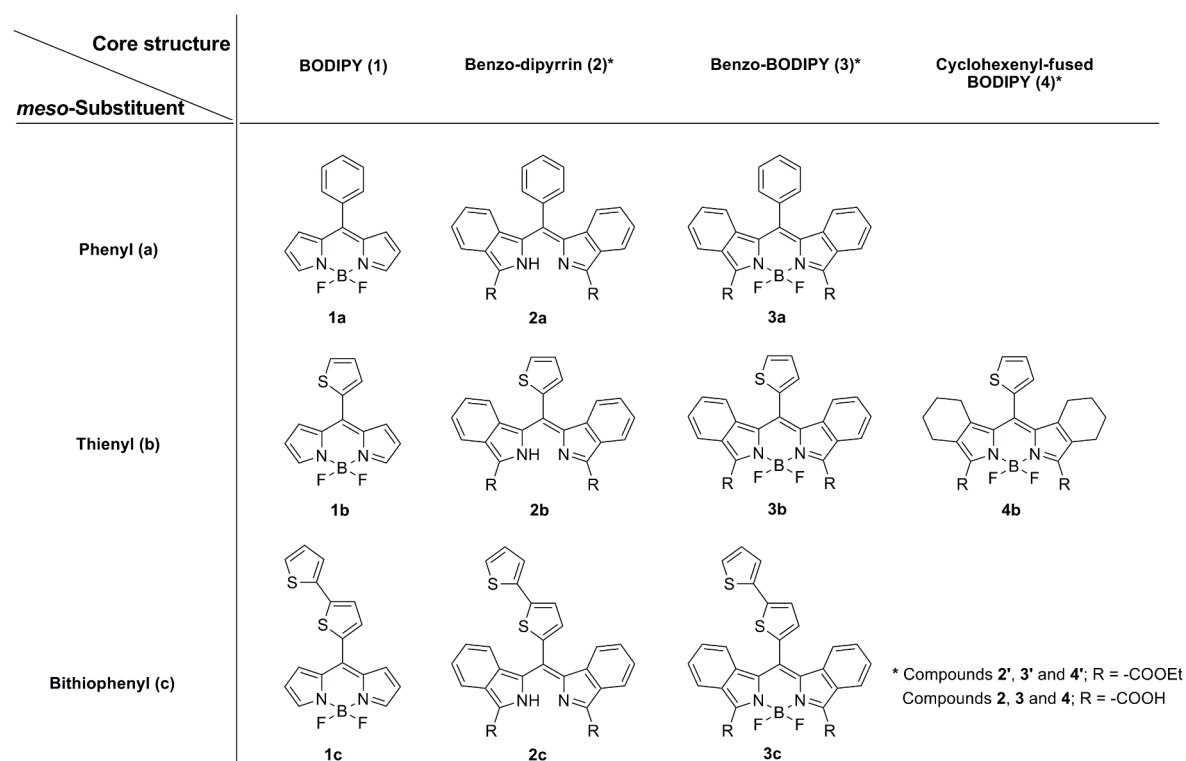


Figure 4.1: Structures of BODIPYs and dipyrins of interest are shown. Compounds **2**, **3** and **4** have carboxyl anchor groups (R = -COOH) in the theoretical calculations, whereas in the experiments ethyl ester groups (R = -COOEt) are present for the corresponding compounds **2'**, **3'** and **4'**.

3c, and also **4b** as a comparative molecule, to investigate the effect of the extended conjugated system on the β -benzo-fused rings of the BODIPY core. The details of the systems, calculations and results are presented below.

4.3 Systems under study

To compare our DFT results with the experiments, we first calculate the electronic properties of the **3a**, **3b**, **3c** and **4b** molecules in the gas phase. Since molecule-substrate interactions have a significant impact on device performance, in order to evaluate the potential of the dye molecules as candidates for use in DSSCs, we place the **3a**, **3b**, **3c** and **4b** molecules on the anatase TiO₂(101) surface. The final relaxed geometries of these molecules adsorbed on TiO₂ are shown in Fig. 4.2. Note, as mentioned in Section 2, instead of ethyl ester groups (**3a'**, **3b'**, **3c'**, and **4b'**), carboxyl meso-groups at the α -carbons of the BODIPY core (**3a**, **3b**, **3c**, and **4b**) are used

Table 4.1: The photophysical properties of the target BODIPYs and dipyrrens. λ_{abs} , ϵ , λ_{em} and ϕ_f denote the absorption wavelength, the molar extinction coefficients, emission wavelength and the fluorescence quantum yields, respectively.

Compound	λ_{abs} (nm) [$\epsilon \times 10^5$ ($M^{-1} \text{ cm}^{-1}$)] ^a	λ_{em} (nm)	ϕ_f ^b
BODIPY			
1a [32]	344, 503 (0.5)	521	0.05
1b	393, 514 (0.5)	553 ^c ; 617	0.02
1c ^d	312, 514 (0.5)	341, 567	— ^e
4b'	439, 556 (0.5)	582	0.05
Benzo-dipyrren			
2a'	574 (0.4)	— ^f	— ^g
2b'	579 (0.3)	— ^f	— ^g
2c'	589 (0.2)	— ^f	— ^g
Benzo-BODIPY			
3a'	642 (1.0)	663	0.37
3b'	656 (0.7)	676	0.29
3c'	658 (0.5)	678	0.23

^a Only ϵ at the absorption maximum ($\lambda_{abs,max}$) was determined.

^b The ϕ_f values were calculated by using methylene blue ($\phi_f=0.04$ in ethanol) as reference.[50]

^c Emission signal was observed as a shoulder.

^d The photophysical properties were investigated in CH_2Cl_2 , according to a published report.[41]

^e Data was not provided by published report.[41]

^f No peak was observed.

^g Value could not be calculated.

as anchoring groups for all the molecules to investigate the performance of these molecules as dye-sensitizers. The colour codes for all the atoms are shown in the side panel of Fig. 4.2 (a).

4.4 Computational details

Our *ab initio* DFT calculations are performed using the PWscf package of the QUANTUM ESPRESSO distribution.[33] Interactions between the ion cores and the valence electrons are treated using ultrasoft pseudopotentials.[34] Exchange-correlation effects are taken into account using a generalized gradient approximation (GGA) of the Perdew-Burke-Ernzerhof (PBE) form.[35] A plane-wave basis set is used with a cutoff of 40 Ry for wavefunctions and 400 Ry for charge densities. Van der Waals interactions are incorporated using Grimme’s DFT-D2 scheme.[36, 37] The

anatase $\text{TiO}_2(101)$ surface is modeled using a (6×1) surface unit cell comprised of two layers, each of which contains 24 Ti atoms and 48 O atoms; tests were performed to verify that the results obtained do not change appreciably upon using thicker TiO_2 slabs. A single dye molecule is placed on the surface of this two-layer slab. The Brillouin zone is sampled at the zone center Γ only. In order to ensure that our use of periodic boundary conditions does not introduce spurious interactions between the dye molecule and the TiO_2 slab in the neighboring cell (due to the introduction of artificial periodicity normal to the surface of the slab), we introduce an additional vacuum spacing of $\sim 12 \text{ \AA}$ above the molecule along the y -direction, i.e., perpendicular to the TiO_2 surface. All atoms are allowed to relax, except those in the lower layer of the substrate. The force convergence threshold is kept at 0.001 Ry/bohr along each Cartesian direction.

4.5 Results and discussion

In order to confirm and understand the experimental results, as well as to extend them so as to find a set of descriptors to predict the performance of the dye molecules for use in DSSCs, we have carried out DFT calculations on the **3a**, **3b**, **3c** and **4b** molecules in the gas phase and when adsorbed on the $\text{TiO}_2(101)$ surface.

4.5.1 Adsorption geometry and energetics

Since the mode of attachment of the dye molecules to the substrate is known to affect phenomena, such as electron injection and recombination dynamics, which play a significant role in determining the overall performance of the DSSC,^[6] the details of the adsorption geometry need to be investigated. Therefore, we first determine the preferred adsorption geometry for the dye molecules when adsorbed on the anatase $\text{TiO}_2(101)$ surface. To ensure that we have found the lowest energy configuration of the molecule + substrate system, we have performed calculations starting from several different initial geometries. Previous theoretical studies^[5, 6, 38–42] have shown that in general, three possibilities exist for the preferred anchoring geometry of the COO-

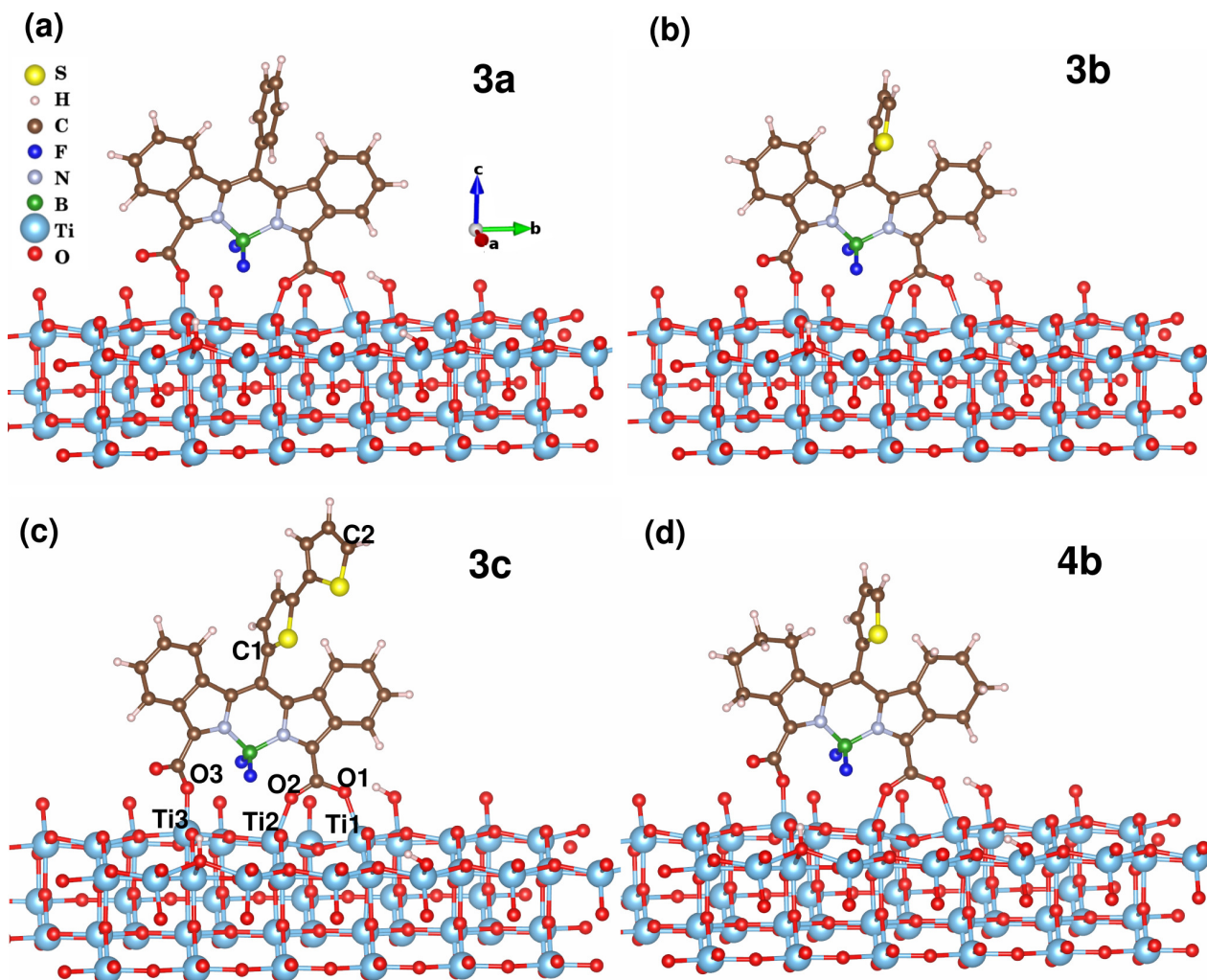


Figure 4.2: Lowest energy adsorption geometries for dye molecules **3a**, **3b**, **3c** and **4b**, adsorbed on TiO_2 substrate. Labels in **3c** indicate the notation used to distinguish various Ti, O and C atoms. The dihedral angles θ_1 and θ_2 are defined as $\angle \text{C1-Ti2-Ti2}'$ and $\angle \text{C2-C1-Ti2}$, respectively, where $\text{Ti2}'$ is the periodic image of Ti2 along the $+a$ direction. Note that all the molecules have a sesquidentate geometry consisting of one monodentate and one bidentate tethering.

Table 4.2: Adsorption geometries as determined from DFT calculations. The bond lengths between O of the dye molecules and Ti of TiO₂, the dihedral angle corresponding to different dye molecules on the TiO₂ substrate, and the adsorption energies of the molecules. See Fig. 4.2 for the naming convention for atoms.

Dye molecule	Bond length (Å)			Dihedral angle (θ)		Adsorption energy (E_{ads}) (eV/mol)
	O1-Ti1	O2-Ti2	O3-Ti3	θ_1	θ_2	
3a	2.163	1.986	1.912	90.2°	— ^a	8.74
3b	2.145	1.990	1.920	92.5°	— ^a	8.62
3c	2.136	1.982	1.920	98.2°	136.7°	9.54
4b	2.149	1.907	1.907	95.3°	— ^a	8.97

^a Due to the absence of C2, the θ_2 value is not available.

group to metal atoms of the substrate, namely (1) monodentate (ester-like),^[43] (2) bidentate (chelating)^[44] and (3) bidentate (bridging) geometries.^[45] Among these, the most commonly found lowest-energy geometry is usually the bidentate bridging one, though in some cases, the monodentate geometry has also been found to be favored.^[43] Interestingly, we find that for all four molecules studied here, the lowest energy geometry is one with a combination of monodentate and bidentate (bridging) anchoring, i.e., the dye molecule is anchored to the substrate at two points, one of which features a single O-Ti bond, while the other features two O-Ti bonds, where the O and the Ti atoms come from the dye molecule and the substrate, respectively (see Figure 4.2). We are unaware of any previous studies where such a tethering of the molecule to the substrate has been observed, and we term this a ‘sesquidentate’ anchoring mode. The relevant bond lengths and dihedral bond angles (θ), as defined in Fig. 4.2(c), are presented in Table 4.2. We find that the bond lengths at the bidentate bridging site (O1-Ti1 and O2-Ti2) are always larger than those at the monodentate bridging site (O3-Ti3) for all the molecules investigated.

In order to ensure long-term stability of the dye + substrate complex in a DSSC, the molecules should have strong binding to the substrate, preferably in the chemisorption range.^[46] In order to understand the nature of adsorption of the dye molecules on the TiO₂(101) surface and compare the corresponding strength of binding of the molecules with the substrate, we calculate the adsorption energy per molecule (E_{ads}),

defined as:

$$E_{\text{ads}} = -[E(\text{TiO}_2 + \text{mol}) - E(\text{TiO}_2) - E(\text{mol})], \quad (4.1)$$

where $E(\text{TiO}_2 + \text{mol})$, $E(\text{TiO}_2)$ and $E(\text{mol})$ denote the total energies (from DFT calculations) of the $\text{TiO}_2 + \text{dye-molecule}$ system, the TiO_2 substrate and the gas-phase dye-molecule, respectively. The magnitudes of the adsorption energies shown in Table 4.2 indicate that all the dye molecules considered above undergo chemisorption on the TiO_2 substrate, with **3c** having the largest E_{ads} . This indicates strong binding for all the dye molecules to the TiO_2 surface, essential for proper injection of charge carriers from the dye-molecule to the substrate.

4.5.2 Alignment of frontier orbitals

Upon photoexcitation of the dye, the efficiency of the transfer of excited electrons from the lowest unoccupied molecular orbital (LUMO) of the dye molecule to the semiconductor is known to be proportional to the energy difference between the LUMO and the conduction band (CB) edge of the semiconductor, and therefore, the LUMO should lie well within the CB of TiO_2 .^[7] Further, for efficient absorption of solar radiation, it then follows that the highest occupied molecular orbital (HOMO) of the dye molecule should lie within the band gap of the semiconductor.^[47] To ensure that the dye molecules considered here satisfy the above mentioned criteria, we examine the alignment of the frontier orbitals of the dye molecules relative to the TiO_2 band edges.

In order to find the position of the HOMO and the LUMO of the dye molecules with respect to the band edges of the TiO_2 substrate, in Fig. 5.5 we plot the projected density of states (PDOS) of the dye molecules adsorbed on TiO_2 . The band gap region of TiO_2 is represented by the shaded area in the PDOS plot. The energy scale in the x-axis is shifted by the HOMO of the dye molecule so that the zero of the x-axis represents the HOMO of the molecule. We see that for all the dye molecules, the HOMO and the LUMO are contributed mostly from the C-atoms (red

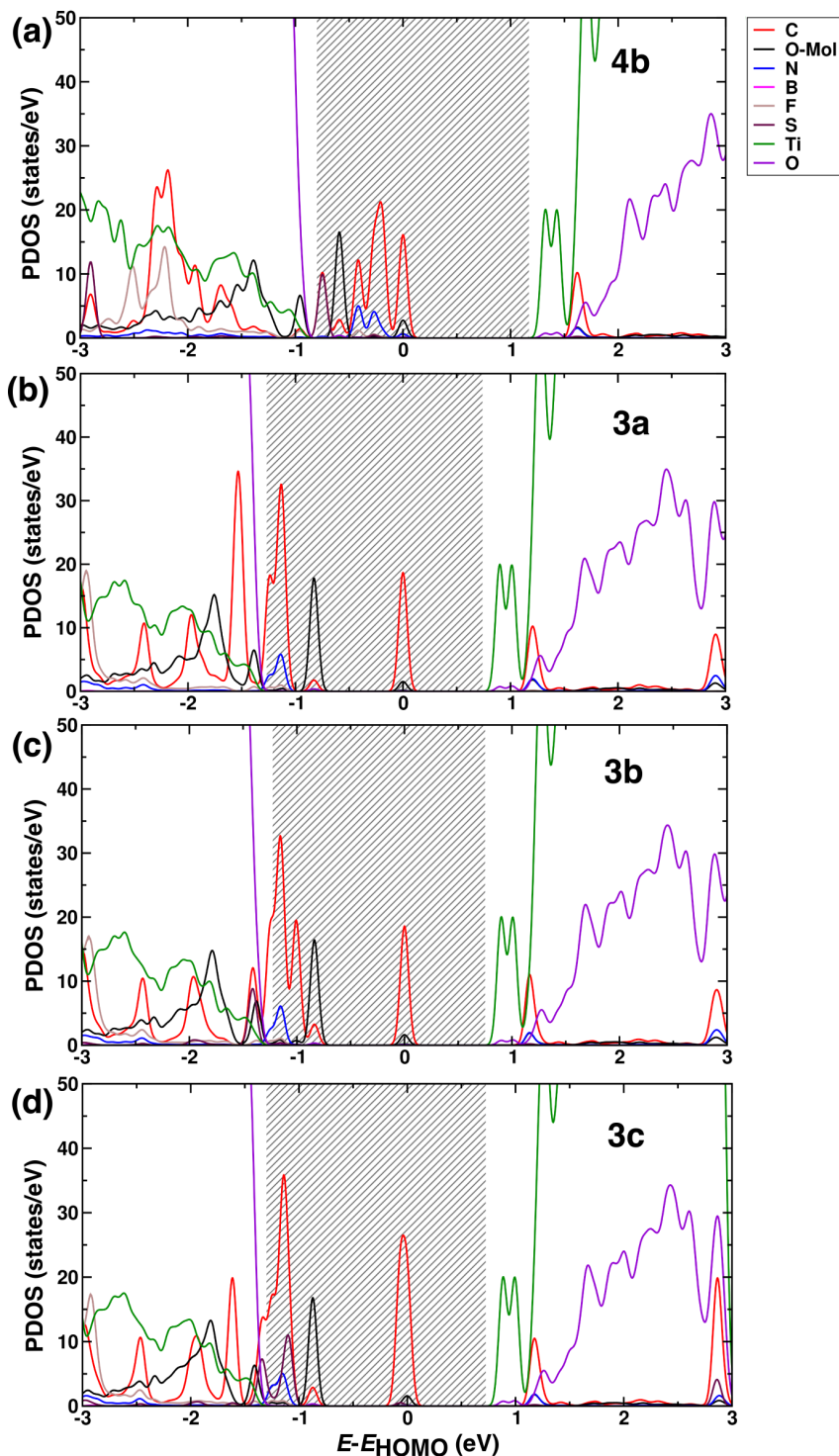


Figure 4.3: The projected density of states of the molecule + TiO₂ system. The energy is shifted by the highest occupied molecular orbital (HOMO) of the corresponding molecule, so that the zero of x-axis represents the HOMO of the molecule. The band gap region of TiO₂ is represented by the black shaded region. The color codes in the legends depict contributions from different atomic species. We see that for all the molecules the HOMO lies within the band gap of TiO₂, whereas the lowest unoccupied molecular orbital (LUMO) is in the conduction band of TiO₂.

solid line). We find that the position of the LUMO with respect to the conduction band (CB) edge of the TiO₂, is almost identical for all the dye molecules considered. Moreover, the HOMO lies within the band gap of TiO₂, whereas the LUMO lies within the CB of TiO₂. Therefore, all the dye molecules under investigation meet the above mentioned criterion for efficient absorption of solar radiation and transfer of photoexcited electrons to the TiO₂. We note here that the band gap of TiO₂ is underestimated by the GGA calculation, which is a well-known shortcoming of DFT. However, as will be discussed further below, this does not affect our procedure for estimating the efficiency of the dye molecules.

To further quantify the alignment of the frontier orbitals, and compare with the experimental results, in Figs. 4.4(a) and (b), we show our experimentally measured and theoretically computed results for the positions of the frontier orbitals of the dye molecules, respectively, as well as their alignment with respect to the band gap of TiO₂. We note that though the experimental results are for compounds **3'** and **4'** in solution, while the calculations are for compounds **3** and **4** when placed on the TiO₂ (see Chart 4.1), this is not expected to have a significant effect on the band gaps.

We see from Fig. 4.4 that the theoretically computed values for the HOMO-LUMO gaps, as well as the band gap of TiO₂, are underestimated with respect to the experimentally measured values. This is a well-known shortcoming of standard DFT calculations. However, it is clear that both experiments and DFT calculations show the same trends. We see from Fig. 4.4(b) that the LUMO of all four molecules is positioned almost identically. We also see that while variation of the meso-substituents on the BODIPY cores does not appreciably affect the position of the HOMO, extension of the BODIPY conjugation system by replacing the β -cyclohexenyl-fused rings with the benzo-fused one in **3a**, **3b** and **3c**, as compared to **4b**, results in a marked upshift in the energy of the HOMO, and thus narrowing of the energy gap. A similar trend is seen in the experimental HOMO-LUMO gaps when **4b'** is compared with **3a'**, **3b'** and **3c'**. Recent work by our experimental collaborators in the group of

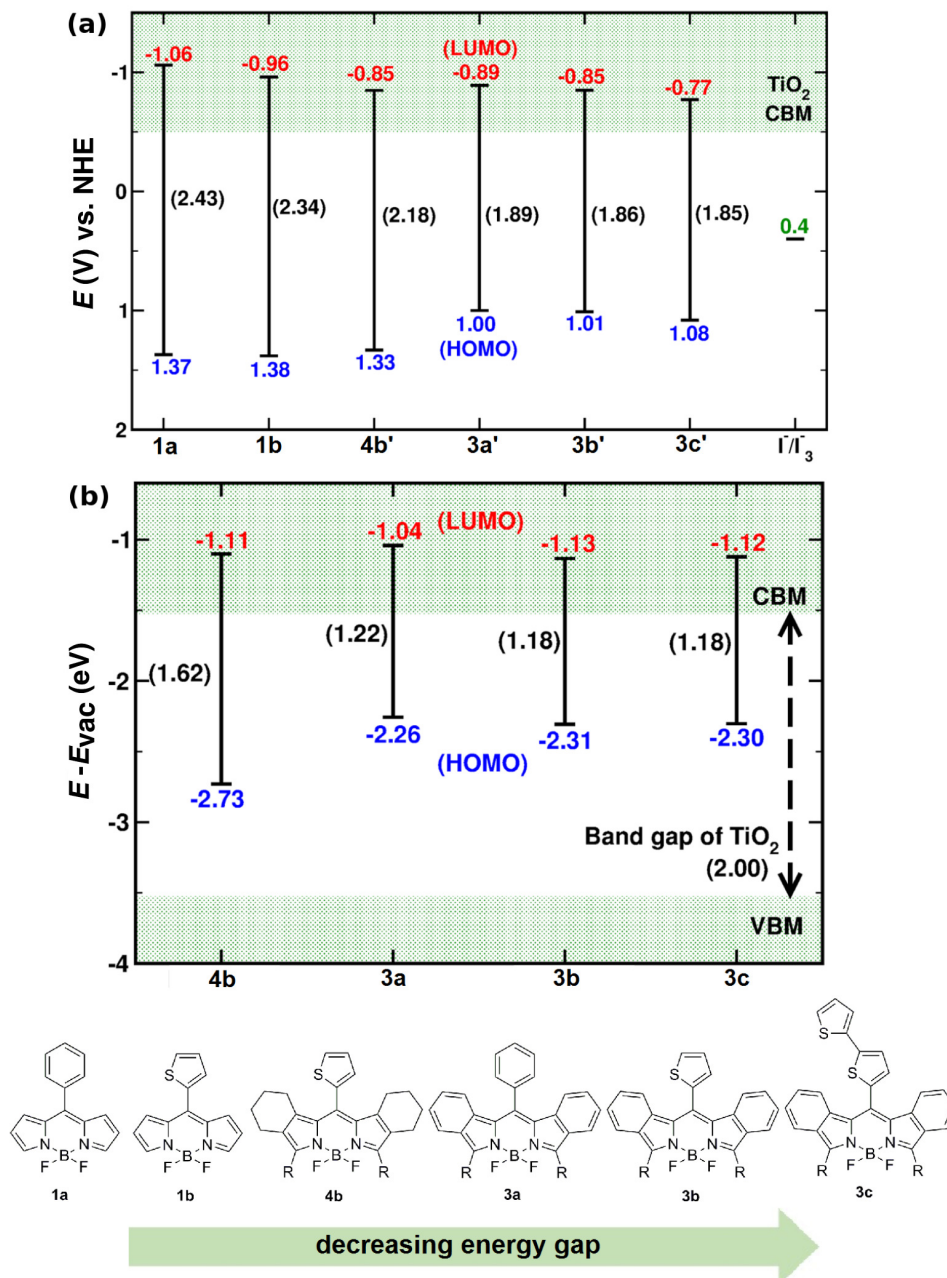


Figure 4.4: Experimental and theoretical energy level diagrams of the target BODIPYs (**1a** and **1b**) and the benzo-BODIPYs in comparison to the conduction band edge of TiO₂ and the I⁻/I₃⁻ oxidation potential. Panel (a) shows the experimentally obtained values for **1a**, **1b**, **4b'**, **3a'**, **3b'** and **3c'**, while panel (b) shows the results from DFT for **4b**, **3a**, **3b** and **3c** when adsorbed on TiO₂. The theoretical values are referenced with respect to the vacuum energy. The shaded regions correspond to the valence and conduction bands of TiO₂; VBM and CBM indicate the theoretically computed valence band maximum and conduction band minimum, respectively. Note that while DFT underestimates the energy gaps, as expected, the trends across the molecules are the same in the experiment and the theory.

Patchanita Thamyongkit, on porphyrin derivatives, also shows that introduction of benzo-fused rings should have considerable impact on the HOMO/LUMO levels of the dye molecules.[48]

The reproduction of the experimental trends in the theoretical calculations is made more evident in Fig. 4.5, where we have plotted the experimental as well as theoretical results for the HOMO-LUMO gaps, with the latter being computed both in the gas phase and for the molecules adsorbed on TiO₂. We note that the experiments were performed for the molecules in solution, whereas the calculations were performed for the molecules when adsorbed on TiO₂; we observe, however, that this does not affect trends. We also note that upon performing calculations for the isolated molecules in the gas phase, we find only a very slight increase in the HOMO-LUMO gap compared to our results for the molecules when deposited on the TiO₂ substrate. To summarize, as presented in both Figs. 4.4 and 4.5, the theoretical calculations confirm the experimental conclusion that all four of the compounds considered in this section satisfy the criteria concerning the alignment of the energies of their frontier orbitals with respect to the band edges of the TiO₂ substrate.

4.5.3 Theoretical prediction of performance of dyes in DSSCs

In this section, we use *ab initio* DFT calculations to compute a set of descriptors that can predict the photosensitizing performance of the four dye molecules when used in combination with the TiO₂ substrate, in the DSSC. It is known that the overall efficiency of the DSSC depends on several parameters, and an understanding of how to predict the performance using theoretical methods is still the subject of intense research. In this respect, the formulation and use of descriptors can help us in the rapid screening of large pools of candidate dye-substrate combinations. Here, the efficiency of four factors that are known to determine the performance of the DSSCs, viz., the alignment of frontier orbitals of the dye molecule with respect to the CB edge of TiO₂, electron transfer from the excited dye molecule to empty states in the TiO₂ substrate, the prevention of electron-hole recombination and change in

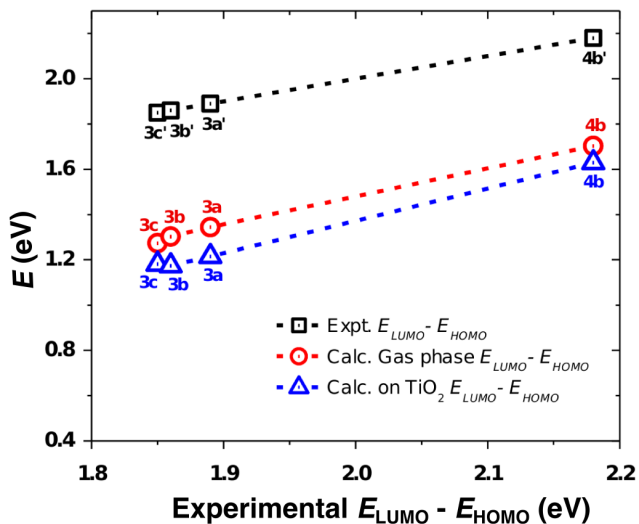


Figure 4.5: Correlation between the experimental results for **3a'**, **3b'**, **3c'** and **4b'**, and the theoretical results for the HOMO-LUMO gaps for **3a**, **3b**, **3c** and **4b**. The black squares show the experimental values, while the red circles and blue triangles show the values as calculated from DFT for the molecules in the gas phase and when adsorbed on TiO_2 , respectively. Note that the same trends are observed in the experiment and the theory, though DFT underestimates the energy gaps, as expected.

dipole moment upon excitation, are theoretically evaluated. These factors are then quantified in the form of descriptors as discussed below.

Role of electronic structure: Descriptors for predicting efficiency of dyes

In order to gain insight into the role played by the electronic structures of the four candidate compounds, we have plotted the charge densities corresponding to the HOMO and the LUMO, for the dye molecules adsorbed on TiO_2 , in Fig. 4.6. It is interesting to note that for the **4b** molecule, the green lobes, corresponding to the isosurfaces of the charge densities of the HOMO, are mostly localized on the C atoms of the BODIPY core, whereas for **3a**, **3b**, and **3c**, the charge densities corresponding to the HOMO are spread throughout the molecule, with significant weight on the bithiophenyl group extending away from the surface, in the case of **3c**; this is in sharp contrast to the LUMO, where the charge density is primarily localized on C atoms close to the substrate. This observation will have implications for electron-hole recombination, which we discuss further below.

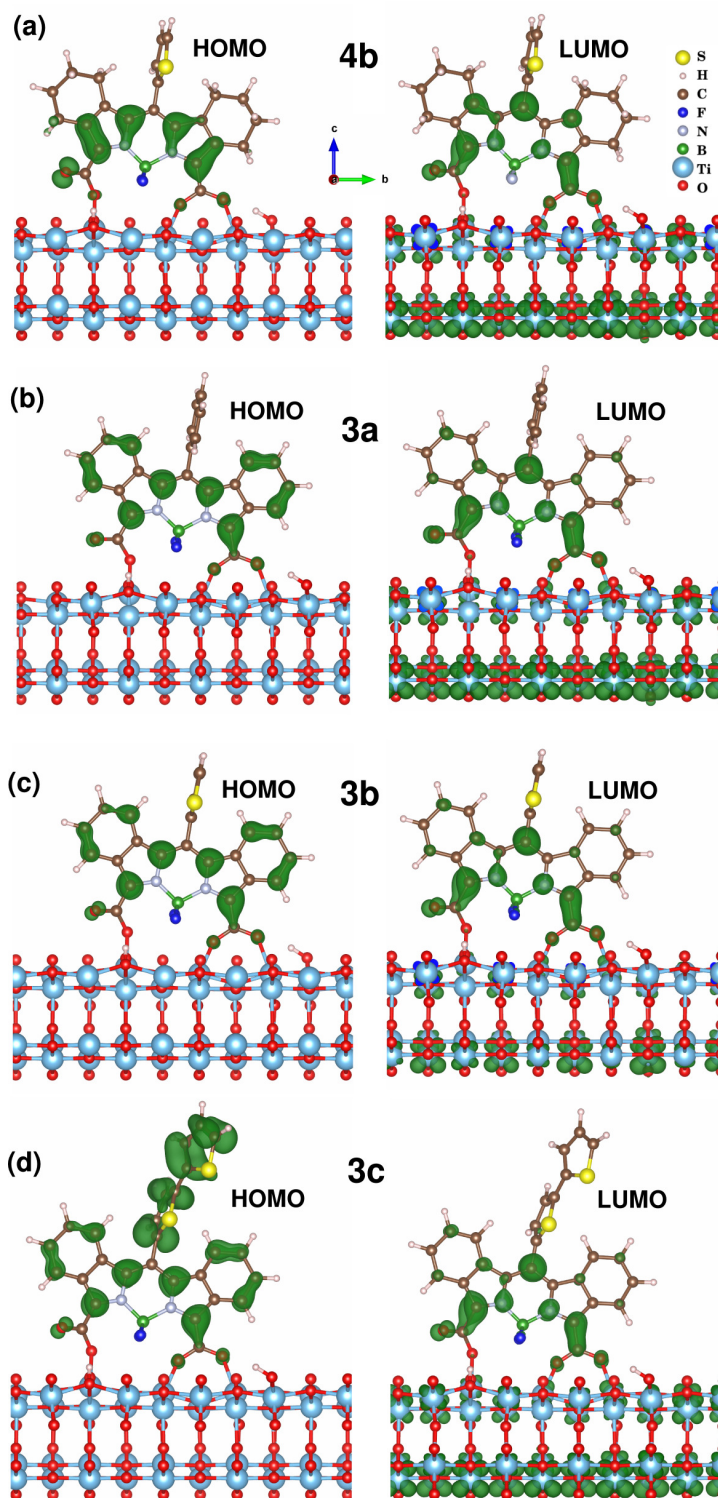


Figure 4.6: The isosurfaces of the charge densities for states corresponding to the HOMO (left image of each panel) and the LUMO (right image for each panel) for **4b**, **3a**, **3b** and **3c** on TiO_2 are shown. The isosurfaces corresponding to a value of $0.004 \text{ e}/\text{\AA}^3$ are plotted as green lobes.)

Electron transfer from the excited states of the dye molecules to the empty states in the CB of TiO₂ depends primarily on two factors: (1) the strength of the matrix element coupling the excited states of the dye molecules to the CB states of TiO₂ and, (2) the density of states available in the CB of TiO₂ for the electronic transition. As mentioned in Section 5.2, for all four molecules, the LUMO is positioned in the midst of the continuum of states of the TiO₂ CB, and is broadened due to coupling (hybridization) between the dye and the substrate. In order to quantify the coupling strength, we first compute the descriptor full width at half maximum (FWHM) of the peak corresponding to the LUMO of the dye molecule in the projected density of states (PDOS) of the system consisting of the dye adsorbed on TiO₂; it has been suggested that this broadening should serve as a good estimate of the strength of the molecule-substrate coupling.^[6] The values of the FWHM for all four dye molecules when adsorbed on TiO₂ are plotted in Fig. 4.7(a). We see that the values of the FWHM are roughly the same for all four molecules, reflecting the similarity in the anchoring groups and anchoring geometries. However, there is a slight variation, with the smallest value of FWHM for **3b** and the largest for **3a**.

The effects of the two factors mentioned above, viz., the density of states available in the CB of TiO₂, and the coupling between the molecule and TiO₂ (appearing implicitly via its effect on the broadening of the dye states) can be both incorporated in a single descriptor by computing the coefficient of injection, C_{inj} , which we define as:

$$C_{\text{inj}} = \int_{\text{FWHM}} g_{\text{Dye}}(E)g_{\text{TiO}_2}(E)dE, \quad (4.2)$$

where $g_{\text{Dye}}(E)$ and $g_{\text{TiO}_2}(E)$ are the electronic densities of states corresponding to the LUMO of the dye molecule and the CB of TiO₂, respectively, and E is the electronic energy. The integration is carried out over an energy interval equal to the FWHM, centered about the LUMO of the dye molecule. We note that our definition of C_{inj} differs from that of previous authors^[49, 50] in that it does not contain a term

explicitly describing the coupling between the molecule and the substrate, which is difficult to compute. Instead, the inclusion of such a term is bypassed in our expression, with its effects being instead implicitly incorporated by the limits of integration being set equal to the FWHM interval that has been computed above. In Fig. 4.7 (b), we have plotted our results for C_{inj} , as given by Eq. (4.2), for the four dye molecules. Reflecting the influence of the values of FWHM, we find that C_{inj} is smallest for **3b** and largest for **3a**, suggesting that, if only charge injection mattered, **3a** should be the optimal choice for use in the DSSCs, among the four compounds considered here. However, we note that the percentage differences in the values of C_{inj} among the four compounds are not large, presumably as a result of the similar sesquidentate type anchoring geometry for all four dye molecules on TiO_2 . While the precise numerical values of C_{inj} may change upon incorporating a more sophisticated treatment of the molecule-substrate coupling, we believe that the basic trends are captured in our simple model.

Another factor determining the performance of the DSSC is the likelihood of electron-hole recombination, which adversely affects the performance of the device, since recombination with holes reduces the photocurrent. When electrons are excited to previously unoccupied states of the dye molecule, holes are created in formerly occupied states. An increase in the spatial separation between these excited electrons in the LUMO and the holes in the HOMO, should increase the probability of successful electron transfer to the electrode. A rigorous calculation of properties of the excited state, such as its charge density,^[7] would require the application of more computationally expensive techniques, such as time-dependent density functional theory (TDDFT). However, we note that within the single particle picture, the relevant spectroscopic quantities, viz., the ground state oxidation potential (GSOP) and the excited state oxidation potentials (ESOP), can be approximated by the HOMO and the LUMO, respectively.^[51] Accordingly, we will estimate a descriptor called the electron-hole separation (*EHS*) by computing the spatial difference between

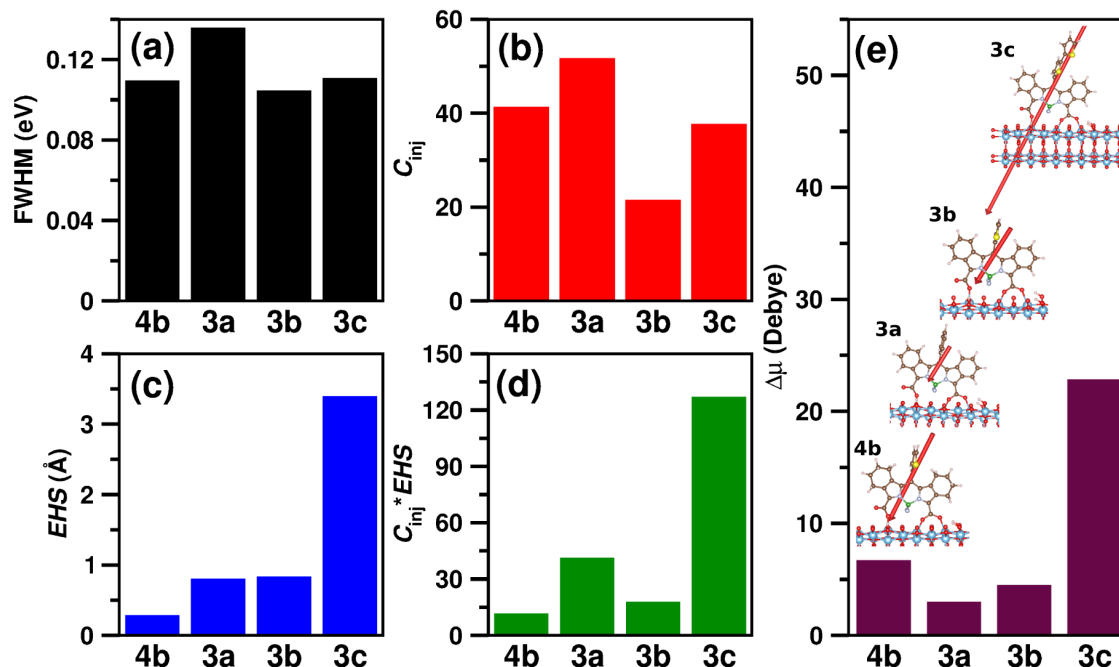


Figure 4.7: DFT results for various factors affecting the performance of the four compounds studied here when used in the DSSCs in combination with TiO_2 . Bar diagrams corresponding to the computed values of (a) full width at half maximum (FWHM) of the LUMO of the dye molecules when adsorbed on TiO_2 , (b) coefficient of injection (C_{inj}), (c) electron-hole separation (EHS), (d) $C_{inj} \times EHS$ and (e) difference of dipole moments correspondin to LUMO and HOMO ($\Delta\mu$).

the positions of the charge centers corresponding to the LUMO and the HOMO. Previously, the practice has been to calculate the EHS between the ground state, and the excited state,[8] but the assumption explained above, relieves us from the computationally expensive excited states calculation. Thus, the EHS is given by:

$$EHS = \frac{\int \mathbf{r} \rho^{LUMO}(\mathbf{r}) d\mathbf{r}}{\int \rho^{LUMO}(\mathbf{r}) d\mathbf{r}} - \frac{\int \mathbf{r} \rho^{HOMO}(\mathbf{r}) d\mathbf{r}}{\int \rho^{HOMO}(\mathbf{r}) d\mathbf{r}}. \quad (4.3)$$

where \mathbf{r} is the position coordinate, and $\rho^{LUMO}(\mathbf{r})$ and $\rho^{HOMO}(\mathbf{r})$ are the charge densities corresponding to the energies of the LUMO and HOMO, respectively. We have plotted $\rho^{LUMO}(\mathbf{r})$ and $\rho^{HOMO}(\mathbf{r})$ for all the dye molecules in Fig. 4.6. As mentioned above, a simple visual examination reveals that for **4b**, the charge density corresponding to the HOMO of the molecule is mostly on the C atoms of the BODIPY core, whereas for the others it is spread throughout the molecule. On the other hand, for **3c** the charge

densities corresponding to the LUMO of the molecules extend on the bithiophenyl group, away from the surface. These observations already hint that the *EHS* may be the shortest for **4b** and longest for **3c**. These conclusions are confirmed by the quantitative results for the *EHS* plotted in Fig. 4.7(c). As pointed out above, the presence of the large bithiophenyl group in **3c** is probably responsible for its large value of the *EHS*.

We note that both the descriptors, C_{inj} and *EHS* affect the efficiency of the dye for DSSC applications by taking care of different aspects of the electronic structure of the dye + TiO₂ system. In order to simultaneously incorporate the contributions of both the descriptors, we have plotted in Fig. 4.7(d) the values of a composite descriptor $C_{\text{inj}} \times \text{EHS}$ for the four dye molecules. It is evident that upon considering both charge injection and *EHS*, **3c** appears to be the optimal candidate for use in DSSCs among all four compounds considered in this section. This is primarily because of the fact that the *EHS* is significantly larger in **3c** than for the other three compounds.

Another descriptor that can provide considerable insight into the performance of the dye molecule as the sensitizer in the solar cell is $\Delta\boldsymbol{\mu}$, the difference in the dipole moment between the HOMO and the LUMO of the dye on TiO₂. The magnitude of this vectorial quantity provides an indication of the probability of the excitation of an electron from the HOMO to the LUMO upon absorption of light, while its direction tells us about the spatial direction of charge transfer upon the excitation. It is given by Eq. (4.4) as follows:

$$\Delta\boldsymbol{\mu} = \boldsymbol{\mu}_{\text{LUMO}} - \boldsymbol{\mu}_{\text{HOMO}},$$

where

$$\boldsymbol{\mu}_s = - \int \mathbf{r} \rho_s(\mathbf{r}) d\mathbf{r} + e \sum_i Z_i \mathbf{r}_i. \quad (4.4)$$

Here, ρ_s is the electronic density in the state s , integrated over an energy window corresponding to the FWHM of state s . Z_i and \mathbf{r}_i are the ionic charge and position

of the i th atom, and e is the unit of electronic charge. In Fig. 4.7(e), we have plotted the values of $\Delta\mu$ for the four compounds, along with figures showing the magnitude and direction of $\Delta\mu$. We note that once again compound **3c** appears to show the optimal features, in that it possesses the highest value of $\Delta\mu$.

Thus using the descriptors $C_{\text{inj}} \times EHS$ and $\Delta\mu$, we incorporate all the factors affecting the effective electronic communication between the dye and the substrate, and conclude that **3c** is the best candidate dye for use in DSSCs.

4.6 Conclusions

We have studied a series of benzo-BODIPY derivatives having phenyl, thiophenyl or bithiophenyl meso-substituents, as candidate dye molecules for potential use in DSSCs. Based on DFT calculations, we found that the dye molecules attach on TiO_2 with a sesquidentate anchoring mode. We observed the same trends in the position (in energy) of their frontier orbitals and in the values of their energy gaps as those obtained from the experiment, upon making the various substitutions, which confirmed the reliability of the calculations. To find the most favorable dye having an effective electronic communication with the TiO_2 substrate, we considered a combination of several factors, viz., efficient charge injection to TiO_2 , the good electron-hole separation and the large change in the dipole moment upon the excitation. Based on these factors we computed a set of descriptors which suggested that the benzo-BODIPY derivatives bearing the bithiophenyl meso-substituents should be the optimal dye sensitizer for the DSSCs among all molecules studied herein.

Bibliography

- [1] J. Songkhao, R. Banerjee, S. Debnath, S. Narasimhan, N. Wannaprom, P. Vanalabhatana, N. Seriani, R. Gebauer, and P. Thamyongkit, "Structure-property relationship of π -extended boron-dipyrromethene derivatives towards optoelectronic applications," *Dyes and Pigments*, vol. 142, pp. 558 – 571, 2017.

-
- [2] J. Gong, J. Liang, and K. Sumathy, “Review on dye-sensitized solar cells (DSSCs): Fundamental concepts and novel materials,” *Renewable and Sustainable Energy Reviews*, vol. 16, no. 8, pp. 5848 – 5860, 2012.
- [3] K. Sharma, V. Sharma, and S. S. Sharma, “Dye-sensitized solar cells: Fundamentals and current status,” *Nanoscale Research Letters*, vol. 13, p. 381, Nov 2018.
- [4] N. Prachumrak, T. Sudyoadsuk, A. Thangthong, P. Nalaoh, S. Jungsuttiwong, R. Daengngern, S. Namuangruk, P. Pattanasattayavong, and V. Promarak, “Improvement of D π A organic dye-based dye-sensitized solar cell performance by simple triphenylamine donor substitutions on the -linker of the dye,” *Mater. Chem. Front.*, vol. 1, pp. 1059–1072, 2017.
- [5] M. Pastore and F. De Angelis, “Aggregation of organic dyes on TiO₂ in dye-sensitized solar cells models: An ab initio investigation,” *ACS Nano*, vol. 4, no. 1, pp. 556–562, 2010.
- [6] M. Pastore and F. De Angelis, “Computational modelling of tio2 surfaces sensitized by organic dyes with different anchoring groups: adsorption modes, electronic structure and implication for electron injection/recombination,” *Phys. Chem. Chem. Phys.*, vol. 14, pp. 920–928, 2012.
- [7] T. Le Bahers, F. Labat, T. Pauport, P. P. Lain, and I. Ciofini, “Theoretical procedure for optimizing dye-sensitized solar cells: From electronic structure to photovoltaic efficiency,” *Journal of the American Chemical Society*, vol. 133, no. 20, pp. 8005–8013, 2011.
- [8] I. Ciofini, T. Le Bahers, C. Adamo, F. Odobel, and D. Jacquemin, “Through-space charge transfer in rod-like molecules: Lessons from theory,” *The Journal of Physical Chemistry C*, vol. 116, no. 22, pp. 11946–11955, 2012.

- [9] D.-Y. Chen, Y.-Y. Hsu, H.-C. Hsu, B.-S. Chen, Y.-T. Lee, H. Fu, M.-W. Chung, S.-H. Liu, H.-C. Chen, Y. Chi, and P.-T. Chou, "Organic dyes with remarkably high absorptivity; all solid-state dye sensitized solar cell and role of fluorine substitution," *Chem. Commun.*, vol. 46, pp. 5256–5258, 2010.
- [10] T. Le Bahers, F. Labat, T. Pauport, and I. Ciofini, "Effect of solvent and additives on the open-circuit voltage of ZnO-based dye-sensitized solar cells: a combined theoretical and experimental study," *Phys. Chem. Chem. Phys.*, vol. 12, pp. 14710–14719, 2010.
- [11] S. Kim, J. K. Lee, S. O. Kang, J. Ko, J.-H. Yum, S. Fantacci, F. De Angelis, D. Di Censo, and M. Grätzel, "Molecular engineering of organic sensitizers for solar cell applications," *J. Am. Chem. Soc.*, vol. 128, no. 51, pp. 16701–16707, 2006.
- [12] M. Katono, M. Wielopolski, M. Marszalek, T. Bessho, J.-E. Moser, R. Humphry-Baker, S. M. Zakeeruddin, and M. Grätzel, "Effect of extended π -conjugation of the donor structure of organic dyes on the photovoltaic performance of dye-sensitized solar cells," *J. Phys. Chem. C*, vol. 118, no. 30, pp. 16486–16493, 2014.
- [13] A. Loudet and K. Burgess, "Bodipy dyes and their derivatives: syntheses and spectroscopic properties," *Chem. Rev.*, vol. 107, pp. 4891–4932, 2007.
- [14] S. Hattori, K. Ohkubo, Y. Urano, H. Sunahara, T. Nagano, Y. Wada, N. V. Tkachenko, H. Lemmetyinen, and S. Fukuzumi, "Charge separation in a nonfluorescent donor-acceptor dyad derived from boron dipyrromethene dye, leading to photocurrent generation," *The Journal of Physical Chemistry B*, vol. 109, no. 32, pp. 15368–15375, 2005.

- [15] T. Rousseau, A. Cravino, T. Bura, G. Ulrich, R. Ziessel, and J. Roncali, "Multi-donor molecular bulk heterojunction solar cells: improving conversion efficiency by synergistic dye combinations," *J. Mater. Chem.*, vol. 19, pp. 2298–2300, 2009.
- [16] B. Kim, B. Ma, V. R. Donuru, H. Liu, and J. M. J. Frchet, "Bodipy-backboned polymers as electron donor in bulk heterojunction solar cells," *Chem. Commun.*, vol. 46, pp. 4148–4150, 2010.
- [17] S. Kolemen, O. A. Bozdemir, Y. Cakmak, G. Barin, S. Erten-Ela, M. Marszalek, J.-H. Yum, S. M. Zakeeruddin, M. K. Nazeeruddin, M. Grtzel, and E. U. Akkaya, "Optimization of distyryl-Bodipy chromophores for efficient panchromatic sensitization in dye sensitized solar cells," *Chem. Sci.*, vol. 2, pp. 949–954, 2011.
- [18] H. Lepidi, A. Benoliel, J. Mege, P. Bongrand, and C. Capo, "Double localization of F-actin in chemoattractant-stimulated polymorphonuclear leucocytes," *Journal of Cell Science*, vol. 103, no. 1, pp. 145–156, 1992.
- [19] J.-S. Lee, N.-y. Kang, Y. K. Kim, A. Samanta, S. Feng, H. K. Kim, M. Vendrell, J. H. Park, and Y.-T. Chang, "Synthesis of a BODIPY library and its application to the development of live cell glucagon imaging probe," *Journal of the American Chemical Society*, vol. 131, no. 29, pp. 10077–10082, 2009.
- [20] J. Rosenthal and S. J. Lippard, "Direct detection of nitroxyl in aqueous solution using a tripodal copper(ii) BODIPY complex," *Journal of the American Chemical Society*, vol. 132, no. 16, pp. 5536–5537, 2010.
- [21] X. Song and B. I. Swanson, "Rational design of an optical sensing system for multivalent proteins," *Langmuir*, vol. 15, no. 14, pp. 4710–4712, 1999.
- [22] Z. Ekmekci, M. D. Yilmaz, and E. U. Akkaya, "A monostyryl-boradiazaindacene (BODIPY) derivative as colorimetric and fluorescent probe for cyanide ions," *Organic Letters*, vol. 10, no. 3, pp. 461–464, 2008.

- [23] L.-Y. Niu, Y.-S. Guan, Y.-Z. Chen, L.-Z. Wu, C.-H. Tung, and Q.-Z. Yang, “BODIPY-based ratiometric fluorescent sensor for highly selective detection of glutathione over cysteine and homocysteine,” *Journal of the American Chemical Society*, vol. 134, no. 46, pp. 18928–18931, 2012.
- [24] S. T. Manjare, J. Kim, Y. Lee, and D. G. Churchill, “Facile meso-BODIPY annulation and selective sensing of hypochlorite in water,” *Organic Letters*, vol. 16, no. 2, pp. 520–523, 2014.
- [25] R. Y. Lai and A. J. Bard, “Electrogenerated chemiluminescence 71. photophysical, electrochemical, and electrogenerated chemiluminescent properties of selected dipyrrometheneBF₂ dyes,” *The Journal of Physical Chemistry B*, vol. 107, no. 21, pp. 5036–5042, 2003.
- [26] M. Ortiz, I. Garcia-Moreno, A. Agarrabeitia, G. Duran-Sampedro, A. Costela, R. Sastre, F. Lpez Arbeloa, J. Baelos Prieto, and I. Lpez Arbeloa, “Red-edge-wavelength finely-tunable laser action from new BODIPY dyes,” *Physical chemistry chemical physics : PCCP*, vol. 12, p. 78047811, July 2010.
- [27] D. Zhang, V. Martn, I. Garca-Moreno, A. Costela, M. E. Prez-Ojeda, and Y. Xiao, “Development of excellent long-wavelength BODIPY laser dyes with a strategy that combines extending -conjugation and tuning ICT effect,” *Phys. Chem. Chem. Phys.*, vol. 13, pp. 13026–13033, 2011.
- [28] J. Roncali, “Synthetic principles for bandgap control in linear -conjugated systems,” *Chemical Reviews*, vol. 97, no. 1, pp. 173–206, 1997.
- [29] J. Roncali, “Linear -conjugated systems derivatized with c60-fullerene as molecular heterojunctions for organic photovoltaics,” *Chem. Soc. Rev.*, vol. 34, pp. 483–495, 2005.
- [30] T. Rousseau, A. Cravino, E. Ripaud, P. Leriche, S. Rihn, A. De Nicola, R. Ziessel, and J. Roncali, “A tailored hybrid BODIPYoligothiophene donor for molecular

- bulk heterojunction solar cells with improved performances,” *Chem. Commun.*, vol. 46, pp. 5082–5084, 2010.
- [31] T. Bura, N. Leclerc, S. Fall, P. Lvque, T. Heiser, P. Retailleau, S. Rihn, A. Mir-loup, and R. Ziessel, “High-performance solution-processed solar cells and ambipo-lar behavior in organic field-effect transistors with thienyl-BODIPY scaffoldings,” *Journal of the American Chemical Society*, vol. 134, no. 42, pp. 17404–17407, 2012.
- [32] A. C. Benniston, S. Clift, and A. Harriman, “Intramolecular charge-transfer interactions in a julolidineBodipy molecular assembly as revealed via ^{13}C NMR chemical shifts,” *Journal of Molecular Structure*, vol. 985, no. 2, pp. 346 – 354, 2011.
- [33] P. Giannozzi, S. Baroni, N. Bonini, M. Calandra, R. Car, C. Cavazzoni, D. Ceresoli, G. L. Chiarotti, M. Cococcioni, I. Dabo, A. D. Corso, S. de Gironcoli, S. Fabris, G. Fratesi, R. Gebauer, U. Gerstmann, C. Gougoussis, A. Kokalj, M. Lazzeri, L. Martin-Samos, N. Marzari, F. Mauri, R. Mazzarello, S. Paolini, A. Pasquarello, L. Paulatto, C. Sbraccia, S. Scandolo, G. Sclauzero, A. P. Seitso-nen, A. Smogunov, P. Umari, and R. M. Wentzcovitch, “QUANTUM ESPRESSO: a modular and open-source software project for quantum simulations of materials,” *Journal of Physics: Condensed Matter*, vol. 21, p. 395502, sep 2009.
- [34] D. Vanderbilt, “Soft self-consistent pseudopotentials in a generalized eigenvalue formalism,” *Phys. Rev. B*, vol. 41, pp. 7892–7895, Apr 1990.
- [35] J. P. Perdew, K. Burke, and M. Ernzerhof, “Generalized gradient approximation made simple,” *Phys. Rev. Lett.*, vol. 77, pp. 3865–3868, Oct 1996.
- [36] S. Grimme, “Accurate description of van der Waals complexes by density func-tional theory including empirical corrections,” *Journal of Computational Chem-istry*, vol. 25, no. 12, pp. 1463–1473, 2004.

- [37] S. Grimme, "Semiempirical GGA-type density functional constructed with a long-range dispersion correction," *Journal of Computational Chemistry*, vol. 27, no. 15, pp. 1787–1799, 2006.
- [38] P. Chen, J. H. Yum, F. D. Angelis, E. Mosconi, S. Fantacci, S.-J. Moon, R. H. Baker, J. Ko, M. K. Nazeeruddin, and M. Grtzel, "High open-circuit voltage solid-state dye-sensitized solar cells with organic dye," *Nano Letters*, vol. 9, no. 6, pp. 2487–2492, 2009.
- [39] A. Vittadini, A. Selloni, F. P. Rotzinger, and M. Grtzel, "Formic acid adsorption on dry and hydrated TiO₂ anatase (101) surfaces by dft calculations," *The Journal of Physical Chemistry B*, vol. 104, no. 6, pp. 1300–1306, 2000.
- [40] H. Tian, X. Yang, R. Chen, R. Zhang, A. Hagfeldt, and L. Sun, "Effect of different dye baths and dye-structures on the performance of dye-sensitized solar cells based on triphenylamine dyes," *The Journal of Physical Chemistry C*, vol. 112, no. 29, pp. 11023–11033, 2008.
- [41] M. Pastore and F. De Angelis, "Computational modeling of stark effects in organic dye-sensitized TiO₂ heterointerfaces," *The Journal of Physical Chemistry Letters*, vol. 2, no. 11, pp. 1261–1267, 2011.
- [42] D. P. Hagberg, T. Marinado, K. M. Karlsson, K. Nonomura, P. Qin, G. Boschloo, T. Brinck, A. Hagfeldt, and L. Sun, "Tuning the HOMO and LUMO energy levels of organic chromophores for dye sensitized solar cells," *The Journal of Organic Chemistry*, vol. 72, no. 25, pp. 9550–9556, 2007.
- [43] H. Cheema, A. Islam, L. Han, and A. El-Shafei, "Monodentate pyrazole as a replacement of labile NCS for Ru (ii) photosensitizers: Minimum electron injection free energy for dye-sensitized solar cells," *Dyes and Pigments*, vol. 120, pp. 93 – 98, 2015.

- [44] B.-S. Chen, K. Chen, Y.-H. Hong, W.-H. Liu, T.-H. Li, C.-H. Lai, P.-T. Chou, Y. Chi, and G.-H. Lee, “Neutral, panchromatic Ru(ii) terpyridine sensitizers bearing pyridine pyrazolate chelates with superior DSSC performance,” *Chem. Commun.*, pp. 5844–5846, 2009.
- [45] N. Kaneza, J. Zhang, H. Liu, P. S. Archana, Z. Shan, M. Vasiliu, S. H. Polansky, D. A. Dixon, R. E. Adams, R. H. Schmehl, A. Gupta, and S. Pan, “Electrochemical and spectroscopic properties of boron dipyrromethenethiophenetriphenylamine-based dyes for dye-sensitized solar cells,” *The Journal of Physical Chemistry C*, vol. 120, no. 17, pp. 9068–9080, 2016.
- [46] F. Ambrosio, N. Martsinovich, and A. Troisi, “What is the best anchoring group for a dye in a dye-sensitized solar cell?,” *The Journal of Physical Chemistry Letters*, vol. 3, no. 11, pp. 1531–1535, 2012.
- [47] T. Le Bahers, C. Adamo, and I. Ciofini, “A qualitative index of spatial extent in charge-transfer excitations,” *Journal of Chemical Theory and Computation*, vol. 7, no. 8, pp. 2498–2506, 2011.
- [48] W. Keawsongsaeng, J. Gasiorowski, P. Denk, K. Oppelt, D. H. Apaydin, R. Romanathanes, K. Hingerl, M. Scharber, N. S. Sariciftci, and P. Thamyongkit, “Systematic investigation of porphyrin-thiophene conjugates for ternary bulk heterojunction solar cells,” *Advanced Energy Materials*, vol. 6, no. 20, p. 1600957, 2016.
- [49] H. Gerischer and F. Willig, “Reaction of excited dye molecules at electrodes,” in *Physical and Chemical Applications of Dyestuffs* (F. P. Schäfer, H. Gerischer, F. Willig, H. Meier, H. Jahnke, M. Schönborn, and G. Zimmermann, eds.), (Berlin, Heidelberg), pp. 31–84, Springer Berlin Heidelberg, 1976.
- [50] H. Gerischer, “Charge transfer processes at semiconductor-electrolyte interfaces

in connection with problems of catalysis,” *Surface Science*, vol. 18, no. 1, pp. 97 – 122, 1969.

- [51] P. Umari, L. Giacomazzi, F. De Angelis, M. Pastore, and S. Baroni, “Energy-level alignment in organic dye-sensitized TiO₂ from gw calculations,” *The Journal of Chemical Physics*, vol. 139, no. 1, p. 014709, 2013.

Chapter 5

Magnetic and structural phase transitions in Fe thin films on Ir(001)

In this chapter, we study the thickness-dependent magnetic and structural phase transitions in Fe/Ir(001) systems. Experiments done on the layer-by-layer growth of Fe on Ir(001), in the group of Prof. PS Anil Kumar at the Indian Institute of Science, Bangalore, show a magnetic transition in the Fe films beyond a certain thickness. Using DFT calculations, we confirm the existence of such a transition, and attempt to gain insight into the driving force for such a transition. We will show that our results on the changes in structural and elastic properties with increase in Fe film thickness agree well also with cantilever stress measurements done in previous experimental studies.^[1]

5.1 Introduction

The structure and magnetic properties of thin films are known to be different from their bulk counterparts. The growth, structure and magnetic properties of ferromagnetic thin films on nonmagnetic substrates are important to understand for

applications in magnetic devices such as giant magnetoresistance (GMR), tunnel magnetoresistance (TMR), magnetic random access memory (MRAM), etc.[2] Pseudomorphic growth, i.e., the epitaxial growth of films with the same in-plane lattice parameter as that of the substrate, allows investigation of strain effects resulting from the epitaxial misfit between the lattice constants of the film and the substrate.

The in-plane lattice parameter of Ir(001) [$a_{||} = a(\text{Ir})/\sqrt{2} = 2.72 \text{ \AA}$] lies in between that of body centered cubic (bcc)-Fe ($= 2.87 \text{ \AA}$) and face centered cubic (fcc)-Fe ($= 2.53 \text{ \AA}$),[1] making Ir(001) an interesting substrate for the epitaxial growth of Fe thin films, on a fcc(001) substrate. Although a lot of theoretical and experimental investigations have been done on the Fe/Ir(001) system,[1, 3–8] the evolution of structure and magnetism of Fe on Ir(001), during layer-by-layer growth, is still a matter for debate. Experiments by Andrieu *et al.*,[5] suggested a body centered tetragonal (bct) phase up to 5 monolayers (ML), and a bcc phase for larger thicknesses. But they did not find any correlation between structure and magnetism of Fe on Ir(001), during its growth. A high resolution transmission electron microscopy study by Snoeck *et al.* also suggested the existence of a bct phase up to 5 ML.[9] For thicker layers they suggested a bct phase near the Fe/Ir interface, and a bcc phase away from it. Recent studies by Martin *et al.*, through strain measurement along with quantitative LEED and STM analysis, reported that the first two monolayers (MLs) of Fe on Ir(001) grow as face-centered tetragonal (fct), 3 to 10 ML grow as bct on the fct precursor, and 11 ML onwards grow as bcc.[1]

In terms of magnetic behavior, bcc Fe is ferromagnetic (FM),[10] whereas fcc Fe exhibits varied magnetic states, such as nonmagnetic (NM), low spin ferromagnetic (LSFM), high spin ferromagnetic (HSFM), and antiferromagnetic (AFM) based on magnetovolume energy dependence on lattice parameters.[5, 11–14] Theoretical calculations on free-standing Fe, have shown thickness dependent FM and AFM solutions; a monolayer of Fe has been shown to be ferromagnetic, but for a bilayer, a competition between FM and AFM configurations has been found.[15, 16] It has

been reported that bct Fe on Ir(001) exhibits low spin ferromagnetism below 5 ML with 2 dead layers.[6, 7] Theoretical calculations by Louzana *et al.* have shown a monolayer of Fe on Ir(001) to be ferromagnetic, however interlayer coupling for 2-3 ML has been found to be AFM along with intralayer FM coupling.[17] Calculations by Hamad *et al.* reported that 1 ML Fe on Ir(001) has a FM configuration, whereas the ground state of 3-4 ML bct Fe can be ferrimagnetic (FiM) or FM, and 5 ML onwards FM ordering starts.[18, 19] Theoretical calculations for noncollinear magnetism of Fe ultra-thin films on Ir(001), based on spin-cluster expansion technique in combination with the relativistic disordered local moment scheme, by Deák *et al.* have suggested the presence of a spin spiral for two monolayers, and noncollinear spin structure with nonzero net magnetization for four monolayers.[20]

The absence of a conclusive understanding of the structure and magnetic ordering of the growth of Fe on Ir(001) has motivated us to perform further experimental and theoretical studies on this system. Our experimental collaborators have grown Fe on Ir(001) pseudomorphically, and studied the structure and magnetic behavior layer by layer, using medium energy electron diffraction (MEED) and magneto-optic Kerr effect (MOKE) measurements. We have performed density functional theory (DFT) calculations on up to 14 ML of Fe on Ir(001) to understand the evolution of structure and preferred magnetic ordering with increase in the number of ML of Fe grown on Ir(001). The theoretical results agree well with the experimental data as we will show further below.

5.2 Recent experimental results

Recently our experimental collaborators in the group of Prof. P S Anil Kumar have performed experiments on the layer-by-layer growth of Fe on Ir(001). The details of the experimental methods and results can be found in the PhD thesis of Pradeep A. V.[21] In order to investigate the magnetic ordering of the Fe/Ir(001) system, they have performed magneto optic Kerr effect (MOKE) measurements on

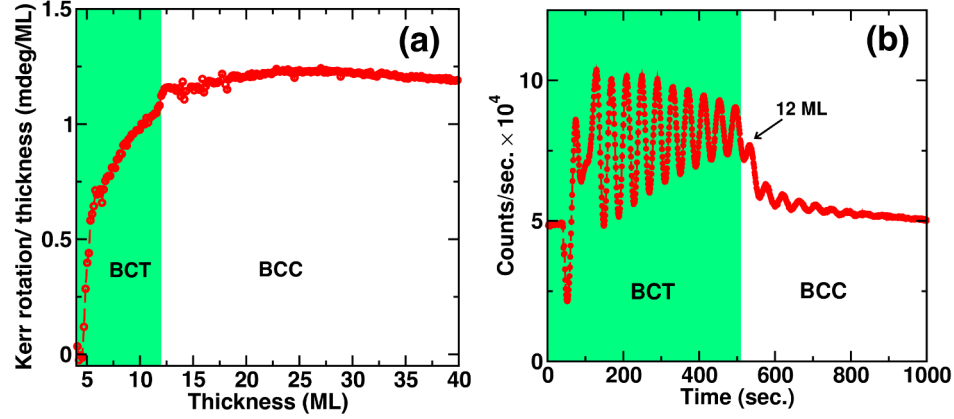


Figure 5.1: Experimental results showing (a) MEED oscillations and (b) Kerr rotation as a function of film thickness for Fe/Ir(001). The sudden decrease in the amplitude of the MEED oscillation signifies a bct to bcc transition beyond 11 MLs of Fe on Ir(001). The non-zero Kerr rotation beyond 4.5 MLs, denotes a *FM* magnetic ordering. Beyond 12 MLs, the Kerr rotation more or less saturates indicating a bulk bcc-Fe phase. Experimental data courtesy of Pradeep A V and PS Anil Kumar.

the layer-by-layer growth of Fe. In Fig. 5.1(a) the plot of Kerr rotation per unit thickness as a function of Fe thickness is shown. A non-zero Kerr rotation is observed beyond 4.5 ML, indicating the onset of ferromagnetic ordering. It is pointed out that the blips present in the MOKE data for small thickness (< 4 ML) are due to mechanical movements of the detector stage, and are magnified for smaller thickness due to normalization by small number of ML. The intensity of MEED oscillations is used to observe the growth and thickness of the Fe films on the Ir(001)-(1 \times 1) surface as shown in Fig. 5.1(b), where each peak of the sinusoidal oscillations signifies the growth of an additional Fe ML. A sudden decrease in the amplitude of the oscillations is observed between 11 ML and 13 ML, which points towards the end of the region of pseudomorphic growth and the beginning of the growth of strain-relaxed bcc Fe. The possibility of the presence of a bct to bcc transition between 11 ML and 13 ML, is expressed by a green background up to 12 ML, indicating the bct phase.

Motivated by the above experimental observations, we will perform density functional theory calculations on the Fe/Ir(001) system to address the following questions: (1) is there a magnetic transition as a function of layer thickness? (2) is there a

structural transition as a function of layer thickness? (3) at what film thicknesses do these transitions occur?

5.3 Systems studied

The Fe/Ir(001) systems are modeled by varying the number of Fe layers (1 – 14 ML) over the Ir(001) substrate. For 1 – 6 ML of Fe, the Ir substrate is modeled by a slab containing 6 ML of Ir, whereas for Fe films with thickness > 6 ML, 12 ML of Ir are used. The Ir(001) substrate has a face-centered cubic (ABAB...) stacking along the [001] direction, and a $\sqrt{2} \times \sqrt{2}$ surface cell with in-plane lattice constant $a_{||}$. Here, $a_{||}$ is equal to $a_{\text{Ir}}^{\text{Bulk}}/\sqrt{2}$, where $a_{\text{Ir}}^{\text{Bulk}}$ is the bulk lattice constant of Ir. This choice of unit cell means that there are two atoms per layer in the unit cell. For all the calculations, we fix the three bottommost layers of Ir at the bulk interlayer separation along [001], while the remaining layers are allowed to relax during the structural optimization. To mimic the pseudomorphic growth of Fe films over Ir(001), the in-plane lattice constant for the Fe layers is kept the same as that of the Ir layers. As discussed further below, as a result, the Fe layers experience a biaxial compressive strain, due to the lattice mismatch between Ir and Fe.

In order to compare the energetics of the various magnetic configurations, we have studied nonmagnetic (*NM*), ferromagnetic (*FM*) and antiferromagnetic (*AFM*) cases in each Fe/Ir(001) system. For the *AFM* cases, different spin configurations, with zero total magnetic moment, are considered. As an illustration, we schematically depict the various *AFM* configurations considered for the 2 ML Fe/Ir (001) system in Fig. 5.2. In the *AFM*₁ and *AFM*₂ configurations, the sum total of the magnetic moments for each layer is zero. However, for *AFM*₃, the spins are coupled ferromagnetically within a layer, but antiferromagnetically between neighboring layers. When the number of Fe layers is > 2 , similar kinds of spin alignments are considered, with the ABAB... stacking maintained. Note however that we consider the *AFM*₃ configuration only when we have an even number of Fe overlayers, as otherwise this spin alignment

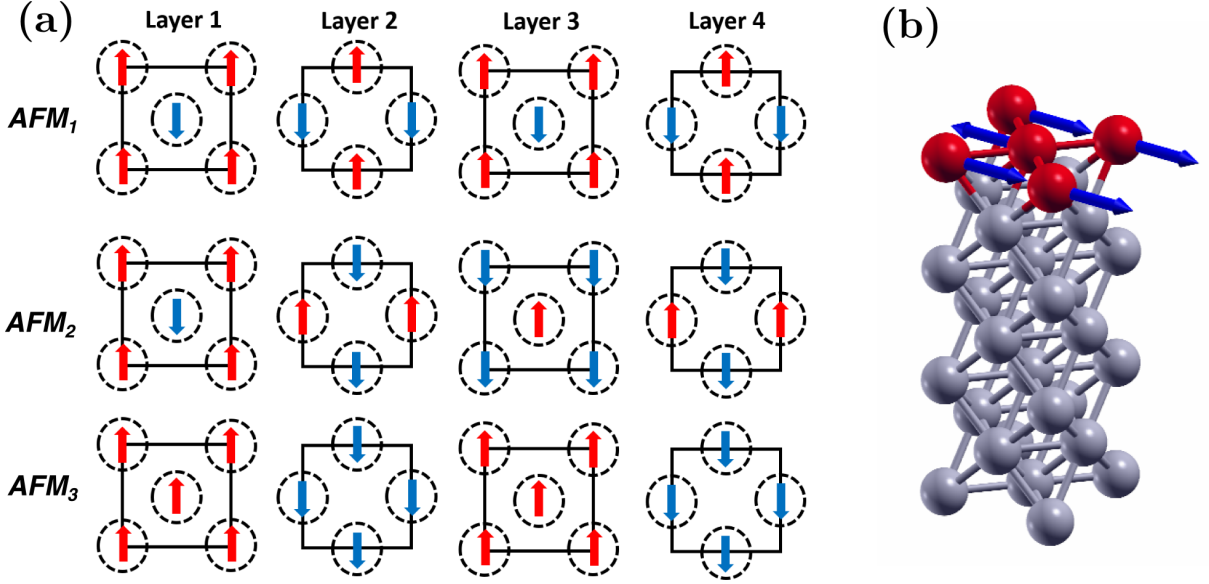


Figure 5.2: Examples of different AFM configurations of the Fe layers considered for DFT calculations are shown in panel (a). Three different *AFM* configurations are considered, and are shown for 1 – 4 ML. Dashed circles denote Fe atoms in the $\sqrt{2} \times \sqrt{2}$ surface cell. Up and down spins are represented by red up and blue down arrows, respectively. The difference between *AFM*₁ and *AFM*₂ configurations can be understood by comparing the spin configurations in layer 1 and 3, in each case. In *AFM*₁, layer 1 and 3 have identical spin configuration, whereas in case of *AFM*₂, in layer 3, up spins of layer 1 is replaced by down spins, and vice versa. *AFM*₃ shows intra-layer *FM* ordering and inter-layer *AFM* ordering. In panel (b), the AFM configuration in the 1Fe/Ir(001) structure is shown. Fe and Ir atoms are shown in red and grey, respectively. The spin orientations are nominally shown to be in-plane, using blue arrows.

cannot lead to a zero total magnetic moment.

5.4 Methods

We have used the Vienna *Ab initio* Simulation Package (VASP) to perform all our density functional theory (DFT) calculations.[22, 23] The electronic wavefunctions are expanded using a plane wave basis set with a cut-off of 360 eV. The exchange-correlation interactions are described using the spin-polarized generalized gradient approximation (GGA), with the Perdew-Burke-Ernzerhof (PBE) functional. [24] To describe the electron-ion interactions, we use the projector augmented wave (PAW) method,[25, 26] which explicitly includes the Fe 3*d* and 4*s* electrons, and the Ir 5*d* and 6*s* electrons, as the valence states. In order to sample the Brillouin zone, we

have used the Monkhorst-Pack scheme.[27] For all our calculations we have used a $16 \times 16 \times 1$ \mathbf{k} -mesh. To avoid interactions between periodic images, a 20 Å vacuum is introduced normal to the surface, in all surface calculations. For all the structural relaxations, a 10^{-3} eV/Å force convergence criterion is used. Using the aforesaid parameters, we obtain the bulk lattice parameters of Ir ($a_{\text{Ir}}^{\text{Bulk}}$) and Fe ($a_{\text{Fe}}^{\text{Bulk}}$) to be 3.89 Å and 2.83 Å, respectively. These values are in excellent agreement with experimental data.[1] Note that this leads to a mismatch of 2.83% between the Fe layers and the Ir substrate.

5.5 Results and Discussion

5.5.1 Magnetic phase transition in Fe thin films on Ir(001)

Table 5.1: Magnetic configurations and the energy differences with respect to the lowest energy configuration (ΔE), for 1 – 6 ML Fe on Ir(001).

Structures	ΔE (eV)				
	AFM_1	AFM_2	AFM_3	FM	NM
1Fe/Ir(001)	0	–	–	0.38	1.25
2Fe/Ir(001)	0.00011	0	0.55	0.41	1.64
3Fe/Ir(001)	1.13	0	–	1.55	2.46
4Fe/Ir(001)	0.21	0	2.49	1.46	2.56
5Fe/Ir(001)	1.49	1.40	–	0	3.96
6Fe/Ir(001)	3.96	4.38	4.74	0	5.54

As mentioned in Section 5.3, we have considered different magnetic configurations for each thickness of Fe film deposited on Ir (001). For each of these systems, we have calculated the energy difference (ΔE) with respect to the corresponding lowest energy configuration. In Table 5.1, we tabulate the ΔE for 1 – 6 ML of Fe on Ir(001). The energy difference per Fe atom, of the AFM , and the FM configurations for 1 – 6 ML of Fe on Ir(001), have been plotted in Fig. 5.3, where we see that an AFM configuration is energetically favourable for ≤ 4 ML Fe film thickness, whereas from 5 ML onwards, the FM configuration is favoured. Since, for the 1 – 4 ML thickness

of Fe film, the AFM_2 structure is the lowest energy one, and for 1 ML Fe/Ir(100), AFM_1 and AFM_2 structures are identical, we therefore consider the AFM_2 structure for all further comparison and analysis. From now on, we refer to it simply as the AFM configuration. The observed AFM to FM transition is in excellent agreement with the experimental finding, where the non-zero Kerr rotation beyond 4.5 ML suggests a non-ferromagnet up to 4 ML of Fe.

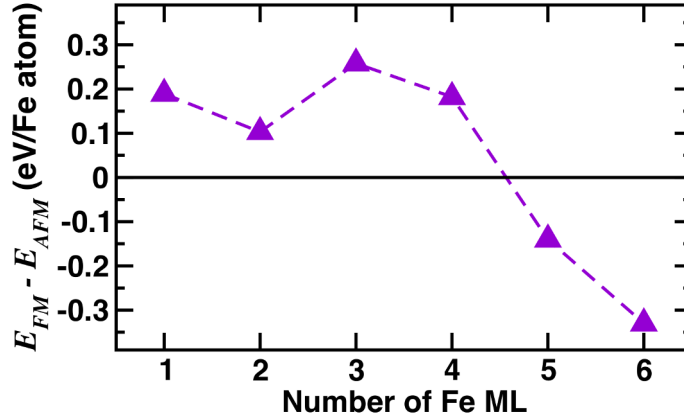


Figure 5.3: Results from DFT calculations for the energy difference between the (lowest energy) AFM and the FM configurations per Fe atom, plotted against the Fe layer thickness. The FM configuration is higher in energy than the AFM configuration for ≤ 4 ML, beyond 4 ML, the FM configuration becomes energetically favorable over the AFM configuration.

The plot in Fig. 5.1(a) showing the experimental result of Kerr rotation per unit thickness as a function of thickness of Fe grown on Ir(001) can be approximately compared to DFT calculated magnetic moment per layer as a function of thickness, as shown in Fig. 5.4(a). The region in blue denotes that for 1 – 4 ML, Fe/Ir(001) prefers AFM ordering with zero net magnetic moment. From 5 ML onwards, the FM ordering is energetically favoured, and is denoted by a blue background. The plot shows that as we move from 5 to 6 ML Fe, the magnetic moment increases a little and then decreases, moving towards the value of $2.16 \mu_B/\text{atom}$, computed for Fe bcc bulk. In order to see the change in the magnetic moment of Fe atoms in the AFM configuration with increasing thickness, in Fig. 5.4(b) we have plotted the magnetic

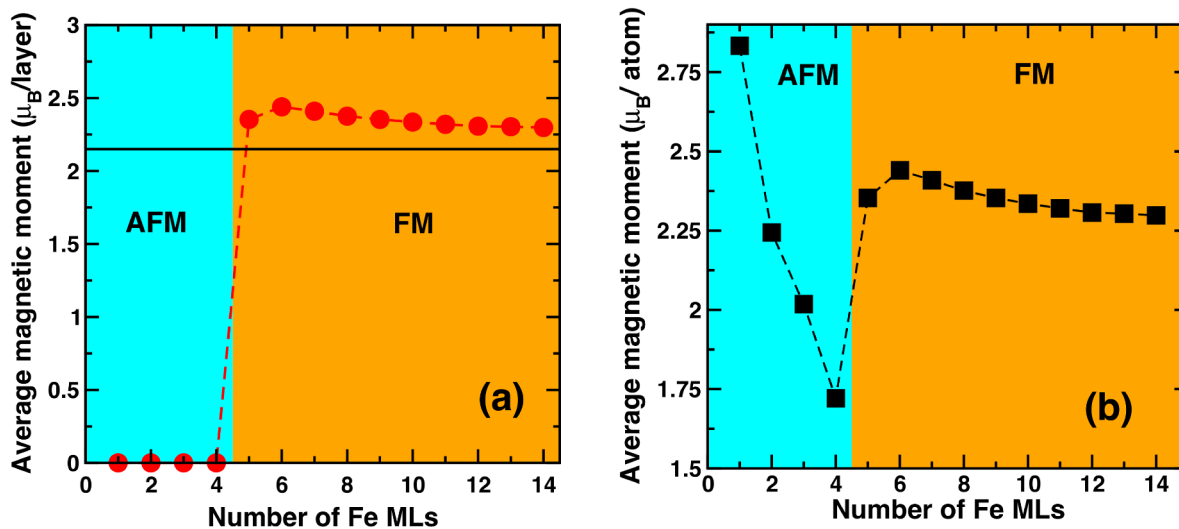


Figure 5.4: DFT results for the evolution of magnetic moments with thickness of the Fe film. Average magnetic moment (μ_B/layer) as a function of Fe layer thickness, is shown in (a). The black line (solid) shows the value of the magnetic moment calculated for Fe BCC bulk. The blue and orange background show, respectively, the regions where *AFM* and *FM* ordering is preferred. Similarly, panel (b) shows average magnetic moment per atom (μ_B/atom), as a function of number of Fe ML.

moment per atom as a function of the thickness of Fe film.

In order to understand the reason behind the *AFM* to *FM* transition beyond 4 ML of Fe on Ir(001), in Fig. 5.5 we plot the projected density of states (per atom) (PDOS) of the Fe-*d* orbitals for 4 ML, 5 ML and 6 ML thick Fe films. In each figure, the plots are arranged in a way such that the topmost panel is the PDOS for the Fe layer (“Layer 1”) at the interface with vacuum. The vertical dashed line at the zero of the x-axis shows the position of the Fermi energy (ϵ_F). The *d*-density of states of the *FM* configurations is represented by brown shaded regions. In the case of the *AFM* configurations, the *d*-density of states of the spin up and down states is represented by solid and broken red lines, respectively. Looking at the PDOS one can clearly see that on going from 4 ML to 5 ML Fe [compare Figs. 5.5 (a) and (b)], there is a sharp splitting of states corresponding to opposite spins, across the Fermi level. This is the exchange splitting, which can be quantified by calculating the difference between the band centers for spin up and spin down states: $\Delta E_{ex} = |\epsilon_{d\uparrow} - \epsilon_{d\downarrow}|$, [28, 29] where the

band center for the d -states (up or down), $\epsilon_{d\sigma}$ is given by the following equation:

$$\epsilon_{d\sigma} = \frac{\int_{\epsilon_{min}}^{\epsilon_{max}} \epsilon g_{d\sigma}(\epsilon) d\epsilon}{\int_{\epsilon_{min}}^{\epsilon_{max}} g_{d\sigma}(\epsilon) d\epsilon}. \quad (5.1)$$

where $g_{d\sigma}(\epsilon)$ is the PDOS of spin up or down d -states. Using Eq. (5.1), the band centers for the d -states of FM configurations of all the systems are plotted in Fig. 5.5, where blue up and down triangles show the band centers for spin up and down states, respectively. In Fig. 5.6 we plot the exchange splitting ΔE_{ex} for 2 – 6 Fe layers on Ir(001). We see that for ≤ 4 ML, $\Delta E_{ex}^{AFM} > \Delta E_{ex}^{FM}$, making the AFM configuration energetically more favourable. Beyond 4 ML, there is a transition, and $\Delta E_{ex}^{FM} > \Delta E_{ex}^{AFM}$, which stabilizes the FM configuration as compared to the corresponding AFM configuration, resulting in the observed AFM to FM transition.

To summarize the results of this section, we have confirmed the magnetic phase transition observed in the experiments, identifying it as an AFM to FM transition, occurring between 4 and 5 ML of Fe/Ir(001), stabilized by the exchange splitting. In the next section, we look into the changes in the structural and elastic properties of the Fe layers, as a function of the layer thickness.

5.6 Structural phases in Fe/Ir(001) system

The in-plane lattice constant of Ir is in between those of bcc-Fe and fcc-Fe, which allows pseudomorphic growth of Fe on Ir. Previous studies show that Fe undergoes structural changes in its layer-by-layer growth on Ir(001).[5, 7, 9] It has been suggested that Fe films begin to grow with the fct structure, and subsequently change to bct, and finally to bcc as the film thickness increases.[1]

Here, we investigate the existence of these different structural phases as a function of film thickness. In order to achieve this goal, we first look at the structural changes, and then see how these structural changes manifest themselves in elastic properties.

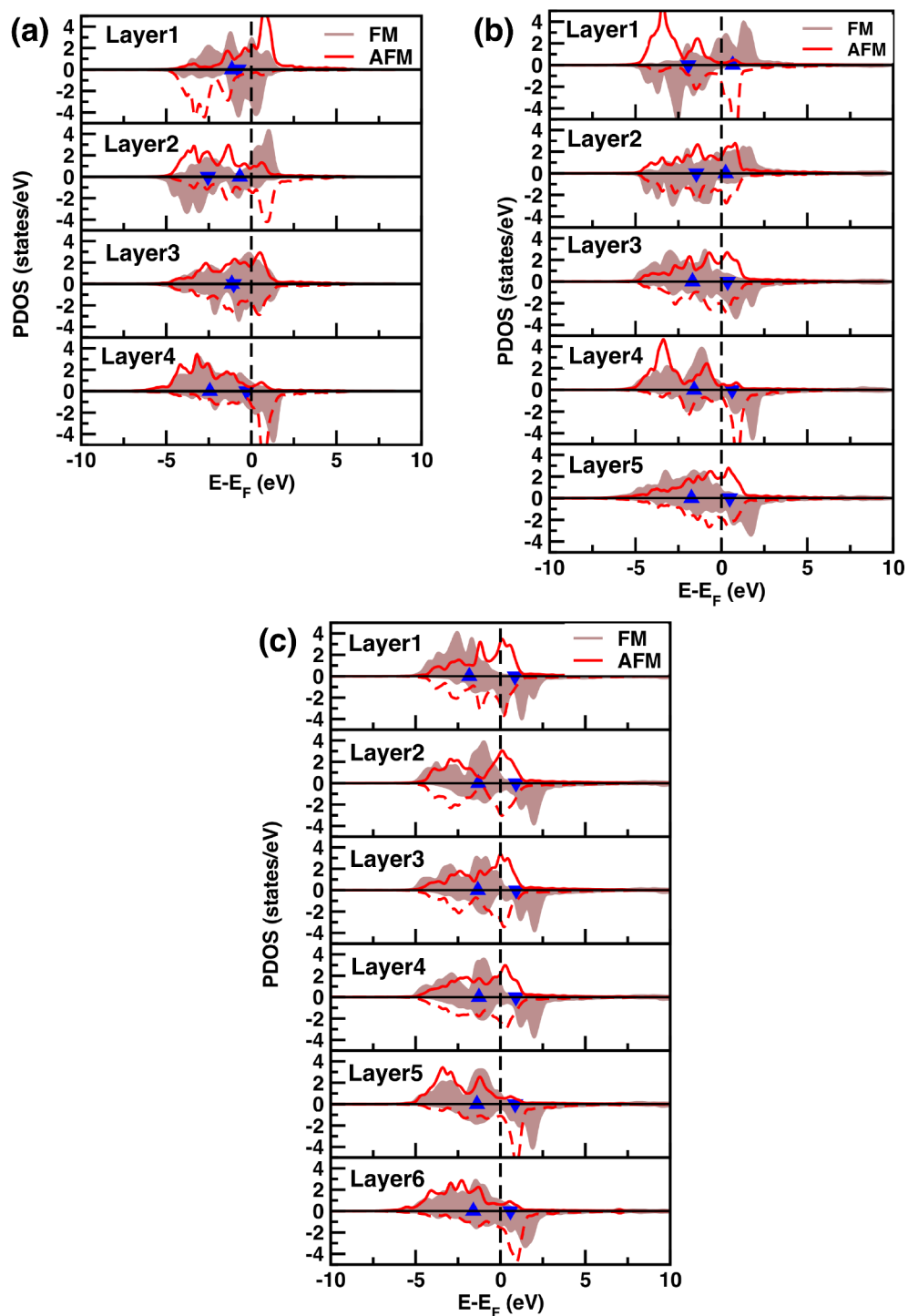


Figure 5.5: Projected density of states (PDOS) per atom, for (a) 4 MLs Fe (b) 5 MLs Fe and (c) 6 MLs Fe films deposited on Ir(001). The blue up and down triangles denote the band centers for the up spin and down spin density of states, respectively, for the FM configuration.

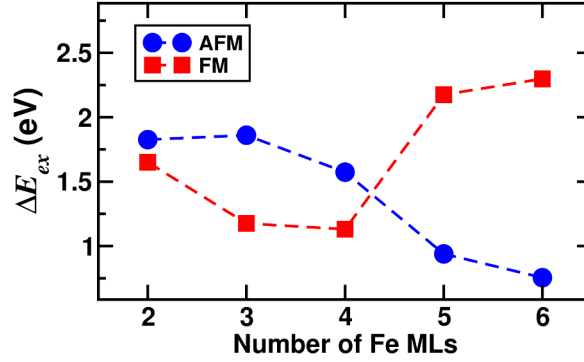


Figure 5.6: Exchange splitting ΔE_{ex} for 2-6 layer Fe/Ir(001). The plots show that the stabilization of *FM* structure over *AFM* structure beyond 4Fe/Ir(001) is due to the increase in ΔE_{ex} , when one goes from 4Fe/Ir(001) to 5Fe/Ir(001).

5.6.1 Structure changes in Fe/Ir(001) as a function of Fe film thickness

We first look at the geometrical parameters of the Fe layers for different film thicknesses. In Fig. 5.7(a) we have plotted the interlayer distances (d_{ij} 's) between the i th and j th Fe layers where the Fe layers are numbered in increasing order from the vacuum toward the interface with Ir. We see that the first two interlayer separations, d_{12} and d_{23} , change only up to film thicknesses of 6 ML. After 6 ML, the d_{12} and d_{23} remain unchanged. This means that as we grow progressively thicker layers of Fe, the effect on the geometry of the Fe/Ir interface decreases, and becomes negligible after 6 ML of Fe grown on Ir(001).

In order to comment further on the structure of the Fe layers, we note that the difference between a bulk bct structure and a bulk fct structure is generally expressed in terms of the difference in the ratio of the out-of-plane and the in-plane lattice constants, c/a . The bct structure is one of the 14 three-dimensional Bravais lattices, unlike the fct structure. However, the fct structure can also be viewed as a bct structure, as is illustrated in Fig. 5.7(a). Here, for $c/a = 1$, we have a bcc structure, and for $c/a = \sqrt{2}$ we have the fcc structure. Thus the larger the deviation of c/a from 1.0, the more that we can say that we have gone away from a bcc structure

towards a fcc structure, or we can alternatively say that we are progressing from a bct to fct structure.

To observe changes in the c/a ratio, in Fig. 5.7(b) we plot the c/a ratio averaged over the number of Fe layers in the entire Fe film, $(c/a)_{\text{avg}}$, as a function of the Fe film thickness. We see that $(c/a)_{\text{avg}}$ increases up to 6 ML, and then there is a monotonic decrease. This decrease in $(c/a)_{\text{avg}}$ is due to two reasons: (i) the absence of the Fe/Ir interface effect beyond 6 ML, as shown in Fig. 5.7(a) and as has already been discussed above, and (ii) an increase in the number of Fe layers in the middle (away from surface and Fe/Ir interface), that have the same (small) interlayer separation. The combination of these two factors leads to a decrease in the c/a ratio when averaged over an increasing number of Fe layers. The monotonic decrease in the $(c/a)_{\text{avg}}$ towards 1.0, suggests that beyond 6 ML, Fe on Ir(001) has a bct structure.

The structural changes discussed above give rise to changes in elastic properties as discussed further below.

5.6.2 Structural changes manifested in elastic properties

Fe thin films grown on a fcc substrate exhibit structural change depending on the strain, film thickness, and temperature.[30] Cantilever stress measurements done by Martin *et al.* suggest that the first two layers of Fe grow as a fct precursor.[1] A bct phase is observed up to 10 ML on further deposition of Fe.

In Fig. 5.8(a), we show the experimental results of cantilever stress measurements, where the cantilever stress change $\Delta(\tau_F t_F)$ is plotted against the film thickness (ML). It is found that in the region between 1 and 4 ML of Fe on Ir(001), the film stress undergoes a transition from positive stress (+6 GPa) to negative stress (−10 GPa), as shown in Fig. 5.8(a). Here the sign convention is that negative stresses correspond to compressive stress, and positive stresses correspond to tensile stress.

In order to comment on the structural phases corresponding to these stresses, Martin *et al.* calculated the film stress from continuum elastic theory.[1, 31–34] They found that for bcc- and fcc-Fe, the in-plane film stresses suggested by continuum

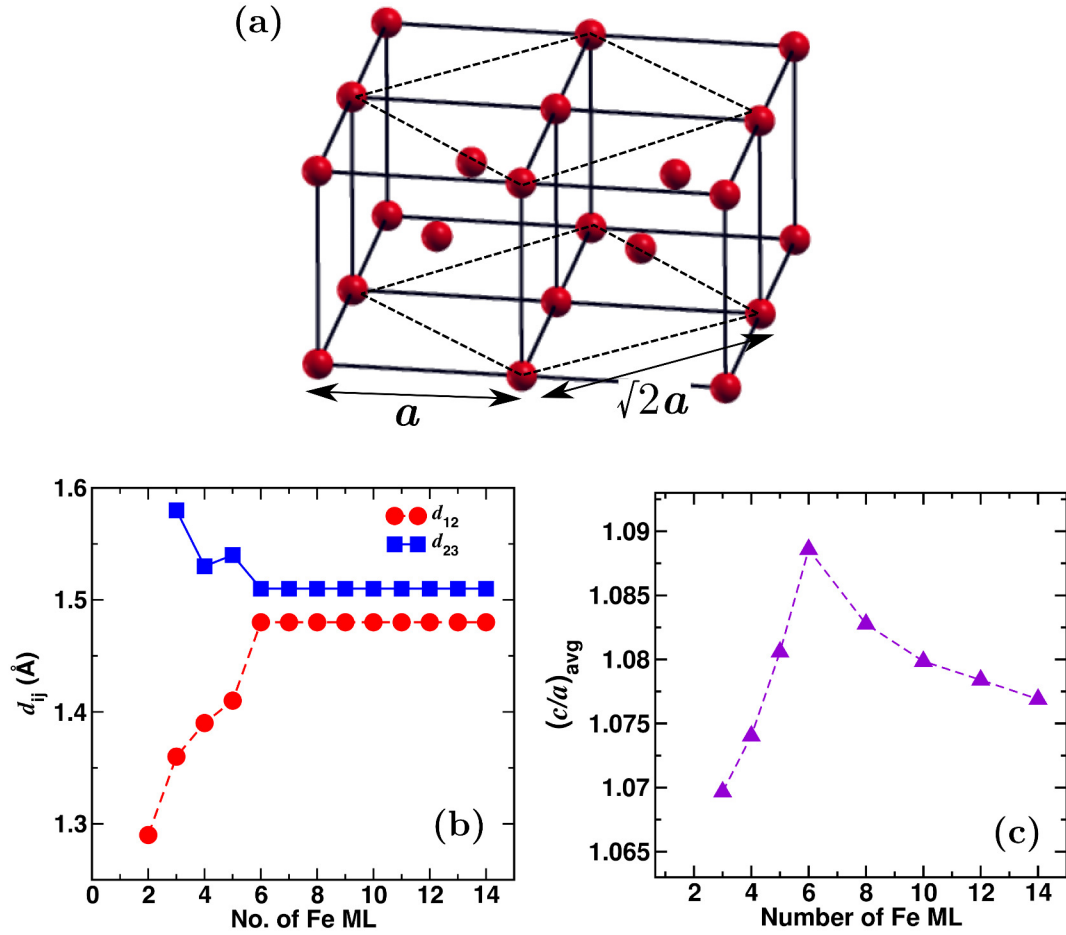


Figure 5.7: Panel (a) shows the schematic of an fct unit cell (dashed lines) of lattice constant $\sqrt{2}a$, inside a bcc lattice of lattice constant a . (b), and (c) show the DFT results for the changes in geometry as a result of Fe film thickness. The first two interlayer spacings (d_{ij}) as a function of the thickness of the Fe film in different Fe/Ir(001) systems are shown in (b). The average c/a ratio of the Fe layers as a function of Fe ML is plotted in (c).

elastic theory are -11 GPa and $+11.4$ GPa, respectively. Comparing these values with the experimental values of stresses, they concluded that for the first two layers, Fe grows in a fct structure. After 2 ML, it grows in a bct structure upto 10 ML. Beyond 10 ML, as indicated by the decrease in the slope of cantilever stress change with increasing thickness, Fe layers move towards a bcc structure.

We perform DFT computations to calculate the in-plane stress as a function of Fe film thickness, and compare our results with the film stress suggested by the continuum elastic theory. In Fig. 5.8(b), we plot the in-plane stress of Fe layers versus

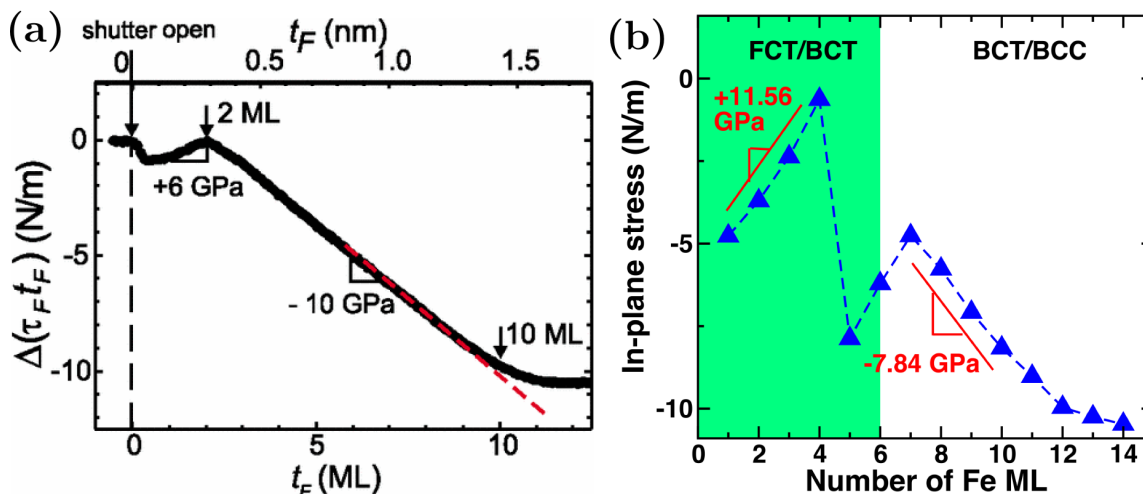


Figure 5.8: Panel (a) shows the results of cantilever stress measurements by Martin *et al.*[1] where the cantilever stress change $[\Delta(\tau_F t_F)]$ versus Fe layer thickness (ML) is plotted. In (b) the DFT results of in-plane stress as a function of number of Fe ML is shown. In both experimental and DFT calculated results, positive/negative slope indicates fct/bct phase of Fe.

the number of Fe ML on Ir(001). We find a positive slope of +11.56 GPa up to 4 ML, and a negative slope of -7.84 GPa beyond 8 ML of Fe. Both the sign and magnitude of these values are in good agreement with the in-plane stresses of fcc (+11.4 GPa) and bcc Fe (-11 GPa), respectively, calculated from continuum elastic theory.[1] This indicates that up to 4 ML, the Fe layers are in a fct structure, and further deposition of Fe beyond 8 ML, leads to growth in a bct structure. As shown in the experimental results in Fig. 5.8(a), we also find a decrease in the slope of in-plane stress beyond 12 ML, suggesting that thicker layers beyond 12 ML, are close to the bcc structure. This finding also agrees well with the MEED oscillation results (see Fig. 5.1(b)), where we see a decrease in the intensity of the oscillation between 11 ML and 13 ML, indicating the end of pseudomorphic growth and beginning of the growth of strain relaxed bcc-Fe. However, we note that in our calculations, the growth is constrained to be pseudomorphic: due to the use of periodic boundary conditions, we do not permit the Fe overlayers to grow with a lattice constant that differs from that of the Ir substrate.

Interestingly, in the plot of in-plane stress as a function of number of Fe ML in Fig. 5.8(b), along with the structural phase transitions, we see the signature of the magnetic phase transition from *AFM* to *FM*, when going from 4 to 5 ML of Fe/Ir(001). The in-plane stress is seen to decrease sharply when the *AFM* to *FM* transition occurs beyond 4 ML.

5.7 Conclusions

We have studied the thickness-dependent magnetic and structural phase transitions in the Fe/Ir(001) system. Experiments on the layer-by-layer growth of Fe on Ir(001), performed by our collaborators, find an onset of ferromagnetic ordering beyond 4 monolayers (ML) of Fe, with no net magnetic moment present below this thickness. Our DFT results show the presence of an *AFM* to *FM* transition beyond 4 ML of Fe/Ir(001), which matches with these experimental findings. We find that above 4 ML, the *FM* ordering is favored over *AFM* ordering due to a higher exchange splitting in the *FM* configuration compared to the *AFM* configuration. DFT calculations of structural and elastic properties indicate the presence of a fct structure up to 4 ML, and a bct structure beyond 8 ML. These results agree well with the results of cantilever stress measurements done in previous experimental studies.

Bibliography

- [1] V. Martin, W. Meyer, C. Giovanardi, L. Hammer, K. Heinz, Z. Tian, D. Sander, and J. Kirschner, “Pseudomorphic growth of fe monolayers on Ir(001)–(1 × 1): From a fct precursor to a bct film,” *Phys. Rev. B*, vol. 76, p. 205418, Nov 2007.
- [2] K. Barmak and K. Coffey, eds., *Metallic Films for Electronic, Optical and Magnetic Applications*, pp. 621 – 634. Woodhead Publishing, 2014.
- [3] J. Chen and J. L. Erskine, “Surface-step-induced magnetic anisotropy in thin epitaxial Fe films on W(001),” *Phys. Rev. Lett.*, vol. 68, pp. 1212–1215, Feb 1992.

-
- [4] Z. Tian, *Magnetoelastic coupling in ferromagnetic films and surface stress studies on Ir(100)*. PhD thesis, Martin-Luther-Universität Halle-Wittenberg, 2008.
- [5] S. Andrieu, F. Lahatra Razafindramisa, E. Snoeck, H. Renevier, A. Barbara, J. M. Tonnerre, M. Brunel, and M. Piecuch, “bct to bcc iron in (001) Fe/Ir superlattices: Relation between structure and magnetism,” *Phys. Rev. B*, vol. 52, pp. 9938–9954, Oct 1995.
- [6] S. Andrieu, J.-F. Bobo, J. Hubsch, and M. Piecuch, “Magnetic properties of body-centered tetragonal iron/iridium superlattices,” *Journal of Magnetism and Magnetic Materials*, vol. 126, no. 1, pp. 349 – 351, 1993.
- [7] D. C. Stoeffler, “Stress-induced ferrimagnetic orders in Fe/Ir multilayers,” *Journal of Magnetism and Magnetic Materials*, vol. 198-199, pp. 306 – 308, 1999.
- [8] P.-C. Jiang, W.-H. Chen, C.-Y. Hsieh, and J.-S. Tsay, “Layered structure and related magnetic properties for annealed Fe/Ir(111) ultrathin films,” *Journal of Applied Physics*, vol. 117, no. 17, p. 17B742, 2015.
- [9] E. Snoeck, S. Frechengues, M. Casanove, C. Roucau, and S. Andrieu, “HREM study of the epitaxial growth of Fe on Ir(001),” *Journal of Crystal Growth*, vol. 167, no. 1, pp. 143 – 150, 1996.
- [10] D. Bagayoko and J. Callaway, “Lattice-parameter dependence of ferromagnetism in bcc and fcc iron,” *Phys. Rev. B*, vol. 28, pp. 5419–5422, Nov 1983.
- [11] V. L. Moruzzi, P. M. Marcus, and J. Kübler, “Magnetovolume instabilities and ferromagnetism versus antiferromagnetism in bulk fcc iron and manganese,” *Phys. Rev. B*, vol. 39, pp. 6957–6961, Apr 1989.
- [12] G. L. Krasko, “Metamagnetic behavior of fcc iron,” *Phys. Rev. B*, vol. 36, pp. 8565–8569, Dec 1987.

-
- [13] J. Häglund, “Fixed-spin-moment calculations on bcc and fcc iron using the generalized gradient approximation,” *Phys. Rev. B*, vol. 47, pp. 566–569, Jan 1993.
- [14] S. Peng and H. J. F. Jansen, “Electronic structure of face-centered tetragonal iron,” *Journal of Applied Physics*, vol. 67, no. 9, pp. 4567–4569, 1990.
- [15] S. Blügel, B. Drittler, R. Zeller, *et al.*, “Magnetic properties of 3d transition metal monolayers on metal substrates,” *Appl. Phys. A*, vol. 49, p. 547, 1989.
- [16] H. Nait-Laziz and C. Demangeat, “On a possible antiferromagnetic-to-ferromagnetic transition in terms of the slab thickness,” *Applied Surface Science*, vol. 65-66, pp. 165 – 169, 1993.
- [17] K. Louzazna and A. Haroun, “Magnetic and electronic properties of strained fcc Fe on Ir(001),” *Thin Solid Films*, vol. 374, no. 1, pp. 114 – 118, 2000.
- [18] B. Hamad, J. Khalifeh, and C. Demangeat, “Metastable magnetic configurations of (V, Cr, Mn and Fe) on Ir(001) surfaces,” *Surface Science*, vol. 601, no. 2, pp. 346 – 351, 2007.
- [19] J. Kudrnovský, F. Máca, I. Turek, and J. Redinger, “Substrate-induced antiferromagnetism of a Fe monolayer on the Ir(001) surface,” *Phys. Rev. B*, vol. 80, p. 064405, Aug 2009.
- [20] A. Deák, L. Szunyogh, and B. Ujfalussy, “Thickness-dependent magnetic structure of ultrathin Fe/Ir(001) films: From spin-spiral states toward ferromagnetic order,” *Phys. Rev. B*, vol. 84, p. 224413, Dec 2011.
- [21] A. V. Pradeep, *Development of a spin-polarized low energy electron diffraction system and investigations on spin-orbit and exchange interactions on Ir(100) and ultrathin Fe(100) grown on Ir(100)*. PhD thesis, Department of Physics, Indian Institute of Science, 2016.

-
- [22] G. Kresse and J. Furthmüller, “Efficiency of ab-initio total energy calculations for metals and semiconductors using a plane-wave basis set,” *Computational Materials Science*, vol. 6, no. 1, pp. 15 – 50, 1996.
- [23] G. Kresse and J. Furthmüller, “Efficient iterative schemes for ab initio total-energy calculations using a plane-wave basis set,” *Phys. Rev. B*, vol. 54, pp. 11169–11186, Oct 1996.
- [24] J. P. Perdew, K. Burke, and M. Ernzerhof, “Generalized gradient approximation made simple,” *Phys. Rev. Lett.*, vol. 77, pp. 3865–3868, Oct 1996.
- [25] P. E. Blöchl, “Projector augmented-wave method,” *Phys. Rev. B*, vol. 50, pp. 17953–17979, Dec 1994.
- [26] G. Kresse and D. Joubert, “From ultrasoft pseudopotentials to the projector augmented-wave method,” *Phys. Rev. B*, vol. 59, pp. 1758–1775, Jan 1999.
- [27] H. J. Monkhorst and J. D. Pack, “Special points for Brillouin-zone integrations,” *Phys. Rev. B*, vol. 13, pp. 5188–5192, Jun 1976.
- [28] S. Blundell, *Magnetism in condensed matter*. Oxford ; New York: Oxford University Press, 2001.
- [29] M. Čák, M. Šob, and J. Hafner, “First-principles study of magnetism at grain boundaries in iron and nickel,” *Phys. Rev. B*, vol. 78, p. 054418, Aug 2008.
- [30] J. Thomassen, F. May, B. Feldmann, M. Wuttig, and H. Ibach, “Magnetic live surface layers in Fe/Cu(100),” *Phys. Rev. Lett.*, vol. 69, pp. 3831–3834, Dec 1992.
- [31] D. Sander, “The correlation between mechanical stress and magnetic anisotropy in ultrathin films,” *Reports on Progress in Physics*, vol. 62, pp. 809–858, jan 1999.

-
- [32] M. Kottcke and K. Heinz, “A new approach to automated structure optimization in LEED intensity analysis,” *Surface Science*, vol. 376, no. 1, pp. 352 – 366, 1997.
- [33] J. Zarestky and C. Stassis, “Lattice dynamics of γ -Fe,” *Phys. Rev. B*, vol. 35, pp. 4500–4502, Mar 1987.
- [34] J. J. Adams, D. S. Agosta, R. G. Leisure, and H. Ledbetter, “Elastic constants of monocrystal iron from 3 to 500k,” *Journal of Applied Physics*, vol. 100, no. 11, p. 113530, 2006.

Chapter 6

Electronic and magnetic structure of thin films: V deposited on Ag(001)

In this chapter, we study the structure and magnetic properties of a monolayer of V deposited on Ag(001). Experiments performed in the group of Prof. K. S. R. Menon at the Saha Institute of Nuclear Physics, Kolkata, show evidence of V going sub-surface upon deposition on Ag(001). We perform density functional theory calculations to investigate the tendency of V to go sub-surface, and its preferred magnetic ordering.

6.1 Introduction

The reduced dimensionality of ultrathin films may lead to very different magnetic properties compared to their bulk counterparts. This behaviour can be exploited in applications like magnetic storage and spintronic devices.[1–3] In this respect, monolayers of $3d$ transition metals which show itinerant magnetism, serve as good model systems to study two-dimensional magnetism.

At the thickness of a few monolayers, materials show very different magnetic behaviour compared to their bulk behaviour. Theoretical calculations by Blügel *et al.*

have shown that Mn and Cr monolayers prefer antiferromagnetic (AFM) ordering on Pd(001).[4] Fe and Ni show thickness dependent magnetic phases, when grown on Ag(001) and Cu(111), respectively.[5, 6] Using *ab initio* electronic structure calculations, Krüger *et al.* showed that although V, Cr, and Mn prefer antiferromagnetic ordering in their monolayer over Ag(001), changing the substrate to Ag(111), can change their magnetic configuration.[7] While Cr and Mn show row-by-row antiferromagnetism, V becomes ferrimagnetic on Ag(111). Recently Biswas *et al.* have shown that a monolayer of Cr on Ag(001), not only prefers $c(2 \times 2)$ AFM ordering, but also goes sub-surface instead of making an overlayer.[8]

The magnetic state of V ultra-thin films has been the subject of research for a long time without any conclusive study till date. Early experiments by Rau *et al.* on 1 – 7 monolayers (ML) of V on Ag(001) using electron capture spectroscopy, suggested that there was long-range ferromagnetic ordering with a thickness-dependent Curie temperature.[9] On the other hand, another study by M. Stampanoni *et al.* on 1 – 3 ML of V on Ag(001) using spin-polarized photoemission spectroscopy, has not found any evidence of ferromagnetism.[10] The authors of this study concluded that this could be due to the existence of a Curie temperature below the temperature at which the experiment has been performed (30 K), or may indicate the presence of other types of magnetic order.

Magneto optic Kerr effect (MOKE) measurements by R. Fink *et al.* did not seem to provide any evidence for the existence of ferromagnetism. The authors measured the LEED pattern, to check for a weak $c(2 \times 2)$ antiferromagnetic order, but did not find any evidence of elastic exchange scattering from an antiferromagnetic lattice. However, they also pointed out that the sensitivity of the LEED apparatus could be questioned, and therefore claimed the null LEED results could not be cited as evidence of the absence of antiferromagnetic order. More recent experiments using X-ray magnetic circular dichroism, by M. Finazzi *et al.* have also failed to see any signature of ferromagnetic ordering.[11, 12]

Theoretical calculations using the full potential linearized augmented plane wave (FPLAPW) method by S. Blügel *et al.* suggested that the V monolayer on Ag(001), favours an antiferromagnetic $c(2 \times 2)$ superstructure.[13] They also showed theoretically, the presence of $c(2 \times 2)$ antiferromagnetic ordering in monolayers of Cr and Mn, while Ti, Fe, Co, and Ni order in the ferromagnetic $p(1 \times 1)$ configuration. Experiments by J. Moodera and R. Meservey, have also detected antiferromagnetic coupling between V atoms for a coverage less than 1.5 ML,[14] beyond which they report the occurrence of ferromagnetism.

One should also note that the absence of a conclusive result in the previous studies can arise from the fact that the growth of a flat monolayer of V on Ag(001) is unlikely since the surface energy of vanadium (3 J/m^2) is more than the surface energy of silver (1.2 J/m^2).[11] This suggests that intermixing at the interface may be unfavourable, but cluster formation, or Ag segregation on top of V, can be thermodynamically favoured over a layer-by-layer growth.[11] In order to find (i) the structure and stability of monolayer of V on Ag(001) and (ii) the preferred magnetic ordering of such a system, we perform both experiments and theoretical calculations, as discussed further below.

6.2 Experimental motivation

Our experimental collaborators in the group of Prof. K. S. R. Menon, have performed ARPES and LEED studies on the growth of V films on Ag(001) at different substrate temperatures (108 K – 473 K). The details of the experimental setup and results can be found in the PhD thesis of Asish Kundu.[15] Upon deposition of a monolayer of V on Ag(001), the appearance of an additional surface state near the high symmetry \bar{M} point, at 300 meV higher binding energy than the bulk band (see Fig. 6.1) is observed. This feature suggests that the V layer is going sub-surface, resulting in a change in the surface potential. It is pointed out that although LEED measurements do not show the presence of a weak $c(2 \times 2)$ superstructure indicating

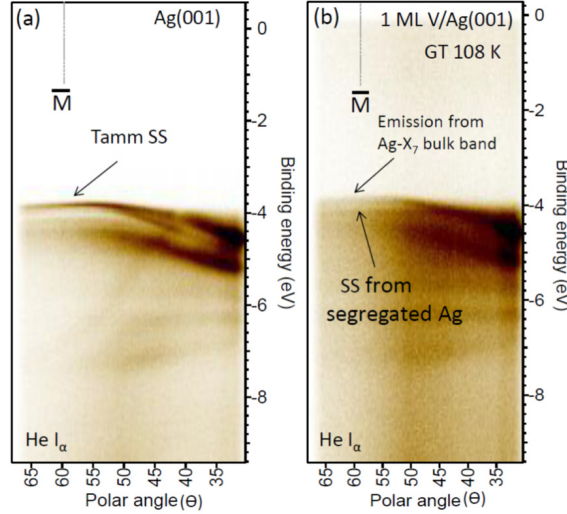


Figure 6.1: ARPES data showing surface states at \bar{M} for (a) bare Ag(001), and (b) 1 ML V/Ag(001) grown at 108 K. Upon deposition of V, additional surface states can be seen to occur near the \bar{M} point in (b), suggesting Ag segregation over V.

an antiferromagnetic configuration, this cannot be treated as a compelling evidence of the absence of antiferromagnetic order in the monolayer V film. It is possible that the intensity of the half-order spots is much weaker, and below the sensitivity of the LEED setup. Moreover, the Néel temperature can be lower than 108 K, which is the lowest temperature that could be achieved in the existing experimental setup.

Motivated by these results, we perform density functional theory (DFT) calculations to address the following issues: (i) does V want to stay on surface, or prefers to go sub-surface, (ii) what is the preferred magnetic ordering of V on Ag(001)? and (iii) how does the electronic structure get modified upon V deposition?

6.3 Computational details and systems

All calculations have been performed within the framework of spin-polarized density functional theory (DFT), as implemented in the Quantum ESPRESSO package.[16] The electronic wavefunctions are expanded in a plane-wave basis set with cutoffs of kinetic energy and charge densities set to 45 Ry and 450 Ry, respectively. The exchange-correlation interactions are treated using the Perdew-Burke-Ernzerhof (PBE) form of the generalized gradient approximation.[17] The ion-electron interactions

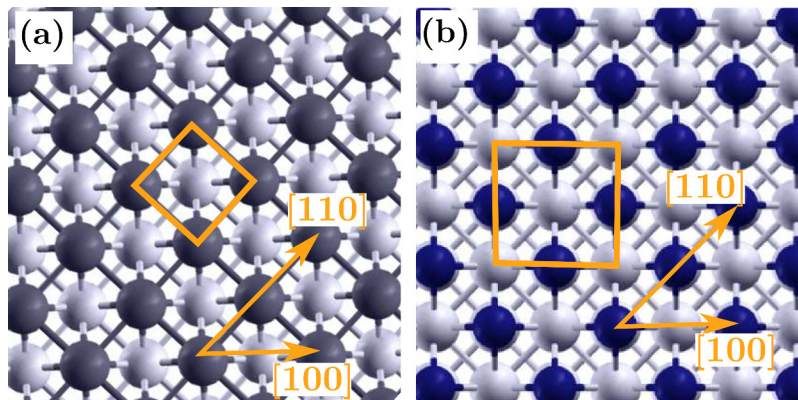


Figure 6.2: The top view of atomic arrangements of (a) Ag(001) and (b) V/Ag(001) systems are shown. The dark blue, dark gray, and light gray spheres represent V, first substrate layer, and second substrate layers of Ag atoms, respectively. The primitive surface unit cells are indicated by solid orange lines.

are described using ultrasoft pseudopotentials.[18]

The surface of Ag(001) is modeled by a 15 atomic layer thick slab of Ag in the [001] direction. We deposit the V monolayers symmetrically on the Ag substrate, i.e., on both the top and the bottom surfaces of the slab. Four different atomic configurations of V monolayers on Ag(001) are considered: (1) V/Ag(001), where each surface of Ag(001) has an overlayer of V monolayer, (2) 1Ag/V/Ag(001), where each surface of V/Ag(001) has an overlayer of Ag, (3) 2Ag/V/Ag(001), where two Ag layers cover the surface of V/Ag(001), and (4) 3Ag/V/Ag(001), where each surface of V/Ag(001) is buried under 3 layers of Ag. Since each of the above mentioned configurations consists of 17 atomic layers (15 atomic layers of Ag and 2 atomic layers of V), we can compare their energies directly. We introduce a vacuum separation of ~ 18 Å to minimize the interaction between the periodic images along the direction normal to the surface.

The coordinates of all atoms of the slab except the middle three layers are relaxed using Hellmann-Feynman forces, using a force convergence threshold of 0.001 Ry/bohr along each Cartesian direction. The Brillouin zone is sampled using a $12 \times 12 \times 1$ Monkhorst-Pack [19] k -point grid for the $\sqrt{2} \times \sqrt{2}$ surface unit cell.

All calculations have been performed using the optimized lattice constant of Ag,

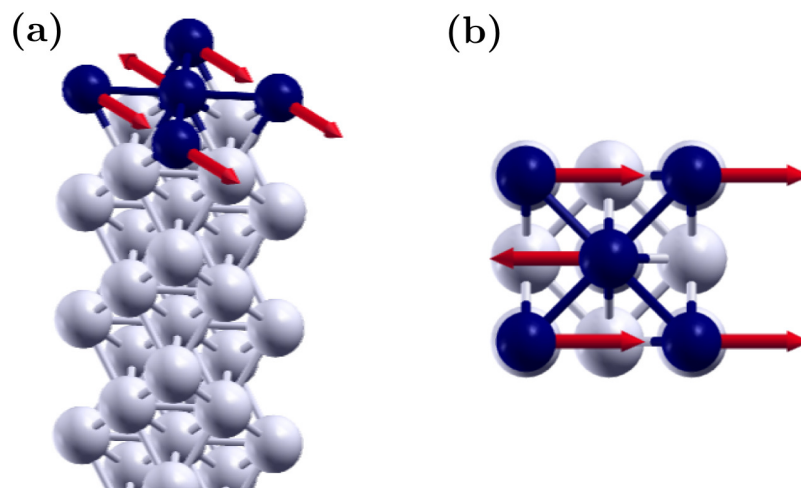


Figure 6.3: The (a) side view, and (b) the top view of the atomic structure of V/Ag(001) in the antiferromagnetic configuration. Blue and gray spheres represent V and Ag atoms, respectively. The red arrows indicate the direction of the spins, which, here, are shown to be in-plane. However, the out-of-plane directions are also equivalent.

which is found to be 4.16 Å, very close to the experimental lattice constant of 4.09 Å.[20] Ag has a face-centered cubic (fcc) crystal structure while V crystallizes in a body-centered cubic (bcc) structure. The lattice constant of bulk V is found to be 3.00 Å, whereas the in-plane Ag-Ag distance is $(4.16/\sqrt{2}=) 2.94$ Å. A 1×1 surface unit cell is shown in Fig. 7.1(a) by an orange square; note that this unit cell is rotated by 45° with respect to the fcc surface unit cell. The small mismatch between the Ag(001) and V(001) surface unit cell allows pseudomorphic growth of V on Ag(001).

We have performed nonmagnetic (NM), antiferromagnetic (AFM) and ferromagnetic (FM) calculations on all the four systems described above. In the AFM configuration, a V atom of a particular spin is surrounded by four V atoms of opposite spin, in the same layer. For a direct comparison of the energetics of AFM, FM and NM configurations, all calculations have been performed in a $\sqrt{2} \times \sqrt{2}$ surface unit cell [see Fig. 7.1(b)].

The use of a surface supercell in real-space as described above, results in a ‘folding’ of bands in the supercell Brillouin zone (BZ). In order to compare the computed band structure with the ARPES data, one needs to ‘unfold’ the bands. We have employed

a band-unfolding scheme as described by Biswas *et al.*[8] for this purpose, and as also described in detail below.

6.3.1 Unfolding and projection of band structure

In order to describe the method of unfolding, let us denote all the wave-vectors in the primitive Brillouin zone (PBZ) and supercell Brillouin zone (SBZ), as \mathbf{k} , and \mathbf{K} , respectively, and the volume of the PBZ and SBZ as Ω_{PBZ} , and Ω_{SBZ} , respectively. For each \mathbf{K} of the SBZ, there are $N_{\mathbf{G}}$ number of \mathbf{G}^{SBZ} vectors of the supercell that satisfy the following equation,[21]

$$\mathbf{k}_i = \mathbf{K} + \mathbf{G}_i^{\text{SBZ}} \quad \text{where } i = 1 \dots N_{\mathbf{G}}, \quad (6.1)$$

where \mathbf{k}_i is any vector in the primitive BZ and $N_{\mathbf{G}} = \frac{\Omega_{\text{PBZ}}}{\Omega_{\text{SBZ}}}$.

Let us consider the single-particle Kohn-Sham (KS) states of the supercell to be $\psi_{\mathbf{K},m}^{\text{SC}}$; these can be obtained by solving the KS equations self-consistently by performing calculations using the supercell. When using a plane-wave basis, one can write:

$$|\psi_{\mathbf{K},m}^{\text{SC}}\rangle = \sum_{\{\mathbf{G}^{\text{SBZ}}\}} c_{\mathbf{K}-\mathbf{G}^{\text{SBZ}},m} |\mathbf{K} - \mathbf{G}^{\text{SBZ}}\rangle, \quad (6.2)$$

where m is a band index, $|\mathbf{K} - \mathbf{G}^{\text{SBZ}}\rangle$ represents the plane-wave basis functions, and $c_{\mathbf{K}-\mathbf{G}^{\text{SBZ}},m}$ are the plane-wave expansion coefficients. Similarly, the single-particle Kohn-Sham states of the primitive cell $\psi_{\mathbf{k},\nu}^{\text{PC}}$ are written as:

$$|\psi_{\mathbf{k},\nu}^{\text{PC}}\rangle = \sum_{\{\mathbf{G}^{\text{PBZ}}\}} c_{\mathbf{k}-\mathbf{G}^{\text{PBZ}},\nu} |\mathbf{k} - \mathbf{G}^{\text{PBZ}}\rangle, \quad (6.3)$$

where ν is the band index in the primitive cell. Note that the set of vectors $\{\mathbf{G}^{\text{PBZ}}\}$

is only a subset of $\{\mathbf{G}^{\text{SBZ}}\}$. Thus Eq. (6.2) can be rewritten as:

$$|\psi_{\mathbf{K},m}^{\text{SC}}\rangle = \sum_{\{\mathbf{G}^{\text{PBZ}}\}} c_{\mathbf{K}-\mathbf{G}^{\text{PBZ}},m} |\mathbf{K} - \mathbf{G}^{\text{PBZ}}\rangle + \sum_{\{\mathbf{G}^{\text{SBZ}} \neq \mathbf{G}^{\text{PBZ}}\}} c_{\mathbf{K}-\mathbf{G}^{\text{SBZ}},m} |\mathbf{K} - \mathbf{G}^{\text{SBZ}}\rangle \quad (6.4)$$

Our aim is to obtain the $\{\mathbf{G}^{\text{PBZ}}\}$ from the given set of $\{\mathbf{G}^{\text{SBZ}}\}$. This can be obtained by employing the condition:

$$\mathbf{G}^{\text{SBZ}} \cdot \mathbf{A} = 2\pi M \quad \forall \{\mathbf{G}^{\text{SBZ}}\}, \quad (6.5)$$

where M is an integer and \mathbf{A} is a lattice vector of the primitive unit cell. Eq. (6.5) gives non-zero contributions only for $\{\mathbf{G}^{\text{PBZ}}\}$.

The probability of $\psi_{\mathbf{K},m}^{\text{SC}}$ having the same character as a primitive cell state with wave-vector \mathbf{k} , is given by the spectral weight $P_{\mathbf{K},m}(\mathbf{k})$. The spectral weight then can be obtained as:[21]

$$P_{\mathbf{K},m}(\mathbf{k}) = \sum_{\nu} |\langle \psi_{\mathbf{K},m}^{\text{SC}} | \psi_{\mathbf{k},\nu}^{\text{PC}} \rangle|^2. \quad (6.6)$$

As we are interested in obtaining the band structure in the PBZ, we can ignore the second term in Eq. (6.4). Then, from Eqs. (6.3) and (6.4), and (6.6), we can write

$$P_{\mathbf{K},m}(\mathbf{k}) = \sum_{\{\mathbf{G}^{\text{PBZ}}\},\nu} |c_{\mathbf{K}-\mathbf{G}^{\text{PBZ}},m}|^4 \delta_{m\nu}. \quad (6.7)$$

To obtain the contributions coming from the atomic states to the bands, one can write $\psi_{\mathbf{K},m}^{\text{SC}}$, as

$$\psi_{\mathbf{K},m}^{\text{SC}} = \sum_q A_q \phi_q, \quad (6.8)$$

where $\{q\}$ is the set of good quantum numbers. ϕ_q is the atomic orbital of the state q , and A_q 's are the coefficients. The probability of the wavefunction $\psi_{\mathbf{K},m}^{\text{SC}}$ having the same character as a wavefunction ϕ_q is given by:

$$|\langle \phi_q | \psi_{\mathbf{K},m}^{\text{SC}} \rangle|^2 = |A_q|^2. \quad (6.9)$$

Now, to obtain the contributions coming from the atomic states to the unfolded bands, one needs to calculate the probability of the primitive cell wavefunction $\psi_{\mathbf{k},\nu}^{\text{PC}}$ having the same character as a wavefunction ϕ_q . Thus, this projection can be written as:

$$|\langle \phi_q | \psi_{\mathbf{k},\nu}^{\text{PC}} \rangle|^2 = |\langle \phi_q | \psi_{\mathbf{k},m}^{\text{SC}} \rangle \langle \psi_{\mathbf{k},m}^{\text{SC}} | \psi_{\mathbf{k},\nu}^{\text{PC}} \rangle|^2 = |A_q|^2 P_{\mathbf{k},\nu}(\mathbf{k}). \quad (6.10)$$

In Section 4.2, we employ this method to obtain the band structure in order to compare with the experimental ARPES data.

6.4 Results and Discussion

We first look at the relative stability of the four systems, and see how the magnetic ordering plays a key role in determining the stability. We restrict ourselves only to collinear magnetic ordering, i.e. FM and AFM ordering. In Section 4.2, we compare our results with the experimental ARPES data.

6.4.1 Stability and magnetic ordering

We have obtained the optimized geometries of all the four systems in AFM, FM and NM configurations. Table 4.1 shows the tabulated values of the relative stability (ΔE) of different structures with respect to the lowest energy structure. We find that the most energetically favourable structure is 1Ag/V/Ag(001), indicating that V prefers to be buried under one monolayer of Ag. Comparing the energetics we find that for each structure the AFM configuration is the most favourable one, whereas the NM configuration is energetically the most unfavourable. The AFM structures of 2Ag/V/Ag(001) and 3Ag/V/Ag(001) lie higher in energy than 1Ag/V/Ag(001) by only 39 and 99 meV/V atom, respectively. The reason for favouring the AFM configuration over FM, is discussed further below.

In Fig. 6.4 we show the interlayer distances denoted as d_{ij} 's, the distance between the i^{th} and j^{th} layers, of all the systems studied here. Note that d_{ij} 's are numbered starting from the surface, e.g., d_{12} denotes the interlayer separation between the surface

Table 6.1: Energetics of FM, AFM and NM configurations of V on Ag(001) systems are presented. ΔE represents the difference in energy of a given configuration with that of the lowest energy configuration.

System	Magnetic structures				Non-magnetic structures	
	FM		AFM		NM	
	ΔE (meV/V atom)	m_V^{FM} (μ_B)	ΔE (meV/V atom)	m_V^{AFM} (μ_B)	ΔE (meV/V atom)	m_V^{NM} (μ_B)
V/Ag(001)	830	3.03	751	2.91	1160	0
1Ag/V/Ag(001)	181	2.29	0	2.56	302	0
2Ag/V/Ag(001)	185	2.05	39	2.44	256	0
3Ag/V/Ag(001)	221	2.24	99	2.54	329	0

layer, and the layer below it. Since a symmetric slab is taken, distances up to d_{78} are shown. The interlayer distances of both the FM and AFM magnetic configurations are found to be similar, indicating that the preferred magnetic configurations of the system have negligible effect on the d_{ij} 's. For all the systems, the interlayer distances are found to be sensitive to the position of the V atom in the slab, due to the formation of interface with Ag. For NM systems [see orange diamonds in Fig. 6.4], the interlayer distances involving layers forming interfaces between V and Ag atoms are found to be less than the corresponding interlayer distances of the magnetic systems; this is the well-known magnetovolume effect, where the introduction of a magnetic moment results in an expansion of interlayer distances in its vicinity.

To understand the reason behind the preference of AFM configuration over FM, we first compare the projected density of states (PDOS) of the d -orbital of V in the AFM and FM configuration in each structure (see Fig. 6.5). Positive and negative values represent majority and minority spins, respectively. The red dashed and blue solid curves indicate the AFM and FM configurations, respectively. We notice that for a given system, the density of states of the majority states of V atom near the Fermi energy (E_F) is narrower for the AFM configuration than the FM configuration. Since the width of the peaks in the density of states of the d -states for FM configurations is much broader, this leads to less exchange splitting between the majority and minority spin states. To quantify the splitting between the energy levels of majority and

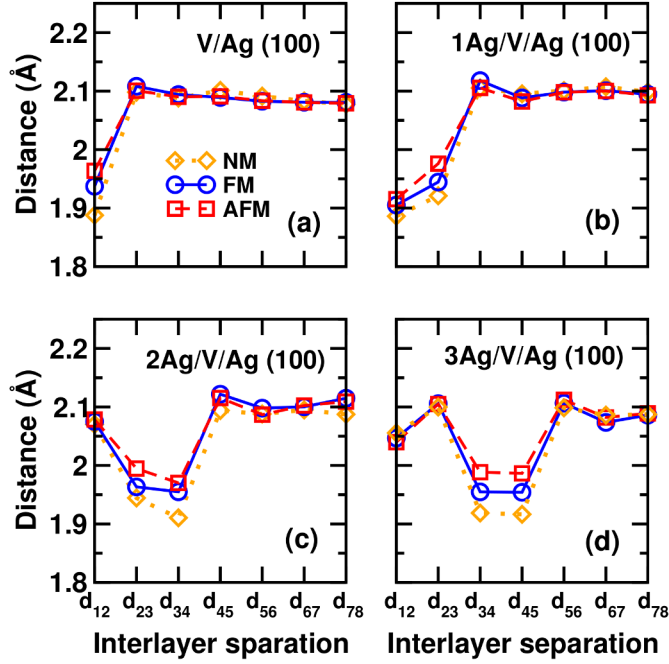


Figure 6.4: The variation of interlayer distance d_{ij} for (a) V/Ag(001), (b) 1Ag/V/Ag(001), (c) 2Ag/V/Ag(001), and (d) 3Ag/V/Ag(001) in NM (shown in orange diamonds), FM (shown in blue circles) and AFM (shown in red squares) configurations.

minority spin states, we calculate the exchange splitting ΔE_{ex} , defined as the energy difference between the band center of density of states of majority and minority d -states (ϵ_d) of V, $\Delta E_{ex} = (\epsilon_d^\uparrow - \epsilon_d^\downarrow)$. The d -band center is defined as:

$$\epsilon_{d\sigma} = \frac{\int_{\epsilon_{min}}^{\epsilon_{max}} \epsilon g_{d\sigma}(\epsilon) d\epsilon}{\int_{\epsilon_{min}}^{\epsilon_{max}} g_{d\sigma}(\epsilon) d\epsilon}. \quad (6.11)$$

where $g_{d\sigma}(\epsilon)$ is the density of states of the d -band of a given spin σ of V atom. In the case of 1Ag/V/Ag(001) system, the calculated Δ_{ex} for AFM is found to be 1.75 eV, which is higher than the exchange splitting of 1.67 eV in the FM configuration. This makes the AFM configuration energetically more favourable than the FM configuration.

In Table 6.1 we have also listed the magnetic moment per V atom (m_V) for both the FM and AFM configurations, for all the structures. One might expect that as the V layer goes deeper into the Ag substrate, the increased hybridization of V atoms

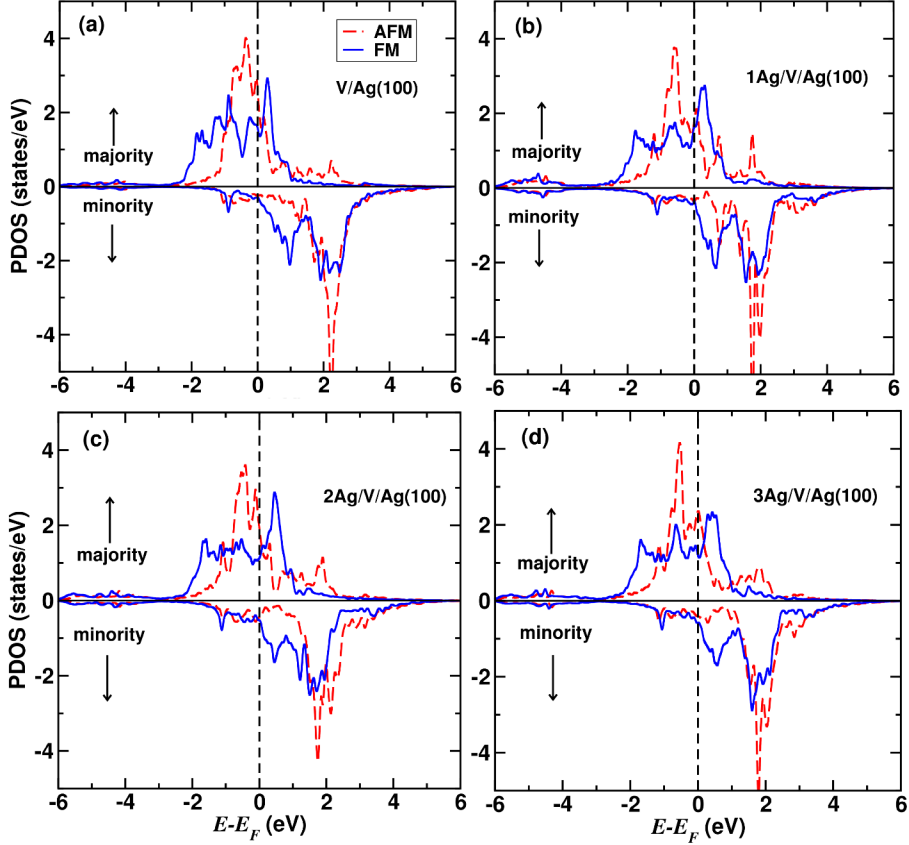


Figure 6.5: The projected density of states (PDOS) of the 3d states of V atoms of both AFM (shown in red dashed lines) and FM (shown in solid blue lines) configuration in (a) V/Ag(001), (b) 1Ag/V/Ag(001), (c) 2Ag/V/Ag(001) and (d) 3Ag/V/Ag(001).

with Ag atoms will decrease the m_V . Surprisingly, we find m_V does not get reduced significantly as the V monolayer goes sub-surface. To understand the reason behind this observation, we plot the PDOS of V 3d orbitals and the Ag 4d orbitals (both above and below the V layer) in Fig. 6.6 We find that 3d majority spin states of V (blue curve) are well separated in energy from the 4d majority spin states of the nearest neighbour Ag atoms indicating weak hybridization. This allows the V atom to retain a significant magnetic moment even when it is buried under 3 layers of Ag, as seen in 3Ag/V/Ag(001).

So far we have found that V prefers to go sub-surface and that the most stable structure is 1Ag/V/Ag(001). The structure prefers AFM ordering over FM ordering, and the NM structure is always the least favourable one. For the lowest energy

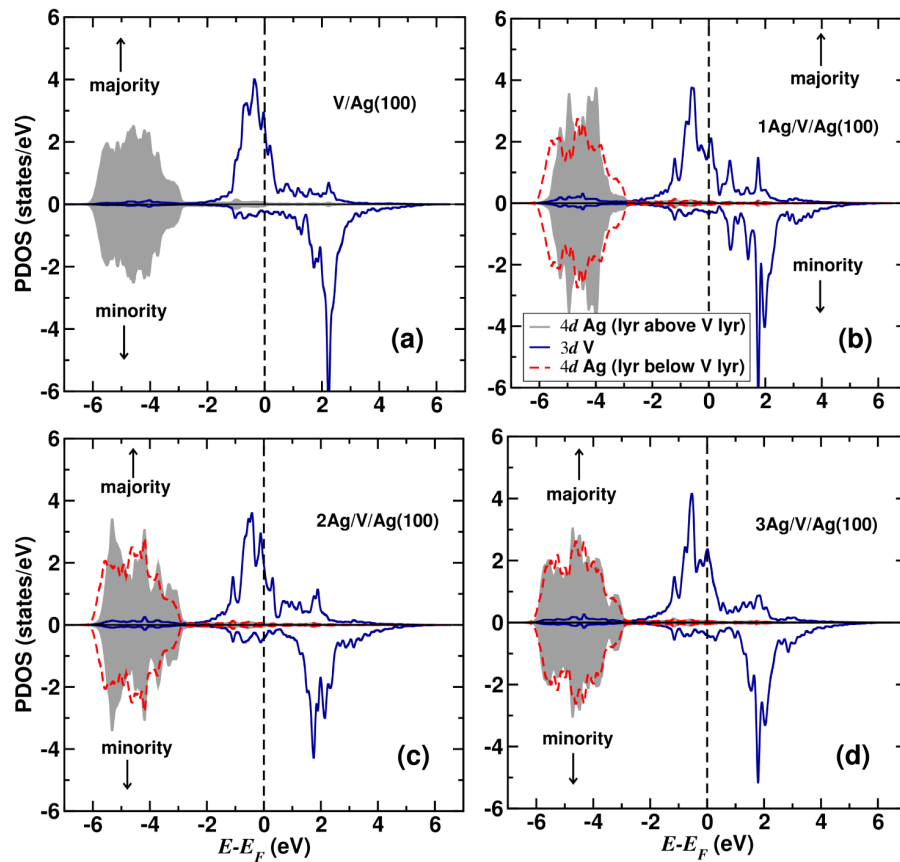


Figure 6.6: The projected density of states (PDOS) of the Ag $4d$ states (shown by gray filled curve for the layer above V monolayer and by red dashed lines for the layer below the V monolayer) and V $3d$ states (shown by solid blue lines) in the antiferromagnetic (AFM) configuration of (a) V/Ag(001), (b) 1Ag/V/Ag(001), (c) 2Ag/V/Ag(001) and (d) 3Ag/V/Ag(001).

configuration, we next compare our results with the ARPES data.

6.4.2 Comparison with experimental results

Our experimental collaborators have obtained both LEED and ARPES data for one monolayer of V grown on Ag(001). Although they do not find evidence of a $c(2 \times 2)$ superstructure in the LEED data, it is pointed out that this does not necessarily mean the absence of an AFM order, since short-range AFM ordering in the film can have length scales larger than the photoemission correlation length, but smaller than the LEED coherence length.[15] One can therefore, still expect AFM bands in the ARPES spectra. We have already shown that the 1Ag/V/Ag(001) structure in the AFM configuration is energetically most favoured. In order to confirm the experimental

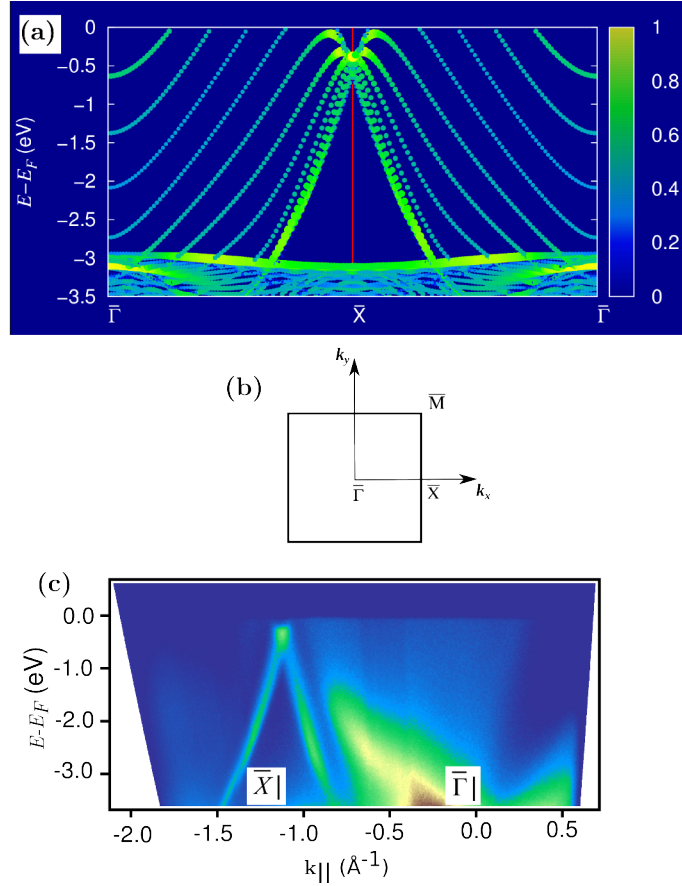


Figure 6.7: (a) shows the calculated projected band structure of the bare Ag(001) along the high symmetry direction $\bar{\Gamma} - \bar{X} - \bar{\Gamma}$, as shown in the surface Brillouin zone in (b). The ARPES data along the same path is shown in (c). Experimental data provided courtesy of K. S. R. Menon. E_F denotes the Fermi energy. In the colour scale of the calculated band structure, ‘yellow’ and ‘dark blue’ indicates highest (one) and lowest (zero) projection.

findings, in this section we compare the AFM results for the 1Ag/V/Ag(001) structure with the experimental ARPES data.

We first compare our calculated band structure with the ARPES data obtained for the bare Ag(001) surface in Fig. 6.7 along the high-symmetry direction $\bar{\Gamma} - \bar{X} - \bar{\Gamma}$. In Fig. 6.7(a), the band structure is produced by projection on atoms in the first three layers (both top and bottom) of the slab. The color bar represents the amount of projection from these layers with highest projection normalized to one, and denoted by yellow, whereas zero projection is represented by blue colour. Since this band structure is produced using a 1×1 unit cell, no unfolding is required. We find that

the band structure is in good agreement with the ARPES data, in the sense that the linearly dispersive band with highest intensity near \bar{X} matches well with the corresponding band seen in the ARPES spectra.

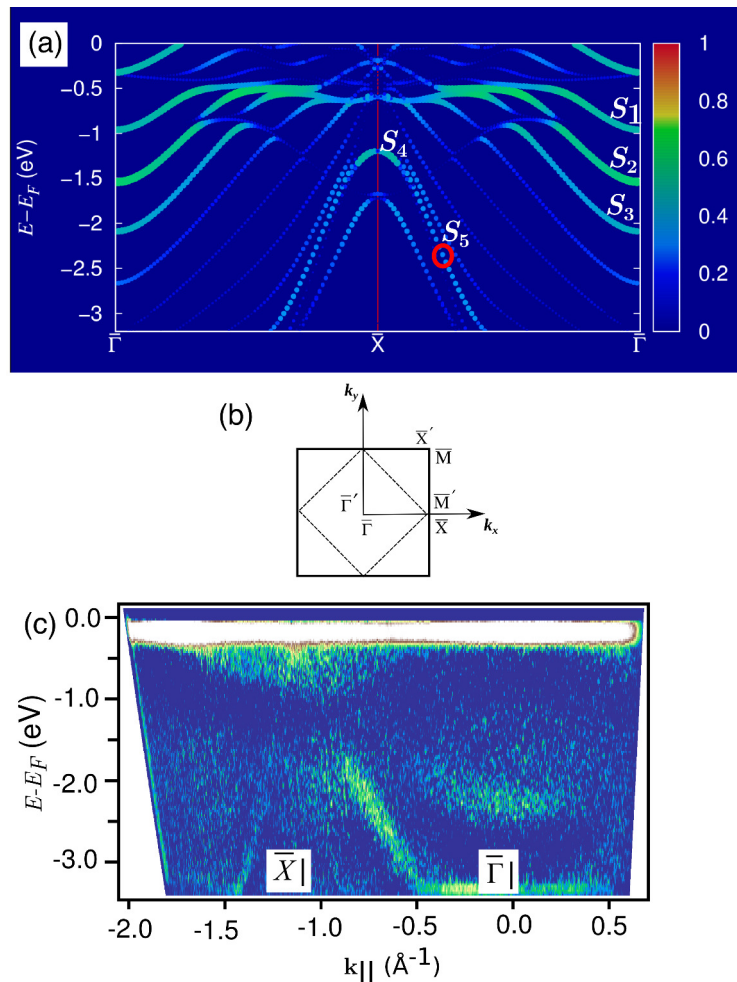


Figure 6.8: Calculated band structure of 1Ag/V/Ag(001) system for the AFM configuration is plotted in (a), along the high-symmetry direction $\bar{\Gamma} - \bar{X} - \bar{\Gamma}$. (b) shows the surface Brillouin zone corresponding to the 1×1 cell (solid square and high symmetry points $\bar{\Gamma}, \bar{X},$ and $\bar{\Gamma}$), and $\sqrt{2} \times \sqrt{2}$ cell (dashed square and high symmetry points $\bar{\Gamma}', \bar{X}'$ and $\bar{\Gamma}'$). The second derivative of the ARPES data along the same direction is shown in (c). Experimental data provided courtesy of K. S. R. Menon. E_F denotes the Fermi energy. In the colour scale of the calculated band structure, ‘red’ and ‘dark blue’ indicates highest (one) and lowest (zero) projection.

We have plotted the calculated band structure of the AFM configuration of the 1Ag/V/Ag(001) system in Fig. 6.8(a), along with the second derivative of the corresponding ARPES data in Fig. 6.8(c). The unfolding of band structure from the Brillouin zone of the $\sqrt{2} \times \sqrt{2}$ cell [shown in the figure by the dashed square

and high symmetry points $\bar{\Gamma}'$, \bar{X}' and \bar{M}' in Fig. 6.8 (c)] to the Brillouin zone of the 1×1 cell [shown in the figure in the figure by the solid square and high symmetry points $\bar{\Gamma}$, \bar{X} and \bar{M} in Fig. 6.8 (c)] is necessary since an AFM configuration cannot be defined in the primitive chemical unit cell. The colour scale denotes the amount of projection of the atomic states corresponding to the top two layers of the slab, i.e., the overlayer Ag atoms and the subsurface V atoms. Both the radius and the colour of the circles change proportional to the amount of projection. The ‘red’ represents highest projection while ‘dark blue’ represents zero projection. In the case of the calculated AFM band structure in Fig. 6.8(a), we find the majority and minority bands are degenerate in the entire energy range considered here.

In order to compare the AFM band structures with the ARPES data, we choose five states, namely, $S_1 - S_3$ at the $\bar{\Gamma}$ point, S_4 at the \bar{X} point and S_5 at a k -point [(0.3580, 0.3580, 0) in $2\pi/a$ units, marked by a red circle] in the $\bar{X} \rightarrow \bar{\Gamma}$ direction in the surface Brillouin zone, as shown in Fig. 6.8(a). We find that, upon deposition of V, the morphology of the bands changes considerably, as can be seen by comparing the projected band structure of bare Ag(001) [see Fig. 6.7 (a)], with that of the 1Ag/V/Ag(001) [see Fig. 6.8(a)]. When we compare the experimental ARPES data of the 1Ag/V/Ag(001) system in Fig. 6.8(c) with that of the bare Ag(001) in Fig. 6.7(c), we note the appearance of an extra band at the $\bar{\Gamma}$ point at ~ -2 eV. The dispersion of this band correlates well with that of S_2 at -1.5 eV in the calculated band structure [see Fig. 6.8 (a)], having the highest intensity among $S_1 - S_3$. This provides further evidence that the 1Ag/V/Ag(001) structure prefers AFM ordering. It should be noted that there is an offset in energy in the position of the states at the $\bar{\Gamma}$ point when comparing calculated and experimental results. This is due to the fact that the ARPES data is taken at 428 K, and it is found that with lowering the temperature the bands at the $\bar{\Gamma}$ point go up in energy.[15] Thus ARPES data at lower temperature should show better agreement with the calculated band structure. Unfortunately, at the same time, when the temperature is lowered, the quality of the ARPES data is

found to degrade, and therefore, we present comparison with the high temperature ARPES data.

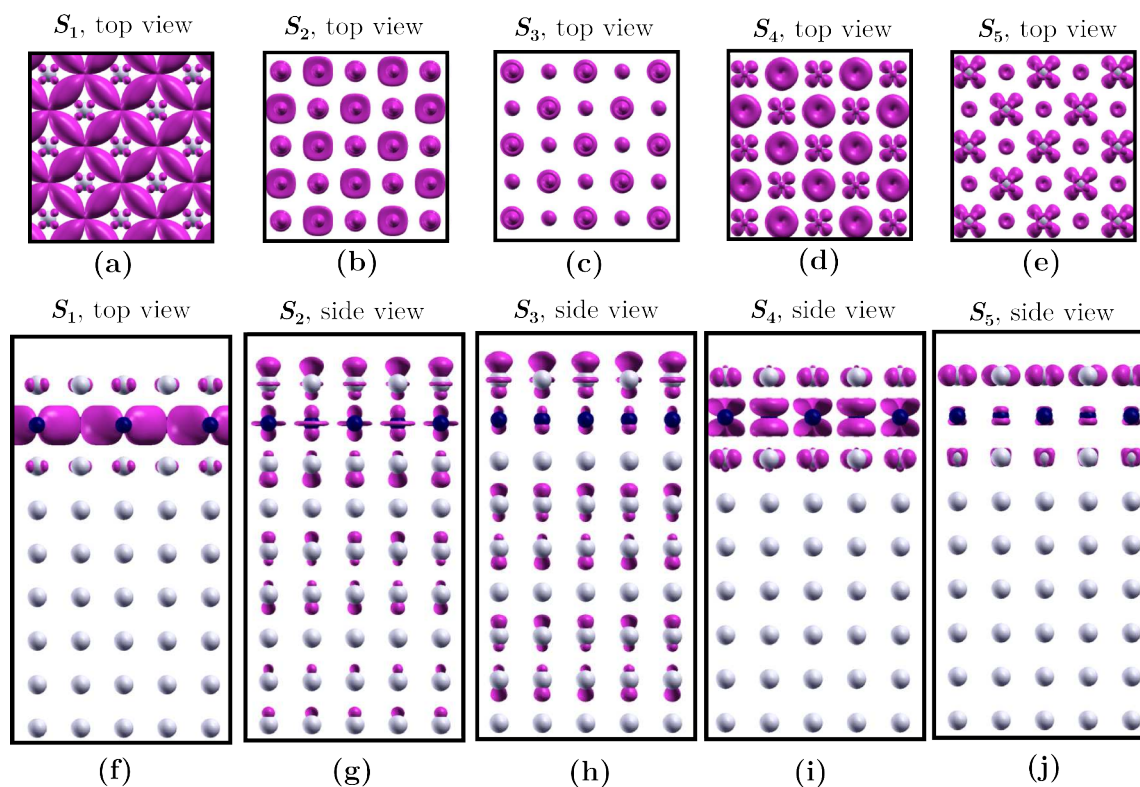


Figure 6.9: The top [(a)-(e)] and side views [(f)-(j)] of the electronic charge densities (magenta) corresponding to states $S_1 - S_5$ of the AFM 1Ag/V/Ag(001) system. The top view correspond to the $x - y$ plane whereas side views correspond to $x - z$ plane. The blue and gray spheres represent V and Ag atoms respectively. The isosurface value used for the charge density is 0.002 electron/a.u.³.

To gain further insight into the origin of these states, in Fig. 6.9 we plot the electronic charge densities corresponding to these states for the AFM configuration of 1Ag/V/Ag(001) structure. The states S_1 , S_2 , S_3 , S_4 and S_5 appear at energies $E - E_F$ of -0.99 eV, -1.54 eV, -2.14 eV, -1.2 eV, and -2.59 eV, respectively. Analyzing the charge density profiles and the corresponding PDOS, we see that S_1 and S_4 have major contributions from subsurface V atoms; S_1 originates primarily from the $3d_{xy}$ orbitals of the sub-surface V atoms, whereas S_4 arises mostly from from $3d_{zx}$ and $3d_{zy}$ orbitals of V atoms. While S_2 shows partial contribution from the $3d_{z^2}$ orbital of the V atoms, S_5 arises primarily from Ag atoms at the surface. S_3 shows major contribution from the $4d_{z^2}$ orbital of the Ag atom at the surface, and

the charge density is found to decay gradually into the bulk.

6.5 Conclusions

Using density functional theory, we have studied the structural and magnetic properties of a monolayer of V deposited on Ag(001). Experiments find additional surface states in the ARPES spectra upon deposition of V on Ag(001), when compared to bare Ag(001). This suggests Ag segregation on top of V. The energetics computed using DFT, of different V/Ag(001) systems which differ in how far the V layer is buried under the Ag layer, show that V wants to go sub-surface, i.e., V gets buried under a single layer of Ag, and prefers AFM ordering. The larger exchange splitting in the AFM ordered 1Ag/V/Ag(001) system, stabilizes it over the FM ordered one. The DFT calculated band structure projected on the surface layers, shows the presence of surface states, whose dispersion agrees with that seen in the ARPES data. We find that these surface states arise from the sub-surface V atoms.

Bibliography

- [1] V. Baltz, A. Manchon, M. Tsoi, T. Moriyama, T. Ono, and Y. Tserkovnyak, “Antiferromagnetic spintronics,” *Rev. Mod. Phys.*, vol. 90, p. 015005, Feb 2018.
- [2] V. K. Joshi, “Spintronics: A contemporary review of emerging electronics devices,” *Engineering Science and Technology, an International Journal*, vol. 19, no. 3, pp. 1503 – 1513, 2016.
- [3] P. Grundy, “Review article: Thin film magnetic recording media,” *Journal of Physics D Applied Physics*, vol. 31, pp. 2975–2990, 11 1998.
- [4] S. Blügel, M. Weinert, and P. H. Dederichs, “Ferromagnetism and antiferromagnetism of 3d-metal overlayers on metals,” *Phys. Rev. Lett.*, vol. 60, pp. 1077–1080, Mar 1988.

- [5] M. Stampanoni, A. Vaterlaus, M. Aeschlimann, and F. Meier, “Magnetism of epitaxial bcc iron on Ag(001) observed by spin-polarized photoemission,” *Phys. Rev. Lett.*, vol. 59, pp. 2483–2485, Nov 1987.
- [6] C. A. Ballentine, R. L. Fink, J. Araya-Pochet, and J. L. Erskine, “Magnetic phase transition in a two-dimensional system: $p(1 \times 1)$ -Ni on Cu(111),” *Phys. Rev. B*, vol. 41, pp. 2631–2634, Feb 1990.
- [7] P. Krüger, M. Taguchi, and S. Meza-Aguilar, “Magnetism of 3d transition-metal monolayers on Cu(111) and Ag(111),” *Phys. Rev. B*, vol. 61, pp. 15277–15283, Jun 2000.
- [8] J. Das, S. Biswas, K. Ulman, R. Banerjee, G. Gautam, A. K. Kundu, S. Narasimhan, and K. S. R. Menon, “Electronic structure of a buried two-dimensional antiferromagnetic layer: Experimental and theoretical investigation of Ag/Cr/Ag(001),” *Phys. Rev. B*, vol. 98, p. 075137, Aug 2018.
- [9] C. Rau, G. Xing, and M. Robert, “Ferromagnetic order and critical behavior at surfaces of ultrathin V(100) $p(1 \times 1)$ films on Ag(100),” *Journal of Vacuum Science & Technology A*, vol. 6, no. 3, pp. 579–581, 1988.
- [10] M. Stampanoni, A. Vaterlaus, D. Pescia, M. Aeschlimann, F. Meier, W. Dürr, and S. Blügel, “Lack of evidence for ferromagnetism in the vanadium monolayer on Ag(001),” *Phys. Rev. B*, vol. 37, pp. 10380–10382, Jun 1988.
- [11] R. L. Fink, C. A. Ballentine, J. L. Erskine, and J. A. Araya-Pochet, “Experimental probe for thin-film magnetism in $p(1 \times 1)$ Pd and V on Ag(100),” *Phys. Rev. B*, vol. 41, pp. 10175–10178, May 1990.
- [12] M. Finazzi, E. Kolb, J. Prieur, C. Boeglin, K. Hricovini, G. Krill, C. Chappert, and J.-P. Renard, “X-ray circular dichroism of thin $\text{Fe}_{0.82}\text{V}_{0.18}$ interlayers in Au(111),” *Journal of Magnetism and Magnetic Materials*, vol. 165, no. 1, pp. 373–376, 1997. Symposium E: Magnetic Ultrathin Films, Multilayers and Surfaces.

- [13] S. Blügel and P. H. Dederichs, “Ferromagnetism and antiferromagnetism of 3d metal overlayers on noble-metal substrates,” *Europhysics Letters (EPL)*, vol. 9, pp. 597–602, jul 1989.
- [14] J. S. Moodera and R. Meservey, “Exchange interactions of quench-condensed vanadium atoms on metal surfaces,” *Phys. Rev. B*, vol. 40, pp. 8541–8544, Oct 1989.
- [15] A. K. Kundu, *Growth, electronic structure and antiferromagnetism of early transition metal and metal oxide ultra-thin films*. PhD thesis, University of Calcutta, 1 2017.
- [16] P. Giannozzi, S. Baroni, N. Bonini, M. Calandra, R. Car, C. Cavazzoni, D. Ceresoli, G. L. Chiarotti, M. Cococcioni, I. Dabo, A. D. Corso, S. de Gironcoli, S. Fabris, G. Fratesi, R. Gebauer, U. Gerstmann, C. Gougoussis, A. Kokalj, M. Lazzeri, L. Martin-Samos, N. Marzari, F. Mauri, R. Mazzarello, S. Paolini, A. Pasquarello, L. Paulatto, C. Sbraccia, S. Scandolo, G. Sclauzero, A. P. Seitsonen, A. Smogunov, P. Umari, and R. M. Wentzcovitch, “QUANTUM ESPRESSO: a modular and open-source software project for quantum simulations of materials,” *Journal of Physics: Condensed Matter*, vol. 21, p. 395502, sep 2009.
- [17] J. P. Perdew, K. Burke, and M. Ernzerhof, “Generalized gradient approximation made simple,” *Phys. Rev. Lett.*, vol. 77, pp. 3865–3868, Oct 1996.
- [18] D. Vanderbilt, “Soft self-consistent pseudopotentials in a generalized eigenvalue formalism,” *Phys. Rev. B*, vol. 41, pp. 7892–7895, Apr 1990.
- [19] H. J. Monkhorst and J. D. Pack, “Special points for brillouin-zone integrations,” *Phys. Rev. B*, vol. 13, pp. 5188–5192, Jun 1976.
- [20] L. Liu and W. A. Bassett, “Compression of Ag and phase transformation of NaCl,” *Journal of Applied Physics*, vol. 44, no. 4, pp. 1475–1479, 1973.

-
- [21] P. V. C. Medeiros, S. Stafström, and J. Björk, “Effects of extrinsic and intrinsic perturbations on the electronic structure of graphene: Retaining an effective primitive cell band structure by band unfolding,” *Phys. Rev. B*, vol. 89, p. 041407, Jan 2014.

Chapter 7

Topological Phase Transitions

Induced by Giant Strains

Produced by Chemical Pressure

In this chapter, we study an alternative route of applying strain in germanene-like systems, namely, the chemical pressure, through functionalization of the germanene lattice. We show that chemical pressure can induce a topological phase transition in germanene-like systems and can, in principle, produce topological insulators at ambient conditions.

7.1 Introduction

Topological insulators (TIs), also known as quantum spin Hall insulators, are a recently identified class of materials.^[1] These materials possess an insulating band gap in the bulk, but the Fermi level is crossed by topologically protected edge states which are robust against disorder. These edge states allow dissipationless transport of charge and spin, making such materials promising candidates for use in a wide range of applications. ^[2–6]

The concept of topological insulators were first put forward by Kane and Mele in

2005,[1] where graphene was shown to be a topological insulator. But the extremely small spin-orbit gap in gap in graphene makes it unsuitable for application in devices. Subsequently the first realization of topological insulator was done in HgTe quantum wells.[7] Around the same time, Liang Fu *et al.* proposed three-dimensional topological insulators.[8] The class of topological insulators is identified by what is called by the Z_2 topological invariant. Whereas a single Z_2 index is used to identify two-dimensional TIs, in three-dimensions (3D) there are four invariants (one strong topological index, and three weak topological indices) which broadly classify 3D TIs into two classes, viz., the weak topological insulators (WTI), and the strong topological insulators (STI). For inversion symmetric systems, the calculation of Z_2 indices is quite straightforward, involving the computation of the parity of the bands at the time reversal invariant momenta (TRIM) points.[9] On the other hand, for the systems without inversion symmetry, one generally employs the method suggested by Soluyanov and Vanderbilt *et al.*, based on the concept of time-reversal polarization.[10] Since its discovery, many topological insulator materials in two- and three-dimensions have been suggested, and experimentally realized.[2, 4, 11]

Due to the presence of a strong topological index, and the potential ease of control of charge carriers by gating in nanoelectronic devices, two-dimensional (2D) TIs are of especial interest.[12, 13] However, compared to three-dimensional TIs, relatively few 2D TIs have been identified thus far, especially at ambient conditions. Considerable effort and ingenuity have been devoted to modifying the native prototypical structure of various 2D materials, either physically or chemically, so as to induce topological transitions. There are two general approaches for realization of 2D TIs:[14] (1) opening a band gap in 2D Dirac materials, such as graphene, germanene, and silicene by spin-orbit coupling, and (2) by inducing a band inversion in narrow-gap semiconductors, through strain, or electric field. For example, it has been shown that As and Sb bilayers become topological insulators at mechanical strains $> 6\%$.[15] Phosphorene bilayer has been shown to undergo a topological phase transition with an electric

field of $0.3 \text{ V}/\text{\AA}$.[\[16\]](#)

As mentioned above, some of the routes explored to obtain topological phase transition have been the application of strain, chemical functionalization, and doping.[\[13, 17–22\]](#) Some authors have explored the possibility of inducing a topological transition in 2D systems by doping or chemical pressure. Weeks *et al.* have tried to introduce large spin-orbit gap in graphene, by doping it with heavy adatoms like indium and thalium.[\[23\]](#) Chen Si *et al.* have tried to functionalize germanene by halogen atoms, achieving a maximum strain of 5% due to functionalization by iodine.[\[17\]](#) Xu *et al.* achieved a strain of 3.6% by changing the concentration of sulfur and selenium in $\text{BiTl}(\text{S}_{1-\delta}\text{Se}_\delta)_2$, to obtain a topological phase transition.[\[24\]](#) Thus, to date, the strains achieved, while admittedly large compared to the values that can be achieved by mechanical means, are still relatively modest.[\[24, 25\]](#) Here, we show that it is possible to achieve far larger values of strain through chemical pressure, that can induce topological transition at ambient conditions, or reduce the magnitude of the mechanical strain needed for the transition.

Germanene is analogous to graphene in that it is a monolayer of germanium atoms arranged in a honeycomb lattice, though the structure is buckled perpendicular to the plane of the monolayer.[\[26\]](#) Cahangirov *et al.* have shown theoretically, that the low-buckled structure (buckling $\Delta = 0.44\text{\AA}$) of germanene is more stable than the high-buckled one ($\Delta = 2.23\text{\AA}$).[\[27\]](#) It is pointed out that the transverse acoustic phonon branch of low-buckled structure of germanene has small imaginary frequencies near the zone center, which may be interpreted as implying that small flakes of germanene can be stable. At its equilibrium lattice constant of 3.97\AA , calculations have predicted that germanene should be a TI with a spin-orbit coupling (SOC) band gap of $\sim 24 \text{ meV}$.[\[27–30\]](#) Although small flakes of germanene have been shown to be stable, fabrication of germanene on a substrate without destroying its topological properties, has not yet been achieved.[\[14\]](#)

Ways of stabilizing germanene include functionalizing with -H and -CH₃ groups.[\[31,](#)

32] It is found that GeH is stable up to 75 °C, beyond which amorphization and dehydrogenation begins to occur. GeCH₃ has been shown to be stable up to 250 °C. Calculations have predicted that GeH and GeCH₃ should become TIs at tensile strains of 10% and 12%, respectively. [13, 33] Unfortunately, these values of strain are still rather high to be easily achievable.

In this work, we explore the alternative possibility of straining the germanene monolayer by systematically applying increasing chemical pressure. We do this by functionalizing instead with -CX₃ groups, where *X* is, in turn, one of the halogens F, Cl, Br and I. It is well-known that the atomic size increases as one progresses downward along a column of the periodic table. We show that one can also tune the induced strain in the system by using a combination of different halogen atoms in the form of functionalization by -CXY₂, where *X* and *Y* can be F or Cl atoms. This gives us flexibility in producing intermediate values of strain, not achieved in GeCX₃.

Below, we show that these chemical substitutions impose giant strains on the germanene lattice, which significantly modify the electronic structure, yet allow one to have a topologically non-trivial phase at either ambient conditions or at a smaller strain than for germanene functionalized with -CH₃.

7.2 Systems under study

To study the effect of chemical pressure, we have considered two types of functionalization of a single monolayer of germanene, viz., functionalization by -CX₃, and by -CXY₂. In the case of GeCX₃, the H atoms in GeCH₃ are replaced by a halogen *X* (*X* = F, Cl, Br and I). In GeCXY₂, the H atoms in GeCH₃ are replaced by a combination of two different halogen atoms *X* and *Y* (*X*, *Y* = F or Cl), resulting in GeCFCl₂ and GeCF₂Cl structures.

Figs. 7.1(a) and (b) show schematic top and side views of the parent structure of GeCX₃, we will refer to this as the *P* structure. We note that the *P* structure has a three-fold symmetry which can get destroyed upon applying chemical pressure,

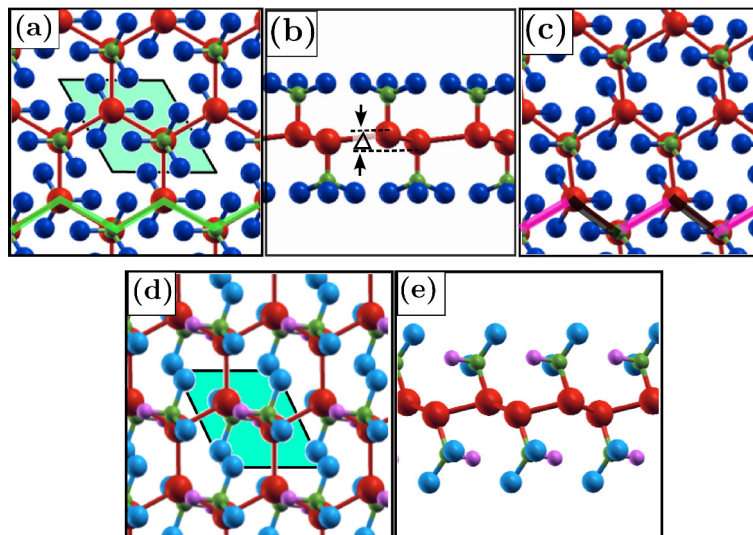


Figure 7.1: Panels (a) and (b) show schematic top and side views, respectively for the P - GeCX_3 structure. Panel (c) shows the top view of the D -structure of GeCCl_3 . (d) and (e) show the top and side views, respectively for the GeCXY_2 structure. The shaded rhombuses in (a) and (d) denote the unit cells of the respective structures. Red, Green and Blue spheres indicate Ge, C and X atoms, respectively. X can be H, F, Cl, Br or I in GeCX_3 , whereas X and Y can be F or Cl in GeCXY_2 . The black and magenta colored zigzag lines in (c) show bonds of different lengths due to distortion. In contrast, all the Ge-Ge bonds in (a) are equal in length.

resulting in a distorted (D) structure with lower symmetry, as shown in Fig. 7.1 (c). Figs. 7.1(d) and (e) show schematic top and side views, respectively of the GeCXY_2 structure. Each Ge atom is connected to a $-\text{CX}_3$ group, or a $-\text{CXY}_2$ group in the case of GeCX_3 , or GeCXY_2 , respectively. In GeCX_3 , the Ge atoms form a buckled honeycomb lattice, with alternate Ge atoms in each hexagon of the honeycomb displaced along $+\hat{z}$ and $-\hat{z}$, where the z direction is normal to the plane of the monolayer. In contrast, GeCXY_2 departs slightly from a pure honeycomb lattice, in the sense that the two in-plane primitive lattice vectors are unequal in length. GeCXY_2 also presents a buckled structure like GeCX_3 . The buckling in both the structures is characterized by Δ (see Fig. 7.1(b)), which is the sum of the displacements (from the central plane) of the alternate Ge atoms in each hexagon, along the $+\hat{z}$ and $-\hat{z}$ directions, perpendicular to the plane of the monolayer.

7.3 Computational details

Our calculations have been performed using *ab initio* density functional theory (DFT) as implemented in the Quantum-ESPRESSO package,[34] using a plane wave basis set, ultrasoft pseudopotentials [35] and the PBE form of the generalized gradient approximation.[36] The cut-offs for wave functions and charge densities are 40 Ry and 400 Ry respectively. Most calculations are also repeated using the HSE06 hybrid functional,[37] together with norm-conserving pseudopotentials.[38] van der Waals interactions are incorporated using the ‘DFT-D2’ method.[39, 40] Spin-orbit interactions are treated using fully relativistic pseudopotentials.[41] To minimize interactions between artificially periodic images along the z direction, a supercell length of 20 Å is used along z . A $12 \times 12 \times 1$ k -point mesh is used for Brillouin zone (BZ) summations. All atomic coordinates are relaxed until forces are $< 1.0 \times 10^{-3}$ Ry/bohr.

All structures considered in this paper are found to possess inversion symmetry. Therefore the topological invariant Z_2 is computed by evaluating the parity of the bands at the four time reversal invariant momenta (TRIM) points in the BZ, using the following equations:[4, 9]

$$\delta_i = \prod_m \xi_m(\Lambda_i), \quad (7.1)$$

where the product is over the pairs of parity eigenvalues of the occupied Kramers doublets resulting from the time reversal symmetry, at the TRIM points Λ_i , given by $\xi_m(\Lambda_i)$, without multiplying the corresponding time reversed partners. The Z_2 invariant ν is then given by

$$(-1)^\nu = \prod_{i=1}^4 \delta_i. \quad (7.2)$$

The nature of the bonding in the systems considered is analyzed by making use of the Crystal Orbital Hamilton Population (COHP), as implemented in the LOBSTER package.[42, 43]

7.4 Results and Discussion

7.4.1 Geometry and energetics

In this section we look at the geometrical parameters of the optimized structures of GeCX_3 , and GeCXY_2 . To get an idea of the chemical pressure induced in the respective systems due to functionalization, we will measure the strains in the systems when compared to GeCH_3 . Finally we will compare the thermodynamic stability of the various systems in terms of the cohesive energies. The details of the geometrical parameters, functionalization induced strains, and cohesive energies of the GeCX_3 , and GeCXY_2 systems, are summarized in Tables 7.1 and 7.2, respectively.

We find that the lattice constant of a monolayer of germanene is 4.00 \AA , while that of $P\text{-GeCH}_3$ is $a_0^H = 3.98 \text{ \AA}$, in good agreement with previous values.[27, 28, 32, 33] On replacing H by a halogen X in $P\text{-GeCH}_3$, the corresponding equilibrium lattice constant a_0^X increases relative to a_0^H . In Fig. 7.2(a), we have plotted our results for a_0^X , as well as the corresponding values of strain $\epsilon = (a_0^X - a_0^H)/a_0^H$. We see that as expected, by terminating germanene with -CX_3 containing halogen atoms X of increasingly larger size, we have succeeded in considerably expanding the lattice constant, thereby mimicking the effect of applying a significant tensile strain to the underlying germanene lattice: $\epsilon = 9.5\%$, 37.4% , 48.9% and 62.8% for $X = \text{F}$, Cl , Br and I , respectively. Achieving such large strains by mechanical means would of course be unfeasible. If a_0^X is determined primarily by steric interactions between the X atoms, then based on a hard sphere model, one would expect $a_0^X = 2\sqrt{3}r_X$, where r_X is the van der Waals radius for the element X . We see from Fig. 7.2(a) that the predictions of the hard sphere model are satisfied to a large extent for all the halogens X . We find that with the increase in lattice constant of GeCX_3 due to functionalization with larger halogen atoms, the buckling Δ reduces, as shown in Fig. 7.2(b).

In the GeCXY_2 systems, we find that the in-plane lattice constants a_1 and a_2 ,

Table 7.1: The following table shows the lattice constants (a_0^X), Ge-Ge bond lengths, buckling (Δ), strains with respect to P -GeCH₃ lattice constant (ϵ) and cohesive energies (E_{coh}), of germanene, P -GeCH₃ and P -GeCX₃ (X = F, Cl, Br and I) systems.

System	a_0^X (Å)	Ge-Ge bond length (Å)	Δ (Å)	ϵ (%)	E_{coh} (eV/formula unit)
Germanene	4.00	2.41	0.68	–	3.39
P -GeCH ₃	3.98	2.44	0.80	0	12.57
P -GeCF ₃	4.36	2.58	0.58	9.5	18.03
P -GeCCl ₃	5.47	3.19	0.39	37.4	11.30
P -GeCBr ₃	5.93	3.44	0.34	48.9	10.16
P -GeCl ₃	6.48	3.75	0.33	62.8	9.19

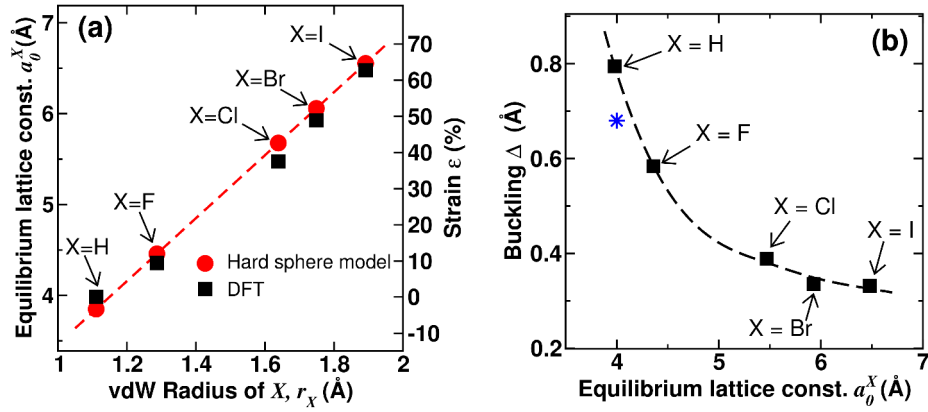


Figure 7.2: We compare equilibrium lattice constants as obtained from DFT and a hard-sphere model in (a). Panel (b) shows how the buckling Δ changes with the lattice constant of GeCX₃. The star in (b) denotes the value for germanene monolayer.

are unequal, as can be seen from the values presented in Table 7.2. The presence of two Cl atoms per Ge atom in GeCFCl₂, as compared to one Cl atom per Ge atom in GeCF₂Cl, increases the steric interaction in GeCFCl₂, compared to GeCF₂Cl, which results in larger chemical pressure in GeCFCl₂. This is reflected in the larger lattice constants a_1 and a_2 , and strains $\epsilon_{1,2} = (a_{1,2} - a_0^H)/a_0^H$ in GeCFCl₂, as compared to GeCF₂Cl. We note that the strains $\epsilon_{1,2}$ generated along the lattice vectors a_1 or a_2 , in GeCFCl₂, are larger than that in GeCF₃, but smaller than in GeCCl₃. This has implications on both the stability and the topological properties of GeCFCl₂, as will be discussed further below.

In order to compare the thermodynamic stability of the different systems considered,

Table 7.2: The following table shows the in-plane lattice constants along x and y, a_1 and a_2 , respectively, Ge-Ge bond lengths, buckling (Δ), strains with respect to P -GeCH₃ lattice constants along a_1 and a_2 , ϵ_1 and ϵ_2 , respectively, and cohesive energies (E_{coh}), of GeCF₂Cl and GeCFCl₂ systems.

System	a_1 (Å)	a_2 (Å)	Ge-Ge bond length (Å)	Buckling (Δ) (Å)	ϵ_1 (%)	ϵ_2 (%)	E_{coh} (eV)
GeCF ₂ Cl	4.33	4.24	2.58	0.69	8.8	6.5	15.83
GeCFCl ₂	4.77	4.83	2.77	0.65	19.8	21.4	13.47

we compute their cohesive energies. The cohesive energies of the GeCX₃ (E_{coh}^X), and the GeCXY₂ ($E_{\text{coh}}^{XY_2}$) are defined as:

$$E_{\text{coh}}^X = -[E_{\text{tot}}(\text{GeCX}_3) - 2E_{\text{tot}}^{\text{iso}}(\text{Ge}) - 2E_{\text{tot}}^{\text{iso}}(\text{C}) - 6E_{\text{tot}}^{\text{iso}}(\frac{1}{2}X_2)]/2, \quad (7.3)$$

and,

$$E_{\text{coh}}^{XY} = -[E_{\text{tot}}(\text{GeCXY}_2) - 2E_{\text{tot}}^{\text{iso}}(\text{Ge}) - 2E_{\text{tot}}^{\text{iso}}(\text{C}) - 2E_{\text{tot}}^{\text{iso}}(\frac{1}{2}X_2) - 4E_{\text{tot}}^{\text{iso}}(\frac{1}{2}Y_2)]/2. \quad (7.4)$$

where $E_{\text{tot}}(\text{GeCX}_3)$, and $E_{\text{tot}}(\text{GeCXY}_2)$ are the total energies, as computed using DFT, of a unit cell of GeCX₃ and GeCXY₂, respectively (containing two formula units), and $E_{\text{tot}}^{\text{iso}}(A)$ is the total energy of an isolated atom A . We note that all the cohesive energies presented in Tables 7.1 and 7.2, are positive, signifying that it is thermodynamically feasible to form these structures. Interestingly, GeCF₃ has the highest cohesive energy among all the structures. GeCF₂Cl and GeCFCl₂ have higher cohesive energies than GeCH₃, whereas GeCCl₃ has marginally lower cohesive energy than GeCH₃. This shows that by substituting H in GeCH₃ by different halogen atoms of larger size, one can improve the thermodynamic stability of the system. In terms of thermodynamic stability, GeCF₃, GeCF₂Cl, GeCFCl₂, and GeCCl₃ have higher cohesive energies among the systems considered, and thus we will focus on these systems to explore their electronic and topological properties.

7.4.2 Electronic properties: effect of mechanical strain in GeCH₃ and GeCF₃

In this section we look at the electronic properties of the GeCH₃ and GeCF₃ systems at ambient conditions and under external mechanical strain. To apply mechanical tensile and compressive strain on the respective structures, the in-plane lattice vectors are stretched or compressed equally. The strain is defined as $\epsilon^X \equiv (a - a_0^X)/a_0^X$, with its positive/negative value indicating tensile/compressive strains. Note that unlike ϵ [presented in Fig. 7.2 (a) above], here the strain ϵ^X is defined relative to a_0^X , the equilibrium lattice constant not of GeCH₃ but of GeCX₃.

We first consider the effects of replacing H by F in *P*-GeCH₃. We find that at their equilibrium lattice constants, *P*-GeCH₃ and *P*-GeCF₃ exhibit direct band gaps E_g of 1.15 eV (1.75 eV) and 0.44 eV (0.86 eV), at the zone center, when computed with the PBE (HSE) functional; the experimental value for GeCH₃ is 1.7 eV.[32] In Figs. 7.3(a) and (b), we show how E_g varies with strain for GeCH₃ and GeCF₃, in the absence of SOC. We see that for GeCH₃, E_g decreases upon applying tensile strain, becoming zero at a critical value $\epsilon_c^X = 10\%$ (14%) with PBE (HSE). Fig. 7.3(b) shows that for GeCF₃, the value of ϵ_c^X is considerably reduced, to 5% (7%) with PBE (HSE). On including SOC, the band gaps at ϵ_c^X for GeCH₃ and GeCF₃ are 0.12 eV and 0.09 eV, respectively. In the subsequent section we will show that at these critical strains GeCH₃ and GeCF₃ undergo topological phase transitions, and become topological insulators (TIs). The data in Figs. 7.3(a) and (b) are re-plotted in Fig. 7.3(c), with the abscissa as the lattice constant a of GeCX₃. We see that E_g appears to be primarily determined by the lattice constant a , though the slight differences in E_g for GeCH₃ and GeCF₃ at the same values of a suggest that there may also be small chemical effects.

The observed non-monotonic behaviour of the band gap E_g as a function of strain ϵ^X for GeCH₃ (see Fig. 7.4) is not uncommon in two-dimensional materials; similar behavior has also been seen for other monolayer systems, e.g., MoS₂ and

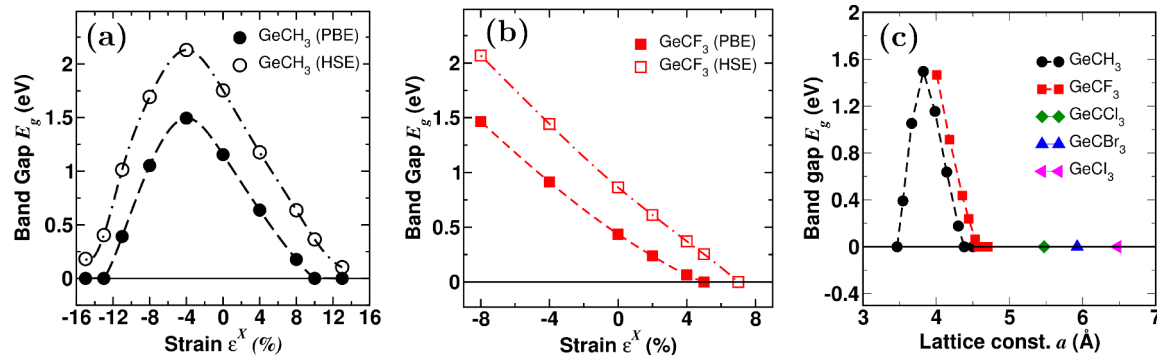


Figure 7.3: Straining the germanene lattice by chemical pressure: the P structure of GeCX_3 . Panels (a) and (b) show the band gap E_g (without SOC) for GeCH_3 and GeCF_3 , respectively. Negative (positive) strains correspond to compressive (tensile) strains, and filled (empty) symbols represent PBE (HSE) results. In (c) we show how E_g varies with lattice constant a for all halogens X .

phosphorene.[44, 45] To understand the reason behind such a behaviour, we compute the Crystal Overlap Hamilton[ian] Population (COHP),[42] making use of the LOBSTER package.[43] The COHP separates out pairwise atom-resolved contributions to the band-structure energy of a system; most notably if the negative of the COHP is positive/negative, then the corresponding state has bonding/antibonding character. We recall the expectation that in general (e.g., for the simple case of a two-level system in a diatomic molecule), as two interacting systems are brought closer together, bonding states move down in energy, whereas anti-bonding states move up in energy. In Fig. 7.4 we plot the COHP for the VBM and CBM for GeCH_3 , as a function of strain ϵ^X , for Ge-Ge and Ge-C bonds. We see that the COHP does not change appreciably with strain for the VBM, whereas there are pronounced changes in the COHP for the CBM. This suggests that changes in E_g are governed primarily by changes in the nature of the CBM. As expected, the behavior of the CBM is governed mainly by the nature of Ge-Ge bonds. We see that as we move away from $\epsilon^X = 0\%$, i.e., as we apply either a compressive or tensile strain, $-\text{COHP}$ becomes progressively more positive for Ge-Ge bonds. This means that the contribution from Ge-Ge bonds acquires a more bonding character, and the CBM should move down in energy, which would tend to decrease the band gap. However, we note that the behavior of

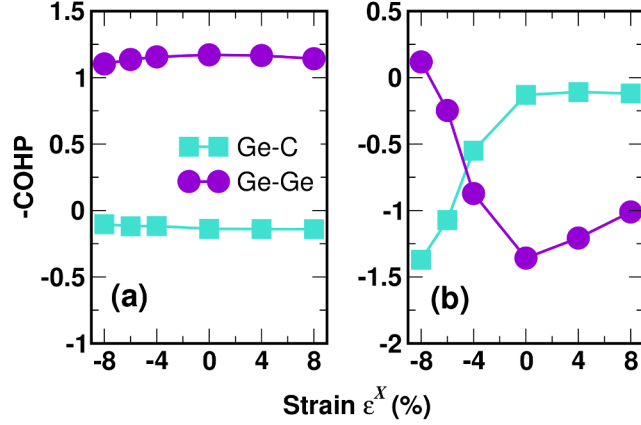


Figure 7.4: -COHP plots of GeCH₃ for (a) VBM and (b) CBM, at different values of strain. Turquoise squares and violet circles indicate contributions to COHP from Ge-C and Ge-Ge pairwise interactions.

the $-\text{COHP}$ for the Ge-C bonds is opposite that for Ge-Ge bonds, with the states acquiring a more antibonding character as compressive strain is applied. Due to the CBM having a small contribution from Ge-C bonds, the maximum band gap is moved away from zero strain to $\epsilon^X = -4\%$. This explains the observed behaviour of the electronic band gap with strain in GeCH₃. We expect that the approach developed above is quite general and can be applied to understand the non-monotonic behaviour in the band gap as a function of strain in other two-dimensional systems as well.

7.4.3 Topological phase transitions

We discuss here the topological phase transitions in the GeCX₃ and GeCXY₂ systems. We will see that replacing H atoms in GeCH₃ with bigger halogen atoms can induce topological phase transitions at ambient conditions, or reduce the strain needed for the transition.

We find that GeCH₃ and GeCF₃ become TIs at tensile strains ϵ^X of 10% and 5%, respectively (PBE values). While this result is known for GeCH₃, for GeCF₃, this represents a new finding, and shows that replacing H by F considerably reduces the strain at which the topological transition occurs. The presence of the topological insulator phase has been verified by computing the Z_2 invariant using Eqd. (8.1) and

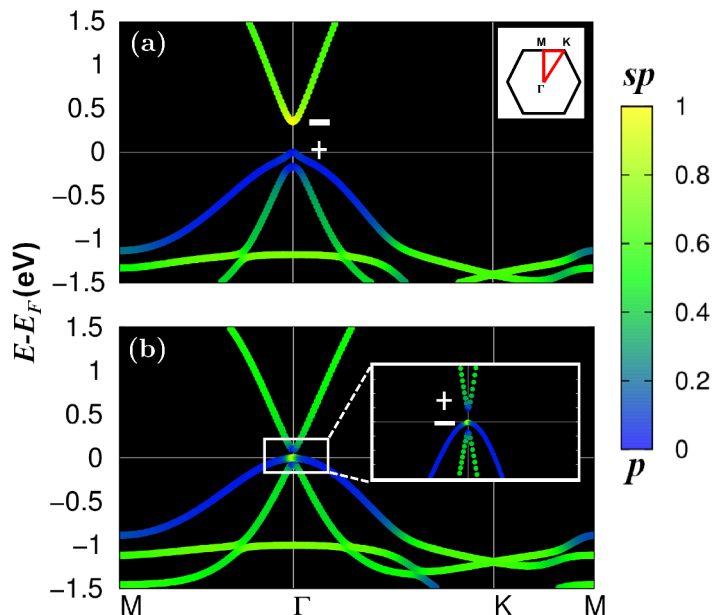


Figure 7.5: Orbital projected band structure of $P\text{-GeCF}_3$ at strain $\epsilon^X =$ (a) 0% and (b) 5%. The color indicates the fractional contribution of Ge- sp orbitals (yellow) relative to Ge- p orbitals (blue).

(8.2), as well as observing band inversion and the presence of conducting edge states.

In order to demonstrate the existence of band inversion, in Fig. 7.5 we plot the orbital-projected electronic band structure of GeCF_3 (using PBE+SOC) at strains ϵ^X of 0% and 5%. In these figures, the color of the bands shows the orbital nature, with yellow and blue colors indicating purely sp -like and purely p -like character, respectively; intermediate colors indicate a mixed nature, according to the drawn color bar. We see that at $\epsilon^X = 0\%$, the valence band maximum (VBM) at the Γ point has p -like nature with parity +1, whereas the conduction band minimum (CBM) has sp nature with parity -1 . This situation is reversed at $\epsilon^X = 5\%$, with the VBM having sp -like nature with parity -1 , and the CBM having p -like nature with parity +1. In other words, a band inversion has occurred.

The presence of the conducting edge states has been verified by calculating the band structure of a nanoribbon of the strained (5%) GeCF_3 , periodic in the [100] direction and of length 23.8 nm in the [010] direction. The band structure shown in Fig. 7.6 is obtained using the tight-binding approximation, with parameters obtained

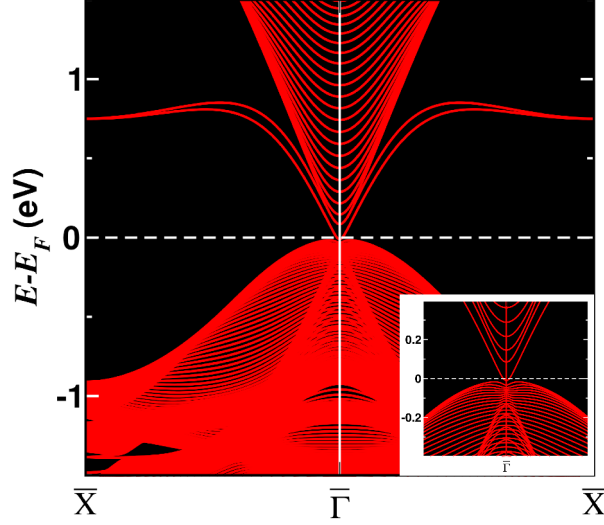


Figure 7.6: Band structure of a nanoribbon of GeCF_3 under 5% tensile strain. A pair of topologically protected edge states can be seen to cross the Fermi level at the zone center. The inset shows the zoomed in view of the pair of edge states crossing the Fermi level near the zone center.

by Wannierization of our DFT results, using the WannierTools package.[46] In this figure, one can see a pair of topologically protected edge states crossing the Fermi level at the center of the one-dimensional Brillouin zone corresponding to the nanoribbon.

Next we replace the H atoms in GeCH_3 by Cl atoms. We find that it is no longer necessary to strain the system to observe a topologically non-trivial phase: calculation of Z_2 for $P\text{-GeCCl}_3$ at $\epsilon^X = 0$ reveals that it is a TI. However, computing the phonon frequencies for this structure reveals the presence of imaginary modes, i.e., this compound is not dynamically stable in the P structure. By displacing the atoms along the eigenvectors of the imaginary mode, we find a lower-energy stable structure for GeCCl_3 , we call this the distorted or D structure [see Fig. 7.1(c)]. The stabilization in energy due to distortion is small (35 meV/primitive unit cell), and the lattice constant is unchanged. The distortion consists primarily of a symmetry-lowering in-plane distortion of the Ge atoms within the unit cell for GeCCl_3 , similar to the Peierls distortion of one-dimensional atomic chains. Thus, while all the ‘green’ Ge-Ge bonds in $P\text{-GeCCl}_3$ [see Fig. 7.1(a)] have length 3.18 Å, the ‘magenta’ and ‘black’ Ge-Ge bonds in $D\text{-GeCCl}_3$ [see Fig. 7.1(c)] have lengths of 3.57 Å and 3.04 Å,

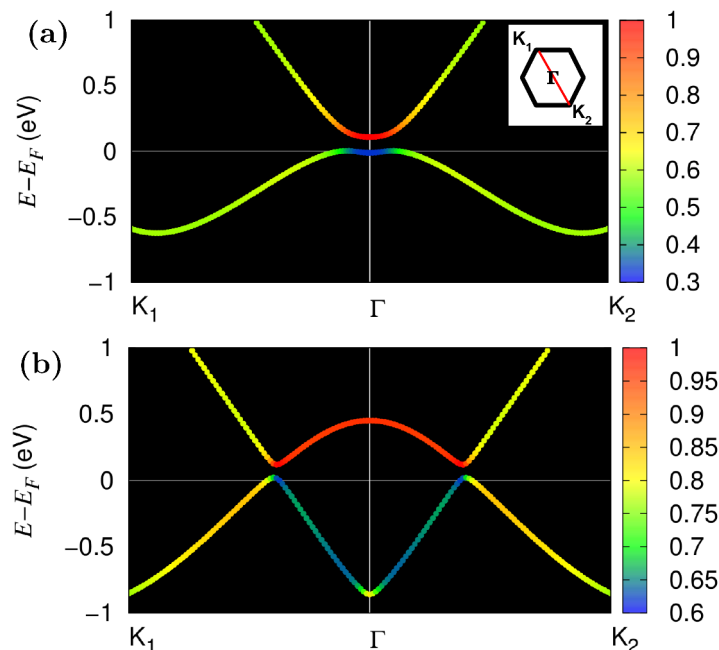


Figure 7.7: (Projected band structures (PBE+SOC) of (a) P -GeCCl₃ and (b) D -GeCCl₃, for the topmost valence band and lowest-lying conduction band. The color indicates the fractional contribution of p , $j = 3/2$ relative to p , $j = 1/2$, with red color corresponding to totally $j = 3/2$ character; note that the color scales are different in (a) and (b). The inset in (b) shows the 2D Brillouin zone.

respectively. The dynamical stability of the D -GeCCl₃ structure has been studied in detail in the next section. The electronic structure, in particular the topography of the valence and conduction bands, is significantly modified as a result of the distortion. In Figs. 7.7(a) and (b), we have plotted the orbital-projected band structure along high-symmetry directions of the BZ for the P and D structures; we see that as a result of the distortion, the VBM and CBM shift from Γ to two points in the BZ lying along the K_1 - Γ - K_2 direction. Interestingly and importantly, the D structure is also a topological insulator, with a SOC band gap of 0.1 eV. The band inversion for D -GeCCl₃ is evident in Fig. 7.7(b).

In Fig. 7.8(a), we show the topography of the topmost valence band and lowest-lying conduction band, for the whole BZ, for D -GeCCl₃. The band-structure is characterized by the presence of two Dirac-cone-like features. In Fig. 7.8(b), we have plotted the band structure of a nanoribbon of D -GeCCl₃, periodic in the $[100]$ direction and of length 28.4 nm in the $[010]$ direction. A pair of edge states can

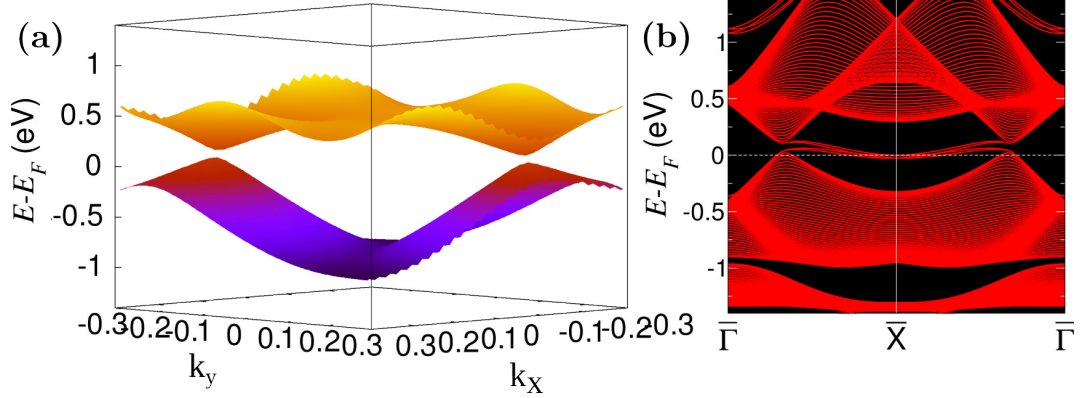


Figure 7.8: Band structure of D -GeCCl₃ (PBE+SOC): Panel (a) shows the topography of the topmost valence band and the bottommost conduction band, and (b) shows the band structure of a nanoribbon, characterized by the presence of topologically protected edge states crossing the Fermi level.

be seen to cross the Fermi level at the edge of the one-dimensional Brillouin zone corresponding to the nanoribbon [see Fig. 7.8(b)].

We find that both GeCBr₃ and GeCl₃ are TIs in the P structure, but are again dynamically unstable. However, unlike the case of GeCCl₃, GeCBr₃, on going to the D -structure, becomes a trivial insulator with an indirect band gap of 0.63 eV. For GeCl₃, we are unable to find a dynamically stable structure.

In section 4.1, we have seen that GeCFCl₂ has a lattice constant in between that of GeCF₃ and GeCCl₃, which reduces the chemical pressure in GeCFCl₂, compared to GeCCl₃. It is also thermodynamically more stable than GeCCl₃. The next step is therefore to see whether one can achieve topological phase transition in GeCFCl₂ in absence of any external mechanical strain. Importantly, we find that the Z_2 invariant of the GeCFCl₂ system is 1, signifying the existence topological insulator phase at a lower chemical pressure than GeCCl₃ and at ambient conditions. The orbital projected band structure (using PBE+SOC) of GeCFCl₂ in Fig. 7.9 shows the presence of sp -type band inversion as is found in GeCF₃, at 5 % strain. Interestingly, GeCFCl₂ has a band gap (PBE+SOC) of 0.23 eV, which is twice the band gap of D -GeCCl₃, making it a large-gap TI.

We find that GeCF₂Cl, with a chemical pressure much lower than GeCFCl₂, is a

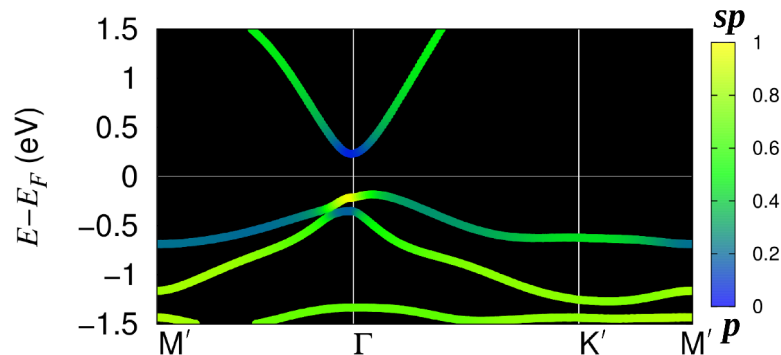


Figure 7.9: Orbital projected band structure (PBE+SOC) of GeCFCl_2 . The color indicates the fractional contribution of Ge- sp orbitals (yellow) relative to Ge- p orbitals (blue).

trivial insulator with a band gap (GGA) of 0.70 eV at zero strain.

7.4.4 Dynamical stability

We now look at the dynamical stability of the systems which we find to be TIs either at ambient conditions, or under mechanical strain, namely, GeCF_3 , GeCCl_3 , and GeCFCl_2 . For this purpose we calculate the phonon band structures of these systems along the high symmetry paths in the BZ.

In Figs. 7.10(a) and (b), we present the phonon band structures of the GeCF_3 system, at 0%, and at 5% strains, respectively. The absence of imaginary modes as shown in Fig. 7.10 (a), suggests that GeCF_3 is dynamically stable at ambient conditions. At 5% strain, we see a softening of the acoustic branch very close to the zone center, which generally corresponds to long wavelength ripples in the structure, and is a well-known feature in monolayer systems, such as graphene and MoS_2 , under strain.[47, 48] The absence of imaginary phonon frequencies at other k -points away from the zone-center, indicates that GeCF_3 is dynamically stable at 5% strain, where it is shown to be a TI. Further verification of the stability of these structures is obtained by performing *ab initio* molecular dynamics (MD) simulations using a 3×3 orthorhombic supercell containing 180 atoms, where we find that the structure do remains stable at a temperature of 300 K, for a 8 picoseconds run.

The presence of imaginary modes at all the k -points in the BZ, for P - GeCCl_3

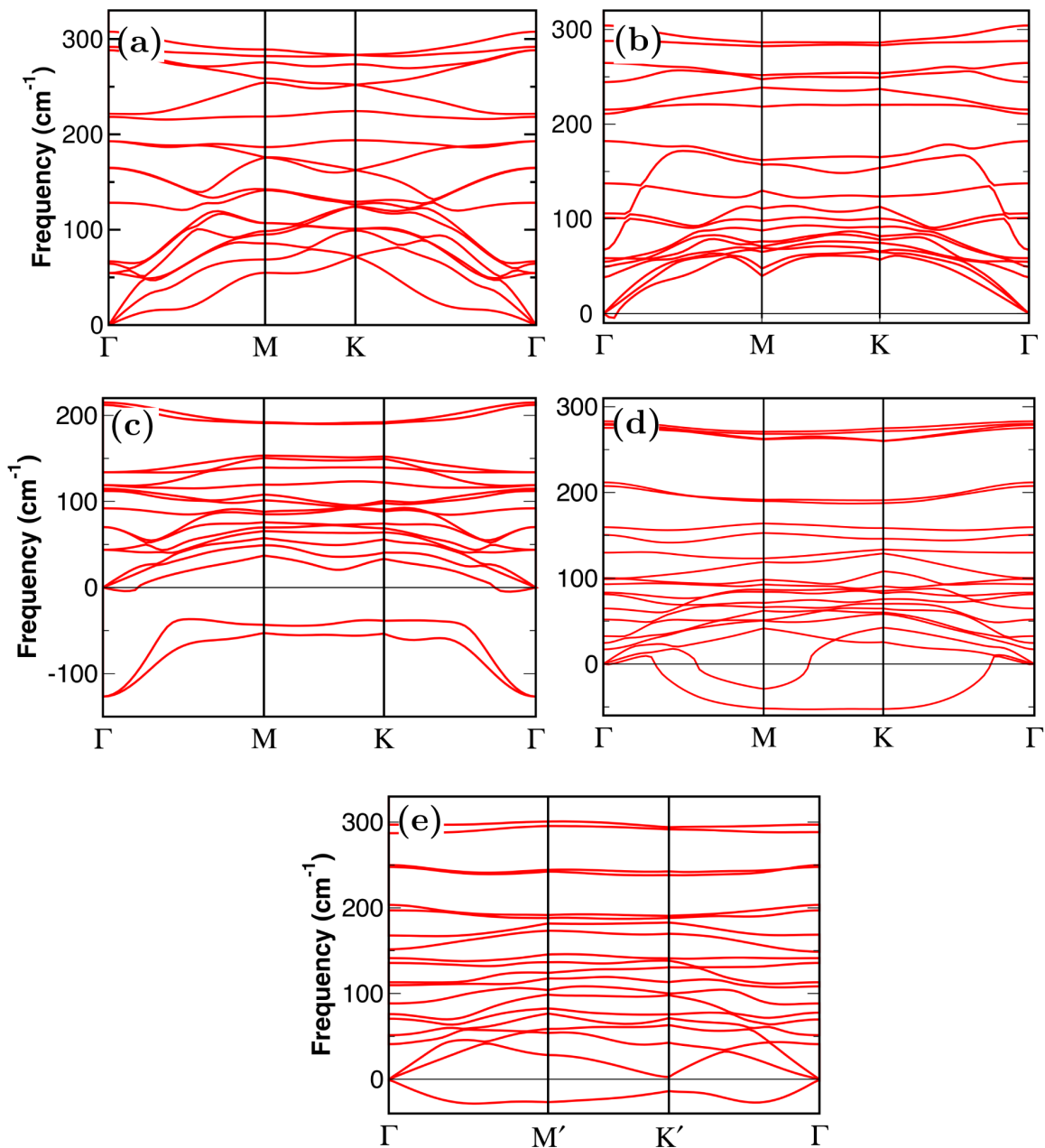


Figure 7.10: Phonon band structures of GeCF₃ at (a) 0%, and (b) 5% strains. In panels (c) and (d) we plot the phonon bands for the *P*-GeCCl₃, and *D*-GeCCl₃ systems. (e) shows the phonon band structure of GeCFCl₂.

[see Fig. 7.10 (c)], suggests that the structure is dynamically unstable. As mentioned above in section 4.3, removal of imaginary modes by displacing the atoms along the eigenvectors of the imaginary mode at the zone center, results in the D -GeCCl₃ structure. In Fig. 7.10 (d), we plot the phonon band structure of D -GeCCl₃. We find that the symmetry lowering distortion removes the negative phonon frequencies near the zone center, although it fails to remove imaginary modes from other k -points, e.g., near the M and K high-symmetry points in the BZ. We find that this distortion breaks the three-fold symmetry of the honeycomb lattice, resulting in unequal Ge-Ge bond lengths, as shown by magenta and black lines in Fig. 7.1 (c), though the lattice parameters remain unchanged.

As discussed in Section 4.1, comparison of cohesive energies shows that GeCFCl₂ is thermodynamically more stable than GeCCl₃. The phonon band structure of GeCFCl₂ shown in Fig. 7.10 (e), reveals that although GeCFCl₂ contains imaginary modes like D -GeCCl₃, the magnitude of the frequencies is much less negative than compared to D -GeCCl₃. *ab initio* MD simulation using a 4×4 orthorhombic supercell containing 320 atoms, shows that the structure remains stable at temperature 20 K, during a 8 picoseconds run. Therefore, we expect that GeCFCl₂ can prove to be a suitable candidate for low temperature applications, e.g., dissipationless transistors in quantum computers.[49]

7.5 Conclusions

In summary, we have found that by functionalizing germanene by $-CX_3$ groups, where X is a halogen, as one goes down the column, one produces a progressively greater strain in the system due to increased steric repulsion between neighboring $-CX_3$ groups. The giant strains thus induced are significantly larger than can be achieved by mechanical means or by deposition on a substrate with a lattice mismatch. One can also manipulate the chemical pressure in the system through the use of a combination of different halogen atoms in the functional group, e.g. $-CXY_2$ ($X, Y =$

F or Cl). We show that, as a result, GeCCl_3 and GeCFCl_2 are topological insulators at ambient conditions, while GeCF_3 displays a topological transition at a relatively small tensile strain of 5%. These results can be compared to the strains of 10% and 12% at which GeH and GeCH_3 have been predicted to become topological insulators. Moreover, GeCFCl_2 is found to be a large-gap TI. We hope our work will stimulate experimental work on the synthesis and measurement of the properties of GeCFCl_2 , GeCCl_3 , and GeCF_3 . Our results have significant implications for the prospective use of these materials in future devices.

Bibliography

- [1] C. L. Kane and E. J. Mele, “ Z_2 topological order and the quantum spin Hall effect,” *Phys. Rev. Lett.*, vol. 95, p. 146802, 2005.
- [2] M. Z. Hasan and C. L. Kane, “Colloquium: Topological insulators,” *Rev. Mod. Phys.*, vol. 82, pp. 3045–3067, 2010.
- [3] X.-L. Qi and S.-C. Zhang, “Topological insulators and superconductors,” *Rev. Mod. Phys.*, vol. 83, pp. 1057–1110, 2011.
- [4] A. Bansil, H. Lin, and T. Das, “Colloquium: Topological band theory,” *Rev. Mod. Phys.*, vol. 88, p. 021004, 2016.
- [5] G. Fiori, F. Bonaccorso, G. Iannaccone, T. Palacios, D. Neumaier, A. Seabaugh, S. K. Banerjee, and L. Colombo, “Electronics based on two-dimensional materials,” *Nat. Nanotech.*, vol. 9, p. 768, 2014.
- [6] A. C. Ferrari, F. Bonaccorso, V. Fal’ko, K. S. Novoselov, S. Roche, P. Boggild, S. Borini, F. H. L. Koppens, V. Palermo, N. Pugno, *et al.*, “Science and technology roadmap for graphene, related two-dimensional crystals, and hybrid systems,” *Nanoscale*, vol. 7, pp. 4598–4810, 2015.

-
- [7] B. A. Bernevig, T. L. Hughes, and S.-C. Zhang, “Quantum spin hall effect and topological phase transition in HgTe quantum wells,” *Science*, vol. 314, no. 5806, pp. 1757–1761, 2006.
- [8] L. Fu, C. L. Kane, and E. J. Mele, “Topological insulators in three dimensions,” *Phys. Rev. Lett.*, vol. 98, p. 106803, Mar 2007.
- [9] L. Fu and C. L. Kane, “Topological insulators with inversion symmetry,” *Phys. Rev. B*, vol. 76, p. 045302, 2007.
- [10] A. A. Soluyanov and D. Vanderbilt, “Computing topological invariants without inversion symmetry,” *Phys. Rev. B*, vol. 83, p. 235401, Jun 2011.
- [11] Y. Ando, “Topological insulator materials,” *Journal of the Physical Society of Japan*, vol. 82, no. 10, p. 102001, 2013.
- [12] L. Fu, C. L. Kane, and E. J. Mele, “Topological insulators in three dimensions,” *Phys. Rev. Lett.*, vol. 98, p. 106803, 2007.
- [13] C. Si, J. Liu, Y. Xu, J. Wu, B.-L. Gu, and W. Duan, “Functionalized germanene as a prototype of large-gap two-dimensional topological insulators,” *Phys. Rev. B*, vol. 89, p. 115429, 2014.
- [14] L. Kou, Y. Ma, Z. Sun, T. Heine, and C. Chen, “Two-dimensional topological insulators: Progress and prospects,” *The Journal of Physical Chemistry Letters*, vol. 8, no. 8, pp. 1905–1919, 2017.
- [15] Z.-Q. Huang, C.-H. Hsu, F.-C. Chuang, Y.-T. Liu, H. Lin, W.-S. Su, V. Ozolins, and A. Bansil, “Strain driven topological phase transitions in atomically thin films of group IV and v elements in the honeycomb structures,” *New Journal of Physics*, vol. 16, p. 105018, oct 2014.
- [16] Q. Liu, X. Zhang, L. B. Abdalla, A. Fazzio, and A. Zunger, “Switching a normal insulator into a topological insulator via electric field with application

- to phosphorene,” *Nano Letters*, vol. 15, no. 2, pp. 1222–1228, 2015. PMID: 25607525.
- [17] E. Taghizadeh Sisakht, F. Fazileh, M. H. Zare, M. Zarenia, and F. M. Peeters, “Strain-induced topological phase transition in phosphorene and in phosphorene nanoribbons,” *Phys. Rev. B*, vol. 94, p. 085417, 2016.
- [18] W. Liu, X. Peng, C. Tang, L. Sun, K. Zhang, and J. Zhong, “Anisotropic interactions and strain-induced topological phase transition in Sb_2Se_3 and Bi_2Se_3 ,” *Phys. Rev. B*, vol. 84, p. 245105, 2011.
- [19] Y. Liu, Y. Y. Li, S. Rajput, D. Gilks, L. Lari, P. L. Galindo, M. Weinert, V. K. Lazarov, and L. Li, “Tuning dirac states by strain in the topological insulator Bi_2Se_3 ,” *Nat. Phys.*, vol. 10, p. 294, 2014.
- [20] Y. L. Chen, J. G. Analytis, J.-H. Chu, Z. K. Liu, S.-K. Mo, X. L. Qi, H. J. Zhang, D. H. Lu, X. Dai, Z. Fang, *et al.*, “Experimental realization of a three-dimensional topological insulator, Bi_2Te_3 ,” *Science*, vol. 325, pp. 178–181, 2009.
- [21] J. Li, C. He, L. Meng, H. Xiao, C. Tang, X. Wei, J. Kim, N. Kioussis, G. Malcolm Stocks, and J. Zhong, “Two-dimensional topological insulators with tunable band gaps: Single-layer HgTe and HgSe ,” *Sci. Rep.*, vol. 5, p. 14115, 2015.
- [22] F.-C. Chuang, C.-H. Hsu, C.-Y. Chen, Z.-Q. Huang, V. Ozolins, H. Lin, and A. Bansil, “Tunable topological electronic structures in $\text{Sb}(111)$ bilayers: A first-principles study,” *Appl. Phys. Lett.*, vol. 102, p. 022424, 2013.
- [23] C. Weeks, J. Hu, J. Alicea, M. Franz, and R. Wu, “Engineering a robust quantum spin Hall state in graphene via adatom deposition,” *Phys. Rev. X*, vol. 1, p. 021001, Oct 2011.
- [24] S.-Y. Xu, Y. Xia, L. A. Wray, S. Jia, F. Meier, J. H. Dil, J. Osterwalder, B. Slomski, A. Bansil, H. Lin, R. J. Cava, and M. Z. Hasan, “Topological phase

- transition and texture inversion in a tunable topological insulator,” *Science*, vol. 332, no. 6029, pp. 560–564, 2011.
- [25] Y. Xu, B. Yan, H.-J. Zhang, J. Wang, G. Xu, P. Tang, W. Duan, and S.-C. Zhang, “Large-gap quantum spin Hall insulators in tin films,” *Phys. Rev. Lett.*, vol. 111, p. 136804, Sep 2013.
- [26] A. Hermann, J. Furthmüller, H. W. Gaggeler, and P. Schwerdtfeger, “Spin-orbit effects in structural and electronic properties for the solid state of the group-14 elements from carbon to superheavy element 114,” *Phys. Rev. B*, vol. 82, p. 155116, 2010.
- [27] S. Cahangirov, M. Topsakal, E. Aktürk, H. Şahin, and S. Ciraci, “Two- and one-dimensional honeycomb structures of silicon and germanium,” *Phys. Rev. Lett.*, vol. 102, p. 236804, 2009.
- [28] C.-C. Liu, W. Feng, and Y. Yao, “Quantum spin Hall effect in silicene and two-dimensional germanium,” *Phys. Rev. Lett.*, vol. 107, p. 076802, 2011.
- [29] M. Ezawa, “Monolayer topological insulators: Silicene, germanene, and stanene,” *J. Phys. Soc. JPN*, vol. 84, p. 121003, 2015.
- [30] A. Acun, L. Zhang, P. Bampoulis, M. Farmanbar, A. van Houselt, A. N. Rudenko, M. Lingenfelder, G. Brocks, B. Poelsema, M. I. Katsnelson, and H. J. W. Zandvliet, “Germanene: the germanium analogue of graphene,” *J. Phys. Condens. Matter*, vol. 27, p. 443002, 2015.
- [31] E. Bianco, S. Butler, S. Jiang, O. D. Restrepo, W. Windl, and J. E. Goldberger, “Stability and exfoliation of germanane: A germanium graphane analogue,” *ACS Nano*, vol. 7, pp. 4414–4421, 2013.
- [32] S. Jiang, S. Butler, E. Bianco, O. D. Restrepo, W. Windl, and J. E. Goldberger,

- “Improving the stability and optical properties of germanane via one-step covalent methyl-termination,” *Nat. Commun.*, vol. 5, p. 3389, 2014.
- [33] Y. Ma, Y. Dai, W. Wei, B. Huang, and M. H. Whangbo Ma, “Strain-induced quantum spin Hall effect in methyl-substituted germanane GeCH_3 ,” *Sci. Rep.*, vol. 4, p. 7297, 2014.
- [34] P. Giannozzi, S. Baroni, N. Bonini, M. Calandra, R. Car, C. Cavazzoni, D. Ceresoli, G. L. Chiarotti, M. Cococcioni, I. Dabo, *et al.*, “Quantum espresso: a modular and open-source software project for quantum simulations of materials,” *J. Phys. Condens. Matter*, vol. 21, p. 395502, 2009.
- [35] D. Vanderbilt, “Soft self-consistent pseudopotentials in a generalized eigenvalue formalism,” *Phys. Rev. B*, vol. 41, pp. 7892–7895, 1990.
- [36] J. P. Perdew, K. Burke, and M. Ernzerhof, “Generalized gradient approximation made simple,” *Phys. Rev. Lett.*, vol. 77, pp. 3865–3868, 1996.
- [37] J. Heyd, G. E. Scuseria, and M. Ernzerhof, “Hybrid functionals based on a screened Coulomb potential,” *J. Chem. Phys.*, vol. 118, pp. 8207–8215, 2003.
- [38] N. Troullier and J. L. Martins, “Efficient pseudopotentials for plane-wave calculations,” *Phys. Rev. B*, vol. 43, pp. 1993–2006, 1991.
- [39] S. Grimme, “Accurate description of van der waals complexes by density functional theory including empirical corrections,” *J. Comput. Chem.*, vol. 25, pp. 1463–1473, 2004.
- [40] S. Grimme, “Semiempirical GGA-type density functional constructed with a long-range dispersion correction,” *J. Comput. Chem.*, vol. 27, pp. 1787–1799, 2006.

- [41] A. Dal Corso and A. Mosca Conte, “Spin-orbit coupling with ultrasoft pseudopotentials: Application to Au and Pt,” *Phys. Rev. B*, vol. 71, p. 115106, 2005.
- [42] R. Dronskowski and P. E. Bloechl, “Crystal orbital hamilton populations (COHP): energy-resolved visualization of chemical bonding in solids based on density-functional calculations,” *J. Phys. Chem.*, vol. 97, p. 8617, 1993.
- [43] S. Maintz, V. L. Deringer, A. L. Tchougreff, and R. Dronskowski, “Lobster: A tool to extract chemical bonding from plane-wave based dft,” *Journal of Computational Chemistry*, vol. 37, no. 11, pp. 1030–1035, 2016.
- [44] Y. L. Huang, Y. Chen, W. Zhang, S. Y. Quek, C.-H. Chen, L.-J. Li, W.-T. Hsu, W.-H. Chang, Y. J. Zheng, W. Chen, *et al.*, “Bandgap tunability at single-layer molybdenum disulphide grain boundaries,” *Nature Communications*, vol. 6, p. 6298, 2015.
- [45] G. Q. Huang and Z. W. Xing, “Band-gap tunability and dynamical instability in strained monolayer and bilayer phosphorenes,” *Journal of Physics: Condensed Matter*, vol. 27, p. 175006, apr 2015.
- [46] Q. Wu, S. Zhang, H.-F. Song, M. Troyer, and A. A. Soluyanov, “Wanniertools : An open-source software package for novel topological materials,” *Comput. Phys. Commun.*, vol. 224, pp. 405 – 416, 2018.
- [47] S. Kumar, K. P. S. S. Hembram, and U. V. Waghmare, “Intrinsic buckling strength of graphene: First-principles density functional theory calculations,” *Phys. Rev. B*, vol. 82, p. 115411, Sep 2010.
- [48] H. Soni and P. K. Jha, “Ab-initio study of dynamical properties of two dimensional MoS₂ under strain,” *AIP Advances*, vol. 5, no. 10, p. 107103, 2015.

-
- [49] Y. P. Chen, “Topological insulator-based energy efficient devices,” *SPIE Proceedings*, vol. 8373, 2012.

Chapter 8

GeCCl₃: A Model Topological Material

In this chapter, using density functional theory calculations, we show that it is possible to observe a number of non-trivial topological phases, such as strong and weak topological insulators, Dirac and Weyl nodal line semimetals, in the three-dimensional bulk of a single material, GeCCl₃, under suitable conditions.

8.1 Introduction

Materials with non-trivial band topology have drawn tremendous attention in the past few years since the discovery of topological insulators (TIs). [1–5] Topological semimetals, such as Weyl semimetals (WSMs), Dirac semimetals (DSMs) and nodal-line semimetals (NLSs) provide useful test systems to check fundamental theories of physics (e.g., Dirac and Weyl fermions) beside providing possibility of novel device applications. They also make it feasible to study new types of fermions which do not have their counterpart in high-energy physics. e.g., type-II Weyl, spin-1 Weyl, double Dirac, etc. [6–9]

Topological insulators, or quantum spin Hall (QSH) insulators are materials with a bulk insulating gap, and conducting edge states. In three-dimensions (3D) there can be weak (WTI) or strong topological insulators (STI) depending on whether the edge

states are topologically protected, or in other words, robust against disorder, or not. Kane and Mele proposed graphene as the first TI, with a very small band gap (~ 0.04 meV), introduced due to spin-orbit coupling (SOC).[10] However, the extremely small band gap in graphene makes it unsuitable for use in devices. Subsequently, the HgTe-CdTe semiconductor quantum well was predicted to show QSH effect in two-dimensions (2D), and this was soon experimentally realized.[11, 12] Since then a lot of materials have been shown to display topological insulator properties, either at ambient conditions, or under the application of strain, or electric field.[13, 14]

Topological semimetals, like topological insulators, are also characterized by surface states, but do not show a bulk band gap. WSMs are semimetals whose low-energy excitations are Weyl fermions that manifest themselves as linearly dispersive bands in three-dimensional (3D) momentum space through nodes called Weyl points. The Weyl points always appear in pairs. In a WSM, either the time reversal symmetry (TRS) or the inversion symmetry (IS) is broken. The existence of Weyl fermions was first proposed by Wan *et al.* in pyrochlore iridates,[15] where the appearance of surface states in the form of Fermi arcs, has been theoretically observed. Subsequent theoretical proposals of Weyl semimetals include the materials HgCr₂Se₄,[16] and Hg_{1-x-y}Cd_xMn_yTe.[17]

When both TRS and IS are present, the pair of Weyl points becomes degenerate, leading to a DSM phase. [18] The possibility of the existence of a four-fold degenerate Dirac point in the 3D bulk of a material was first proposed by Abrikosov and Beneslavskii,[19] and more recently by Wang *et al.*, and Young *et al.*[20] In some instances, the Dirac point is found to be protected by space group symmetries. Examples of such symmetry-protected DSMs include Cd₃As₂,[21] and Na₃Bi.[22]

In a Dirac or Weyl semimetal the bands can cross along a line or a closed curve, resulting in a NLS. NLSs have been theoretically proposed in a number of materials,[23] but conclusive experimental evidence, using angle resolved photoemission spectroscopy (ARPES), has only been found recently for TiB₂,[24] and ZrB₂. [25]

Although these distinct topological phases have been realized separately in different materials, a study of all these phases in a single material is absent due to lack of multitunability of a material in general. In this chapter we discuss the results from density functional theory calculations on bulk GeCCl_3 in inversion symmetric and non-inversion symmetric form. We show that since GeCCl_3 is a layered material, one can use thickness and stacking in addition to strain or pressure to tune its topological properties. We see that the topological property of GeCCl_3 is different in the bulk as compared to its monolayer, leading to different topological phases in them. Inversion symmetry in the system can be broken by altering the stacking from AA - to AB -type, which results in a further topological phase transition. Moreover, we show that by applying a moderate amount of hydrostatic pressure, one can make both the IS and NIS (non-inversion symmetric) systems transition into STIs. The details of these results are presented further below.

8.2 Systems under study

In our previous study (see Chapter 8), we have shown that the removal of the dynamic instability at the Γ point of the Brillouin zone of monolayer of GeCCl_3 (in-plane lattice constant $a = 5.47 \text{ \AA}$) results in a symmetry-lowering distortion, achieved by displacing the atoms in the unit cell along the eigenvectors of the imaginary phonon mode at the zone center. As a result of the distortion, the Ge-Ge bonds along the zigzag direction of GeCCl_3 are unequal: the ‘magenta’ and ‘black’ Ge-Ge bonds are of lengths 3.57 \AA and 3.04 \AA respectively (see Fig. 8.1(a)). The D - GeCCl_3 structure is more stable than its parent structure, P - GeCCl_3 (35 meV/unit cell lower in energy), and the lattice constant remains unchanged. The distorted GeCCl_3 (D - GeCCl_3) monolayer is shown to be a topological insulator. In the following discussion, we will study the topological properties of the bulk D - GeCCl_3 , in 3D.

In Fig. 8.1(a) we show the top view of the bulk unit cell (blue shaded rhombus) of inversion symmetric D - GeCCl_3 , with an AA stacking, whereas in (b) the inversion

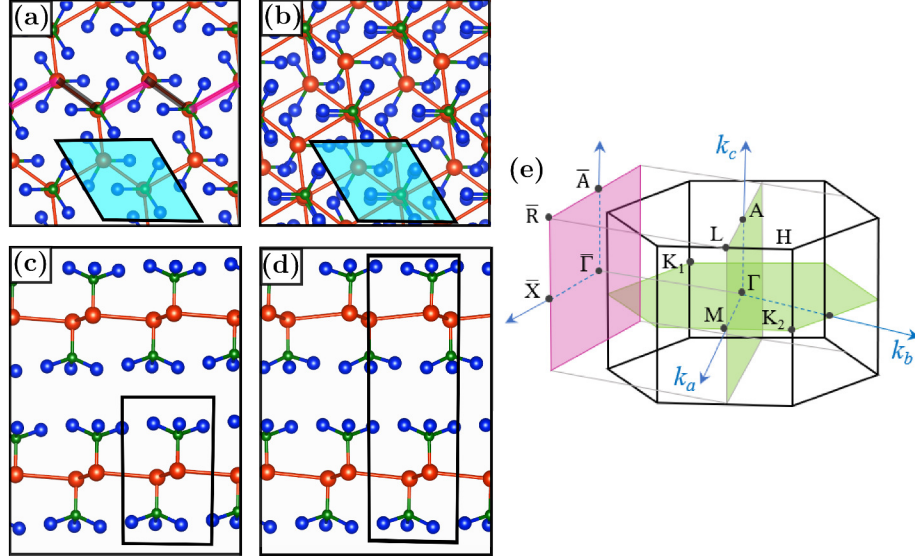


Figure 8.1: Structures of $D\text{-GeCCl}_3$: panels (a) and (b) [(c) and (d)] show the schematic top (side) views of $D\text{-GeCCl}_3$. (a) and (c) correspond to AA -stacking (with IS), whereas (b) and (d) correspond to AB -stacking (without IS). The shaded rhombus in Blue in (a) and (b) depicts a unit cell. Red, Green and Blue spheres indicate Ge, C and Cl atoms, respectively. Magenta and black colored lines in (a) show bonds of different lengths due to in-plane distortion. Panel (e) shows the bulk BZ and its (010) surface (in pink).

symmetry is broken by AB -stacking. Panels (c) and (d) show the side views of the AA - and AB -stacked $D\text{-GeCCl}_3$, respectively, along with the corresponding unit cells. Note, in the AB -stacking the cell length has doubled in the direction perpendicular to the plane of $D\text{-GeCCl}_3$. The in-plane lattice constant, which is the same as that of monolayer $D\text{-GeCCl}_3$, of both AA - and AB -stacked systems, is 5.47 \AA . The interlayer separation between two consecutive $D\text{-GeCCl}_3$ layers for the AA -stacked structure is 3.24 \AA . The AB -stacked $D\text{-GeCCl}_3$ is found to have a slightly larger interlayer separation of 3.39 \AA .

8.3 Computational details

Our calculations have been performed using *ab initio* density functional theory (DFT) as implemented in the Quantum-ESPRESSO package. [26] The Kohn-Sham equations are expanded in a plane wave basis set, together with ultrasoft pseudopotentials, [27] and the PBE form of the generalized gradient approximation. [28] The

cut-offs for wave functions and charge densities are 40 Ry and 400 Ry respectively. $8 \times 8 \times 6$, and $8 \times 8 \times 3$ Monkhorst-Pack k -point meshes are used to sample the Brillouin zones (BZs) of the AA -stacked and AB -stacked D -GeCl₃, respectively.[29] All atomic coordinates are relaxed until forces are $< 1.0 \times 10^{-3}$ Ry/Bohr. van der Waals interactions are incorporated using the ‘DFT-D2’ method.[30, 31] Spin-orbit interactions are treated using fully relativistic pseudopotentials.[32]

The structures of the nodal lines, surface states and Fermi arcs have been computed using the WannierTools package, [33] which involves wannierization of the plane wave basis, and subsequent implementation in a tight binding approximation, using the Hamiltonian overlap matrix elements obtained from the wannierization.

The Z_2 topological index for the inversion symmetric structure has been calculated using the parity of the bands at the eight time reversal invariant momenta (TRIM) points in the Brillouin zone (BZ), using the following equation:[34]

$$\delta_i = \prod_m \xi_m(\Lambda_i), \quad (8.1)$$

where the product is over the pairs of parity eigenvalues of the occupied Kramers doublets resulting from the time reversal symmetry, at the TRIM points Λ_i , given by $\xi_m(\Lambda_i)$, without multiplying the corresponding time reversed partners. The strong topological invariant ν_0 is then expressed as

$$(-1)^{\nu_0} = \prod_{i=1}^8 \delta_i. \quad (8.2)$$

The other three weak invariants are given by the product of the δ_i ’s for which the TRIM points $\Lambda_{i=(n_1 n_2 n_3)} = \frac{1}{2}(n_1 \mathbf{b}_1 + n_2 \mathbf{b}_2 + n_3 \mathbf{b}_3)$, ($\mathbf{b}_1, \mathbf{b}_2$, and \mathbf{b}_3 being the reciprocal lattice vectors), reside in the same plane, given as

$$(-1)^{\nu_k} = \prod_{n_k=1; n_j \neq k=0,1} \delta_{i=(n_1 n_2 n_3)}. \quad (8.3)$$

To compute the Z_2 index for the structures without inversion symmetry we use the Wannier charge center method as implemented in WannierTools,[33, 35] which computes the number of jumps in the Wannier charge centers, when plotted against a k -point path in the Brillouin zone (BZ). Even/odd number of jumps indicate trivial/topological insulator.

8.4 Results and Discussion

8.4.1 Nodal lines in $D\text{-GeCCl}_3$

In chapter 7, we have seen that $D\text{-GeCCl}_3$, in its monolayer, is a topological insulator. In this chapter, we look at the topological properties of $D\text{-GeCCl}_3$ in its 3D bulk. Henceforth, in this chapter, when we refer to $D\text{-GeCCl}_3$, we always mean the layered bulk structure.

In order to observe the presence of Dirac or Weyl nodes, we start by looking at the 3D band structure of the AA (IS) and AB stacked (NIS) $D\text{-GeCCl}_3$, excluding spin-orbit interactions. In Fig. 8.2(a), we plot the 3D band structure (without incorporating SOC), of the topmost valence band, and the bottommost conduction band, of the inversion symmetric, or AA -stacked $D\text{-GeCCl}_3$, at $k_z = 0$. To capture the details of the morphology of the bands near the Dirac or Weyl nodes, we use a fine k -mesh of $49 \times 80 \times 1$ k -points, in the portion of the BZ which contains the Dirac or Weyl points. We see the presence of a pair of Dirac cones which lie close to the high-symmetry line $K_1\text{-}\Gamma\text{-}K_2$ (see Fig. 8.1 (e)) in the BZ. Upon breaking the inversion symmetry through stacking in AB -stacked $D\text{-GeCCl}_3$, each of these Dirac nodes is found to get split into pairs of Weyl nodes as shown in Fig. 8.2(b).

To understand how these Dirac or Weyl nodes extend in the BZ, we plot the nodal line structure of the Dirac and Weyl points in Figs. 8.2(c) and (d), respectively. The nodes represent points in the 3D BZ where the band gap is ≤ 3 meV. We note that the use of a finer k -point mesh can result in a lower threshold of band gap, closer to 0 eV, for the generation of the nodal lines. In Fig. 8.2(c), we see that the Dirac points

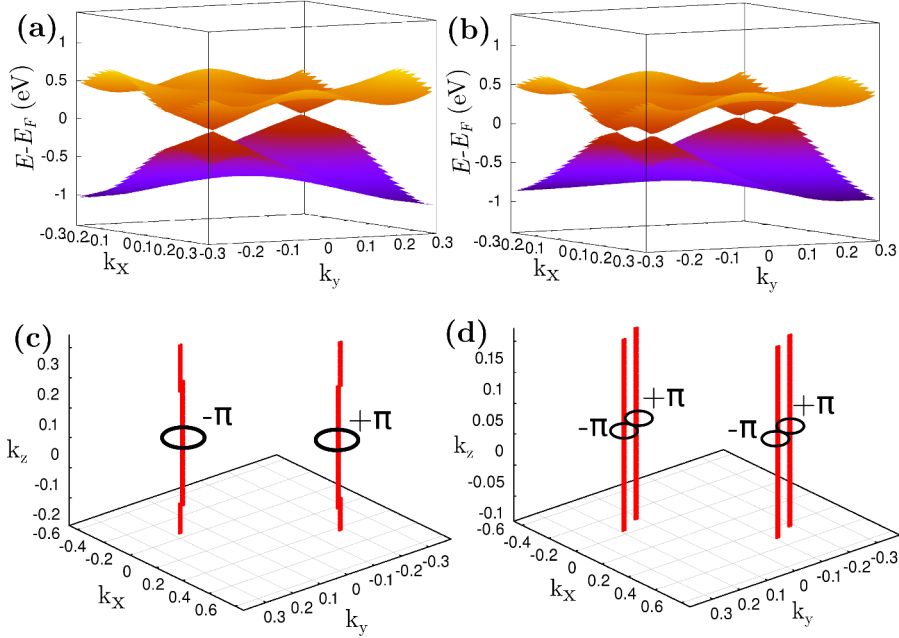


Figure 8.2: 3D band structures (without SOC) and structure of nodal lines: panels (a) and (b) show the 3D band structures of Dirac and Weyl NLSs, respectively at $k_z = 0$. Two Dirac nodes can be seen in (a), each of which splits into a pair of Weyl nodes as the inversion symmetry is broken by stacking, as shown in (b). The straight lines in Red in (c) [(d)] shows the structure of the nodal lines of Dirac (Weyl) NLS. The computed Berry phases in closed loops around nodal lines are also shown in (c) and (d).

in the BZ form a pair of nodal straight lines, extending in the k_z direction of the BZ. Each of these Dirac nodal straight lines splits into a pair of Weyl nodal straight lines as shown in Fig. 8.2(d) when the inversion symmetry is broken by AB stacking.

We confirm the topologically non-trivial nature of the nodal lines, by computing the Berry phase on a closed loop around the nodal lines. The Berry phase is calculated using the following equation:[36]

$$\gamma_n = \oint \mathbf{A}_n(\mathbf{k}) \cdot d\mathbf{l}, \quad (8.4)$$

where $\mathbf{A}_n(\mathbf{k}) = i \langle u_n(\mathbf{k}) | \nabla_{\mathbf{k}} | u_n(\mathbf{k}) \rangle$ is the Berry connection, and $u_n(\mathbf{k})$ is the Bloch wavefunction of the n -th band. We find that the Dirac and Weyl nodal lines have a non-zero Berry phase of either $+\pi$ or $-\pi$ as shown in Figs. 8.2(c) and (d). This provides evidence of the non-trivial topological nature of the nodal lines. The opposite

signs of the Berry phases indicate the opposite chirality of the Dirac and Weyl nodal lines. This observation is important as the surface states are known to connect the nodes of opposite chirality, as will be seen further below.

8.4.2 Surface states in $D\text{-GeCCl}_3$

The signature of the Dirac and Weyl nodal lines are the *drumhead* or flat surface states near the Fermi level. We have used the surface Green's function technique, as implemented in the WannierTools package,[\[33\]](#) to calculate the surface state spectrum, where the intensity of the bands is proportional to the spectral function, which is the imaginary part of the surface Green's function.

Figs. [8.3\(a\)](#) and [\(b\)](#) show the surface states at the (010) surface of $D\text{-GeCCl}_3$, corresponding to the Dirac and Weyl nodal straight lines, respectively. The surface BZ is shown in Fig. [8.1\(e\)](#). The low dispersion or flat nature of these surface states should be noted, which is a characteristic feature of the surface states corresponding to the nodal line semimetals. In Figs. [8.3\(c\)](#) and [\(d\)](#) a zoomed-in view of the surface states near the Fermi energy is shown. A single surface state connecting the Dirac nodal lines, and a pair of surface states connecting the Weyl nodal lines of opposite chirality, are visible in Figs. [8.3\(c\)](#) and [\(d\)](#), respectively.

8.4.3 Effect of SOC and hydrostatic pressure

We find that the inclusion of SOC results in the opening up of a band gap in both the IS and NIS systems. The band gap introduced by spin orbit splitting turns out to be 0.11 eV (0.21 eV), for the IS (NIS) structure. The 3D band structure of the IS (NIS) system is plotted in Fig. [8.4 \(a\)](#) [[\(b\)](#)], which shows clearly the opening of band gap in both the systems.

The inclusion of SOC not only introduces a band gap, but also changes the topological nature of the systems. The Z_2 invariants for the inversion symmetric system turn out to be (0; 0, 0, 1) indicating that the system becomes a weak topological insulator (WTI), since the strong topological index is 0, whereas one of

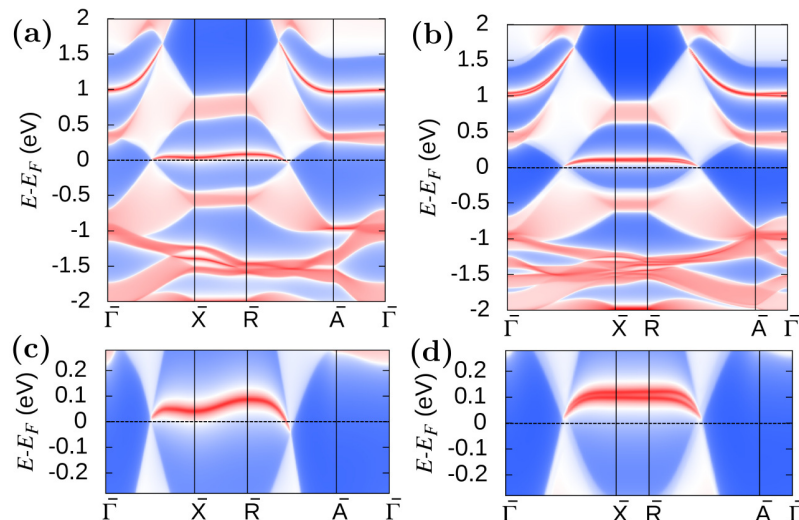


Figure 8.3: Surface states: panels (a) and (b) show the *drumhead* surface states corresponding to the Dirac and Weyl NLSs, respectively. In (c) [(d)] the zoomed in view of the surface states near the Fermi energy is shown for the Dirac (Weyl) NLS. In case of the Dirac NLS, a single surface state connects the Dirac nodes, whereas in Weyl NLS, a pair of surface states connects the pair of Weyl nodes.

the weak topological indices is 1. On the other hand the non-inversion symmetric system turns out to be a trivial insulator as all the Z_2 indices become 0.

It has been shown previously, that application of hydrostatic pressure in 3D bulk systems, such as Bi_2Se_3 ,^[37] NaBaBi ,^[38] BiTeI ,^[39] etc., can induce topological phase transitions leading to TIs. Therefore, it is instructive to further investigate whether the inversion symmetric (IS) or non-inversion symmetric (NIS) $D\text{-GeCCl}_3$ can be made to undergo a further topological phase transition through the application of hydrostatic pressure.

We find that applying a hydrostatic pressure as small as 2.0 GPa (volume compression ratio $V/V_0 = 0.90$) would turn the topologically trivial (with SOC) NIS system into a WTI with $Z_2 = (0;0,0,1)$. At the same amount of hydrostatic pressure, the IS system is found to remain a WTI.

We further increase the hydrostatic pressure to see whether the $D\text{-GeCCl}_3$ systems can be turned into a STI. At a hydrostatic pressure of 6.3 GPa, we find that the strong topological index of both the IS, and the NIS systems turns out to be 1. This indicates that both the systems become STIs, irrespective of the presence of inversion

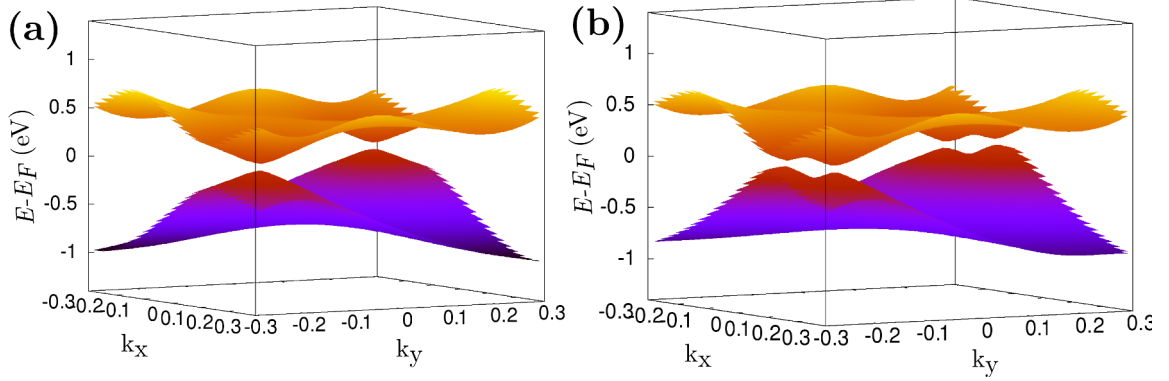


Figure 8.4: 3D band structure of $D\text{-GeCCl}_3$ (with SOC): panels (a), and (b) show the 3D band structures (with SOC) of the IS (AA -stacked), and NIS (AB -stacked) systems, respectively. In both cases we see opening of band gap due to spin-orbit interactions.

symmetry in the system. Both the IS and NIS systems are found to remain strong topological insulators even when the pressure is increased, e.g., at 8.7 GPa, both of them show $Z_2 = (1; 0, 0, 1)$.

In order to look into the band inversion mechanism, we plot the orbital projected band structures (PBE + SOC) of the IS system in the upper panel in Figs. 8.5 (a)-(c), and of the NIS system in the lower panel in Figs. 8.5 (d)-(f), for different amounts of hydrostatic pressures, viz., 2.0 GPa, 4.5 GPa, and 6.3 GPa. The corresponding values of the volume compression ratios are $V/V_0 = 0.90, 0.84$ and 0.80 , respectively. The color indicates the fractional contribution of $p, j = 3/2$ relative to $p, j = 1/2$, with red color corresponding to completely $p, j = 3/2$ character.

Comparing the projected band structures of IS (NIS) $D\text{-GeCCl}_3$, at 4.5 GPa (see Fig. 8.5(b) {(e)}) with that of 6.3 GPa [see Fig. 8.5(c) {(f)}], we can clearly see the character of the valence band maximum (VBM) and the conduction band minimum (CBM) being flipped, indicating that the band inversion occurs between the VBM and CBM at the Γ point in the BZ, when one goes beyond a hydrostatic pressure of 4.5 GPa. Interestingly, in the NIS system, the inversion happens once between the VBM and the CBM at ~ 5.4 GPa and then between CBM and CBM+1 as the pressure is increased further. We find that the band inversion between CBM and

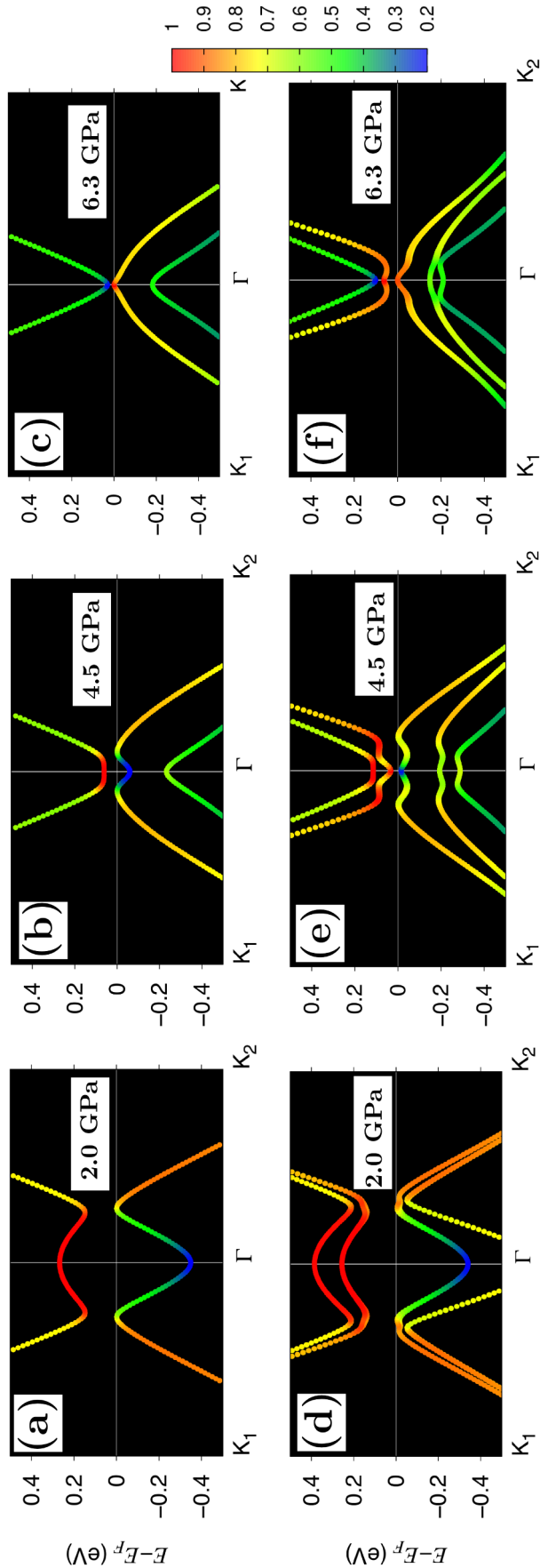


Figure 8.5: Projected band structures (PBE+SOC) for IS (*AA*-stacked) [panels (a), (b) and (c)] and NIS (*AB*-stacked) [panels (d), (e) and (f)] *D*-GeCCl₃ at different hydrostatic pressures. The corresponding magnitudes of hydrostatic pressure are also shown. The color indicates the fractional contribution of $p, j = 3/2$ relative to $p, j = 1/2$, with red color corresponding to totally $j = 3/2$ character.

CBM+1 occurs when the hydrostatic pressure exceeds 5.4 GPa.

To summarize, we have observed a number of topological phases in the 3D bulk of D -GeCCl₃. The Dirac and Weyl NLS phases can be observed in the bulk GeCCl₃ in 3D, in the absence of SOC. When both inversion and time reversal symmetries are present, GeCCl₃ is a Dirac NLS, and it turns into a Weyl NLS when the inversion symmetry is broken by changing stacking from AA to AB . From the structure of the nodes in the 3D BZ, we see that these are nodal straight line semimetals in the sense that the nodes form a straight line in the three-dimensional BZ. We note that the occurrence of nodal straight lines is rare, and has been reported recently only in the phonon band structure of MgB₂. [40] Inclusion of SOC turns the IS system into a WTI, and the NIS system, into a trivial insulator. One can reach a STI phase in both the IS, and NIS systems, through a WTI phase, by applying an appropriate amount of hydrostatic pressure.

8.5 Conclusions

Using density functional theory calculations, we have found that the bulk inversion symmetric D -GeCCl₃ (excluding SOC) is a Dirac nodal straight line semimetal. Breaking the inversion symmetry turns it into a Weyl nodal straight line semimetal. Inclusion of SOC introduces a band gap and turns the inversion symmetric system into a weak topological insulator, whereas the inversion asymmetric structure now becomes a trivial insulator. One can further make both the weak topological insulator and the trivial insulator turn into a strong topological insulator by applying hydrostatic pressure. Thus, one can in principle obtain all the four topologically non-trivial phases (Dirac semimetal, Weyl semimetal, weak topological insulator and strong topological insulator) in the three-dimensional bulk of a single material. Recently layered materials have been found to show robust magnetism down to the monolayer limit. [41, 42] Very recently superconductivity has also been demonstrated in monolayer van der Waals materials. [43, 44] Engineering heterostructures which combine GeCCl₃ with these

systems could be a promising playground for realizing novel phases by introducing magnetism or superconductivity in conjunction with topology.

Bibliography

- [1] X. Wan, A. M. Turner, A. Vishwanath, and S. Y. Savrasov, “Topological semimetal and Fermi-arc surface states in the electronic structure of pyrochlore iridates,” *Phys. Rev. B*, vol. 83, p. 205101, May 2011.
- [2] S. M. Young, S. Zaheer, J. C. Y. Teo, C. L. Kane, E. J. Mele, and A. M. Rappe, “Dirac semimetal in three dimensions,” *Phys. Rev. Lett.*, vol. 108, p. 140405, Apr 2012.
- [3] A. A. Burkov, M. D. Hook, and L. Balents, “Topological nodal semimetals,” *Phys. Rev. B*, vol. 84, p. 235126, Dec 2011.
- [4] N. P. Armitage, E. J. Mele, and A. Vishwanath, “Weyl and Dirac semimetals in three-dimensional solids,” *Rev. Mod. Phys.*, vol. 90, p. 015001, Jan 2018.
- [5] M. Hirayama, R. Okugawa, and S. Murakami, “Topological semimetals studied by ab initio calculations,” *Journal of the Physical Society of Japan*, vol. 87, no. 4, p. 041002, 2018.
- [6] A. A. Soluyanov, D. Gresch, Z. Wang, Q. Wu, M. Troyer, X. Dai, and B. A. Bernevig, “Type-ii Weyl semimetals,” *Nature*, vol. 527, no. 1, p. 495, 2015.
- [7] Y. Xu, F. Zhang, and C. Zhang, “Structured Weyl points in spin-orbit coupled Fermionic superfluids,” *Phys. Rev. Lett.*, vol. 115, p. 265304, Dec 2015.
- [8] B. Bradlyn, J. Cano, Z. Wang, M. G. Vergniory, C. Felser, R. J. Cava, and B. A. Bernevig, “Beyond Dirac and Weyl fermions: Unconventional quasiparticles in conventional crystals,” *Science*, vol. 353, no. 6299, 2016.
- [9] B. J. Wieder, Y. Kim, A. M. Rappe, and C. L. Kane, “Double Dirac semimetals in three dimensions,” *Phys. Rev. Lett.*, vol. 116, p. 186402, 2016.

-
- [10] C. L. Kane and E. J. Mele, “ Z_2 topological order and the quantum spin Hall effect,” *Phys. Rev. Lett.*, vol. 95, p. 146802, Sep 2005.
- [11] B. A. Bernevig and S.-C. Zhang, “Quantum spin Hall effect,” *Phys. Rev. Lett.*, vol. 96, p. 106802, Mar 2006.
- [12] M. König, S. Wiedmann, C. Brüne, A. Roth, H. Buhmann, L. W. Molenkamp, X.-L. Qi, and S.-C. Zhang, “Quantum spin Hall insulator state in HgTe quantum wells,” *Science*, vol. 318, no. 5851, pp. 766–770, 2007.
- [13] A. Bansil, H. Lin, and T. Das, “Colloquium: Topological band theory,” *Rev. Mod. Phys.*, vol. 88, p. 021004, Jun 2016.
- [14] L. Kou, Y. Ma, Z. Sun, T. Heine, and C. Chen, “Two-dimensional topological insulators: Progress and prospects,” *The Journal of Physical Chemistry Letters*, vol. 8, no. 8, pp. 1905–1919, 2017.
- [15] X. Wan, A. M. Turner, A. Vishwanath, and S. Y. Savrasov, “Topological semimetal and Fermi-arc surface states in the electronic structure of pyrochlore iridates,” *Phys. Rev. B*, vol. 83, p. 205101, May 2011.
- [16] G. Xu, H. Weng, Z. Wang, X. Dai, and Z. Fang, “Chern semimetal and the quantized anomalous Hall effect in HgCr_2Se_4 ,” *Phys. Rev. Lett.*, vol. 107, p. 186806, Oct 2011.
- [17] D. Bulmash, C.-X. Liu, and X.-L. Qi, “Prediction of a Weyl semimetal in $\text{Hg}_{1-x-y}\text{Cd}_x\text{Mn}_y\text{Te}$,” *Phys. Rev. B*, vol. 89, p. 081106, Feb 2014.
- [18] B. Yan and C. Felser, “Topological materials: Weyl semimetals,” *Annual Review of Condensed Matter Physics*, vol. 8, no. 1, pp. 337–354, 2017.
- [19] A. A. Abrikosov and S. D. Beneslavskii, “Some properties of gapless semiconductors of the second kind,” *Journal of Low Temperature Physics*, vol. 5, pp. 141–154, Aug 1971.

- [20] S. M. Young, S. Zaheer, J. C. Y. Teo, C. L. Kane, E. J. Mele, and A. M. Rappe, “Dirac semimetal in three dimensions,” *Phys. Rev. Lett.*, vol. 108, p. 140405, Apr 2012.
- [21] S. Borisenko, Q. Gibson, D. Evtushinsky, V. Zabolotnyy, B. Büchner, and R. J. Cava, “Experimental realization of a three-dimensional Dirac semimetal,” *Phys. Rev. Lett.*, vol. 113, p. 027603, Jul 2014.
- [22] Z. K. Liu, B. Zhou, Y. Zhang, Z. J. Wang, H. M. Weng, D. Prabhakaran, S.-K. Mo, Z. X. Shen, Z. Fang, X. Dai, Z. Hussain, and Y. L. Chen, “Discovery of a three-dimensional topological Dirac semimetal, Na_3Bi ,” *Science*, vol. 343, no. 6173, pp. 864–867, 2014.
- [23] H. Weng, X. Dai, and Z. Fang, “Topological semimetals predicted from first-principles calculations,” *Journal of Physics: Condensed Matter*, vol. 28, p. 303001, jun 2016.
- [24] Z. Liu, R. Lou, P. Guo, Q. Wang, S. Sun, C. Li, S. Thirupathaiah, A. Fedorov, D. Shen, K. Liu, H. Lei, and S. Wang, “Experimental observation of Dirac nodal links in centrosymmetric semimetal TiB_2 ,” *Phys. Rev. X*, vol. 8, p. 031044, Aug 2018.
- [25] R. Lou *et al.*, “Experimental observation of bulk nodal lines and electronic surface states in ZrB_2 ,” *npj Quantum Materials*, vol. 3, no. 43, pp. 2397–4648, 2018.
- [26] P. Giannozzi, S. Baroni, N. Bonini, M. Calandra, R. Car, C. Cavazzoni, D. Ceresoli, G. L. Chiarotti, M. Cococcioni, I. Dabo, *et al.*, “Quantum espresso: a modular and open-source software project for quantum simulations of materials,” *J. Phys. Condens. Matter*, vol. 21, no. 39, p. 395502, 2009.
- [27] D. Vanderbilt, “Soft self-consistent pseudopotentials in a generalized eigenvalue formalism,” *Phys. Rev. B*, vol. 41, pp. 7892–7895, Apr 1990.

-
- [28] J. P. Perdew, K. Burke, and M. Ernzerhof, “Generalized gradient approximation made simple,” *Phys. Rev. Lett.*, vol. 77, pp. 3865–3868, Oct 1996.
- [29] H. J. Monkhorst and J. D. Pack, “Special points for Brillouin-zone integrations,” *Phys. Rev. B*, vol. 13, pp. 5188–5192, Jun 1976.
- [30] G. Stefan, “Accurate description of van der Waals complexes by density functional theory including empirical corrections,” *Journal of Computational Chemistry*, vol. 25, no. 12, pp. 1463–1473, 2004.
- [31] G. Stefan, “Semiempirical GGA-type density functional constructed with a long-range dispersion correction,” *Journal of Computational Chemistry*, vol. 27, no. 15, pp. 1787–1799, 2006.
- [32] A. D. Corso and A. Mosca Conte, “Spin-orbit coupling with ultrasoft pseudopotentials: Application to Au and Pt,” *Phys. Rev. B*, vol. 71, p. 115106, Mar 2005.
- [33] Q. Wu, S. Zhang, H.-F. Song, M. Troyer, and A. A. Soluyanov, “Wanniertools : An open-source software package for novel topological materials,” *Computer Physics Communications*, vol. 224, pp. 405 – 416, 2018.
- [34] L. Fu and C. L. Kane, “Topological insulators with inversion symmetry,” *Phys. Rev. B*, vol. 76, p. 045302, Jul 2007.
- [35] A. A. Soluyanov and D. Vanderbilt, “Computing topological invariants without inversion symmetry,” *Phys. Rev. B*, vol. 83, p. 235401, Jun 2011.
- [36] M. V. Berry, “Quantal phase factors accompanying adiabatic changes,” *Proceedings of the Royal Society of London. A. Mathematical and Physical Sciences*, vol. 392, no. 1802, pp. 45–57, 1984.
- [37] M. Yang, Y. Z. Luo, M. G. Zeng, L. Shen, Y. H. Lu, J. Zhou, S. J. Wang, I. K.

- Sou, and Y. P. Feng, “Pressure induced topological phase transition in layered Bi_2S_3 ,” *Phys. Chem. Chem. Phys.*, vol. 19, pp. 29372–29380, 2017.
- [38] Y. Sun, Q.-Z. Wang, S.-C. Wu, C. Felser, C.-X. Liu, and B. Yan, “Pressure-induced topological insulator in NaBaBi with right-handed surface spin texture,” *Phys. Rev. B*, vol. 93, p. 205303, May 2016.
- [39] M. Bahramy, B.-J. Yang, R. Arita, and N. Nagaosa, “Emergence of non-centrosymmetric topological insulating phase in BiTeI under pressure,” *Nature Communications*, vol. 3, p. 679, 2012.
- [40] Q. Xie, J. Li, M. Liu, L. Wang, D. Li, Y. Li, and X.-Q. Chen, “Phononic Weyl Nodal Straight Lines in High-Temperature Superconductor MgB_2 ,” *arXiv e-prints*, p. arXiv:1801.04048, Jan 2018.
- [41] C. Gong *et al.*, “Discovery of intrinsic ferromagnetism in two-dimensional van der Waals crystals,” *Nature*, vol. 546, p. 265, 2017.
- [42] B. Huang *et al.*, “Layer-dependent ferromagnetism in a van der Waals crystal down to the monolayer limit,” *Nature*, vol. 546, p. 270, 2017.
- [43] V. Fatemi, S. Wu, Y. Cao, L. Bretheau, Q. D. Gibson, K. Watanabe, T. Taniguchi, R. J. Cava, and P. Jarillo-Herrero, “Electrically tunable low density superconductivity in a monolayer topological insulator,” *arXiv:1809.04637*, vol. 546, p. 270, 2017.
- [44] E. Sajadi, T. Palomaki, W. Zhao, P. Bement, C. Olsen, X. Xu, J. A. Folk, and D. H. Cobden, “Gate-induced superconductivity in a monolayer topological insulator,” *arXiv:1809.04691*, vol. 546, p. 270, 2017.

Chapter 9

Summary and Outlook

We now summarize the main findings of this thesis and provide a brief outlook for the possible future directions of research.

Throughout the thesis, we have followed the broad theme of rational design of nanomaterials. Using density functional theory calculations, we have designed the materials to tune their electronic, magnetic, chemical, or topological properties, with desired applications in mind. Except for the results presented in Chapters 7 and 8, all the work has been done in collaboration with experimentalists.

We started with tuning the ionization and etching properties of Pt nanoparticles, by changing their size and chemical environment. We found a radical reversal of the usual sintering tendency of Pt nanoparticles, to a tendency of etching, in the presence of π -acidic azo-aromatic ligands, and their derivatives. We found that one can tune the maximum nanoparticle size for which etching (instead of sintering) occurs, by changing the ligand environment. Based on the thermodynamics of etching, a simple equation was derived that could predict this maximum nanoparticle size. We believe that our results can open new avenues in Pt-chemistry, and can provide applications regarding dissolution, collection and reuse of Pt nanoparticles in catalytic converters, synthesis of anti-cancer drugs, etc. Further research needs to be carried out to find appropriate ligands for size-selective etching of nanoparticles of other noble metals,

such as Au and Ag.

Next, in Chapter 4, we formulated a set of descriptors that can predict the efficacy of dye molecules in a dye sensitized solar cell, without going through expensive excited states calculations. Using these descriptors, we predicted the best candidate dye molecule from a set of dye molecules suggested to us by our experimental collaborators. We note that these descriptors can be used to screen a large set of dye molecules to find suitable dyes to be used in the dye sensitized solar cells. The possibility of extending this work by using machine learning models to predict the solar cell conversion efficiency, is also open.

In Chapter 5, we tuned the thickness of Fe thin films, to tune their magnetic properties. We found that Fe goes through both magnetic and structural phase transitions, in its layer-by-layer growth on Ir(001). Exchange splitting was found to stabilize the ferromagnetic ordering of Fe over antiferromagnetic ordering, beyond 4 monolayer thickness of Fe. *Ab initio* stress calculations suggested that Fe layers prefer a face centered tetragonal structure up to 4 monolayers, and body centered tetragonal structure beyond 8 monolayers. Our results put a lower limit to the thickness of the Fe thin films, when used as ferromagnetic films on Ir(001).

In Chapter 6, we tried to shed light on the long standing debate on the structure and magnetic configuration of a V monolayer, grown on Ag(001). We found that the V monolayer, instead of forming an overlayer on Ag(001), preferred to go subsurface, and favored an antiferromagnetic ordering stabilized by exchange splitting. Our results matched well with the experimental angle resolved photoemission spectroscopy data. We note that a similar strategy can be applied to study the structure and magnetic properties of monolayers of other metals that are nonmagnetic in the bulk.

Finally, in Chapters 7 and 8, we proposed chemical pressure as a route to induce topologically non-trivial phases in germanene-like systems, in two and three-dimensions. We showed that chemical functionalization of monolayer germanene by $-CX_3$, where X is a halogen, as one goes down the column of the periodic table,

produces progressively larger strains due to steric repulsion between neighbouring $-CX_3$ groups. This strain, in effect can induce topological phase transitions in the systems at moderate external strains, or at ambient conditions. We found that $GeCF_3$ is a topological insulator at 5% strain, whereas $GeCCl_3$ is a topological insulator at ambient conditions. We also tried using different halogen atoms together in the functional group in the form of $-CXY_2$ ($X, Y = F$ or Cl). It turned out that $GeCFCl_2$ is a large gap topological insulator at ambient conditions. Calculations excluding the spin-orbit interactions showed that going from the monolayer to the three-dimensional bulk in $GeCCl_3$, based on presence or absence of inversion symmetry, one can produce Dirac, or Weyl nodal straight line semimetal, respectively. Inclusion of spin-orbit coupling makes the Dirac (Weyl) nodal line semimetal turn into weak (trivial) topological insulator. One can further make both of them turn into strong topological insulator by application of appropriate amount of hydrostatic pressure. We hope that our work will motivate experiments to synthesize these materials. It also opens up the possibility to use these layered materials to make heterostructures with magnetic monolayers, to realize novel phases by introducing magnetism in conjunction with topology.